Probing the Giant Dipole Resonance Using Nuclear Resonance Fluorescence

Untersuchung der Dipol-Riesenresonanz mittels Kernresonanzfluoreszenz
Zur Erlangung des Grades eines Doktors der Naturwissenschaften (Dr. rer. nat.)
Genehmigte Dissertation von Jörn Kleemann aus Frankfurt am Main
Tag der Einreichung: 14. Oktober 2024, Tag der Prüfung: 20. November 2024

1. Gutachten: Prof. Dr. Dr. h. c. mult. Norbert Pietralla
2. Gutachten: Prof. Dr. Joachim Enders
Darmstadt, Technische Universität Darmstadt

TECHNISCHE
UNIVERSITÄT
DARMSTADT

Fachbereich Physik
Institut für Kernphysik
AG Pietralla

Probing the Giant Dipole Resonance Using Nuclear Resonance Fluorescence
Untersuchung der Dipol-Riesenresonanz mittels Kernresonanzfluoreszenz

Accepted doctoral thesis by Jörn Kleemann

Date of submission: 2024-10-14
Date of thesis defense: 2024-11-20

Darmstadt, Technische Universität Darmstadt

Erklärungen laut Promotionsordnung

§ 8 Abs. 1 lit. d PromO

Ich versichere hiermit, dass zu einem vorherigen Zeitpunkt noch keine Promotion versucht wurde. In diesem Fall sind nähere Angaben über Zeitpunkt, Hochschule, Dissertationsthema und Ergebnis dieses Versuchs mitzuteilen.

§ 9 Abs. 1 PromO

Ich versichere hiermit, dass die vorliegende Dissertation – abgesehen von den in ihr ausdrücklich genannten Hilfen – selbstständig verfasst wurde und dass die „Grundsätze zur Sicherung guter wissenschaftlicher Praxis an der Technischen Universität Darmstadt" und die „Leitlinien zum Umgang mit digitalen Forschungsdaten an der TU Darmstadt" in den jeweils aktuellen Versionen bei der Verfassung der Dissertation beachtet wurden.

§ 9 Abs. 2 PromO

Die Arbeit hat bisher noch nicht zu Prüfungszwecken gedient.

Darmstadt, 14. Oktober 2024

J. Kleemann

Abstract

This work focuses on the experimental investigation of γ decay of the nuclear isovector giant dipole resonance (GDR). While it is a key property of one of the most fundamental nuclear excitations, it has remained poorly characterized despite decades of research on the GDR. To address this long-standing issue, a novel experimental method to systematically study γ decay of the GDR has been developed in this work. It combines the well-established nuclear resonance fluorescence (NRF) technique with state-of-the-art laser-Compton back-scattering (LCB) photon sources for measurements in the GDR's energy domain. A key innovation lies in the usage of linearly polarized LCB photon beams to excite the GDR. This allows resolving its γ decays to final states close in energy, such as the 2_1^+ and 0_1^+ states of deformed nuclei, based on the distinct angular distributions of their NRF reactions.

The newly devised approach was successfully applied in a pilot photonuclear experiment on the GDRs of the semi-magical, spherical nuclide ^{140}Ce and the well-deformed ^{154}Sm at the High Intensity γ-ray Source (HIγS) in Durham, NC, USA. Data was taken at six excitation energies, covering the full evolution of the GDRs of these nuclides. For both, a smooth evolution of the γ-decay behavior of their GDRs with energy is observed and the determined γ-decay branching ratios of the order of 1 % are in agreement with previous measurements. The elastic-scattering cross sections are found to be consistent with the interpretation of the GDR as one coherent excitation. For ^{140}Ce, no γ decay of its GDR to the 2_1^+ state is detected, resulting in stringent upper limits on this decay channel. Contrarily, for the deformed ^{154}Sm significant γ decay of its double-humped GDR to the 2_1^+ state is observed and found to be subject to a strong energy dependence.

The data is well described by the geometrical model of the GDR, demonstrating for the first time its capability to reproduce the GDR's photoabsorption, elastic-scattering, and 2_1^+ Raman-scattering cross sections simultaneously with great accuracy. This

high descriptive power is a novel, compelling argument for the model's validity. Furthermore, γ decay is established as an experimental probe highly sensitive to the structure of the GDR. Finally, this sensitivity is exploited to place strong constraints on the nuclear shape of ^{154}Sm, including its degree of triaxiality. The derived shape parameters agree well with those of other experimental approaches and recent Monte Carlo Shell-Model calculations.

Zusammenfassung

Diese Arbeit konzentriert sich auf die experimentelle Untersuchung des γ-Zerfalls der nuklearen isovektor Dipol-Riesenresonanz (GDR). Obwohl es sich hierbei um eine Schlüsseleigenschaft einer der fundamentalsten Kernanregungen handelt, blieb das γ-Zerfallsverhalten der GDR trotz jahrzehntelanger Forschung zur GDR größtenteils unbekannt. Um dieses seit langem bestehende Problem endlich anzugehen, wurde in dieser Arbeit eine neue experimentelle Methode zur systematischen Untersuchung des γ-Zerfalls der GDR entwickelt. Sie kombiniert die bewährte Methode der Kernresonanzfluoreszenz (KRF) mit modernsten, auf der Laser-Compton-Rückstreuung (LCB) basierenden Photonenquellen für Messungen im Energiebereich der GDR. Dabei besteht eine wesentliche Innovation in der Verwendung von linear polarisierten LCB-Photonenstrahlen zur Anregung der GDR. Dies ermöglicht die Auflösung ihrer γ-Zerfälle zu energetisch naheliegenden Endzuständen, wie den 2_1^+ und 0_1^+ Zuständen deformierter Kerne, durch die charakteristischen Winkelverteilungen ihrer KRF-Reaktionen.

Der neu entwickelte experimentelle Ansatz wurde in einem Pilotexperiment an den GDRs des semi-magischen, sphärischen Nuklids [140]Ce und des wohl-deformierte Nuklids [154]Sm an der High Intensity γ-ray Source (HIγS) befindlich in Durham, NC, USA, erfolgreich angewendet. Dabei wurden Messungen bei sechs Anregungsenergien durchgeführt, welche die gesamte Entwicklung der GDRs dieser Nuklide abdecken. Für beide Nuklide wurde eine glatte Entwicklung des γ-Zerfallsverhaltens ihrer GDRs mit der Anregungsenergie beobachtet und die ermittelten γ-Zerfallsverzweigungsverhältnisse in der Größenordnung von 1 % stimmen mit früheren Messungen überein. Weiterhin sind die gemessenen Wirkungsquerschnitte für elastischen Streuung mit der Interpretation der GDR als eine kohärente Anregung kompatibel. Für [140]Ce wurde kein γ-Zerfall seiner GDR in den 2_1^+ Zustand beobachtet, was zu strikten oberen Limits für diesen Zerfallskanal führt. Im Gegensatz dazu wurde für das deformierte [154]Sm

signifikanter γ-Zerfall seiner aufgespaltenen GDR in den 2_1^+ Zustand beobachtet, der zudem eine starke Energieabhängigkeit aufweist.

Die Daten können durch das geometrische Modell der GDR gut beschrieben werden, was zum ersten Mal zeigt, dass es in der Lage ist, die Wirkungsquerschnitte der Photoabsorption, der elastischen Streuung und der 2_1^+-Raman-Streuung der GDR gleichzeitig mit hoher Genauigkeit zu reproduzieren. Diese große Beschreibungsvermögen ist ein neues, überzeugendes Argument für die Gültigkeit des Modells. Darüber hinaus wird der γ-Zerfall als eine experimentelle Observable etabliert, die sehr empfindlich auf die Struktur der GDR ist. Schließlich wird diese Empfindlichkeit ausgenutzt, um starke Aussagen über die Kernform von ^{154}Sm, einschließlich des Grades seiner Triaxialität, abzuleiten. Die ermittelten Formparameter stimmen gut mit denen anderer experimenteller Ansätze und neuester Berechnungen im Monte-Carlo Schalenmodell überein.

Contents

List of Figures

List of Tables

Terminology and Abbreviations

Beam profile   The shape of the spectral density $\frac{\mathrm{d}\Phi}{\mathrm{d}E}$ of a photon or particle beam with respect to the energy E.

BG   Background

BW   Breit-Wigner. See Section 2.4.

Clover detector   A type of HPGe semiconductor detector for detection of ionizing radiation, such as γ rays. It consists of four HPGe crystals arranged in a close 2×2 cloverleaf-like geometry along its main axis. Thus, in principle, a clover detector represents four separate HPGe detectors housed in a common cryostat. The individual sub-detectors are referred to as clover leaves and their signals can be read out independently.

DAQ   Data acquisition

DEP   Double-escape peak

Detector response   The (conditional) probability distributions of the energy deposited in a detector, and thus measured by it, when singular particles, here always photons, are being emitted with a specific energy from the target position of the setup following a specific angular distribution. The detector response to a particular photon energy, hence, describes the shape of the detector's spectrum expected for a respective mono-energetic photon source and, on an absolute scale, the expected number of counts in the spectrum for a given number of emitted photons. Notably, the detector response contains the FEP, SEP and DEP efficiencies. However, resolution effects are not considered part of the detector response in this work. Unless otherwise noted, the angular distribution is implicitly assumed to be isotropic. Often, the term detector response is also used to refer solely to the expected shape

of the detector's spectrum or even just those parts of it, which are not the FEP. See also Section 4.4.

DFELL   Duke Free Electron Laser Laboratory. A research facility located at Duke University in Durham, North Carolina, USA.

ENRF   Elastic nuclear resonance fluorescence. The special ES case of NRF, in which a nucleus returns to its initial state (usually the ground state) by a single γ emission after the photoexcitation.

ES   Elastic scattering. A scattering process in which the total kinetic energy of the system is conserved, and no energy is transferred to internal degrees of freedom of the scattering partners.

FEL   Free-electron laser

FEP   Full-energy peak

FWHM   Full width at half maximum. The difference between the two values of the independent variable x at which the dependent variable $f(x)$ is equal to half of its maximum value. Hence, for a normal distribution with variance σ^2, the FWHM is $2\sqrt{2\ln(2)}\sigma \approx 2.355\sigma$.

GDR   Isovector giant dipole resonance. See Chapter 1.

GEANT4   A software toolkit for the computer simulation of the passage of particles through matter developed by the GEANT4 Collaboration. Based on a Monte-Carlo approach and an extensive data set on electromagnetic, strong and weak interaction processes of particles in matter. See also Section 4.4.

GS   Ground state

HDI   Highest density interval. The shortest interval containing a given fraction of the probability mass of a distribution. Also known as shortest credible interval. To give an example, the 68.3 % HDI of a normal distribution with mean μ and variance σ^2 is the commonly used 1-σ interval $[\mu - \sigma, \mu + \sigma]$.

HIγS   The High Intensity γ-ray Source. A LCB facility operated by the TUNL. See Section 3.1.2.

HPGe   High-purity germanium. A material used in semiconductor detectors for detection of ionizing radiation, such as γ rays.

J^{π} Spin J and parity $\pi \in \{+, -\}$ quantum numbers of a (nuclear) state

J_k^{π} State labeled k with spin J and parity π of a nucleus. If k is a number and J and π concrete values, this refers to the k-th state of spin J and parity π of a nucleus. For example, 2_1^+ is the first state with spin and parity 2^+. Typical choices for the label variable instead of k are i for an initial state, x for an excited state, f for a final state and GS for the ground state.

$J_i^{\pi} \rightarrow J_f^{\pi}$ Transition from an initial state J_i^{π} to a final state J_f^{π}. Multiple arrows such as $J_i^{\pi} \rightarrow J_x^{\pi} \rightarrow J_f^{\pi}$ indicate a cascade of transitions.

LCB   Laser-Compton back-scattering. The process of back-scattering laser light off a relativistic electron beam used to produce high energy photon beams. See Section 3.1.1.

MCMC   Markov chain Monte Carlo

mvme   A ready-to-use DAQ system provided by mesytec GmbH & Co. KG for use with their commercial, off-the-shelf DAQ hardware. The mvme software with mesytec hardware was used as the DAQ for the experiments of this work. See Section 3.3.2.

n   Neutron

np-nh n-particle-n-hole

NRF   Nuclear resonance fluorescence. See Chapter 2.

p   Proton

PDF   Probability density function

Photon flux   The number of photons Φ passing through the plane perpendicular to the beam direction at the target position in a measurement. Often the term is also used to refer to its temporal density $\frac{d\Phi}{dt}$, spatial density $\frac{d^2\Phi}{dx\,dy}$, spectral density $\frac{d\Phi}{dE}$ or a combination of these. In this work, total photon flux and the symbol Φ always refer to the total number of photons and never to a density. If the differences are important, the respective quantity is explicitly stated in text or by its analytical form.

ΠL   Multipolarity $L \in \{0, 1, 2, \dots\}$ and electromagnetic radiation character $\Pi \in \{E, M\}$. For example, E1 strength refers to electric dipole strength and an M2 transition is short for a magnetic quadrupole transition. See also Section 2.3.

Real photon   A Photon that can exist as a free particle. Used to emphasize the difference to a virtual photon which is only exchanged as an intermediate particle in interactions via the electromagnetic force and doesn't necessarily obey the energy-momentum relation $E = pc$.

SEP   Single-escape peak

Σn   Used as an index to refer to the total photoneutron cross section $\sigma_{\Sigma n}$ defined in Eq. (1.4).

SLO   Standard Lorentzian. See Section 2.4 for discussion of the SLO model and Eq. (1.1) for the SLO parametrization of the GDR's photoabsorption cross section.

TRK   Thomas-Reiche-Kuhn. See Chapter 1.

TUNL   Triangle Universities Nuclear Laboratory. A nuclear physics research laboratory located at Duke University in Durham, North Carolina, USA.

UTR   Upstream target room. The experimental site at HIγS at which the experiments of this work were conducted.

(x,y)   Compact notation for nuclear reactions with incident particle x and outgoing particle(s) y. For example, (n,γ) denotes neutron capture reactions and (γ,γ') NRF reactions. Can also include the target and/or the reaction product in the notation. Examples for this are ^{140}Ce(γ,n)^{139}Ce and ^{154}Sm(γ,p) for photonuclear reactions on ^{140}Ce and ^{154}Sm, respectively.

1. Introduction: The giant dipole resonance

1.1. Overview of the giant dipole resonance and its importance

The photoresponse of atomic nuclei is an elementary aspect of nuclear physics and plays a crucial role in many areas of research, basic and applied, ranging from nuclear structure and astrophysics to reactor design, nuclear non-proliferation and medical-isotope production [1–11]. As illustrated in Fig. 1.1, it is dominated by the isovector giant dipole resonance (GDR), a collective, electric dipole (E1) excitation of the nucleus, which involves all its nucleons [12]. In the macroscopic geometrical model, the GDR corresponds to an out-of-phase oscillation of the protons against the neutrons, while microscopically it is regarded as a collective one-particle-one-hole (1p-1h) excitation built on the ground state [12–14]. The GDR is inherent to all nuclei, except the very lightest [12], which, together with its reign over the electric dipole response, makes it one of the most fundamental nuclear excitations, if not the most. As such, it allows to probe the elementary structure and dynamics of the complex many-body systems of atomic nuclei and, in particular, their bulk properties, such as shape and symmetry energy [12]. For this reason it also acts as an important benchmark for testing nuclear models and theories.

The excitation energy of the GDR typically lies between 10 to 30 MeV [12, 19], depending smoothly on the mass number of the nucleus, as typical for a collective excitation. It usually appears as a pronounced Lorentzian peak in the photoabsorption cross section of spherical nuclei with widths of several MeV [19, 20]. In heavy, deformed nuclei, a clear splitting of the GDR into two overlapping Lorentzians is
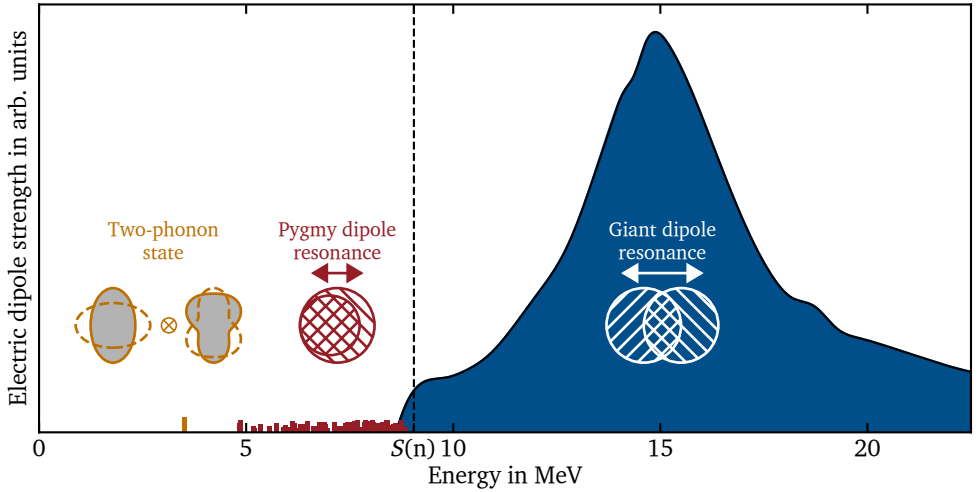
Figure 1.1.: Sketch of a typical electric dipole response expected for a heavy spherical nucleus [12, 15]. The electric dipole response constitutes the majority of the photoabsorption cross section of atomic nuclei and is itself dominated by the GDR. As illustrated, the GDR, located above the neutron separation threshold $S(n)$, dwarfs all other excitations relevant to the nuclear photoresponse, such as the Pygmy Dipole Resonance [16, 17] and the two-phonon state [1, 18].

observed. The phenomenon is evident for ^{154}Sm in Fig. 1.2. This splitting is considered one of the prime signatures of nuclear deformation [24]. It is easily understood in the geometrical model, where an axial deformation of the nucleus allows the oscillation of protons and neutrons against each other either along the nuclear symmetry axis or perpendicular to it [25–28]. Since the axes have different lengths, the frequencies of the oscillations differ, and therefore, the GDR splits into two peaks with a stronger splitting for stronger deformations [29, 30]. One commonly assigns K-quantum numbers[1] $K = 0$ and $K = 1$ to these two oscillation modes, reflecting the geometric interpretation of the distinct oscillation axes [12]. The $K = 0$ mode corresponds to the oscillation along the symmetry axis, while the $K = 1$ mode corresponds to the

---

[1]The K-quantum number gives the projection of the angular momentum $\vec{J}$ onto the symmetry axis of the nucleus. Consequently, it is only a good quantum number in the case of axially symmetric nuclei [31].
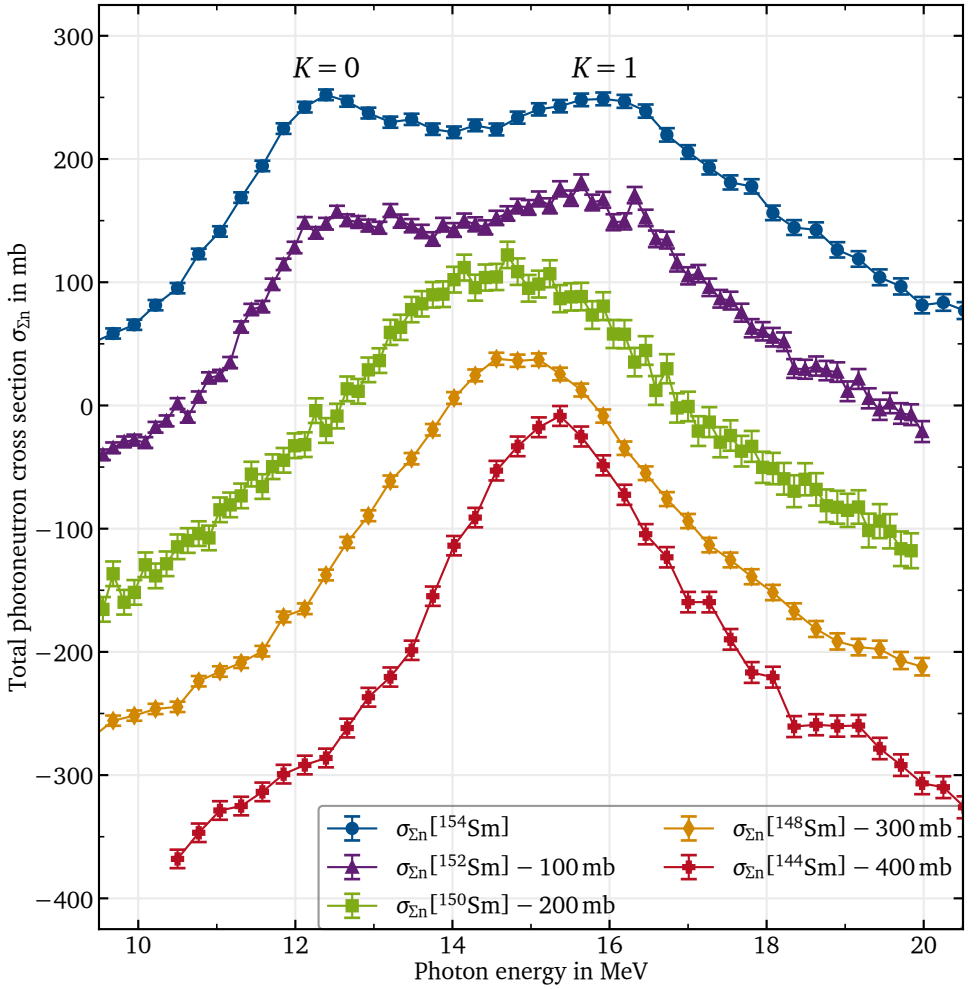
Figure 1.2.: Experimental total photoneutron cross sections of samarium isotopes. The K splitting of the GDR emerges as the deformation increases with mass number from the semi-magical, spherical ^{144}Sm to the well-deformed ^{154}Sm. The data, measured by Carlos *et al.* [21], was retrieved from the EXFOR database [22, 23] and has been offset in magnitude across the isotopes for better visibility.

oscillation perpendicular to it. Naturally, in triaxial nuclei, the GDR is expected to split into three peaks, corresponding to the three possible oscillation modes along the three principal, now distinct, axes of the nucleus. The photoabsorption cross section σ_{Abs} is therefore usually parametrized by a sum of up to three standard Lorentzians (SLOs) [12, 19], i.e.,

$$\sigma_{\text{Abs}}(E) = \sum_{k=1}^{3} \sigma_k^{\text{SLO}}(E) = \sum_{k=1}^{3} \frac{\hat{\sigma}_k}{1 + \left(\frac{E^2 - \hat{E}_k^2}{E \Gamma_k} \right)^2}, \tag{1.1}$$

where $\hat{E}_k$, Γ_k and $\hat{\sigma}_k$ are the resonance energy, the full width at half maximum (FWHM) and the on-resonance photoabsorption cross section of the respective sub-resonances and E the incident photon energy. Due to the similar nature of the sub-resonances in the geometrical picture, it is expected that the energy-integrated photoabsorption cross sections

$$\int \sigma_k^{\text{SLO}}(E)\, \mathrm{d}E = \frac{\pi}{2} \hat{\sigma}_k \Gamma_k \tag{1.2}$$

of the three principal sub-resonances have similar magnitudes. In axially deformed nuclei this leads to the expectation of a $2:1$ ratio of the $K = 1$ and $K = 0$ sub-resonances, which is indeed in rough agreement with experimental data [12].

A benchmark for the integrated photoabsorption cross section of a resonance is the Thomas-Reiche-Kuhn (TRK) sum rule [32–34]. The TRK sum rule gives an idealized theoretical limit of the integrated E1 photoabsorption cross section of a nucleus with Z protons and N neutrons [12, 14]. It states

$$\int_0^\infty \sigma_{\text{Abs}}^{\text{E1}}(E)\, \mathrm{d}E = \frac{2\pi^2 e^2 \hbar c}{4\pi \epsilon_0 \, m_{\text{N}} c^2} \frac{ZN}{N+Z} \approx 60 \frac{ZN}{N+Z} \, \text{MeV}\,\text{mb} \tag{1.3}$$

in SI units, where $\sigma_{\text{Abs}}^{\text{E1}}(E)$ is the E1 photoabsorption cross section at photon energy E, m_{N} is the average nucleon mass, and ϵ_0 is the vacuum permittivity. The GDR usually exhausts 100 % or more[2] of this sum rule, which justifies its designation as a giant resonance.

---

[2]The TRK sum rule underestimates the E1 limit due to the omission of neutron-proton exchange contributions. To account for these, the sum rule is usually corrected by multiplying it by a factor of $(1 + \kappa)$ [14], where κ is the so-called enhancement factor, which ranges from about 0 to 30 % according to experimental data [19].

Finally, due to its location above the particle separation thresholds, the GDR is particle unbound and decays predominantly through particle emission [19]. For medium and heavy nuclei neutron emission is by far the dominant decay channel due to their rather high Coulomb barriers. Therefore, the photoabsorption cross section of the GDR is commonly approximated by the total photoneutron cross section $\sigma_{\Sigma n}$ in these cases, i.e. by

$$\sigma_{\text{Abs}}(E) \approx \sigma_{\Sigma n}(E) := \sum_{k=1}^{\infty} \left(\sigma_{(\gamma, kn)} + \sum_{X \neq n} \sigma_{(\gamma, kn+X)} \right), \tag{1.4}$$

where X denotes any particle or combination of particles not including neutrons (n). In this approximation the contributions of any non-neutron-emitting photonuclear reactions to the photoabsorption cross section are neglected. The photoabsorption cross section of the GDR has been extensively studied in a vast number of experiments throughout the entire nuclear chart [19, 20]. A majority of the data was obtained from photoneutron measurements using real photon beams and the approximation of Eq. (1.4).

Still, the GDR is known to also decay internally by γ emission with a branching ratio of about 1 % [35–42]. Although the effect of this decay branch on the photoabsorption cross section may be small, its implications on the structure of the resonance are profound. The γ-decay behavior is a fundamental aspect that provides a unique window into the internal structure of the GDR and, therefore, also the nucleus as a whole. In particular, the geometrical model of the GDR makes explicit predictions about its γ-decay behavior to the $J^{\pi} = 2^+$ and 0^+ members of the ground-state band [40, 43–45]. These predictions are parameter-free with respect to a given photoabsorption cross-section parameterization and therefore provide an opportunity for a stringent test of the model, especially in the case of deformed nuclei, where its predictions are the most distinct and the model itself is the most regarded [12]. Yet, despite its importance and decades of research on the GDR, the γ decay is still scarcely studied. Only a few experiments have been conducted to investigate it, paling in comparison to the vast number of photoneutron experiments. Moreover, the few available measurements either cover only low GDR excitation energies [37–39] or suffer from insufficient resolution and statistics [40–42]. Thus, a comprehensive experimental assessment of the γ-decay behavior of the GDR and its energy evolution is still missing. In particular, for deformed nuclei, the evolution of the γ-decay branching ratios to the 2_1^+ and 0_1^+ states remains unmeasured, leaving the predictions by the geometrical model of the GDR for these observables largely untested. This is because

until the recent advent of laser-Compton back-scattering (LCB) photon sources [46–49], offering MeV-ranged photon beams with unprecedented intensity, polarization, and energy resolution, it has simply been impossible to efficiently excite the GDR in narrow, freely selectable energy regions to study its γ decay with high resolution and statistics. To address this long-standing issue, it is the purpose of this work to pioneer a novel experimental approach to systematically study the γ decay of the GDR of both spherical and deformed nuclei, thereby launching a new experimental campaign in GDR research using state-of-the-art LCB photon sources.

1.2. A brief history of the giant dipole resonance

The GDR was already discovered in the early days of nuclear physics [50–52] and has since continuously attracted a great deal of attention [3, 12, 14, 19, 20, 53].

First hints of the GDR were found in 1937 by W. Bothe and W. Gentner [50] when they studied nuclear transmutation induced by 17 MeV γ rays for various samples. Based on the strong variance they observed in the photodisintegration cross sections across different nuclei, they hypothesized that resonance phenomena might be involved in the process.

N. Bohr further elaborated on this hypothesis in 1938 [54]. In particular, he showed that a resonance in the photoabsorption cross section is not in contradiction to the compound-nucleus model, which was widely used at the time to explain neutron-induced reactions.

In 1944 A. Migdal published a hydrodynamical theory, which explicitly predicted the existence of a collective nuclear dipole resonance at energies above the neutron separation threshold [55, 56]. However, his work was not widely recognized at the time.

The first clear observation of the GDR was reported by G. C. Baldwin and G. S. Klaiber in 1946 [51, 52]. A new betatron electron accelerator enabled them to produce continuous Bremsstrahlung radiation with an endpoint energy up to 100 MeV. With this tunable photon source, they measured the energy dependence of the cross sections of uranium and thorium photofission as well as ^{12}C and ^{63}Cu (γ,n) photodisintegration.

In all four cases, a similar resonance peak in the cross sections was observed with centroid energies ranging from about 15 MeV for uranium to 30 MeV for ^{12}C.

Unaware of Migdal's publication, M. Goldhaber and E. Teller [25] independently proposed a similar hydrodynamical model to explain this new resonance phenomenon shortly after, which was then regarded as the first theoretical explanation of the GDR. Assuming that the nucleus behaves like a macroscopic drop of proton and neutron fluids, the GDR was interpreted as a collective isovector dipole oscillation of these two fluids against each other, resonantly excited by photoabsorption in the experiments by Baldwin and Klaiber. In such a geometrical model, the GDR must be a universal feature of all nuclei, since no microscopical structure details of the nucleus are considered. The excitation energy scales inversely with the radius of the nucleus, and thus inversely with the cube root of its mass number. The resonance width is understood in analogy to frictional damping of the collective motion.

H. Steinwedel, J. H. D. Jensen and P. Jensen further built on this model in 1950 [26–28]. Goldhaber and Teller had effectively modeled the oscillation of two interpenetrating rigid spheres, which required an arbitrary parameter for the restoring force and changes in total nucleon density. Steinwedel, Jensen, and Jensen, however, considered the oscillation of proton against neutron fluid within a common volume of fixed shape. While Goldhaber and Teller had previously noted this as a potential alternative treatment, Steinwedel, Jensen and Jensen showed that, in this approach, the restoring force of the oscillation can be derived from the nuclear symmetry energy already known from the semi-empirical Bethe-Weizsäcker mass formula.

The next major step in the development of the geometrical, collective model of the GDR was the work by M. Danos and K. Okamoto in 1958 [29, 30]. They both independently concluded that the GDR of axially deformed nuclei should split into two overlapping sub-resonances of different energies, corresponding to the oscillation modes along and perpendicular to the symmetry axis of the nucleus. This provided an explanation for the previously observed splitting of the GDR in the photoabsorption cross sections of deformed nuclei compared to spherical ones.

Since then, numerous aspects of the GDR have been studied across many nuclei, both experimentally and through macroscopic and microscopic theories. In addition to the GDR, several other giant resonances have been found in nuclei, such as the isoscalar giant quadrupole resonance [12]. Furthermore, analogues to the nuclear

GDR were identified in other multiparticle systems [57] such as atoms [58–63], metallic clusters [64–66], and fullerenes [67, 68].

Still, despite decades of research on the nuclear GDR, many questions remain unanswered. What is the true microscopic structure of the GDR? How do the current microscopic and macroscopic models relate to each other and its true structure? What is its lifetime, and does it vary across the energy range of the GDR? What role does internal decay play compared to particle emission? How does the decay behavior of the GDR evolve as a function of excitation energy? These are just a few of the unresolved questions. To address them, more work is needed from both, the experimental and the theoretical side. New experimental data are needed to challenge and refine current theories, ultimately deepening our understanding of the GDR and the nucleus as a whole. This work seeks to contribute to these efforts by developing and applying a novel method to measure the γ decay of the GDR.

1.3. Objectives and structure of this work

As previously stated, this work focuses on the investigation of hitherto hardly studied γ decay of the GDR. Its goal is to establish the γ decay as an experimental observable sensitive to the internal structure of the GDR of spherical and deformed nuclei and thereby the nuclei themselves. In particular, one of the main purposes of this work is to resolve the γ decays of the GDR to the 2_1^+ and 0_1^+ states at arbitrary excitation energies of the GDR and, thus for the first time, measure their individual energy evolution in a deformed nucleus. This will enable a long-overdue, rigorous experimental test of the geometrical model of the GDR through its predictions on the γ-decay branching ratios of the GDR to the ground-state band.

To this end, first a novel experimental approach to measure γ decay of the GDR has to be developed, surpassing the limitations of previous experiments. This is achieved by combining the established nuclear resonance fluorescence (NRF) and photoactivation techniques with state-of-the-art LCB photon sources in the GDR's energy domain. LCB photon beams enable a selective and efficient photoexcitation of the GDR within narrow, freely tunable energy regions. Its γ decay in the induced NRF reactions can then be measured with high resolution and statistics. The ability to conduct such measurements at arbitrary excitation energies allows for a systematic study of this

observable's evolution with energy across the entire GDR. To resolve γ decays to final states close in energy, such as the 2_1^+ and 0_1^+ states of deformed nuclei where the decay signals overlap and cannot be energy-resolved, linearly polarized LCB photon beams are utilized. Excitation of the GDR with linearly polarized photon beams results in distinct angular distributions of its γ decays to various states, allowing for the experimental disentanglement of these overlapping signals. Finally, simultaneous photoactivation measurements are employed to calibrate the photon flux, enabling the determination of absolute γ-decay cross sections from the NRF data.

The next milestone is to apply this experimental approach to study the γ-decay behavior of the GDR for spherical and deformed even-even nuclei. Thus, experiments have been conducted at the High Intensity γ-ray Source (HIγS) at the Triangle Universities Nuclear Laboratory (TUNL) in Durham, North Carolina, USA. The nuclei that have been selected for the pilot study are the deformed ^{154}Sm and the semi-magical, spherical ^{140}Ce. Data have been collected for both rare-earth nuclei at six excitation energies, covering the full evolution of their GDRs. The analysis of this data to extract the γ-decay behavior of their GDRs constitutes the core of this work. Building on the success of the pilot study, a follow-up experiment has furthermore been conducted on the deformed ^{232}Th and the doubly magic, spherical ^{208}Pb extending the GDR research campaign from the rare-earth to the actinide region of the nuclear chart. However, the data from these experiments have yet to be analyzed and will be the subject of future studies.

Finally, the implications of the ^{140}Ce and ^{154}Sm experimental data on the nature of their GDRs and the nuclei themselves are discussed. In particular, the long-overdue, rigorous test of the geometrical model of the GDR is performed by comparing the novel GDR γ-decay data to the model's predictions, thus accomplishing the final objective of this work.

The subsequent chapters follow these objectives. First, the basic physics of photonuclear reactions and their application as an experimental technique are introduced in Chapter 2, focusing on NRF as the photonuclear reaction most relevant to this work. This includes a discussion of the peculiarities of performing NRF experiments on the GDR due to interference effects, and the predictions of the geometrical model on the GDR's γ-decay behavior. Chapter 3 begins with a brief overview of the LCB technique and the HIγS facility implementing this technique, followed by a detailed description of the experimental approach developed to measure γ decay of the GDR via NRF reactions induced by LCB photon beams. This chapter also covers the pilot experiment

on ^{140}Ce and ^{154}Sm realized with this approach. Chapter 4 then elaborates on the data analysis of this experiment, culminating in the extraction of the γ-decay branching ratios of the GDRs of these nuclei to their 2_1^+ and 0_1^+ states from the measured NRF spectra. The results of this analysis on the γ decay of the ^{140}Ce and ^{154}Sm GDRs are presented in Chapter 5 and discussed in Chapter 6. In particular, Chapter 6 compares the experimental results to the predictions of the geometrical model of the GDR on its γ-decay behavior. Finally, Chapter 7 concludes this work with a summary and outlook.

The complete dataset and analysis codes at the core of this work are openly accessible in Ref. [69] via the TUdatalib repository of Technische Universität Darmstadt, enabling full reproduction of all results. Furthermore, parts of this work will be published soon in Ref. [70].

2. Photonuclear reactions

In the following, the fundamentals of photonuclear reactions are laid out, with a focus on NRF, the photonuclear reaction most relevant to this work.

After introducing the notion of photonuclear reactions and their experimental application, this chapter covers the kinematics, selection rules and cross sections of photonuclear reactions in general and NRF specifically. In particular, Section 2.7 illustrates how observables accessible through NRF may in practice be extracted from raw experimental data. Finally, Section 2.9 discusses two specific aspects of NRF on the GDR: significant interference with Thomson scattering and the geometrical model's predictions for the cross sections of elastic and 2_1^+ Raman scattering on the GDR.

For further details on photonuclear reactions and NRF, readers may consult the extensive array of review articles published on the topic [1, 2, 15, 18, 44, 71–73], upon which this chapter is primarily based.

2.1. Introduction to photonuclear reactions and nuclear resonance fluorescence

Photonuclear reactions are nuclear reactions induced by the interaction of real photons with atomic nuclei. Most important for this work is nuclear resonance fluorescence (NRF), which terms the process of resonant absorption and subsequent spontaneous re-emission of photons by atomic nuclei and, hence, belongs to the class of photonuclear reactions. NRF is analogous to the more widely known fluorescence of atoms, where electrons are first excited to higher atomic energy levels and subsequently emit photons

when returning to lower levels again. In the case of NRF, the complex quantum many-body system of the atomic nucleus itself is excited to a higher nuclear energy level through the resonant photoabsorption and likewise subsequently emits photons when returning to lower levels. Since the excitation process in photonuclear reactions only involves photons, it is purely electromagnetic and, therefore, very well understood in contrast to weak or strong interaction processes. This fact makes photonuclear reactions and in particular NRF, where the de-excitation is purely electromagnetic as well, a powerful tool to study the structure of nuclei experimentally, since the well-understood interaction process allows observables to be deduced in an essentially model-independent way from raw data [1]. Observables accessible through NRF include excitation energies, spin and parity quantum numbers, level widths/lifetimes, and decay branching ratios of states, as well as radiation characters, multipolarities, multipole mixing ratios, (integrated) cross sections, and strengths of transitions.

To use photonuclear reactions experimentally for nuclear structure studies, a target containing a macroscopic quantity of the nuclide of interest is irradiated with a photon beam of appropriate intensity and energy to excite the nuclei within through resonant absorptions of single photons. Since the lifetimes of states accessible through photonuclear reactions are typically in the fs regime [1], the excited states will promptly decay to energetically lower-lying states, which will potentially further decay until a ground state (GS) is reached. In the case of NRF, these de-excitations occur through the emission of γ rays by definition. By measuring their energies, emission directions (angular distribution), polarizations, and counts (intensities), information about the overall emitted radiation field, and therefore about the nuclear structure causing it, can be deduced. Of course, other decay modes belonging to different photonuclear reactions, such as internal conversion or photodisintegration, might be possible or even dominating, depending on the nuclear structure and excited level and can likewise provide experimental information about the nuclear structure. Figure 2.1 illustrates NRF and photodisintegration reactions within a nuclear level scheme.

As the excitation energies of nuclear states are usually in the range from hundreds of keV to tens of MeV, so are the energies of photons involved in photonuclear reactions and thus the necessary beam energies for photonuclear experiments. Photons in this energy regime are often called γ rays regardless of their origin, although in the original definition the term γ ray only referred to photons emitted by a nucleus regardless of their energy. Moreover, owing to the typically very short lifetimes of states involved
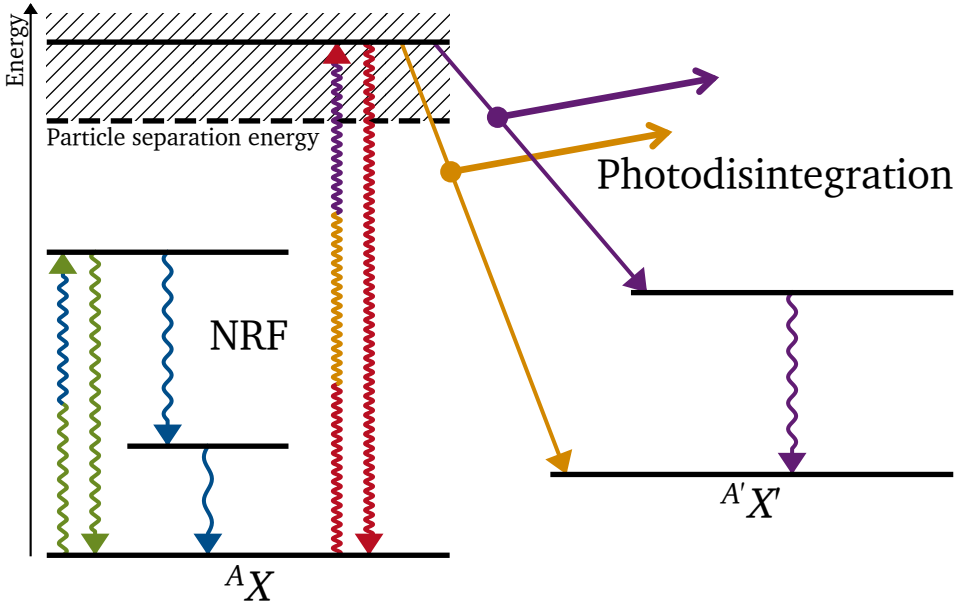
Figure 2.1.: Schematic nuclear level scheme illustrating several possible photonuclear reactions on a nucleus ^{A}X for two incident photon energies. In NRF the nucleus is resonantly excited by absorption of a photon (upward wavy arrows) and subsequently deexcites by emitting one (green and red) or more (blue) photons (downward wavy arrows). NRF primarily, but not exclusively, occurs when the photoexcitation leads to particle-bound states. For photoexcitations to particle-unbound states in the continuum (hatched area) above the neutron or proton separation energies, photodisintegration reactions (straight arrows) can occur. These reactions then usually dominate, leading to the emission of one or more nucleons (circles with arrows) from the nucleus, resulting in a different nucleus $^{A'}X'$, which is left in either its ground state (yellow) or in an excited state (purple). Each color represents a specific reaction sequence, with multicolored arrows belonging to each of their colors' reactions.

in photonuclear reactions, the excitation and ensuing prompt de-excitation process of a nucleus in NRF is occasionally referred to as a cascade. Likewise, due to the resulting similarity of NRF to a scattering process, it is often also denoted as photon scattering, or in reaction notation (γ, γ'), glossing over the detail that in NRF the incident photon is absorbed and a different photon re-emitted, unlike in true photon scattering processes such as Compton/Thomson scattering. This scattering picture additionally leads to two common terms distinguishing two types of de-excitation paths in an NRF cascade: Elastic transitions lead directly to the ground state after the photoexcitation, while inelastic transitions to energetically lower-lying excited states.

2.2. Kinematics of photonuclear reactions

For a nucleus at rest to be able to resonantly absorb a photon, the photon has to carry a little more energy $E_\gamma > E_x - E_i$ than just the difference in excitation energies of the nucleus' initial state i and one of its energetically higher-lying states x. This is due to not only the conservation of energy having to be met in the process, but the conservation of momentum as well, requiring the nucleus to also absorb the photon's momentum $p_\gamma = \frac{E_\gamma}{c}$ through recoil, for which additional energy must be brought in by the photon in the first place. For the same reason, photons emitted by γ decay of an excited nucleus at rest carry a little less energy than the difference of the excitation energies of the nucleus' initial and final state.

The exact on-resonance energy

$$E_\gamma = (E_x - E_i) + \frac{(E_x - E_i)^2}{2(Mc^2 + E_i)} = (E_x - E_i)\left(1 + \underbrace{\frac{(E_x - E_i)}{2(Mc^2 + E_i)}}_{\text{usually} \ll 1}\right) \tag{2.1}$$

of a photon for excitation of a nucleus of ground-state mass M at rest from a level at energy E_i to a level at E_x is obtained by solving the equation system

$$E = \quad E_\gamma + Mc^2 + E_i = E_{\text{Kin}} + Mc^2 + E_x \tag{2.2}$$

$$p = \quad \frac{E_\gamma}{c} = \frac{1}{c}\sqrt{(E_{\text{Kin}} + Mc^2 + E_x)^2 - (Mc^2 + E_x)^2} \tag{2.3}$$

of the conservation of energy E and momentum p, where E_{Kin} is the kinetic energy of the nucleus after photoabsorption and the relativistic energy-momentum relation $E^2 = (pc)^2 + (Mc^2 + E_x)^2$ is used.

Likewise, the energy

$$E_\gamma = (E_x - E_f) - \frac{(E_x - E_f)^2}{2(Mc^2 + E_x)} = (E_x - E_f)\left(1 - \underbrace{\frac{(E_x - E_f)}{2(Mc^2 + E_x)}}_{\text{usually} \ll 1}\right) \qquad (2.4)$$

of a photon emitted by a nucleus initially at rest during γ decay of an excited state E_x to a final state at lower energy E_f is obtained by solving the equation system

$$E = \qquad Mc^2 + E_x = E_{\text{Kin}} + Mc^2 + E_f + E_\gamma \qquad\qquad (2.5)$$

$$p = \qquad 0 = \frac{1}{c}\sqrt{(E_{\text{Kin}} + Mc^2 + E_f)^2 - (Mc^2 + E_f)^2} - \frac{E_\gamma}{c}, \qquad (2.6)$$

where E_{Kin} is now the kinetic energy of the nucleus due to recoil after photoemission.

Since the rest energies Mc^2 of nuclei, ranging from a few to hundreds of GeV, are typically orders of magnitude larger than their excitation energies, which are at most tens of MeV, both energy shifts are usually very small compared to the excitation energies of the involved states, i.e., $E_\gamma \approx |E_f - E_i|$. Nevertheless, these small shifts are of major physical relevance, as the typical nuclear level widths of particle-bound states are in the meV regime, meaning they are still considerably smaller than these energy shifts. Thus, a photon emitted by the γ decay of a nuclear state cannot excite the same state of another identical nucleus, even when typical Doppler-broadening of the level width is taken into account [1]. However, this effect can be overcome, for instance, by embedding the nuclei into crystal lattices, where the recoil momentum can be absorbed by the entire lattice. This leads to the Mössbauer effect [74], where the energy shift becomes negligible, even compared to the level widths.

Finally, when considering an NRF reaction, in which a nucleus of ground-state mass M initially at rest with initial excitation energy E_i is first excited by absorption of a photon of energy E_γ and then, without any change to its momentum gained through the photoabsorption in between, decays back to a state at E_f by emitting a photon of

energy $E_{\gamma'}$, the energy of the emitted photon is given by

$$E_{\gamma'} = \frac{E_\gamma - (E_f - E_i) - \frac{(E_f - E_i)^2}{2(Mc^2 + E_i)}}{1 + \frac{E_\gamma}{Mc^2 + E_i}(1 - \cos\theta)}, \tag{2.7}$$

where θ is the angle between the momenta of the initial and the emitted photon. Naturally, the energy E_γ of the incident photon has to satisfy the photoabsorption energy relation of Eq. (2.1) within the level width for the photoabsorption to be somewhat likely at all. Again, the relation is a direct consequence of the conservation of energy and momentum, which in this case reads

$$E = \qquad E_\gamma + Mc^2 + E_i = E_{\text{Kin}} + Mc^2 + E_f + E_{\gamma'} \tag{2.8}$$

$$\vec{p} = \qquad \vec{p}_\gamma = \vec{p}_{\text{Rec}} + \vec{p}_{\gamma'} \tag{2.9}$$

with

$$|\vec{p}_{\text{Rec}}| = \frac{1}{c}\sqrt{(E_{\text{Kin}} + Mc^2 + E_f)^2 - (Mc^2 + E_f)^2} \tag{2.10}$$

being the momentum of the nucleus after re-emission of the photon and $\vec{p}_\gamma$ and $\vec{p}_{\gamma'}$ being the momenta of the absorbed respectively emitted photons. To solve this system of equations, it is useful to rearrange and square the conservation of momentum equation, yielding the much simpler relation

$$\vec{p}_{\text{Rec}}^2 = (\vec{p}_\gamma - \vec{p}_{\gamma'})^2 \tag{2.11}$$

$$\Leftrightarrow (E_{\text{Kin}} + Mc^2 + E_f)^2 - (Mc^2 + E_f)^2 = E_\gamma^2 + E_{\gamma'}^2 - E_\gamma E_{\gamma'}\cos\theta, \tag{2.12}$$

which together with the conservation of energy of Eq. (2.8) allows solving for $E_{\gamma'}$ now comparatively easy. Except in rare special cases, such as NRF on ^{180m}Ta, an extremely long-lived nuclear isomer, $E_i = 0$ is typically the case in NRF experiments. Considering for a moment furthermore only the case of elastic ground-state NRF, i.e., $E_i = E_f = 0$, the energy of the emitted photon further simplifies to

$$E_{\gamma'} \overset{E_i = E_f = 0}{=} \frac{E_\gamma}{1 + \frac{E_\gamma}{Mc^2}(1 - \cos\theta)}, \tag{2.13}$$

which is the well-known Compton scattering formula for the energy of a photon elastically scattered by a particle of mass M at rest, as it has to be, since both processes

share the same kinematics. Plugging the on-resonance energy E_γ of Eq. (2.1) for photoabsorption to excite a state E_x into Eq. (2.13) yields

$$E_{\gamma'} \overset{E_i = E_f = 0}{=} \frac{E_x \left(1 + \frac{E_x}{2Mc^2}\right)}{1 + \frac{E_x}{Mc^2}\left(1 + \frac{E_x}{2Mc^2}\right)(1 - \cos\theta)} \tag{2.14}$$

and allows realizing that

$$E_{\gamma'} \overset{E_i = E_f = 0}{=} E_x \quad \text{for} \quad \theta = \cos^{-1}\left(\frac{E_x + Mc^2}{E_x + 2Mc^2}\right) \overset{Mc^2 \gg E_x}{\approx} 60° \tag{2.15}$$

with $E_{\gamma'} > E_x$ at smaller scattering angles θ (up to $E_{\gamma'} = E_\gamma$ at $\theta = 0$) and $E_{\gamma'} < E_x$ at larger scattering angles. So depending on its scattering angle θ, the energy of the re-emitted photon in an elastic NRF reaction can be greater or less than the energy of the excited state.

2.3. Selection rules of electromagnetic transitions

Besides its energy, the radiation resonantly absorbed or spontaneously emitted in form of single photons by a nucleus during its transition from an initial state J_i^π to a final state J_f^π is characterized by its participating multipolarities L and their electromagnetic radiation characters Π, which can be either electric $\Pi = E$ or magnetic $\Pi = M$, and their relative intensity shares in the overall radiation. Commonly the shorthand notations $J_i^\pi \to J_f^\pi$ for such a transition and ΠL for a single participating radiation character are used.

For the multipolarity $L \in \mathbb{N}$ of electromagnetic radiation absorbed or emitted by a transition $J_i^\pi \to J_f^\pi$ the selection rules

$$\left|J_f - J_i\right| \le L \le J_f + J_i \qquad \text{and} \qquad L \ne 0 \tag{2.16}$$

apply. The combination of both rules in particular prohibits $0^\pi \to 0^\pi$ transitions mediated by real photons. The $L \ne 0$ rule is due to real photons having spin $S = 1\hbar$ and helicity $h = \pm 1\hbar$, the latter being the projection of the spin onto the direction of

momentum and corresponding to the two and only two possible polarization states of photons. Due to its non-zero helicity, a real photon's spin cannot be oriented perpendicular to its momentum, while a photon's orbital angular momentum $\vec{l} = \vec{r} \times \vec{p}$ is by definition always perpendicular to its momentum. Therefore, a real photon's spin can never be superimposed with an orbital angular momentum in a way that both cancel to zero total angular momentum L, resulting in real photons always having $L \neq 0$ and the corresponding selection rule. If a transition's radiation is composed of more than one multipolarity, as the selection rules allow in many cases, it is called a mixed transition. The other case of only one multipolarity taking part is referred to as a pure transition. In particular, due to the selection rules, transitions in which a 0^+ state participates are always pure.

The multipole mixing ratio

$$\delta = \frac{\langle J_f \| \vec{j}_N \, \vec{A}_{L_0+1}^{(\Pi')} \| J_i \rangle}{\langle J_f \| \vec{j}_N \, \vec{A}_{L_0}^{(\Pi)} \| J_i \rangle} \tag{2.17}$$

$$= \left\{ \begin{matrix} -1 \text{ for } \Pi = \text{E} \\ +1 \text{ for } \Pi = \text{M} \end{matrix} \right\} \cdot \frac{\sqrt{L_0(L_0+2)}}{(L_0+1)(2L_0+3)} \frac{E_\gamma}{\hbar c} \frac{\langle J_f \| T(\Pi'(L_0+1)) \| J_i \rangle}{\langle J_f \| T(\Pi L_0) \| J_i \rangle}, \tag{2.18}$$

here in the phase convention of Krane, Steffen and Wheeler [1, 75, 76], is a measure of the share of a higher multipole moment, here the second-lowest possible multipole moment $L_0 + 1$, in the radiation of a transition $J_i^\pi \to J_f^\pi$ relative to the share of a lower one, here the lowest possible multipole moment L_0. Accordingly, here $\delta = 0$ holds for pure transitions of the lowest possible multiple order by their definition. In Eq. (2.17) the $\vec{A}_L^{(\Pi)}$ denote the respective electromagnetic ΠL multipole field operators and $\vec{j}_N$ the nuclear current operator [76]. Equation (2.18) gives a connection to the reduced transition matrix elements of the corresponding multipole operators $T(\Pi L)$ used by Bohr and Mottelson [75–77]. Note the double vertical bars in the $\langle J_f \| O \| J_i \rangle$, which indicate a reduced matrix element of O as defined by the Wigner-Eckart theorem [78, 79].

As already stated, the electromagnetic radiation character Π specifies whether radiation and part of its associated transition is of electric $\Pi = \text{E}$ or of magnetic $\Pi = \text{M}$ type. The concrete electromagnetic radiation character Π belonging to the multipolarity L of a transition $J_i^\pi \to J_f^\pi$ depends on whether the transition induces a parity change $\pi_f = -\pi_i$ in the nuclear configuration or not. This is due to the conservation of parity

$\pi_i = \pi_\gamma \cdot \pi_f$ in electromagnetic processes requiring the involved γ radiation to have the appropriate parity

$$\pi_\gamma = (-1)^L \cdot \begin{cases} +1 \text{ for } \Pi = \text{E} \\ -1 \text{ for } \Pi = \text{M} \end{cases} \quad (2.19)$$

and therefore the appropriate electromagnetic radiation character Π [1] according to

$$(-1)^L \cdot \pi_i \cdot \pi_f = \begin{cases} +1 \text{ for } \Pi = \text{E} \\ -1 \text{ for } \Pi = \text{M}. \end{cases} \quad (2.20)$$

Conversely, measuring radiation characters and multipolarities in a transition allows for conclusions on the parities of the involved states. A determination of the involved radiation characters ΠL is possible by measuring the angular distribution of γ rays emitted in the transition, as they affect the angular distribution which is explained in Section 2.7.2.

With increasing multipolarity the probability of respective electromagnetic transitions in general decreases quickly. Therefore, considering only the two lowest multipolarities in the multipole mixing ratio δ is reasonable, as all higher multipolarities should not yield a notable contribution. Furthermore, magnetic transitions are typically less likely than electric transitions of the same multipolarity. Taking both these factors into account, an $\text{M}(L_0 + 1)$ contribution in a transition is usually negligible compared to the $\text{E}L_0$ contribution, yielding $\delta \approx 0$ in such cases. An $\text{E}(L_0 + 1)$ contribution, however, can indeed have comparable strength to an $\text{M}L_0$ contribution or even dominate the transition. As a result of the low probability of electromagnetic transitions with high multipolarities and as real photons tend to carry no or only little orbital angular momentum due to their comparatively low momenta, in NRF predominantly dipole (E1 and M1) and to a lesser extent electric quadrupole (E2) transitions are induced, resulting in a high selectivity of excitable states [1].

2.4. The photoabsorption cross section

Cross sections are a measure for the likelihood of a beam-induced reaction to occur, and their unit is that of an area, which justifies their naming. For a fixed target

reaction with incident beam along the z-axis, the overall reaction count Y of some reaction can be expressed in a very general form as

$$Y = \iiiiiii \frac{\mathrm{d}^2\sigma(E,E',\theta,\varphi)}{\mathrm{d}\Omega\,\mathrm{d}E'} \frac{\mathrm{d}^3 N_{\mathrm{T}}(x,y,z,t)}{\mathrm{d}x\,\mathrm{d}y\,\mathrm{d}z}$$
$$\cdot \frac{\mathrm{d}^4\Phi(E,x,y,z,t)}{\mathrm{d}E\,\mathrm{d}x\,\mathrm{d}y\,\mathrm{d}t}\,\mathrm{d}\Omega\,\mathrm{d}E\,\mathrm{d}E'\,\mathrm{d}x\,\mathrm{d}y\,\mathrm{d}z\,\mathrm{d}t, \quad (2.21)$$

where $\frac{\mathrm{d}^2\sigma(E,E',\theta,\varphi)}{\mathrm{d}\Omega\,\mathrm{d}E'}$ is the double-differential cross section of the reaction for incident beam particles of energy E to scatter particles into an infinitesimal energy interval $\mathrm{d}E'$ at energy E' and into an infinitesimal solid angle $\mathrm{d}\Omega$ at spherical coordinates (θ, φ); $\frac{\mathrm{d}^3 N_{\mathrm{T}}(x,y,z,t)}{\mathrm{d}x\,\mathrm{d}y\,\mathrm{d}z}$ is the spatial number density of the target's scattering centers at position (x, y, z) and time t; $\frac{\mathrm{d}^4\Phi(E,x,y,z,t)}{\mathrm{d}E\,\mathrm{d}x\,\mathrm{d}y\,\mathrm{d}t}$ is the spectral, areal and temporal density of the incident beam at position (x, y, z), time t and energy E; and the integrals are taken over the full range of the respective variables. Naturally, in usual cases many of the dependencies of $\frac{\mathrm{d}^2\sigma(E,E',\theta,\varphi)}{\mathrm{d}\Omega\,\mathrm{d}E'}$, $\frac{\mathrm{d}^3 N_{\mathrm{T}}(x,y,z,t)}{\mathrm{d}x\,\mathrm{d}y\,\mathrm{d}z}$, and $\frac{\mathrm{d}^4\Phi(E,x,y,z,t)}{\mathrm{d}E\,\mathrm{d}x\,\mathrm{d}y\,\mathrm{d}t}$ on some variables can be neglected, approximated and integrated out, simplifying the expression considerably. For example, while the spatial number density of the target's scattering centers can in principle change with time due to reactions transmuting the target, this effect is usually completely negligible considering the overall reaction count being orders of magnitude smaller than the total number of scattering centers, hence, allowing to integrate out the time dependency by considering a time-integrated beam flux. Likewise, by approximating the beam flux and target to be spatially homogeneous, the spatial dependencies can be integrated out as well. By using a total cross section

$$\sigma(E) = \iint \frac{\mathrm{d}^2\sigma(E,E',\theta,\varphi)}{\mathrm{d}\Omega\,\mathrm{d}E'}\,\mathrm{d}\Omega\,\mathrm{d}E' \quad (2.22)$$

the relation can be further simplified. Finally, in many cases either the cross section or the beam's spectral density can be considered constant in incident energy with respect to the other one, allowing to integrate out the respective energy dependency as well and use either an energy-integrated cross section or energy-integrated beam flux. One common considerably simplified expression for the reaction count Y is then

$$Y = \int \sigma(E)\,\frac{\mathrm{d}^2 N_{\mathrm{T}}}{\mathrm{d}x\,\mathrm{d}y}\,\frac{\mathrm{d}^3\Phi(E)}{\mathrm{d}E\,\mathrm{d}x\,\mathrm{d}y}\,\mathscr{A}_{T\cap\Phi}\,\mathrm{d}E, \quad (2.23)$$

where the beam was taken to be spatially homogeneous with sharp spatial boundaries, the target to have a homogeneous areal density $\frac{d^2 N_T}{dx\,dy}$ of its scattering centers in the x-y-plane stationary in time and with sharp spatial boundaries, beam and target to share an overlap area of $\mathscr{A}_{T\cap\Phi}$ in the x-y plane, and the total cross section $\sigma(E)$ was used. Assuming the beam to be spatially homogeneous with respect to its propagation direction z is commonly known as the thin target approximation, as a "thick" target will attenuate the beam with increasing target penetration depth according to

$$\frac{\mathrm{d}\left(\frac{\mathrm{d}^4\Phi(E,x,y,z,t)}{\mathrm{d}E\,\mathrm{d}x\,\mathrm{d}y\,\mathrm{d}t}\right)}{\mathrm{d}z} = -\sigma(E)\frac{\mathrm{d}^3 N_T(x,y,z,t)}{\mathrm{d}x\,\mathrm{d}y\,\mathrm{d}z}\frac{\mathrm{d}^4\Phi(E,x,y,z,t)}{\mathrm{d}E\,\mathrm{d}x\,\mathrm{d}y\,\mathrm{d}t} \tag{2.24}$$

depending of course on the cross section $\sigma(E)$ itself. This interplay of beam attenuation and cross section in NRF reactions, known as self-absorption, can be used as a precision experimental technique to determine the cross section of NRF reactions [1, 80].

For the orientation-averaged cross section $\sigma_{\mathrm{Abs}}(E)$ for resonant photoabsorption of a photon of energy E by unpolarized nuclei at rest in their ground-state J_{GS}^π to excite a state J_x^π at excitation energy E_x, unfortunately, two, while similar, still conflicting analytical forms are found in the literature. One [1] is

$$\sigma_{\mathrm{Abs}}^{\mathrm{BW}}(E) = \hat{\sigma}\frac{\Gamma^2}{4\left(E-\hat{E}\right)^2+\Gamma^2} = \frac{\hat{\sigma}}{1+\left(2\frac{E-\hat{E}}{\Gamma}\right)^2}, \tag{2.25}$$

sometimes referred to as the Breit-Wigner (BW) model[1] [2], while the other one [44] is

$$\sigma_{\mathrm{Abs}}^{\mathrm{SLO}}(E) = \hat{\sigma}\frac{E^2\Gamma^2}{\left(E^2-\hat{E}^2\right)^2+E^2\Gamma^2} = \frac{\hat{\sigma}}{1+\left(\frac{E^2-\hat{E}^2}{E\Gamma}\right)^2}, \tag{2.26}$$

usually referred to as the standard-Lorentzian model. In both cases

$$\hat{\sigma} := \sigma_{\mathrm{Abs}}\left(\hat{E}\right) = 2\pi\frac{2J_x+1}{2J_{GS}+1}\left(\frac{\hbar c}{\hat{E}}\right)^2\frac{\Gamma_{GS}}{\Gamma} = 2\pi g\,\hat{\mathchar'26\mkern-9mu\lambda}^2\frac{\Gamma_{GS}}{\Gamma} \tag{2.27}$$

---

[1]Unfortunately, there is no consensus on the naming of the functions in the literature. The form of Eq. (2.25) is sometimes also referred to as a Lorentzian or Cauchy distribution, while the form of Eq. (2.26) is sometimes referred to as a (relativistic) Breit-Wigner distribution.

is the on-resonance cross section, Γ is the natural width of the state J_x^π, Γ_{GS} is the partial decay width of the state J_x^π to the ground state, which appears here due to time-reversal symmetry and is also referred to as (partial) ground-state transition width, and $\hat{E}$ the on-resonance energy for the photoabsorption process, which takes the nuclear recoil into account as given by Eq. (2.1) [1, 71]. The commonly used definitions of the spin statistical factor

$$g = \frac{2J_f + 1}{2J_i + 1} \tag{2.28}$$

for an initial spin J_i and a final spin J_f, which here are J_{GS} and J_x, respectively, and the reduced on-resonance wavelength

$$\hat{\lambdabar} = \frac{\hbar c}{\hat{E}} \approx \frac{197.3\,\text{MeV fm}}{\hat{E}} \tag{2.29}$$

are introduced for convenience.

The natural width Γ of a state J_x^π is the sum

$$\Gamma = \sum_f \Gamma_f \tag{2.30}$$

of all partial decay widths Γ_f of the state J_x^π to all possible final states J_f^π. It is also equivalent to the inverse of the state's lifetime τ according to

$$\Gamma = \frac{\hbar}{\tau} \approx \frac{658.2\,\text{meV fs}}{\tau}, \tag{2.31}$$

represents the FWHM of the photoabsorption cross section at rest in both forms since

$$\sigma_{\text{Abs}}^{\text{BW}}\left(\hat{E} \pm \frac{\Gamma}{2}\right) = \frac{1}{2}\hat{\sigma} \tag{2.32}$$

and

$$\sigma_{\text{Abs}}^{\text{SLO}}\left(\sqrt{\hat{E}^2 + \frac{\Gamma^2}{4}} \pm \frac{\Gamma}{2}\right) = \frac{1}{2}\hat{\sigma} \tag{2.33}$$

hold, and for particle-bound states, as already stated, is typically in the meV regime. Hence, while the on-resonance photoabsorption cross section at rest $\hat{\sigma}$ is typically

in the regime of hundreds of b for particle-bound states at a few MeV of excitation energy, and thus much larger than the cross sections for most other nuclear reactions, still high spectral densities of the incident photon beam are required to achieve a reasonable reaction count due to the narrow widths of the states.

While Eq. (2.25) and Eq. (2.26) are obviously not mathematically identical, they are very similar and Eq. (2.25) can even be obtained as the approximation of Eq. (2.26) when $\left(\frac{E^2-\hat{E}^2}{E\Gamma}\right)^2$ is simply replaced by its second-order Taylor expansion in E around $\hat{E}$, i.e., for $E \approx \hat{E}$. With respect to the absolute scale set by the on-resonance cross section $\hat{\sigma}$, this approximation holds extremely well for small natural widths $\Gamma \ll \hat{E}$ with

$$\frac{\left|\sigma_{\mathrm{Abs}}^{\mathrm{BW}}(E) - \sigma_{\mathrm{Abs}}^{\mathrm{SLO}}(E)\right|}{\hat{\sigma}} \approx 0 \quad \text{for} \quad \Gamma \ll \hat{E} \tag{2.34}$$

as in these cases $\sigma_{\mathrm{Abs}}(E)$ simply approaches 0 very quickly for $E \not\approx \hat{E}$ in both forms as expected for a narrow resonance. Hence, while the two forms are not identical, they are practically equivalent for particle-bound states with their small natural widths.

Moreover, thermal motion of the nuclei in a target will always lead to some Doppler shifts of the energies of incident photons in the rest frames of the nuclei. Accordingly, the overall photoabsorption cross section $\tilde{\sigma}_{\mathrm{Abs}}(E)$ of the whole ensemble of nuclei will appear Doppler-broadened in the laboratory frame and the on-resonance cross section will be somewhat reduced [1]. Still, the integrated cross section

$$\begin{aligned} I_{\mathrm{Abs}} &= \int \sigma_{\mathrm{Abs}}(E)\,\mathrm{d}E = \int \tilde{\sigma}_{\mathrm{Abs}}(E)\,\mathrm{d}E \\ &= \frac{\pi}{2}\Gamma\hat{\sigma} \\ &= \pi^2 g\,\hat{\lambdabar}^2\,\Gamma_{GS} \end{aligned} \tag{2.35}$$

will remain unchanged by this thermal Doppler-broadening in the laboratory frame and is the same for both forms of the cross section.

Since furthermore the spectral density $\frac{\mathrm{d}\Phi(E)}{\mathrm{d}E}$ of considered photon beams is usually quasi-constant over the narrow resonances of particle-bound states, the approximation

$$\int \sigma_{\mathrm{Abs}}(E)\,\frac{\mathrm{d}\Phi(E)}{\mathrm{d}E}\,\mathrm{d}E \approx \int \sigma_{\mathrm{Abs}}(E)\,\mathrm{d}E\,\frac{\mathrm{d}\Phi(\hat{E})}{\mathrm{d}E} = I_{\mathrm{Abs}}\,\frac{\mathrm{d}\Phi(\hat{E})}{\mathrm{d}E} \tag{2.36}$$

holds with high accuracy, and therefore integrated cross sections I are usually more practical quantities in NRF experiments than the cross sections themselves. Thus, the exact form of the photoabsorption cross section at rest is commonly of little practical importance. In particular, Eq. (2.23) can be further simplified to

$$Y = I \frac{\mathrm{d}^2 N_\mathrm{T}}{\mathrm{d}x \, \mathrm{d}y} \frac{\mathrm{d}^3 \Phi(\hat{E})}{\mathrm{d}E \, \mathrm{d}x \, \mathrm{d}y} \mathscr{A}_{T \cap \Phi} \tag{2.37}$$

in these cases.

2.5. Decay of excited states

Naturally, with their finite lifetimes $\tau = \frac{\hbar}{\Gamma}$ excited states will eventually decay back to lower-lying states following the law of radioactive decay. Since a state has no memory of the time it has already existed, radioactive decay is a memoryless stochastic process in continuous time t, i.e., the (conditional) probability $P\left(t > t_0 + \Delta t \,|\, t > t_0\right)$ for a state to decay after the time $t_0 + \Delta t$ is independent of the (current) time t_0, if the state has not yet decayed at t_0. Therefore, the probability density function (PDF) for an excited state still living at t_0 to decay at time t is the exponential distribution

$$\mathscr{P}_{t_0}(t) = \begin{cases} \frac{1}{\tau} e^{-\frac{t - t_0}{\tau}} & \text{for } t \geq t_0 \\ 0 & \text{for } t < t_0 \end{cases} \tag{2.38}$$

since the exponential distribution is the only memoryless continuous probability distribution. Consequently, the expectation value at t_0 for the decay time of a state is

$$\langle t \rangle_{t_0} = \int_{-\infty}^{\infty} t \mathscr{P}_{t_0}(t) \, \mathrm{d}t = t_0 + \tau \tag{2.39}$$

explaining the interpretation of τ as the (mean) lifetime of a state.

The mean probability for an excited state x to eventually decay to a specific final state f is given by

$$P(x \to f) = \frac{\Gamma_f}{\Gamma} \tag{2.40}$$

and referred to as the decay branching ratio of the state x to the final state f. Due to Eq. (2.30) the decay branching ratios of a state to all possible final states indeed sum up to unity as required for a probability. However, since it may be impractical to determine this absolute probability from experiments, other branching-ratio definitions are commonly used as well, which are independent of the total width Γ. For example, the branching ratio given by

$$\frac{P(x \rightarrow f)}{P(x \rightarrow GS)} = \frac{\Gamma_f}{\Gamma_{GS}} \tag{2.41}$$

represents the probability of decay to a specific final state f relative to the probability of ground-state decay. This relative branching ratio is frequently used in NRF experiments because, unlike the absolute decay branching ratio, it can be directly determined from the observed γ-ray intensities.

However, Eq. (2.40) and likewise Eq. (2.41) cannot hold in general if the actual energy the state held at the time of decay is considered. After all, the decay branching ratio can depend on this energy, as will be demonstrated in Section 2.9.1. This energy dependence is particularly relevant when the energies of the photons emitted during decays of the state are precisely measured. Therefore, an energy-dependent partial decay width $\mathcal{G}_f(E)$ for decay of the state x holding energy E to the final state f must be introduced to define an energy-dependent branching ratio

$$P(x \rightarrow f; E) = \frac{\mathcal{G}_f(E)}{\Gamma} \tag{2.42}$$

which again gives the probability of decay to a specific final state f, but now for a specific energy E held by the state x. Obviously, the energy-dependent partial widths mus satisfy

$$0 \leq \mathcal{G}_f(E) \leq \Gamma \quad \text{for all } f \text{ and } E \qquad \text{and} \qquad \sum_f \mathcal{G}_f(E) = \Gamma \quad \text{for all } E \tag{2.43}$$

due to their probabilistic connection. The definition of this energy-dependent branching ratio enables the derivation of cross sections for specific photonuclear reactions as

$$\sigma_f(E) = \frac{\mathcal{G}_f(E)}{\Gamma} \sigma_{\text{Abs}}(E) \tag{2.44}$$

and therefore the associated integrated cross sections as

$$I_f = \int \frac{\mathscr{G}_f(E)}{\Gamma} \, \sigma_{\text{Abs}}(E) \, dE$$
$$= \frac{1}{\Gamma} I_{\text{Abs}} \left\langle \mathscr{G}_f \right\rangle_{\sigma_{\text{Abs}}} \tag{2.45}$$

where

$$\left\langle \mathscr{G}_f \right\rangle_{\sigma_{\text{Abs}}} := \frac{1}{I_{\text{Abs}}} \int \mathscr{G}_f(E) \, \sigma_{\text{Abs}}(E) \, dE \tag{2.46}$$

denotes the photoabsorption-cross-section-weighted energy-average of the energy-dependent partial decay width, effectively using the normalized photoabsorption cross section as a PDF in energy. Still, it is well known [1] that

$$I_f = \frac{\Gamma_f}{\Gamma} I_{\text{Abs}} \tag{2.47}$$

holds for integrated cross sections of specific photonuclear reactions. Combining this with Eq. (2.45) yields the relation

$$\left\langle \mathscr{G}_f \right\rangle_{\sigma_{\text{Abs}}} = \Gamma_f \tag{2.48}$$

which establishes the partial decay width Γ_f as the photoabsorption-cross-section-weighted energy-average of the energy-dependent partial decay width $\mathscr{G}_f(E)$. And since the normalized photoabsorption cross section $\sigma_{\text{Abs}}(E)$ essentially represents the probability distribution for populating the state x at energy E when the populating photon energies are not specifically controlled, Eq. (2.40) yields the mean observed branching ratio when the state x is populated "freely".

Finally, the energy-differential form $\frac{d\sigma_f(E,E')}{dE'}$ of the cross section for NRF reactions should be briefly discussed, where the energy E' of the emitted photon is considered in addition to the energy E of the absorbed photon. Due to the strict energy relation of Eq. (2.7), it is approximately given by

$$\frac{d\sigma_f(E,E')}{dE'} \approx \sigma_f(E) \, \delta(E - E_f - E'), \tag{2.49}$$

where δ denotes the Dirac delta distribution, E_f is the excitation energy of the final state f and the small recoil effect was neglected.

2.6. Transition strengths

Reduced transition probabilities $B(\Pi L)$, usually referred to as (reduced) transition strengths, are another frequently used measure for the probability of transitions as they are particularly well suited for comparisons with theory or across nuclei. This is due to the relation

$$B(\Pi L; J_i^\pi \to J_f^\pi) = \frac{1}{2J_i + 1} \left| \langle \Psi_f \| T(\Pi L) \| \Psi_i \rangle \right|^2 \tag{2.50}$$

connecting them immediately with the absolute square of the reduced matrix element $\langle \Psi_f \| T(\Pi L) \| \Psi_i \rangle$ of their corresponding electromagnetic transition operator $T(\Pi L)$ for radiation character ΠL [77]. Here Ψ_i and Ψ_f denote the wave functions of the initial and final state in the transition $J_i^\pi \to J_f^\pi$.

As a single transition strength $B(\Pi L)$ is always associated with only one particular radiation character ΠL, mixed transitions are characterized by multiple transition strengths. Furthermore, in transition strengths excitation $B(\Pi L) \uparrow$ and de-excitation $B(\Pi L) \downarrow$ processes must be distinguished. The two associated transition strengths are, however, simply related to each other through

$$B(\Pi L) \downarrow = \frac{1}{g} B(\Pi L) \uparrow \tag{2.51}$$

with the spin statistical factor g as already defined in Eq. (2.28). This is a direct consequence of Eq. (2.50) since the absolute value of the reduced matrix element is invariant under the interchange of Ψ_i and Ψ_f.

The partial decay width Γ_f of a state x is connected to the transition strengths $B(\Pi L)$ participating in the transition $x \to f$ by

$$\Gamma_f = 8\pi \sum_{\Pi L} \frac{L+1}{L((2L+1)!!)^2} \left(\frac{1}{\hbar} \right)^{2L+1} B(\Pi L; J_x^\pi \to J_f^\pi) \tag{2.52}$$

with !! denoting the double factorial [1]. By first expanding the partial decay width Γ_f on the right-hand side of Eq. (2.52) similar to Eq. (2.30) into a sum $\Gamma_f = \sum_{\Pi L} \Gamma_{f,\Pi L}$ of contributions by the participating radiation characters ΠL in the transition, then identifying terms corresponding to each other in the sums on both sides, setting

the corresponding terms equal and solving each equality for its respective transition strength $B(\Pi L)$, the relation

$$B(\Pi L; J_x^\pi \to J_f^\pi) = \frac{1}{8\pi} \frac{L((2L+1)!!)^2}{L+1} \lambda^{2L+1} \Gamma_{f,\Pi L} \tag{2.53}$$

is obtained, which puts the transition strengths $B(\Pi L)$ in immediate connection to their respective contribution to the partial decay width Γ_f. While this relation can be used directly in the case of pure transitions, for mixed transitions the leading contributions $\Gamma_{f,\Pi L_0}$ and $\Gamma_{f,\Pi'(L_0+1)}$ first have to be disentangled from the overall partial decay width Γ_f. This is possible by utilizing the relation [1]

$$\delta^2 = \frac{\Gamma_{f,\Pi'(L_0+1)}}{\Gamma_{f,\Pi L_0}} \tag{2.54}$$

in the approximation

$$\Gamma_f \approx \Gamma_{f,\Pi L_0} + \Gamma_{f,\Pi'(L_0+1)} \tag{2.55}$$

yielding

$$\Gamma_{f,\Pi L_0} = \frac{1}{1+\delta^2} \cdot \Gamma_f \tag{2.56}$$

and

$$\Gamma_{f,\Pi'(L_0+1)} = \frac{\delta^2}{1+\delta^2} \cdot \Gamma_f \tag{2.57}$$

with δ being the multipole mixing ratio introduced in Eq. (2.17), which can be determined experimentally through an analysis of the angular distribution of the radiation emitted by the transition as will be explained in Section 2.7.2.

Transition strengths are commonly given using the Gaussian unit system [81, pp. 775–784] in Gaussian units of $\mu_N^2\,\mathrm{fm}^{2L-2}$ for $B(ML)$ and $e^2\,\mathrm{fm}^{2L}$ for $B(EL)$ strengths, where μ_N is the nuclear magneton and e the elementary charge. Being Gaussian units, both have the same dimension for same multipolarity L and are furthermore related by the conversion

$$\underbrace{1\,\mathrm{MeV\,fm}^{2L+1}}_{\text{In SI units}} = \underbrace{0.694\,462\,e^2\,\mathrm{fm}^{2L}}_{\text{In Gaussian units}} = \underbrace{62.8048\,\mu_N^2\,\mathrm{fm}^{2L-2}}_{\text{In Gaussian units}} \tag{2.58}$$

to the SI based units, otherwise commonly used in nuclear physics. The conversion is based on the easily verifiable relations

$$\frac{e^2}{4\pi\epsilon_0} = 1.439\,96\,\text{MeV}\,\text{fm} \qquad \Leftrightarrow \qquad 1\,\text{MeV}\,\text{fm} = 0.694\,462\,\frac{e^2}{4\pi\epsilon_0} \qquad (2.59)$$

and

$$\frac{\mu_0}{4\pi}\mu_N^2 = 0.015\,9223\,\text{MeV}\,\text{fm}^3 \qquad \Leftrightarrow \qquad 1\,\text{MeV}\,\text{fm}^3 = 62.8048\,\frac{\mu_0}{4\pi}\mu_N^2 \qquad (2.60)$$

holding in SI units, where ϵ_0 is the vacuum permittivity and μ_0 the vacuum permeability. Switching to the Gaussian unit system requires conversion of all equations related to electromagnetism. In particular, any appearing charge has to be multiplied by $\sqrt{4\pi\epsilon_0}$ and any magnetic moment by $\sqrt{\frac{4\pi}{\mu_0}}$ for conversion to the Gaussian system [81, p. 782]. Thus, the conversion relations

$$\underbrace{\frac{e^2}{4\pi\epsilon_0}}_{\text{In SI units}} = \underbrace{e^2}_{\text{In Gaussian units}} \qquad \text{and} \qquad \underbrace{\frac{\mu_0}{4\pi}\mu_N^2}_{\text{In SI units}} = \underbrace{\mu_N^2}_{\text{In Gaussian units}} \qquad (2.61)$$

hold, yielding Eq. (2.58) from the SI relations Eqs. (2.59) and (2.60).

Sometimes another measure called Weisskopf units (W.u.) is used to specify the magnitude of a transition strength. The value of a Weisskopf unit is, however, not universal and depends according to

$$1\,\text{W.u.} = \begin{cases} \frac{1}{4\pi}\left(\frac{3}{L+3}\right)^2\left(1.2\,A^{\frac{1}{3}}\right)^{2L} & e^2\,\text{fm}^{2L} \qquad \text{for } \Pi = \text{E} \\[2ex] \frac{10}{\pi}\left(\frac{3}{L+3}\right)^2\left(1.2\,A^{\frac{1}{3}}\right)^{2L-2} & \mu_N^2\,\text{fm}^{2L-2} \quad \text{for } \Pi = \text{M} \end{cases} \qquad (2.62)$$

on the specific radiation character ΠL of the transition and mass number A of the nucleus [77, p. 389].

2.7. Observables in nuclear resonance fluorescence experiments

The four main raw observables in NRF experiments are the energies, directions, polarizations and counts/intensities[2] of γ rays emitted by the nuclei of the irradiated target after photoabsorption. The energies and polarizations[3] can be measured through the interaction of the γ rays with an appropriate detector, and their emission directions are determined simply by the detector's position relative to the target position. Finally, the counts/emission intensities are trivially obtained by counting the number of events in a region of interest with respect to the other raw observables, typically after sorting the observed events into a histogram with respect to the other raw observables, using an appropriate binning.

2.7.1. From peak energies to transition and level energies

The γ-ray energy histogram, also called energy spectrum, inherently provides direct information about the energies of γ rays emitted during level transitions, and thus about the differences in excitation energies between the target nuclei's states connected by these transitions. Due to the statistical counting nature of an NRF experiment, frequently occurring transitions lead to accumulations of counts, commonly referred to as peaks, in the γ-ray spectrum. According to Eq. (2.7) in combination with Eq. (2.1), each peak's centroid energy corresponds to the recoil-corrected excitation energy difference between the excited and final states of a transition. While the transition energies are nearly discrete, since the nuclear level widths are so small, the peaks are broadened to widths much larger than the natural widths of the states due to the limited detector resolution, and typically take the form of a Gaussian normal distribution. As the detector resolution usually decreases with increasing

---

[2] One of course may argue that the counts are not a raw observable since they are not a property of single photons but rather a property of an ensemble of photons, usually with respect to the other raw observables. Still, they are considered a raw observable in this work as counts are directly measurable in experiments.

[3] Measuring the polarization of emitted NRF photons actually has become uncommon due to the availability of fully linearly polarized photon beams suitable for NRF experiments. Using a linearly polarized beam for NRF essentially provides the same information that would be obtained by measuring the polarization of the emitted γ rays, but in a much simpler and typically more reliable manner.

γ-ray energies, the peaks likewise become more broadened at higher energies. Still, NRF experiments utilizing high-purity germanium (HPGe) detectors achieve superb energy resolutions in the sub-keV region. Thus, by simply identifying peaks in the γ-ray spectrum, transition energies can be determined, and by sorting the observed transitions in a level scheme, the level energies be obtained. The construction of a level scheme by transition energies alone, however, is rarely unambiguous.

2.7.2. From angular distributions to spins, parities and multipole mixing ratios

Measuring the angular distribution of the radiation emitted by the de-excitation transition of an NRF cascade can assist in assigning the transition to the two states it connects. More importantly though, it can provide crucial information about the states, namely their spins J and parities π, as well as the transitions, namely their multipole mixing ratios δ. Since the angular distribution depends exclusively on the spins and parities of states and multipole mixing ratios of transitions involved in the corresponding overall cascade, it can conversely be used to determine these fundamental properties. By experimentally probing the angular distribution of the emitted radiation and comparing it to the known angular distributions for the possible values of J, π and δ, one can identify the best match and thus determine these observables. To probe the angular distribution, multiple detectors are simply placed at various angles relative to the target and incoming beam and their efficiency corrected counts (the observed intensities) of γ rays stemming from a transition are compared.

While the electromagnetic radiation emitted by nuclear transitions in principle always has a specific angular distribution, it only becomes apparent if the nuclei are aligned in some way. If this is not the case, like in ordinary radioactive sources, then the superposition of all randomly aligned angular distributions results in an overall isotropic emission of radiation. In conventional NRF experiments, however, there is always at least one axis defined by the incoming photon beam irradiating the target. This reduces the spherical to a cylindrical symmetry, resulting in angular distributions that may be anisotropic with respect to the angle relative to the beam axis. Still, without further symmetry-breaking alignment, the angular distributions remain isotropic with respect to rotations around the beam axis. This is for instance the case in experiments employing unpolarized or circularly polarized beams. When a linearly polarized γ-ray

beam is used though, its polarization plane defines a second common axis. Thus, the previously remaining rotational invariance around the beam axis is broken as well, retaining only a point symmetry around the target, and resulting in possibly almost entirely anisotropic angular distributions.

Mathematically angular distribution functions are basically PDFs for the random directions of emitted photons in a spherical coordinate system and denoted by $W(\theta, \varphi)$, with θ being the polar angle and φ the azimuthal angle. However, they are commonly normalized to

$$\int W(\theta, \varphi) \, \mathrm{d}\Omega = \int_0^{2\pi} \int_0^{\pi} W(\theta, \varphi) \sin(\theta) \, \mathrm{d}\theta \, \mathrm{d}\varphi = 4\pi \tag{2.63}$$

when integrated over the whole solid angle, instead of unity as required for a proper PDF. While this leads to the isotropic angular distribution function corresponding to unity, it requires using the properly normalized PDF $\frac{W(\theta, \varphi)}{4\pi}$ to calculate absolute probabilities for emission of γ rays into finite solid angles $\Delta\Omega$, e.g., those covered by detectors in an experiment. Naturally, since angular distribution functions $W(\theta, \varphi)$ describe the relative distribution of emitted radiation over the solid angle, they are directly related to the differential cross sections according to

$$\frac{W(\theta, \varphi)}{4\pi} = \frac{1}{\sigma} \frac{\mathrm{d}\sigma(\theta, \varphi)}{\mathrm{d}\Omega} \tag{2.64}$$

by simply normalizing it using the total cross section σ.

For the angular distribution of the transition $x \to f$ in an NRF cascade $i \to x \to f$, the spherical coordinate system is centered at the target position. The polar angle θ is defined as the angle between the direction of the incident photon beam and the direction of the emitted γ ray, while the azimuthal angle φ is defined as the angle between the plane spanned by the incident photon beam and its electric field vector[4] (the polarization plane of the incident photon beam) and the plane spanned by the incident photon beam and the emitted γ ray (the scattering plane). As mentioned, the angular distribution depends, besides the beam polarization, solely on the spins J and parities π of states and multipole mixing ratios δ of transitions involved in the

---

[4]Since in the case of unpolarized or circularly polarized beams the resulting NRF angular distribution will, as already stated, be isotropic with respect to rotation around the beam axis, the azimuthal angle φ does not have to be defined in these cases.

corresponding overall NRF cascade $i \rightarrow x \rightarrow f$. While angular distribution functions $W(\theta, \varphi)$ can take rather complex algebraic forms, in principle their derivation from the involved J, π and δ values, though being cumbersome, is straightforward. It is achieved by the well-understood theory of $\gamma\gamma$-angular correlations, as for example elucidated in more detail in Refs. [75, 82–84]. Appendix A of Ref. [1] provides the resulting analytical expressions for the angular distribution functions of many common NRF cascades.

A simple instance of an angular distribution function is obtained in the case of a $0^+ \rightarrow 1^\pi \rightarrow 0^+$ NRF cascade excited by a linearly polarized γ-ray beam as

$$W_{0^+ \rightarrow 1^\pi \rightarrow 0^+}(\theta, \varphi) = \frac{3}{4}\left(1 + \cos^2\theta \pm \sin^2\theta \cos(2\varphi)\right) \tag{2.65}$$

with the $\pm$ sign to be chosen accordingly to the parity π of the intermediate 1^π state. It is worth noting that this angular distribution is identical to the directional characteristic of a Hertzian dipole antenna. This is intuitively understandable, as the cascade $0^+ \rightarrow 1^\pi \rightarrow 0^+$ is due to a pure electric or magnetic dipole excitation and identical subsequent de-excitation of the nucleus. Thus, the nucleus behaves like a Hertzian dipole being excited by the linearly polarized electric or magnetic field of the γ-ray beam in this case. Besides this intuitive analogy, this angular distribution is furthermore of special importance for NRF experiments with linearly polarized γ-ray beams on even-even nuclei. With their $J^\pi = 0^+$ ground state, it is the angular distribution of the ground-state transitions of 1^π states photoexcited from their ground state. Moreover, by placing two detectors perpendicular to the beam axis at $\theta = 90°$, one in the beam's polarization plane at $\varphi = 0°$ and one perpendicular to it at $\varphi = 90°$, the pronounced azimuthal asymmetry of this angular distribution allows to determine a state's parity π immediately by the asymmetry of counts observed on its ground-state transition in the detectors [85, 86]: In the case of a $J^\pi = 1^-$ state, its ground-state transition's angular distribution function, as given by Eq. (2.65) with the negative sign, is maximal for the direction of the detector placed at $\varphi = 90°$, while being zero for the other detector's direction. Hence, the latter detector will only observe a mere fraction of the corresponding γ rays observed by the former, indicating a clear negative parity when comparing their spectra. For a 1^+ state the opposite will hold, as its ground-state transition's angular distribution function with the positive sign is effectively rotated by $\Delta\varphi = 90°$ around the beam axis compared to the $J^\pi = 1^-$ case, thus being zero at $\varphi = 90°$ and maximal at $\varphi = 0°$. For illustration both these angular distribution functions in the $\theta = 90°$ plane as well as for $\theta = 125°$ are plotted
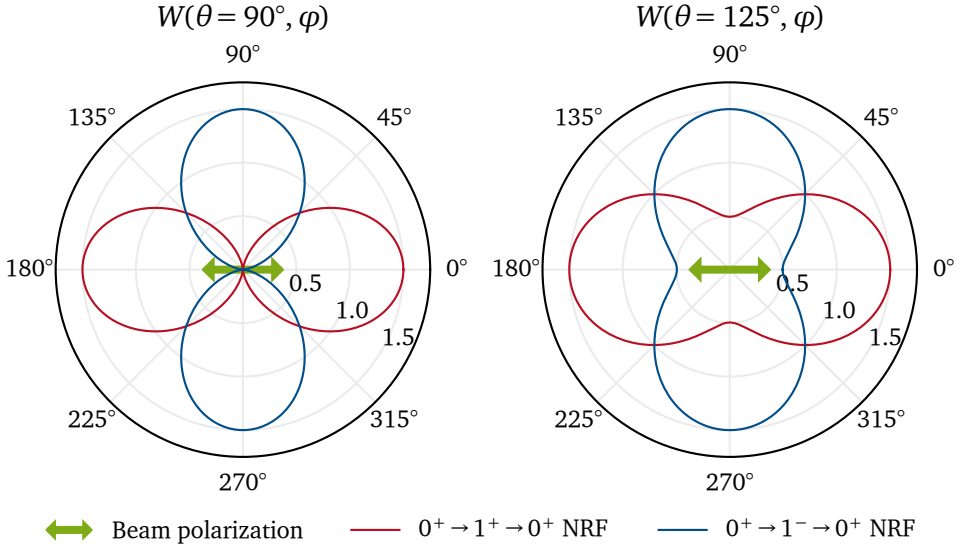
Figure 2.2.: Angular distributions $W(\theta, \varphi)$ of $0^+ \rightarrow 1^\pi \rightarrow 0^+$ NRF cascades excited by a linearly polarized photon beam plotted over the azimuthal angle φ for two values of the polar angle θ. The polar angle θ represents the scattering angle of the emitted γ ray, while the azimuthal angle φ is the angle between the polarization plane (green arrow) of the incident photon beam and the scattering plane. The analytical expressions for these angular distributions are provided in Eq. (2.65).

in Fig. 2.2. Finally, for 2^π, and even higher spin states, though these are usually not accessible in NRF, as reasoned earlier, the same idea still applies, as the angular distributions of their ground-state transitions in the $\theta = 90°$ plane are very similar to the $J = 1$ case. Therefore, using a linearly polarized γ-ray beam in NRF experiments on even-even nuclei allows to determine the parities of excited states unambiguously and directly from the observed azimuthal asymmetry of their ground-state transitions, offering a unique and powerful tool for parity measurements in nuclear physics [85, 86].

2.7.3. From peak counts to branching ratios, integrated cross sections and related observables

Once all peaks identified in the analysis of an NRF experiment are sorted into a level scheme and the associated spins, parities and multipole mixing ratios are determined by an angular distribution analysis, similar to the just outlined approach on parity determination, the next step is usually to determine branching ratios, integrated cross sections and the related partial decay and natural widths from the observed peak counts A. A common, simple approach to determine these quantities is outlined in the following as an example.

In general, a detector, which is covering a solid angle Ω_{Det} with differential full-energy-peak (FEP) efficiency $\frac{\mathrm{d}\epsilon(E,\theta,\varphi)}{\mathrm{d}\Omega}$ to detect γ rays of energy E being emitted from the target position into the direction (θ, φ), is expected to observe

$$A = Y \cdot \int_{\Omega_{\mathrm{Det}}} \frac{\mathrm{d}\epsilon(E_\gamma, \theta, \varphi)}{\mathrm{d}\Omega} W(\theta, \varphi)\, \mathrm{d}\Omega \qquad (2.66)$$

counts at energy E_γ of a number of γ rays Y being emitted from the target position with angular distribution $W(\theta, \varphi)$ and energy E_γ. Hence, each FEP volume A_f observed in an NRF experiment and determinable by integrating the background-subtracted peaks in the γ-ray spectra is directly related to the overall count Y_f of γ rays emitted by the target nuclei's corresponding cascade $GS \rightarrow x \rightarrow f$. To use this relation to obtain Y_f, the FEP efficiencies of the detectors must first be determined though. This can be achieved by measuring known amounts of γ rays emitted from the target position with known angular distributions at multiple energies to determine the efficiencies at those energies, and then interpolating the values in energy. The usual procedure is measuring the γ radiation emitted isotropically by a radioactive calibration source with known activity and decay properties, and thus known amounts Y_{Source} of emitted γ rays at each specific energy during the measurement period. Such data then allows to determine the absolute efficiency of each detector for detecting isotropically emitted γ rays ϵ_{Iso} according to

$$\frac{A_{\mathrm{Source}}(E)}{Y_{\mathrm{Source}}(E)} = \int_{\Omega_{\mathrm{Det}}} \frac{\mathrm{d}\epsilon(E, \theta, \varphi)}{\mathrm{d}\Omega} 1\, \mathrm{d}\Omega =: \epsilon_{\mathrm{Iso}}(E) \qquad (2.67)$$

at each observed γ-ray energy. Then, by assuming the differential FEP efficiency of a detector to be constant over its covered solid angle in the simplest approach[5], i.e., by using

$$\frac{d\epsilon(E_\gamma, \theta, \varphi)}{d\Omega} = \epsilon_{\text{Iso}}(E_\gamma) \frac{1}{\Omega_{\text{Det}}} \,, \tag{2.68}$$

cascade reaction counts Y_f can be directly deduced from the peak volumes A_f using the relation

$$A_f = Y_f \cdot \epsilon_{\text{Iso}} \underbrace{\frac{1}{\Omega_{\text{Det}}} \int_{\Omega_{\text{Det}}} W_f(\theta, \varphi) \, d\Omega}_{\text{Mean value of } W_f \text{ over } \Omega_{\text{Det}}}$$

$$= Y_f \cdot \epsilon_{\text{Iso}} \cdot \langle W_f \rangle_{\Omega_{\text{Det}}} \tag{2.69}$$

based on Eq. (2.66).

Then, without further ado, branching ratios

$$\frac{\Gamma_f}{\Gamma_{GS}} = \frac{Y_f}{Y_{GS}} = \frac{A_f}{A_{GS}} \frac{\epsilon_{\text{Iso}}(E_{\gamma GS}) \cdot \langle W_{GS} \rangle_{\Omega_{\text{Det}}}}{\epsilon_{\text{Iso}}(E_{\gamma f}) \cdot \langle W_f \rangle_{\Omega_{\text{Det}}}} \tag{2.70}$$

can be determined, as can be seen by combining Eq. (2.47) with Eq. (2.37), where almost all factors cancel out here, since in both considered cascades the same state x is photoexcited from the ground state.

To obtain integrated cross sections I_f using Eq. (2.37) (and the assumptions attached to it) next, the areal density of target nuclei $\frac{d^2 N_T}{dx\,dy}$ and the spectral and areal density $\frac{d^3 \Phi(E)}{dE\,dx\,dy}$ of the incident γ-ray beam have to be determined. The here necessarily homogeneous areal density can be deduced by weighing the target material and measuring its dimensions, while the spectral and areal density of the incident γ-ray

---

[5]A more sophisticated approach for relating a detector's efficiencies with respect to specific angular distributions to the isotropic one could, for example, involve computer simulations of the interaction of γ rays with the detector material and geometry. After all, it is intuitive that a detector would have a lower FEP efficiency for detecting γ rays emitted into the edge regions of its face compared to those emitted into its face's center. This difference can be significant when measuring strongly anisotropic angular distributions.

beam can, for example, be calibrated through simultaneous measurement of reactions with already known (integrated) cross sections.

As the integrated cross sections I_f are connected to the product $\frac{\Gamma_{GS}\Gamma_f}{\Gamma}$ according to Eqs. (2.35) and (2.47), naturally only this product can be extracted from a single cascade $GS \rightarrow x \rightarrow f$, but not the individual partial decay widths Γ_{GS} or the total width Γ, if there is not already prior knowledge of the total width for example from a lifetime measurement. To see how to obtain partial decay widths without prior knowledge of the total width, it is useful to rewrite Eq. (2.47) using Eqs. (2.30) and (2.35) to

$$I_f = \pi^2 g \hat{\lambda}^2 \frac{\Gamma_{GS}\Gamma_f}{\sum_k \Gamma_k} = \pi^2 g \hat{\lambda}^2 \frac{\Gamma_f}{\sum_k \frac{\Gamma_k}{\Gamma_{GS}}}, \tag{2.71}$$

where the sum index k runs over all possible decay channels of the state x including the ground-state decay. Obviously, if all branching ratios $\frac{\Gamma_k}{\Gamma_{GS}}$ are known, for example because all decay transitions have been observed in the NRF experiment at hand and their branching ratios have already been determined according to Eq. (2.70), it is now trivial to determine first all partial decay widths Γ_f and then the total width Γ of the state x as their sum from the available integrated cross sections I_f. Unfortunately, however, this is rarely the case, as the number of possible decay channels of a state can be quite large and not all of them can be observed in a single NRF experiment, as many will be quite weak and therefore not lead to observable peaks in the γ-ray spectra. Still, at least a lower limit of $\sum_k \frac{\Gamma_k}{\Gamma_{GS}}$ and therefore of the partial decay widths Γ_f and their sum Γ can be obtained by assuming all unobserved decay channels to have branching ratios of zero. If all unobserved decay channels are indeed very weak, this lower limit should be quite close to the actual value.

Finally, obtained partial decay widths Γ_f can be combined with multipole mixing ratios δ determined from an angular distribution analysis to deduce transition strengths $B(\Pi L)$ according to Eqs. (2.53), (2.56) and (2.57), which typically concludes the analysis of a simple NRF experiment on discrete bound states.

2.8. Thomson scattering

In addition to photon scattering through resonant absorption and subsequent emission of γ rays by nuclei, photons can also be elastically scattered off nuclei without intermediate absorption. The most important elastic scattering (ES) process in the context of NRF experiments, besides elastic NRF scattering itself, is nuclear Thomson scattering, the low-energy limit of Compton scattering off nuclei [87].

As derived in Section 2.2 from the conservation of energy and momentum, the energy $E_{\gamma'}$ of a photon after ES off a particle of mass M at rest is given by Eq. (2.13). Hence, photons with incident energies $E_\gamma \ll Mc^2$ have virtually unchanged energy $E_{\gamma'} \approx E_\gamma$ after ES. In particular, this is the case for γ rays used in NRF experiments when scattering off nuclei, since their energies are tens of MeV at most and thus indeed much smaller than the few to hundreds of GeV rest mass energies of nuclei. Therefore, instead of nuclear Compton scattering, only its low-energy limit, nuclear Thomson scattering, has to be considered in NRF experiments.

The cross section of (nuclear) Thomson scattering off a charge carrier (a nucleus) with charge number Z and mass M can be obtained from the low-energy limit of the corresponding Compton scattering cross section. For example, the differential cross section of Compton scattering of linearly polarized photons off a spinless charge carrier, such as an even-even nucleus, is

$$\frac{\mathrm{d}\sigma_\mathrm{C}}{\mathrm{d}\Omega} = \frac{1}{2}\left(\frac{Z^2\alpha\hbar c}{Mc^2}\right)^2 \frac{1 + \cos^2\theta - \sin^2\theta\cos(2\varphi)}{\left(1 + \frac{E_\gamma}{Mc^2}(1-\cos\theta)\right)^2}, \tag{2.72}$$

where $\alpha \approx \frac{1}{137}$ is the fine-structure constant [88, p. 195]. As before, the employed spherical coordinate system of polar angle θ and azimuthal angle φ has its origin at the scattering center with $\theta = 0$ being the direction of the incident photon and $\varphi = 0$ being in its polarization plane. Forming the low-energy limit for $E_\gamma \ll Mc^2$ of this expression with $\frac{E_\gamma}{Mc^2} \approx 0$ yields the differential Thomson scattering cross section

$$\begin{aligned}
\frac{\mathrm{d}\sigma_\mathrm{T}}{\mathrm{d}\Omega} &= \frac{1}{2}\left(\frac{Z^2\alpha\hbar c}{Mc^2}\right)^2 \left(1 + \cos^2\theta - \sin^2\theta\cos(2\varphi)\right) \\
&= \frac{2}{3}\left(\frac{Z^2\alpha\hbar c}{Mc^2}\right)^2 W_{0^+\to 1^-\to 0^+}(\theta,\varphi),
\end{aligned} \tag{2.73}$$

which is energy independent, valid for charge carriers of any spin, and shares its angular distribution with $0^+ \rightarrow 1^- \rightarrow 0^+$ NRF scattering, as can be seen through comparison with Eq. (2.65). The total Thomson scattering cross section

$$\sigma_{\mathrm{T}} = \frac{8\pi}{3} \left(\frac{Z^2 \alpha \hbar c}{M c^2} \right)^2 \tag{2.74}$$

is then obtained by integrating over the whole solid angle and amounts, for example, to about 125 µb for ^{154}Sm and 1.80 µb for ^{12}C.

The phenomenon of Thomson scattering and its angular distribution can also be understood classically: Due to the low energy of the incident photons, i.e., their long wavelength and low frequency, a charge carrier perceives their electric field as slowly oscillating and spatially homogeneous, which drives it to oscillate along their field vector with the same frequency. In turn, the charge carrier will then emit electric dipole radiation of the same frequency, effectively scattering the incident radiation.

2.8.1. Interference of Thomson scattering and elastic NRF

Since nuclear Thomson scattering and elastic NRF (ENRF) are indistinguishable, coherent processes, they interfere with each other [44, 87]. Hence, the overall differential ES cross section $\frac{\mathrm{d}\sigma_{\mathrm{ES}}}{\mathrm{d}\Omega}$ is not just the sum of the two pure differential cross sections $\frac{\mathrm{d}\sigma_{\mathrm{ENRF}}}{\mathrm{d}\Omega}$ and $\frac{\mathrm{d}\sigma_{\mathrm{T}}}{\mathrm{d}\Omega}$, but the absolute square of the sum of the corresponding, complex valued, energy- and angle-dependent scattering amplitudes $\mathscr{F}(E, \theta, \varphi)$. Without full knowledge of the scattering amplitudes of both processes, only limits on the overall differential ES cross section

$$\frac{\mathrm{d}\sigma_{\mathrm{ES}}}{\mathrm{d}\Omega} = \left| \mathscr{F}_{\mathrm{ENRF}} + \mathscr{F}_{\mathrm{T}} \right|^2 \tag{2.75}$$

can be derived from the pure differential cross sections of the individual processes. Using the triangle inequality on Eq. (2.75), an upper limit

$$\frac{\mathrm{d}\sigma_{\mathrm{ES}}}{\mathrm{d}\Omega} \leq \left| \left| \mathscr{F}_{\mathrm{ENRF}} \right| + \left| \mathscr{F}_{\mathrm{T}} \right| \right|^2 = \left| \sqrt{\frac{\mathrm{d}\sigma_{\mathrm{ENRF}}}{\mathrm{d}\Omega}} + \sqrt{\frac{\mathrm{d}\sigma_{\mathrm{T}}}{\mathrm{d}\Omega}} \right|^2 \tag{2.76}$$

and likewise through the reverse triangle inequality, a lower limit

$$\frac{\mathrm{d}\sigma_{\mathrm{ES}}}{\mathrm{d}\Omega} \geq ||\mathscr{F}_{\mathrm{ENRF}}| - |\mathscr{F}_{\mathrm{T}}||^2 = \left| \sqrt{\frac{\mathrm{d}\sigma_{\mathrm{ENRF}}}{\mathrm{d}\Omega}} - \sqrt{\frac{\mathrm{d}\sigma_{\mathrm{T}}}{\mathrm{d}\Omega}} \right|^2 \qquad (2.77)$$

can be obtained, where both limits utilize the fact that a differential cross section is the absolute square of its associated scattering amplitude.

These limits already allow for an estimation of the interference effect on integrated cross sections for ES in typical NRF experiments on particle-bound states. Integrated cross sections are naturally dominated by the large around-resonance cross sections, which in the considered case are typically about six orders of magnitude larger than the Thomson scattering cross section. So it can be concluded from the above limits that the interference causes at most a sub-percent deviation from the pure ENRF cross sections around resonance and thus on the integrated cross sections. Consequently, the interference of Thomson scattering and ENRF can usually be neglected in the analysis of NRF experiments on particle-bound states. Still, due to its energy-independence, Thomson scattering will contribute significantly to the overall ES in NRF experiments. Therefore, if individual states are not resolved and only average ES cross sections are determined, the contribution by the indistinguishable Thomson scattering cross section has to be subtracted from obtained ES cross sections to obtain the pure ENRF cross sections.

2.9. NRF on the giant dipole resonance

2.9.1. Elastic NRF on the giant dipole resonance

Due to the comparable cross sections of ENRF on the GDR and Thomson scattering, the interference of both processes has to be explicitly considered. For this, the scattering amplitudes of both processes are required. In the case of nuclei with ground-state spin $J_{GS} = 0$, such as even-even nuclei, ENRF on the GDR and Thomson scattering share the same angular distribution

$$W(\theta, \varphi) = W_{0^+ \to 1^- \to 0^+}(\theta, \varphi) = \frac{3}{4} \left(1 + \cos^2 \theta - \sin^2 \theta \cos(2\varphi) \right) \qquad (2.78)$$

of Eq. (2.65) with the negative sign. Hence, the interference of both will also share this angular distribution and knowledge of the forward scattering amplitudes

$$f(E) = \mathcal{F}(E, \theta = 0, \varphi) \tag{2.79}$$

of both processes is sufficient. From these, first the differential forward ES cross section

$$\left. \frac{\mathrm{d}\sigma_{\mathrm{ES}}}{\mathrm{d}\Omega} \right|_{\theta=0} = |f_{\mathrm{ENRF}} + f_{\mathrm{T}}|^2 \tag{2.80}$$

can be obtained, which then allows to determine the differential cross section at any angle according to

$$\frac{\mathrm{d}\sigma_{\mathrm{ES}}}{\mathrm{d}\Omega} = \left. \frac{\mathrm{d}\sigma_{\mathrm{ES}}}{\mathrm{d}\Omega} \right|_{\theta=0} \cdot \frac{W(\theta, \varphi)}{W(0, \varphi)} = \frac{2}{3} |f_{\mathrm{ENRF}} + f_{\mathrm{T}}|^2 \, W(\theta, \varphi) \tag{2.81}$$

through the known angular distribution $W(\theta, \varphi)$, as well as the total cross section

$$\sigma_{\mathrm{ES}} = \frac{8\pi}{3} |f_{\mathrm{ENRF}} + f_{\mathrm{T}}|^2 \tag{2.82}$$

of the coherent ES processes.

The forward Thomson scattering amplitude

$$f_{\mathrm{T}} = -\frac{Z^2 \alpha \hbar c}{M c^2} \tag{2.83}$$

is well known, purely real, negative[6] and energy-independent [44]. Comparing to Eq. (2.73), it indeed yields the same result for the pure forward Thomson scattering cross section through its absolute square.

The forward scattering amplitude of ENRF on the GDR can be obtained through standard tools of scattering theory from the total photoabsorption cross section $\sigma_{\mathrm{Abs}}(E)$ of the GDR. The optical theorem

$$\mathrm{Im}\big(f(E)\big) = \frac{E}{4\pi\hbar c} \, \sigma_{\mathrm{Abs}}(E) \tag{2.84}$$

---

[6]The negative sign of the Thomson scattering amplitude can be classically motivated as the phase shift of 180° of the scattered wave to the incident wave [89, Eq. (B.4)]. The incident wave will drive the charge carrier to oscillate along its electric field vector with a phase shift of 90° to the field, and the scattered wave emitted due to the charge carrier's oscillation will be phase-shifted by another 90° to its oscillation, yielding the total phase shift of 180° to the incident wave.

relates the imaginary part of the forward ES amplitude to the total photoabsorption cross section [90, Eq. (29)], allowing its determination from the latter. The dispersion relation [90, Eq. (30)], also known as Kramers-Kronig relation,

$$
\begin{aligned}
\mathrm{Re}\left(f(E)\right) &= \frac{2E^2}{\pi} \mathscr{P}\int_0^\infty \frac{\mathrm{Im}\left(f(\mathscr{E})\right)}{\mathscr{E}\left(\mathscr{E}^2 - E^2\right)}\, \mathrm{d}\mathscr{E} \\
&= \frac{E^2}{2\pi^2 \hbar c} \mathscr{P}\int_0^\infty \frac{\sigma_{\mathrm{Abs}}(\mathscr{E})}{\mathscr{E}^2 - E^2}\, \mathrm{d}\mathscr{E}
\end{aligned}
\tag{2.85}
$$

then allows to determine the real part of the forward ES amplitude from its imaginary part, where $\mathscr{P}\int$ denotes the Cauchy principal value integral and Eq. (2.84) was used in the last step. For the SLO parametrization of the photoabsorption given in Eq. (2.26) the analytical expression[7]

$$
\begin{aligned}
f^{\mathrm{SLO}}(E) &= \frac{\hat{\sigma}E^2\Gamma}{4\pi\hbar c}\,\frac{\hat{E}^2 - E^2 + \mathrm{i}E\Gamma}{\left(E^2 - \hat{E}^2\right)^2 + E^2\Gamma^2} \\
&= \frac{E}{4\pi\hbar c}\left(\mathrm{i} - \frac{E^2 - \hat{E}^2}{E\Gamma}\right)\sigma^{\mathrm{SLO}}_{\mathrm{Abs}}(E)
\end{aligned}
\tag{2.86}
$$

is obtained for the amplitude of forward ENRF scattering on such a SLO resonance from Eqs. (2.84) and (2.85) [38, 40, 44].

It should be noted, however, that, unlike the photoabsorption cross section, the real part of this forward scattering amplitude does not converge to zero for $E \to \infty$. Consequently, the same is the case for the differential forward ENRF cross section

$$
\left.\frac{\mathrm{d}\sigma^{\mathrm{SLO}}_{\mathrm{ENRF}}}{\mathrm{d}\Omega}\right|_{\theta=0} = \left|f^{\mathrm{SLO}}(E)\right|^2 = \frac{\hat{\sigma}E^2}{(4\pi\hbar c)^2}\,\sigma^{\mathrm{SLO}}_{\mathrm{Abs}}(E)
\tag{2.87}
$$

and the total ENRF cross section. The latter for $J = 1$ resonances in nuclei with

---

[7]Again, the complex phase of the ENRF scattering amplitude of a SLO resonance can be understood in a classical picture by viewing the excitation of the resonance as a harmonic oscillator driven by the electromagnetic wave of an incident photon. When the resonance is driven by a photon below its resonance frequency, the phase shift will be 0° to 90°, above its resonance frequency it will be 90° to 180° and exactly at its resonance frequency it will be 90°.

ground-state spin $J_{GS} = 0$ is

$$
\begin{aligned}
\sigma_{\text{ENRF}}^{\text{SLO}} &= \frac{8\pi}{3} \left| f^{\text{SLO}}(E) \right|^2 \\
&= \frac{\hat{\sigma}}{6\pi} \left(\frac{E}{\hbar c} \right)^2 \sigma_{\text{Abs}}^{\text{SLO}}(E) \\
&= \frac{\Gamma_{GS}}{\Gamma} \left(\frac{E}{\hat{E}} \right)^2 \sigma_{\text{Abs}}^{\text{SLO}}(E),
\end{aligned}
\tag{2.88}
$$

where Eq. (2.27) with $g = 3$ was substituted in the last step. In particular, the forward scattering amplitude's limit is

$$
f^{\text{SLO}}(E) \rightarrow -\frac{\hat{\sigma}\Gamma}{4\pi\hbar c} \quad \text{for} \quad E \rightarrow \infty
\tag{2.89}
$$

and for $E > \sqrt{\frac{\Gamma}{\Gamma_{GS}}}\,\hat{E}$ the total ENRF cross section becomes greater than the photoabsorption cross section. This is obviously unphysical, and simply means that in nature any full photoabsorption cross section cannot just be a simple SLO resonance but must have a more complex structure [44]. Still the SLO photoabsorption cross section allows for a good approximation in analytical form, as long as the energy range of interest is not too far from the resonance energy $\hat{E}$.

At this point, it is also worthwhile to come back to the energy-dependent partial decay width $\mathcal{G}_f(E)$ introduced in Section 2.5. Combining Eqs. (2.44) and (2.88) allows to deduce the energy-dependent ground-state decay width

$$
\mathcal{G}_{GS}(E) = \Gamma \frac{\sigma_{\text{ENRF}}^{\text{SLO}}}{\sigma_{\text{Abs}}^{\text{SLO}}} = \Gamma_{GS} \left(\frac{E}{\hat{E}} \right)^2
\tag{2.90}
$$

of dipole ENRF on a SLO resonance. Ideally, by using Eq. (2.46) as

$$
\begin{aligned}
\langle \mathcal{G}_{GS} \rangle_{\sigma_{\text{Abs}}} &= \frac{1}{I_{\text{Abs}}} \int_0^\infty \Gamma_{GS} \left(\frac{E}{\hat{E}} \right)^2 \sigma_{\text{Abs}}^{\text{SLO}}(E)\, \mathrm{d}E \\
&= \Gamma_{GS} \int_0^\infty \frac{2}{\pi\hat{\sigma}\Gamma} \left(\frac{E}{\hat{E}} \right)^2 \sigma_{\text{Abs}}^{\text{SLO}}(E)\, \mathrm{d}E
\end{aligned}
\tag{2.91}
$$

Eq. (2.48) could be confirmed independently here for the ground-state decay width, but unfortunately the integral does not converge due the aforementioned unphysical

behavior of the ENRF cross section for $E \to \infty$. Still, by performing the last integral numerically only to about twice the resonance energy, it can be seen that it is close to unity as expected from Eq. (2.48), before the onset of the unphysical behavior causes it to ultimately diverge.

Finally, since the photoabsorption cross section of the GDR is usually well describable by a sum of (up to) three SLO resonances, i.e., by

$$\sigma_{\mathrm{Abs}}(E) = \sum_{k=1}^{3} \sigma_k^{\mathrm{SLO}}(E) \tag{2.92}$$

with one resonance for each axis of the nuclear quadrupoloid along which the GDR can oscillate in the geometrical model, and since the optical theorem and dispersion relations are linear in the photoabsorption cross section, the forward scattering amplitude of ENRF on the GDR should be well approximated by the sum of the forward ENRF amplitudes of the individual SLO resonances. Hence, for a nucleus with ground-state spin $J_{GS} = 0$,

$$\sigma_{\mathrm{ES}} = \frac{8\pi}{3} \left| f_{\mathrm{T}} + \sum_{k=1}^{3} f_k^{\mathrm{SLO}}(E) \right|^2 \tag{2.93}$$

is the expected total ES cross section in the energy-domain of the GDR, when assuming the GDR to consist of three SLO resonances. Naturally, the SLO parameters $\hat{E}_k$, Γ_k and $\hat{\sigma}_k$ of the three resonances can be degenerate, for example, in the case of axially symmetric or spherical nuclei.

It should be stressed that for ES the SLO resonances interfere coherently, unlike for the photoabsorption cross section where the resonances simply add up incoherently. This interference effect gives rise to an additional sensitivity of the ES cross section to the structure of the GDR complementary to the one of the photoabsorption cross section. For example, the observed photoabsorption cross sections of the GDR may also be well reproduced using more than three non-degenerate SLO resonances, in contrast to the geometrical model but closer to the microscopical picture of the GDR. Microscopically the GDR is understood to consist of a myriad of states, the product of a strong fragmentation of the collective 1p-1h dipole excitation driven by a strong mixing with more complex configurations [12–14, 91]. A myriad of resonances may only cause an unresolvable fine structure in the photoabsorption cross section not in contradiction to the experimental data. However, such a fine structure of the GDR can

be expected to lead to significant deviations from the predicted behavior of the ES cross section of Eq. (2.93), due to the additional interferences of the many resonances.

To more clearly see the effect of the interference, it is useful to rewrite the absolute square of the sum of scattering amplitudes which occurs in the ES cross section. Using the mathematical properties of complex numbers, this absolute square of a sum of complex numbers can be expanded according to

$$
\begin{aligned}
\left| \sum_k f_k \right|^2 = \left(\sum_k f_k \right) \cdot \overline{\left(\sum_k f_k \right)} &= \left(\sum_k f_k \right) \cdot \left(\sum_k \overline{f_k} \right) \\
= \sum_k \sum_l f_k \overline{f_l} &= \sum_k f_k \overline{f_k} + \sum_k \sum_{l \neq k} f_k \overline{f_l} \\
&= \sum_k |f_k|^2 + \sum_k \sum_{l<k} \left(f_k \overline{f_l} + f_l \overline{f_k} \right) \\
&= \sum_k |f_k|^2 + \sum_k \sum_{l<k} \left(f_k \overline{f_l} + \overline{f_k \overline{f_l}} \right) \\
&= \sum_k |f_k|^2 + \sum_k \sum_{l<k} 2 \operatorname{Re} \left(f_k \overline{f_l} \right) \\
&= \sum_k |f_k|^2 + \sum_k \sum_{l<k} 2 |f_k| |f_l| \cos(\arg(f_k) - \arg(f_l)),
\end{aligned}
\tag{2.94}
$$

where the vinculum denotes the complex conjugate. The two terms in the last line of this derivation can be identified as an incoherent sum and an interference term. When applying Eq. (2.94) to the ES cross section, the incoherent sum term yields the plain sum of the individual pure ES cross sections of the interfering scattering processes, while the interference term yields the non-trivial additional contribution due to the coherent interference of the processes.

2.9.2. Raman scattering on the giant dipole resonance

As discussed in Chapter 1, the geometrical model of the GDR allows to explain the observed photoabsorption cross sections of the GDR, and especially their splitting in deformed nuclei, in a simple way. However, its interpretation of the GDR as the interplay of three orthogonal oscillators in the nucleus, one along each axis of the nuclear quadrupoloid, also has strong implications for the γ decay of the GDR. Similar

to Raman scattering [43, 92] off molecules, the cross section for NRF on the GDR from the ground state into states of the ground-state rotational band with transfer of two units of angular momentum[8] follows from the geometrical model due to the coupling of the GDR to the rotational motion [40, 44, 45]. In the case of nuclei with a ground-state spin of $J_{GS} = 0$, this Raman scattering process is the decay of the GDR after photoexcitation from the ground-state into the $J = 2$ rigid-rotational excitation of the ground state, the latter usually being the 2_1^+ state. Its differential cross section is [40, 44, 45]

$$\frac{d\sigma_{2_1^+}}{d\Omega} = \frac{1}{3} \sum_{k,l=1}^{3} \left| f_k^{SLO}(E) - f_l^{SLO}(E) \right|^2 \underbrace{\frac{3}{40} \left(13 + \cos^2\theta - \sin^2\theta \cos(2\varphi) \right)}_{W_{0^+ \to 1^- \to 2^+}(\theta, \varphi)} \quad (2.95)$$

and its total cross section

$$\sigma_{2_1^+} = \frac{4\pi}{3} \sum_{k,l=1}^{3} \left| f_k^{SLO}(E) - f_l^{SLO}(E) \right|^2, \quad (2.96)$$

where the $f_k^{SLO}(E)$ are the forward ENRF amplitudes of the three orthogonal oscillators of the GDR in the geometrical model as given by Eq. (2.86). According to Eq. (2.96) the 2_1^+ Raman scattering cross section of the GDR becomes larger the more its resonances differ from each other, and vanishes completely if all three resonances are degenerate, due to the destructive interference in this case. Thus, the more a nucleus is deformed, the larger this 2_1^+ Raman scattering cross section should become, while it is expected to vanish for spherical nuclei. Of course, one has to remember that for the latter there is no rotational excitation of the ground state, and therefore Eq. (2.96) should not be applicable in this case. Still, from a simple phonon model, one may expect the 2_1^+ Raman scattering cross section to indeed vanish for spherical nuclei. The 2_1^+ state is a one-phonon vibrational excitation of the ground state in spherical nuclei. Since the GDR itself is considered a one-phonon vibrational excitation of the ground state, the 2_1^+ state should not be populated by γ decay of the GDR in spherical nuclei, as this would require simultaneous destruction of one phonon and creation of another one in a single process. Therefore, one may expect Eq. (2.96) to hold for all nuclear shapes, covering the full range of the continuous transition from spherical to deformed nuclei.

Should Eq. (2.96) be confirmed experimentally, it would provide a compelling argument for the geometrical model of the GDR and its interpretation as three orthogonal

---

[8]This is also referred to as tensor scattering in the literature [43, 44].

oscillators in the nucleus. Furthermore, its dependence on the intricate interplay of the three orthogonal oscillators would provide a high, experimentally accessible sensitivity to the structure of the GDR, complementary to those of the photoabsorption cross section and ES cross section of the GDR. In particular, the 2_1^+ Raman scattering cross section is very sensitive to small differences among the SLO parameters of the three GDR resonances. This, in turn, could establish it as a highly sensitive probe of nuclear deformation, surpassing the sensitivity of the photoabsorption and ES cross sections.

By simply dividing Eq. (2.96) by Eq. (2.93), the (energy-dependent) branching ratio of the GDR decay into the 2_1^+ state relative to ES

$$\frac{\sigma_{2_1^+}}{\sigma_{\mathrm{ES}}} = \frac{1}{2} \frac{\sum_{k,l=1}^{3} \left| f_k^{\mathrm{SLO}}(E) - f_l^{\mathrm{SLO}}(E) \right|^2}{\left| f_{\mathrm{T}} + \sum_{k=1}^{3} f_k^{\mathrm{SLO}}(E) \right|^2} \tag{2.97}$$

can be obtained from theory as well. As a relative quantity, it is, however, much simpler to determine experimentally than the absolute cross sections themselves, while still providing essentially the same information about the GDR structure.

Finally, it is illustrative to compare Eq. (2.97) to the expectation of this branching ratio based on the Alaga rules [93]. The Alaga rules make predictions on intensity ratios for γ transitions to or from rotational states of axially deformed nuclei with well-defined K quantum number assignments. They are based on the assumption that in a rigid rotor nucleus a state's wave function can be separated into a rotational and an intrinsic part. The latter is expected to be identical for states of the same rotational band, and therefore cancels out in γ intensity ratios for such states. The remaining simple ratio of Clebsch-Gordan coefficients, which describe the rotational part of the wave function, is the Alaga prediction for the intensity ratio. Now, to compare Eq. (2.97) to the respective Alaga rule, a deformed, axially symmetric nucleus has to be considered. In this case, the two oscillators of the GDR with $K = 1$ are degenerate, while the oscillator with $K = 0$ is distinct. This can be written as

$$f_2^{\mathrm{SLO}}(E) = f_3^{\mathrm{SLO}}(E) = \frac{1}{2} f_{K=1}^{\mathrm{SLO}}(E) \tag{2.98}$$

and

$$f_1^{\mathrm{SLO}}(E) = f_{K=0}^{\mathrm{SLO}}(E) \tag{2.99}$$

yielding the special case

$$\frac{\sigma_{2_1^+}}{\sigma_{\text{ES}}} = \frac{1}{2} \frac{\left| 2f_{K=0}^{\text{SLO}}(E) - f_{K=1}^{\text{SLO}}(E) \right|^2}{\left| f_{\text{T}} + f_{K=0}^{\text{SLO}}(E) + f_{K=1}^{\text{SLO}}(E) \right|^2} \tag{2.100}$$

of Eq. (2.97) for axially symmetric nuclei. If the two K resonances are furthermore well isolated, i.e., if

$$\Gamma_K \ll \left| \hat{E}_{K=0} - \hat{E}_{K=1} \right| \tag{2.101}$$

holds for both Γ_K, the approximations

$$f_{K=1}^{\text{SLO}}(E) \ll f_{K=0}^{\text{SLO}}(E) \text{ for } E \approx \hat{E}_{K=0} \tag{2.102}$$

and

$$f_{K=0}^{\text{SLO}}(E) \ll f_{K=1}^{\text{SLO}}(E) \text{ for } E \approx \hat{E}_{K=1} \tag{2.103}$$

may be used in Eq. (2.100). Finally, if the interference with Thomson scattering is neglected, this yields

$$\frac{\sigma_{2_1^+}}{\sigma_{0_1^+}} = \begin{cases} 2 & \text{for } E \approx \hat{E}_{K=0} \\ \frac{1}{2} & \text{for } E \approx \hat{E}_{K=1} \end{cases} \tag{2.104}$$

for the branching ratio of the GDR decay into the 2_1^+ state relative to 0_1^+ decay at the two resonances. This result is in agreement with the prediction by the appropriate Alaga rule. Thus, the Alaga prediction can be recovered from Eq. (2.97) for axially symmetric nuclei with well-isolated GDR resonances. However, due to the large observed widths of GDR resonances [19], the employed approximation does not actually hold for the GDR in nature. Therefore, deviations from the Alaga rule predictions are expected for the GDR's γ-decay behavior, due to the interference of its three orthogonal oscillators, an effect that is not considered by the Alaga rules.

3. Experimental approach and realization

This chapter covers all experimental aspects of this work. It starts with a brief overview of the LCB technique and the HIγS facility implementing it which are central for the approach pursued in this work. Next the experimental method developed for the investigation of γ decay of the GDR is presented. Finally, the pilot experiment on the GDRs of ^{140}Ce and ^{154}Sm, realizing this method for the first time, is described in detail.

3.1. Laser-Compton back-scattering and the HIγS facility

3.1.1. The laser-Compton back-scattering technique

Laser-Compton back-scattering (LCB) terms the process of back-scattering laser light off a relativistic electron beam. For a head-on[1] collision of a photon of energy E_γ with a relativistic electron of velocity β in units of the speed of light c, the energy of the scattered photon is [1, 46, 94]

$$E_{\gamma'} = \frac{(1+\beta)\,E_\gamma}{1+\beta\cos\theta + \frac{E_\gamma}{\gamma m_{\mathrm{e}}c^2}(1-\cos\theta)},$$

(3.1)

---

[1]Head-on refers to the photon and electron momenta being anti-parallel.

where θ is the scattering angle of the photon relative to its initial direction, m_e is the electron mass, and

$$\gamma = \frac{1}{\sqrt{1-\beta^2}} \tag{3.2}$$

is the Lorentz factor of the electron. Equation (3.1) is a generalization of Eq. (2.13) and likewise obtained from energy and momentum conservation. For back scattering, i.e., $\theta = 180°$, the energy of the scattered photon is maximized to

$$
\begin{aligned}
E_{\gamma'} &= \frac{(1+\beta)\,E_\gamma}{1-\beta + \frac{E_\gamma}{\gamma m_e c^2}(1+1)} \quad \frac{(1+\beta)\gamma^2}{(1+\beta)\gamma^2} \\
&= \frac{(1+\beta)^2\gamma^2\,E_\gamma}{1 + 2(1+\beta)\,\gamma\,\frac{E_\gamma}{m_e c^2}} \\
&\approx (1+\beta)^2\gamma^2\,E_\gamma,
\end{aligned}
\tag{3.3}
$$

where the last approximation holds for low photon energies and not too high electron energies.

Obviously, the process enables a production of energy-tunable photon beams in the MeV-range through back-scattering of widely available high-intensity laser light off a relativistic electron beam [49, 94, 95]. This is the LCB technique. As visible light has energies in the eV-range, Lorentz factors $\gamma \approx 1000$ corresponding to hundreds of MeV in electron energy are sufficient to produce MeV-ranged photons. Such electron energies are achievable with modern electron accelerators [49]. Since the Compton effect preserves polarization, photon beams of any polarization can be produced by using respectively polarized laser light [95]. Furthermore, if both the electron and laser beam are monochromatic, the scattered photon beam will be monochromatic as well [94]. In practice, a finite energy bandwidth of the electron and laser beams and a small spread in back-scattering angles of the photons constituting the LCB beam will broaden the energy distribution of the latter to a certain extent [1, 46]. Accordingly, at best quasi-monochromatic beams with a finite energy resolution are achieved, with typical FWHMs being a few percent of the beam energy.

So in summary, the LCB technique allows for the production of quasi-monochromatic, energy-tunable, fully polarized photon beams of high intensity in the MeV-range [94, 95]. Such beams are excellently suited for photonuclear experiments [46, 85, 86].

3.1.2. The High Intensity γ-ray Source

The LCB facility used for this work's experiments is the High Intensity γ-ray Source (HIγS) [46, 48]. It is a joined project of the Triangle Universities Nuclear Laboratory (TUNL) and the Duke Free Electron Laser Laboratory (DFELL) and is located on the campus of Duke University in Durham, NC, USA.

As its light source, the HIγS facility utilizes a free-electron laser (FEL) powered by the same electron beam used for the LCB process [46]. Thus, the HIγS facility combines the LCB and FEL techniques for the production of its multi-MeV photon beams. For this purpose, it employs a linear accelerator and a downstream booster synchrotron to accelerate electrons in bunches to kinetic energies of up to 1.2 GeV. These electron bunches are then injected into a storage ring featuring a long straight section enclosed by the wiggler magnets of the FEL. The Lorentz force exerted by the fields of the wiggler magnets onto the electrons forces the latter onto sinusoidal trajectories. As a consequence, they emit polarized eV-ranged synchrotron radiation, which is primarily focused into the electron beam's direction. The polarization of the emitted synchrotron radiation is determined by the wiggler setup. With its available wigglers, the HIγS facility can produce linearly or circularly polarized FEL and LCB beams. In both cases the degree of polarization is nearly 100 % [46]. This FEL beam is then reflected back by an optical mirror into the beamline for LCB on the stored relativistic electron bunches. Any non-scattered photons are reflected again by a second optical mirror forming an optical resonator for the FEL to amplify its beam and, hence, maximize LCB photon production.

The HIγS facility can produce LCB-photon beams of any energy from about 1 to 100 MeV. Due to the time structure of the electron bunches in the storage ring, the LCB beam is pulsed with a repetition rate of 5.58 MHz in its usual two-bunch operation mode, equivalent to intervals of 179 ns between beam pulses. The electron bunches are typically 0.15 to 0.5 ns long and produce FEL pulses of roughly 0.03 to 0.1 ns length [96]. The produced MeV-ranged photons leave the optical resonator of the FEL by simply penetrating the optical mirror and reach the experimental area through evacuated beam pipes. On its way to the experimental setups, the LCB beam passes through an absorber with a circular aperture, typically 20 mm or less in diameter, drilled into it. This absorber acts as a collimator and is positioned approximately 53 m from the interaction point [48]. The collimation is crucial to achieve a high energy resolution of the photon beam by reducing its angular spread. After this collimation

the beam energy-profile follows approximately a Gaussian normal distribution with a FWHM of typically less than 5 % of the beam energy. If LCB beams of higher energy resolution are desired, collimators with small apertures have to be used, which, as a trade-off, however, also reduce the total photon flux. Once the limiting factor of the LCB-beam bandwidth becomes the energy spread of the electron and FEL beams, the HIγS facility can additionally be operated in a special high-resolution mode to further improve the energy resolution at further expense of photon flux. In this operation mode, two electron bunches with substantially different amounts of charge are kept in the storage ring [46]. By preventing the low-charge bunch from reaching lasing, the high-charge bunch is exclusively used for the FEL photon production, while the low-charge bunch is dedicated solely to the LCB process. Through the combination of this high-resolution mode and small-aperture collimators, the HIγS facility can provide photon beams with relative energy resolutions of about 1 % at best [46], though, at the cost of significantly reduced photon fluxes. When both a high energy resolution and a high photon flux are required, the best compromise between the two usually results in a relative beam FWHM of about 2 % of its centroid energy. Finally, if a high energy resolution is of little concern, the HIγS facility can provide LCB beams with photon rates up to about 10^8 γ/s after collimation [46].

3.2. Experimental method

For the aspired experimental investigation of the γ decay of the GDR the NRF technique is well suited, providing a clean probe. Since it predominantly excites dipole transitions [1], NRF allows to selectively excite the GDR and subsequently measure its γ decay. Furthermore, with its purely electromagnetic nature [1], NRF enables the study of γ decay in an essentially model-independent way.

For a comprehensive investigation of the GDR's γ decay through NRF, a (quasi-)monochromatic, MeV-ranged photon beam tunable in energy and of high intensity is necessary. The high energy resolution of the beam is crucial to only excite individual slices of the GDR at a time, and therefore to measure the GDR's γ decay energy-resolved. Likewise, a systematic measurement of its evolution across the full excitation-energy range of the GDR demands an energy-tunable beam, while a high beam intensity is needed to achieve sufficient statistics within a reasonable measurement time.

Previous NRF experiments on the GDR have been lacking in at least one of these aspects [37–42], being limited by the technology of their time. Recently, photon beams offering the required properties became available through the LCB technique [46–49, 94, 95]. Still, at reasonable beam intensities their achievable energy resolutions $\frac{\text{FWHM}}{E_{\text{Beam}}}$ are limited to about 2 % at best at the moment, corresponding to beam energy-profile FWHMs of a few hundred keV in the GDR's energy domain. In turn, even this best-case energy resolution is insufficient to energy-resolve γ decays of the GDR to individual final states close in energy. This is because, unlike for particle-bound states of narrow widths, the GDR's γ-decay signals after photoexcitation are not naturally sharp in energy, owing to its large width. Instead, each individual γ signal from its decay to some final state is effectively an image of the beam profile shifted down in energy by the excitation energy of the decay's final state. This can be seen by considering the spectral density of γ rays of energy E' emitted by NRF reactions[2] to a final state f

$$
\begin{aligned}
\frac{\mathrm{d}Y_f(E')}{\mathrm{d}E'} &= \int \frac{\mathrm{d}\sigma_f(E, E')}{\mathrm{d}E'} \frac{\mathrm{d}^2 N_{\mathrm{T}}}{\mathrm{d}x\,\mathrm{d}y} \frac{\mathrm{d}^3 \Phi(E)}{\mathrm{d}E\,\mathrm{d}x\,\mathrm{d}y} \mathscr{A}_{T \cap \Phi} \,\mathrm{d}E \\
&\approx \int \sigma_f(E)\,\delta(E - E_f - E') \frac{\mathrm{d}^2 N_{\mathrm{T}}}{\mathrm{d}x\,\mathrm{d}y} \frac{\mathrm{d}^3 \Phi(E)}{\mathrm{d}E\,\mathrm{d}x\,\mathrm{d}y} \mathscr{A}_{T \cap \Phi} \,\mathrm{d}E \\
&= \sigma_f(E' + E_f) \frac{\mathrm{d}^2 N_{\mathrm{T}}}{\mathrm{d}x\,\mathrm{d}y} \left. \frac{\mathrm{d}^3 \Phi(E)}{\mathrm{d}E\,\mathrm{d}x\,\mathrm{d}y} \right|_{E = E' + E_f} \mathscr{A}_{T \cap \Phi} \\
&\approx \sigma_f(E_{\text{Beam}}) \frac{\mathrm{d}^2 N_{\mathrm{T}}}{\mathrm{d}x\,\mathrm{d}y} \left. \frac{\mathrm{d}^3 \Phi(E)}{\mathrm{d}E\,\mathrm{d}x\,\mathrm{d}y} \right|_{E = E' + E_f} \mathscr{A}_{T \cap \Phi} \\
&\propto \left. \frac{\mathrm{d}^3 \Phi(E)}{\mathrm{d}E\,\mathrm{d}x\,\mathrm{d}y} \right|_{E = E' + E_f}
\end{aligned}
\tag{3.4}
$$

analogous to Eq. (2.23), where E_f denotes the excitation energy of the final state f and Eq. (2.49) was used. In the penultimate step, the approximation was made that the cross section $\sigma_f(E)$ is constant within the beam's energy profile $\frac{\mathrm{d}^3 \Phi(E)}{\mathrm{d}E\,\mathrm{d}x\,\mathrm{d}y}$, which is reasonable for the narrow bandwidths of the considered beams in comparison to the width of the GDR. The last line explicitly demonstrates the shifted replication of the beam profile by the γ-decay signal. Hence, if final states are too close in energy

---

[2]When setting $E_f = 0$, Eq. (3.4) holds for ES on the GDR as well, since the cross section of this scattering process still has the used properties.

with respect to the beam's bandwidth, their γ-decay signals will overlap, preventing a determination of their individual cross sections from the observed energy-distributions alone[3]. This is especially problematic in the case of deformed nuclei, where the excitation energy of the 2_1^+ state is typically less than 100 keV, causing an overlap of the γ signals from ES and 2_1^+ Raman scattering on the GDR. Yet, as stated in Section 1.3, a primary goal of this work is to develop and apply an experimental technique capable of resolving these scattering processes in a deformed nucleus using an energy-tunable photon source for the first time.

Thus, to overcome this issue, the approach pioneered in this work utilizes linearly polarized photon beams for the excitation of the GDR, which are nowadays readily available through the LCB technique. When photoexciting the $J^\pi = 1^-$ GDR of nuclei with a $J_{GS}^\pi = 0^+$ ground state using such a beam and assuming a pure electric dipole decay to the 2_1^+ state, the angular distributions

$$W_{\mathrm{ES}}(\theta, \varphi) = \frac{3}{4}\left(1 + \cos^2\theta - \sin^2\theta\cos(2\varphi)\right) \tag{3.5}$$

and

$$W_{2_1^+}(\theta, \varphi) = \frac{3}{40}\left(13 + \cos^2\theta - \sin^2\theta\cos(2\varphi)\right) \tag{3.6}$$

of ES and 2_1^+ Raman scattering [1, 75, 82–84] differ significantly. As visible in Fig. 3.1, W_{ES} exhibits a pronounced azimuthal anisotropy while $W_{2_1^+}$ is almost isotropic. This difference in the angular distributions can be used to disentangle the contributions of ES and 2_1^+ Raman scattering to the observed doublet γ signal and, hence, to extract their individual cross sections. To clearly see this, the angular distribution of the

---

[3]It should be noted that the individual cross-section contributions to the overall γ signal could, in principle, be determined from the centroid energy shift of the latter relative to the centroid of the beam profile. However, this requires a very precise measurement of the beam's centroid energy and a very precise energy calibration of the detectors in addition to stability of both over the course of the measurement, which is challenging to achieve in practice.
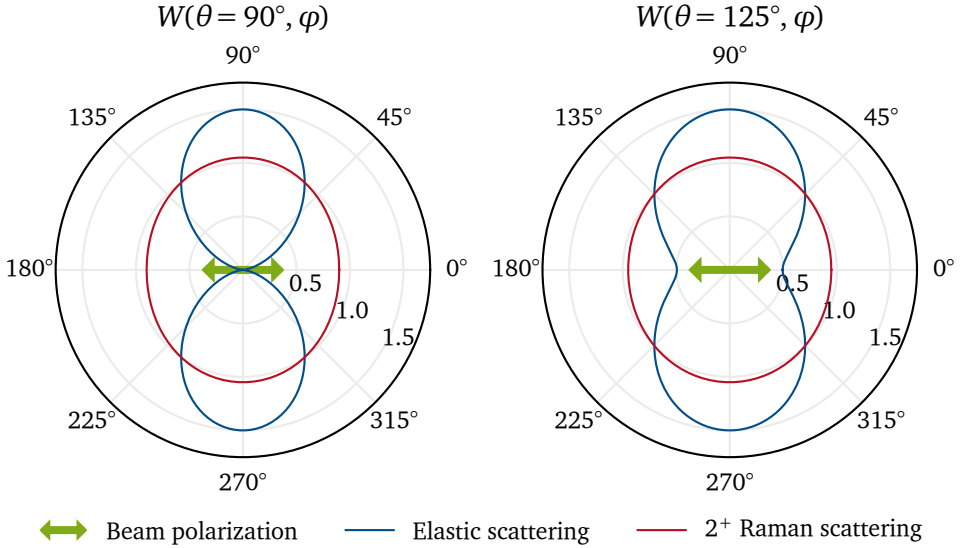
Figure 3.1.: Angular distributions $W(\theta, \varphi)$ of ES (blue) and 2^+_1 Raman scattering (red) of a linearly polarized photon beam on the GDR of a nucleus with a $J^\pi_{GS} = 0^+$ ground state plotted over the azimuthal angle φ for two values of the polar angle θ. The polar angle θ represents the scattering angle of the emitted γ ray, while the azimuthal angle φ is the angle between the polarization plane (green arrow) of the incident photon beam and the scattering plane. The analytical expressions for these angular distributions are provided in Eqs. (3.5) and (3.6).

observed doublet γ signal has to be considered, which is

$$W_{ES+2_1^+}(\theta, \varphi) = \frac{4\pi}{\sigma_{ES+2_1^+}} \frac{d\sigma_{ES+2_1^+}(\theta, \varphi)}{d\Omega}$$

$$= \frac{4\pi}{\sigma_{ES} + \sigma_{2_1^+}} \left(\frac{d\sigma_{ES}(\theta, \varphi)}{d\Omega} + \frac{d\sigma_{2_1^+}(\theta, \varphi)}{d\Omega} \right)$$

$$= \frac{4\pi}{\sigma_{ES} + \sigma_{2_1^+}} \left(\sigma_{ES} \frac{W_{ES}(\theta, \varphi)}{4\pi} + \sigma_{2_1^+} \frac{W_{2_1^+}(\theta, \varphi)}{4\pi} \right) \tag{3.7}$$

$$= \frac{1}{1 + \frac{\sigma_{2_1^+}}{\sigma_{ES}}} \left(W_{ES}(\theta, \varphi) + \frac{\sigma_{2_1^+}}{\sigma_{ES}} W_{2_1^+}(\theta, \varphi) \right),$$

where the additivity of cross sections and their relation to their angular distributions according to Eq. (2.64) have been used. Since it only depends on the branching ratio of 2_1^+ Raman to ES $\frac{\sigma_{2_1^+}}{\sigma_{ES}}$, the latter can be unambiguously determined from a measurement of this angular distribution. To do so, multiple detectors have to be placed at appropriate angles around the target.

The highest sensitivity on the branching ratio is achieved through measurements at angles where the behaviors of the angular distributions of ES and 2_1^+ Raman scattering differ the most. This is the case for $\theta = 90°$ with $\varphi \in \{0°, 180°\}$ and $\varphi \in \{90°, 270°\}$, since with

$$W_{ES}^{\parallel} := W_{ES}(\theta = 90°, \varphi \in \{0°, 180°\}) = 0 = \min_{(\theta, \varphi)}(W_{ES}(\theta, \varphi)), \tag{3.8}$$

$$W_{ES}^{\perp} := W_{ES}(\theta = 90°, \varphi \in \{90°, 270°\}) = 1.5 = \max_{(\theta, \varphi)}(W_{ES}(\theta, \varphi)), \tag{3.9}$$

$$W_{2_1^+}^{\parallel} := W_{2_1^+}(\theta = 90°, \varphi \in \{0°, 180°\}) = 0.9, \tag{3.10}$$

and

$$W_{2_1^+}^{\perp} := W_{2_1^+}(\theta = 90°, \varphi \in \{90°, 270°\}) = 1.05 \tag{3.11}$$

W_{ES} assumes its minimal and maximal values at these angles, while $W_{2_1^+}$ remains almost constant. Hence, by placing detectors accordingly in a cross-like configuration perpendicular to the beam axis around the target with one pair of detectors placed in

and one pair out of the beam's polarization plane, the sensitivity on the branching ratio of 2_1^+ Raman to ES is maximized. The overall experimental principle is illustrated by Fig. 3.2.

For practical reasons, it is useful to consider the azimuthal asymmetry of the doublet γ signal, which is defined as

$$\Sigma := \frac{W_{\text{ES}+2_1^+}^{\perp} - W_{\text{ES}+2_1^+}^{\parallel}}{W_{\text{ES}+2_1^+}^{\perp} + W_{\text{ES}+2_1^+}^{\parallel}} = \frac{W_{\text{ES}}^{\perp} - W_{\text{ES}}^{\parallel} + \frac{\sigma_{2_1^+}}{\sigma_{\text{ES}}} \left(W_{2_1^+}^{\perp} - W_{2_1^+}^{\parallel} \right)}{W_{\text{ES}}^{\perp} + W_{\text{ES}}^{\parallel} + \frac{\sigma_{2_1^+}}{\sigma_{\text{ES}}} \left(W_{2_1^+}^{\perp} + W_{2_1^+}^{\parallel} \right)} \tag{3.12}$$

and is shown as a function of the branching ratio in Fig. 3.3. Since it can be directly related to the efficiency-corrected observed peak areas of the doublet γ signal in the detectors' spectra, it enables a rather straightforward determination of the branching ratio from the data.

Naturally, in a proper analysis the experimental detail of the detectors' limited angular resolution has to be taken into account. According to Eq. (2.69), only mean values of the angular distributions over a detector's solid angle

$$\left\langle W_{\text{ES}+2_1^+} \right\rangle_{\Omega_{\text{Det}}} = \frac{1}{\Omega_{\text{Det}}} \int_{\Omega_{\text{Det}}} W_{\text{ES}+2_1^+}(\theta, \varphi) \, \mathrm{d}\Omega = \frac{A_{\text{ES}+2_1^+}}{Y_{\text{ES}+2_1^+} \cdot \epsilon_{\text{Iso}}} \tag{3.13}$$

can be measured by each detector due to their finite solid-angle coverages Ω_{Det}. Consequently, instead of using Eq. (3.12) directly, in practice its angular distribution values have to be replaced by the corresponding average values over the respective detectors' solid angles which can be calculated from the known angular distribution functions and the geometry of the experimental setup.

Of course, knowledge of the relative efficiencies of the detectors and the geometry of the setup is of utmost importance for the outlined approach to experimentally determine the branching ratio of interest. While the former can be obtained through radioactive source calibration measurements as well as computer simulations and the latter through a simple measurement of the geometry, it is expedient to perform calibration measurements to support the analysis of the data and minimize uncertainties stemming from these characteristics. For this reason, measurements with linearly as well as circularly polarized photon beams on a nucleus with well-separated ES signal,
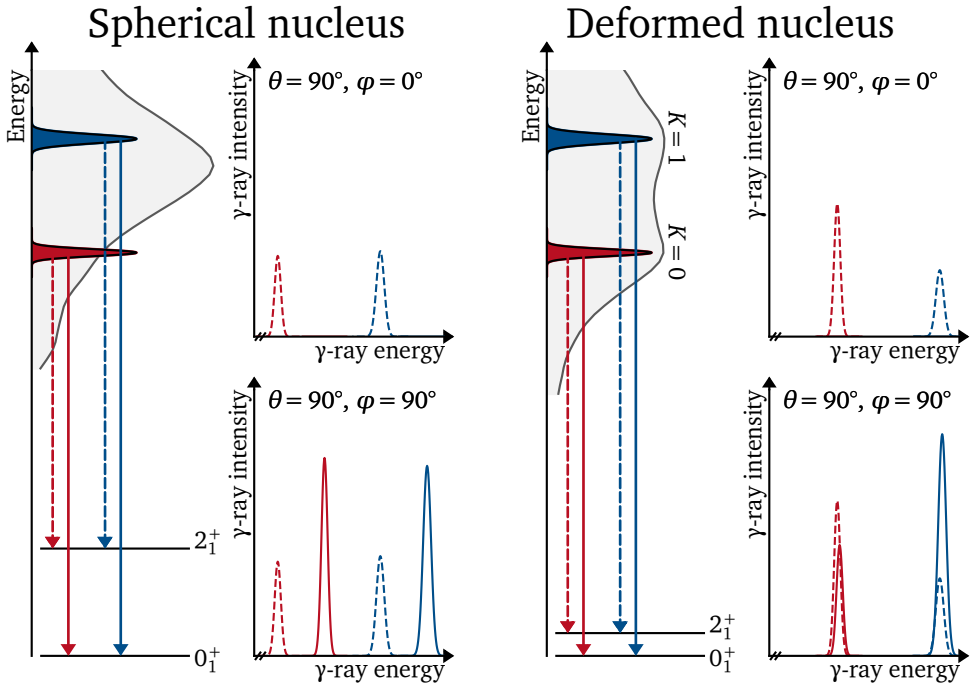
Figure 3.2.: Illustration of the technique devised to measure γ decay (downward arrows) of the GDR (gray) and its evolution with excitation energy (red vs. blue) for spherical (left half) and deformed (right half) nuclei with a 0^+ ground state. Quasi-monochromatic, energy tunable, linearly polarized photon beams are used to photoexcite narrow regions of the GDR (blue or red filled Gaussians) to study their γ decay in the induced ES (blue and red solid lines) and Raman scattering (blue and red dashed lines) reactions to the 0_1^+ and 2_1^+ states, respectively. For a deformed nucleus (right half), the 2_1^+ Raman and ES γ signals overlap, preventing a determination of their branching ratio from a single γ-ray spectrum. Simultaneous measurements of γ rays emitted into the beam's polarization direction (top spectra) and perpendicular to it (bottom spectra) allow to resolve the two, based on their distinct angular distributions when the GDR is excited by a linearly polarized photon beam.
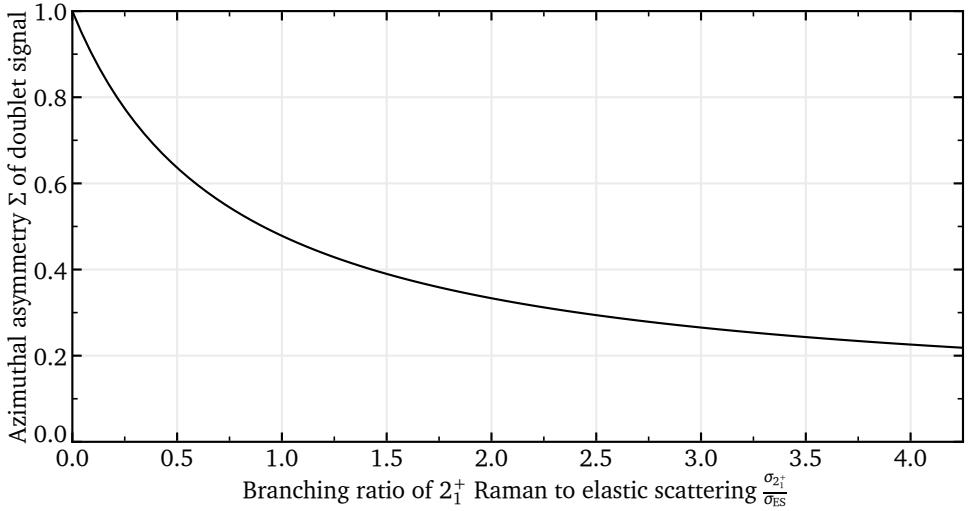
Figure 3.3.: Azimuthal asymmetry of the γ doublet signal from 2_1^+ Raman and ES on the GDR as a function of the branching ratio of the two processes for a nucleus with a $J_{GS}^\pi = 0^+$ ground state and photoexcitation of the GDR with a linearly polarized photon beam. See Eq. (3.12) for the analytical expression of the azimuthal asymmetry.

such as a spherical nucleus, are imperative. When exciting the GDR with a circularly polarized beam, the azimuthal dependency of the angular distribution of any γ signal vanishes. Hence, such measurements are well suited to verify the detectors' relative efficiencies at every investigated excitation energy of the GDR which is impossible to achieve with common radioactive sources. Data taken using a linearly polarized beam on the GDR of a spherical nucleus with sufficiently high-lying first excited state, on the other hand, provide an isolated, anisotropic ES signal. Its parameter-free angular distribution with pronounced azimuthal asymmetry forms an ideal benchmark of the calculated ES angular distribution values and, therefore, of the setup geometry assumed in their calculation. Likewise, calibration measurements in the relevant energy region on strong, narrow NRF resonances of light nuclei can yield similar validation data, but also energy-resolved data on the detector responses as well as energy-calibration data points.

Finally, while the experimental method outlined so far is already well suited to determine the otherwise hardly obtainable branching ratio of 2_1^+ Raman to ES scattering on the GDR $\frac{\sigma_{2_1^+}}{\sigma_{\mathrm{ES}}}$, one piece of information is still missing for an assessment of the cross sections of these processes on an absolute scale. This missing piece is a calibration of the photon flux.

Continuing Eq. (2.23) by again making the approximation that the cross section $\sigma_f(E)$ is constant within the beam profile $\frac{\mathrm{d}^3\Phi(E)}{\mathrm{d}E\,\mathrm{d}x\,\mathrm{d}y}$ yields the relation

$$
\begin{aligned}
Y_f &= \int \sigma_f(E) \frac{\mathrm{d}^2 N_\mathrm{T}}{\mathrm{d}x\,\mathrm{d}y} \frac{\mathrm{d}^3\Phi(E)}{\mathrm{d}E\,\mathrm{d}x\,\mathrm{d}y} \mathscr{A}_{T\cap\Phi}\,\mathrm{d}E \\
&\approx \sigma_f\!\left(E_\mathrm{Beam}\right) \frac{\mathrm{d}^2 N_\mathrm{T}}{\mathrm{d}x\,\mathrm{d}y} \int \frac{\mathrm{d}^3\Phi(E)}{\mathrm{d}E\,\mathrm{d}x\,\mathrm{d}y}\,\mathrm{d}E\,\mathscr{A}_{T\cap\Phi} \\
&= \sigma_f\!\left(E_\mathrm{Beam}\right) \frac{\mathrm{d}^2 N_\mathrm{T}}{\mathrm{d}x\,\mathrm{d}y} \frac{\mathrm{d}^2\Phi}{\mathrm{d}x\,\mathrm{d}y} \mathscr{A}_{T\cap\Phi},
\end{aligned}
\tag{3.14}
$$

which shows that the absolute values of the cross sections σ_f for the reaction f at the beam energy E_Beam can be determined from their observed reaction counts Y_f only if the photon flux $\frac{\mathrm{d}^2\Phi}{\mathrm{d}x\,\mathrm{d}y}$ is known. Naturally, the reaction counts Y_f of ES and 2_1^+ Raman scattering have to be disentangled from the observed doublet γ signal as well, but this is already achieved through the determination of their branching ratio from the angular distribution since

$$
\frac{Y_{2_1^+}}{Y_\mathrm{ES}} = \frac{\sigma_{2_1^+}\!\left(E_\mathrm{Beam}\right)}{\sigma_\mathrm{ES}\!\left(E_\mathrm{Beam}\right)}
\tag{3.15}
$$

follows trivially from Eq. (3.14) as all of its other factors are independent of the reaction f and thus cancel out in this ratio.

The photon flux can be determined through measurements of photon-induced reactions with well-known cross sections in parallel to the NRF measurement using the same photon beam. Suitable reactions for this purpose include Compton scattering, electron-positron pair production and photodisintegration.

For Compton scattering and pair production a dedicated thin target of high atomic number Z should be placed in the beamline and be accompanied by a specialized

detector setup for measurement of the comparably low-energy Compton scattered photons or the 511 keV annihilation photons following pair production, respectively. To obtain a reliable photon-flux calibration from such data, precise knowledge of the setup geometry is crucial and care has to be taken to account for Compton scattering and pair production in other parts of the overall setup in the analysis.

For the photodisintegration approach, on the other hand, it can be sufficient to place appropriate activation targets in the beamline during the NRF measurements and swap them out after each measurement. The activation of these targets through photodisintegrations induced by the beam and therefore its photon flux can then be determined through γ spectroscopy of the subsequent decay of the photoactivated nuclei in a separate detector setup. Naturally, the activation targets have to be chosen such that their photodisintegration cross sections are well known and sufficiently large in the energy range covered by the experiment. Furthermore, their reaction products have to be suitable for decay spectroscopy, i.e., be radioactive with a reasonable half-life and feature decay γ rays of appropriate energies and intensities allowing for a measurement of their activation. For experiments in the GDR energy region, ^{197}Au is commonly used as an activation target since its (γ,n) cross section and product ^{196}Au meet the aforementioned requirements, in addition to ^{197}Au being commercially widely available in the form of thin foils suitable as activation targets. Finally, if the photodisintegration product of a nucleus under investigation meets the prerequisites for an activation experiment, a simultaneous activation measurement on it is always advisable. In such a case the combination of the NRF and activation data taken with the same photon beam enable a direct determination of the GDR's branching ratio of γ decay to the respective photodisintegration process with high precision, independent of an absolute photon-flux calibration.

3.3. The pilot experiment on ^{140}Ce and ^{154}Sm

The experimental approach outlined in the previous section was first realized in an experiment on the semi-magical, spherical nucleus ^{140}Ce and the deformed nucleus ^{154}Sm. The measurements were conducted at the HIγS facility in May 2021 using the at the time newly established Clover Array setup [97]. The complete dataset from this experiment is openly accessible through the data publication [69] associated with this work.

3.3.1. Performed measurements

Data was taken at six photon-beam energies[4] E_{Beam}, namely 11.37, 12.59, 14.27, 15.35, 16.16, and 17.79 MeV. The beam profiles were of slightly asymmetric Gaussian shapes with bandwidths of $\frac{\text{FWHM}}{E_{\text{Beam}}} \approx 2\,\%$. To achieve this, the HIγS facility was operated in its high-resolution mode and a 152 mm long lead collimator with a small aperture of 8 mm diameter was used for beam collimation throughout the experiment. The beam energies were chosen to cover the full evolution of the GDRs of both nuclei, thereby enabling the desired systematic study of the GDRs' γ decays as a function of excitation energy. This is illustrated by Fig. 3.4, which shows the measurement energies in the GDRs of ^{140}Ce and ^{154}Sm, represented by their total photoneutron cross sections.

Measurements were performed with both linearly and circularly polarized photon beams for each beam energy as for the reasons outlined in detail in the previous section. The excitation energies of the 2_1^+ state, which is the first excited state for both nuclei, are 1.596 and 0.082 MeV for ^{140}Ce [99] and ^{154}Sm [100], respectively, with negligible uncertainties in both cases. To briefly reiterate, the measurements with linear polarization of the photon beam were performed to enable a determination of the branching ratio of 2_1^+ Raman to ES of the GDR of ^{154}Sm based on the observed azimuthal asymmetry of the overall γ signal, while those with circular polarization were performed mainly to calibrate the detectors' relative efficiencies at every investigated excitation energy. In contrast to the ^{154}Sm case, due to the high excitation energy of the 2_1^+ state of ^{140}Ce in comparison to the beam bandwidths, its γ signals from ES and 2_1^+ Raman scattering are well separated in energy. Therefore, the measurements on ^{140}Ce with linear and circular polarization of the photon beam are redundant for the determination of its GDR's γ decay behavior. Still, by measuring ^{140}Ce in the same experiment as ^{154}Sm, the data on its isolated γ signals taken with both polarization modes furthermore allows to validate the analysis of the ^{154}Sm data.

---

[4]The beam energies stated here are the energies at which the spectral density of the linearly polarized photon beams peaked. They were determined through the analysis of the ^{140}Ce and ^{154}Sm data taken with these beam settings, see Section 4.6.4 for details. While for the circularly polarized beams of same requested energy slightly different energy values were determined, this detail is omitted here, since all differences in beam energies between the two polarization modes were found to be less than 80 keV. Their actual values are listed in Table 3.2. Finally, it should be noted that all experimentally determined beam energies were found to be 1 to 2 % higher than those requested at the time of the experiment and used in its logbook, which were 11.22, 12.4, 14.0, 15.11, 15.9, and 17.5 MeV.
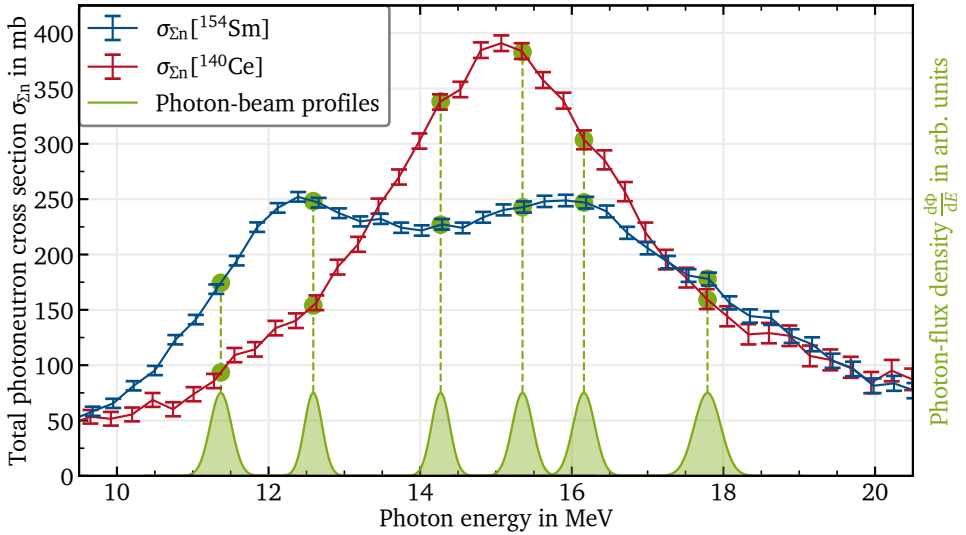
Figure 3.4.: Experimental photoneutron cross sections of the GDRs of ^{140}Ce (red) and ^{154}Sm (blue) along with schematic photon-beam profiles (green), marking the measurement energies of this work's experiment. The ^{140}Ce and ^{154}Sm photoneutron data were measured by Leprêtre *et al.* [98] and Carlos *et al.* [21], respectively, and were retrieved from the EXFOR database [22, 23].

For similar reasons, γ spectra were also taken on ^{12}C and ^{28}Si, again using both polarization modes, at beam energies of 15.35 and 11.37 MeV, respectively. In the specific energy regions covered by these measurements, each of the two nuclei features a 1^+ state of sub-keV width with a large integrated cross section for NRF with subsequent decay to the 0^+ ground state. For ^{12}C this is its 1^+ state at 15.110(3) MeV with an integrated cross section of 1.72(8) keVb for ENRF [101], while for ^{28}Si it is its 1^+ state at 11.4460(2) MeV with an integrated cross section of 2.28(23) keVb [102]. Hence, these measurements on ^{12}C and ^{28}Si produced spectra on strong, isolated, and narrow γ signals of known angular distribution[5] from NRF on these states. This data

---

[5]Their angular distributions are given by Eq. (2.65) with the positive sign when excited by linearly polarized photon beams, while for excitation by circularly polarized beams the φ-dependent term has to be completely omitted. In particular, these angular distributions are identical to those of ES on the GDR rotated by 90° around the beam axis, i.e., after the transformation $\varphi \to \varphi + 90°$.

Table 3.1.: Properties of the NRF-target materials used in the experiment. All targets were of cylindrical shapes. The given diameters and masses refer to the target material and do not include any enclosing containers. The listed enrichments state the relative abundance of the isotope of interest within its chemical element present in the target material.

Nucleus of interest	Chemical form	Enrichment in %	Mass in g	Diameter in mm	Container
^{154}Sm	Sm_2O_3 powder enriched in ^{154}Sm	98.5(1)	2.7414(2)	12.0(2)	Polyethylene capsule
^{140}Ce	CeO_2 powder enriched in ^{140}Ce	99.5(1)	2.3565(2)	20.0(2)	Polyethylene capsule
^{12}C	Graphite crystal	98.93(8)[a]	1.3865(2)	13.0(2)	None
^{28}Si	Silicon crystal	92.22(2)[a]	2.5449(2)	16.0(2)	None

[a] Natural abundance according to Ref. [103] since the target was not artificially isotopically enriched.

is not only well suited to once more scrutinize relative detector efficiencies and the setup geometry, but also provides energy calibration data points and high-resolution data on the detector response in the energy region investigated in this experiment. It thus compliments the usual radioactive source measurements that were performed without photon beam using a ^{56}Co, a ^{60}Co and a ^{152}Eu source for energy and absolute efficiency calibration of the detectors.

The properties of the target materials used for the NRF measurements are listed in Table 3.1. Note that while the ^{154}Sm and ^{140}Ce targets also contained oxygen, carbon, and hydrogen, due to the use of oxide powders encapsulated in polyethylene capsules[6], this did not pose a problem for the experiment and its analysis. None of the naturally occurring isotopes of these elements exhibit a GDR in the energy region relevant to this work [20], and their Thomson scattering cross sections are negligible compared to those of ^{140}Ce and ^{154}Sm.

---

[6] Polyethylene was specifically chosen as the target container material due to its low density and the fact that it only consists of carbon and hydrogen.

3. Experimental approach and realization

Data was furthermore taken without any material at the setup's target position using an 15.35 MeV circularly polarized photon beam and on an empty target container at 12.59 MeV of beam energy using linear polarization mode. The former measurement was performed to check for any potentially problematic photon background originating from the interaction of the photon beam with the setup itself. It confirmed that no significant γ background was present in comparison to the γ signals of interest originating from the targets in their respective measurements. In particular, a contribution to the ^{12}C NRF calibration measurement from ^{12}C naturally occurring in parts of the setup was experimentally excluded by this target-less measurement. Similarly, the data taken with an empty target container at 12.59 MeV verified that indeed no significant γ signal was induced by the polyethylene target containers used in the experiment. A list of all measurements performed in the experiment is given in Table 3.2.

Finally, since both (γ,n) daughter nuclei of the nuclides under investigation met the requirements for activation measurements, (γ,n) photoactivations on ^{140}Ce, ^{154}Sm and ^{197}Au were performed simultaneously to those NRF measurements on ^{140}Ce and ^{154}Sm which used linearly polarized photon beams. For this, thin activation targets were placed in the beamline about 1.37 m downstream of the NRF target position during these measurements. Hence, the activation targets and the NRF targets were irradiated by the same photon beam. Care was taken that the NRF setup's data acquisition was always started shortly before the photon beam began irradiation and only stopped after the beam had been turned off, so that no NRF events were missed. Therefore, the NRF and activation data are directly comparable. The ^{197}Au activation targets were twelve 99.9 % pure, cylindrical gold foils with thicknesses of 20(3) μm, diameters of 12.7(2) mm and masses around 0.05 g. One of these was irradiated during each of the NRF measurements conducted on ^{140}Ce and ^{154}Sm with linearly polarized beams. For the ^{140}Ce and ^{154}Sm activation targets, either about 0.5 g of CeO_2 or about 0.2 g of Sm_2O_3, each in powder form of natural isotopic composition with 99.9 % chemical purity, were pressed into cylindrical shapes with diameters of 12.0(2) mm and enclosed in thin polyethylene capsules. Six targets of each material were produced, with one used in each of the NRF measurements on its corresponding NRF target with linear beam polarization, in addition to the ^{197}Au target, as listed in the notes column of Table 3.2. After irradiation, the activation targets were placed in specialized, high efficiency, low-background γ-spectroscopy setups available at TUNL to measure the γ radiation originating from their photoactivated nuclei. From the number of observed γ rays following β decay of the photodisintegration-daughter

nuclei, the number of (γ,n) reactions[7] caused in each target by the photon beam was determined using the well-known properties [104–106] of the observed radioactive decays. From the reaction counts, in turn, a calibration of the photon flux of the NRF measurements using literature (γ,n) cross-sections values and, independently of this, a determination of the branching ratio of γ to single particle decay of the GDRs of ^{140}Ce and ^{154}Sm is possible, based on the identical irradiation conditions of the NRF and activation targets. The activation data was analyzed by K. Prifti in the scope of her master's thesis [107]. Her results [108] on the photodisintegration reaction counts are combined with the NRF data in Chapters 4 and 5 of this work.

At this point it should be noted that the diameters of all used NRF and activation targets of at least 12 mm were much larger than the beam diameter defined by the 8 mm aperture of the lead collimator. Hence, with proper alignment of the targets in the beamline, all beam photons irradiated all targets[8] in every measurement. This implies that the precise areal densities of the photon beams $\frac{d^2\Phi(x,y)}{dx\,dy}$ were irrelevant for the experiment and its analysis, since all used targets had homogeneous areal densities $\frac{d^2N_\mathrm{T}}{dx\,dy}$ within their uncertainties. In particular, the more general form of Eq. (3.14)

$$Y_f = \sigma_f\left(E_\mathrm{Beam}\right) \iint \frac{d^2N_\mathrm{T}(x,y)}{dx\,dy}\,\frac{d^2\Phi(x,y)}{dx\,dy}\,dx\,dy \qquad (3.16)$$

can be further simplified to

$$\begin{aligned} Y_f &= \sigma_f\left(E_\mathrm{Beam}\right) \frac{d^2N_\mathrm{T}}{dx\,dy} \iint \frac{d^2\Phi(x,y)}{dx\,dy}\,dx\,dy \\ &= \sigma_f\left(E_\mathrm{Beam}\right) \frac{d^2N_\mathrm{T}}{dx\,dy}\,\Phi \end{aligned} \qquad (3.17)$$

for this work's experiment, showing that only the total photon flux Φ, that is the total number of photons that irradiated the targets during a measurement, is of importance to relate GDR reaction counts Y_f to their cross sections σ_f.

---

[7]For ^{154}Sm actually only the sum of the (γ,n) and the (γ,p) reactions counts was determinable, since the ^{154}Sm(γ,p) reaction effectively populates the ^{154}Sm(γ,n) daughter ^{153}Sm as well [104], whose decay γ rays are subsequently measured. See Section 4.6.4 for details.

[8]Ignoring the negligible fraction of photons that were scattered or absorbed in the upstream targets or their containers before reaching the last target.

Table 3.2.: Overview of all performed measurements relevant for this work. The listed targets and sources were placed at the NRF target position during the respective measurements. The beam energies given here were determined from the evaluation of the ^{140}Ce and ^{154}Sm NRF data since it was found in the analysis that these experimental values differed by a few hundred keV from the requested beam energies, see Section 4.6.4 for details. The run numbers are the internal identifiers of individual sub-measurements as used in the experiment's logbook and raw data storage [109]. Some measurements were split across multiple runs due to practical or technical reasons.

Target or source	Beam energy in MeV	Beam polarization	Duration in h	Run numbers	Notes
^{152}Eu			37.588	712, 724, 735, 802	a
^{56}Co			57.780	715, 734, 804	a
^{60}Co			6.982	803	
None	$\approx$15.35[b]	Circular	0.452	716	
Empty container	12.59(1)	Linear	3.005	743	
^{12}C	$\approx$15.35[b]	Circular	2.012	751	
^{12}C	15.35(1)	Linear	2.089	720	
^{28}Si	11.45(1)	Circular	2.001	792	c
^{28}Si	$\approx$11.37[d]	Linear	3.873	739, 790	c
^{140}Ce	11.45(1)	Circular	3.006	782	c
^{140}Ce	11.37(1)	Linear	6.412	788	c e
^{140}Ce	12.66(1)	Circular	2.224	726, 727, 728	
^{140}Ce	12.59(1)	Linear	6.584	742	e
^{140}Ce	14.25(1)	Circular	2.481	747	
^{140}Ce	14.27(1)	Linear	2.410	732	e
^{140}Ce	15.35(1)	Linear	2.581	722	e

Continued on next page

Table 3.2:   (Continued)

Target or source	Beam energy in MeV	Beam polarization	Duration in h	Run numbers	Notes
^{140}Ce	16.18(1)	Circular	3.002	754	
^{140}Ce	16.16(1)	Linear	6.034	761, 762, 764	e
^{140}Ce	17.84(1)	Circular	2.085	776	c
^{140}Ce	17.79(1)	Linear	5.638	767, 768	e
^{154}Sm	11.45(1)	Circular	2.717	783	c
^{154}Sm	11.37(1)	Linear	6.466	786, 787	c f
^{154}Sm	12.66(1)	Circular	2.017	729	
^{154}Sm	12.59(1)	Linear	6.409	741	f
^{154}Sm	14.25(1)	Circular	2.446	746	
^{154}Sm	14.27(1)	Linear	4.285	730, 731	f
^{154}Sm	15.35(1)	Linear	3.088	721	f
^{154}Sm	16.18(1)	Circular	2.786	755	
^{154}Sm	16.16(1)	Linear	6.224	758, 760	f
^{154}Sm	17.84(1)	Circular	2.318	774, 775	c
^{154}Sm	17.79(1)	Linear	5.731	769, 770, 771	f

[a] Some runs of these measurements cannot be used for the calibration of some detectors of the setup. Namely, runs 802 and 804 cannot be used for detector B2 since detector B2 was not operational in these runs and runs 724, 734 and 735 cannot be used for the LaBr$_3$ detectors due to an accidental misconfiguration of the data acquisition system during these runs.

[b] The precise beam energy of these measurements is unknown since no NRF data on ^{140}Ce or ^{154}Sm was taken at this energy in circular polarization mode. The value given here is the one experimentally determined for linear polarization mode at the same requested beam energy, which should be close to the unknown energy of the circularly polarized beam.

[c] Detector B2 was not operational during these measurements.

[d] The runs 739 and 790 were actually performed with slightly different requested beam energies of 11.36 MeV and 11.22 MeV, respectively. However, since this small difference in beam energy does not matter for the analysis of the ^{28}Si NRF data here, the two runs are treated as one measurement for simplicity. Since the precise beam energy of run 739 could, furthermore, not be experimentally determined, the value obtained for the beam settings of run 790 is given here.

[e] A ^{154}Sm and a ^{197}Au activation target was simultaneously irradiated during this measurement.

[f] A ^{140}Ce and a ^{197}Au activation target was simultaneously irradiated during this measurement.

3.3.2. Experimental setup

For this work's NRF measurements, the Clover Array setup [97] was employed. It was installed in the upstream target room (UTR) of the HIγS facility, which is the first experimental site of HIγS downstream of the room housing the here-used lead collimator of 8 mm aperture. The detector setup was shielded from background radiation caused by the collimation of the beam by a thick concrete wall which separates the two rooms. To also minimize background from scattering of the photon beam on air particles, the setup featured a 44.5 mm inner-diameter acrylic-glass beam pipe, which was evacuated during all measurements. It started just downstream of the collimator, passed through a hole in the concrete wall into the UTR and ended about 0.6 m downstream of the NRF target position with an acrylic-glass end cap of about 2 mm thickness. The NRF target position itself was at the center of the Clover Array setup and located about 3 m downstream of the collimator. The alignment of both, the NRF target position in the beam pipe and the activation target position further downstream, to the photon beam itself was achieved by taking 2D spatial images of the beam downstream of both target positions. To take such images, a charge-coupled-device-camera setup with sub-mm resolution is available in the UTR [110]. Through it, the alignment is then simply accomplished by ensuring that the shadows of an alignment target, placed once at each target position, is centered in the beam's images.

Detectors

The Clover Array setup was equipped with four $3'' \times 3''$ LaBr$_3$ scintillation detectors[9], six HPGe clover semiconductor detectors and ten $2'' \times 2''$ CeBr$_3$ scintillation detectors for this work's experiment. Each of the clover detectors consists of four HPGe crystals in a close 2×2 clover-like arrangement along its main axis. So in principle, they all represent four separate HPGe detectors in one common housing. These individual sub-detectors are referred to as clover leaves and their signals were read out independently.

Typically, HPGe detectors offer a superior energy resolution with peak FWHMs of a few keV and a high degree of linearity in their photon-energy response. In comparison,

---

[9]While the detectors' lanthanum(III) bromide is actually doped with cerium, it is still referred to as LaBr$_3$ instead of the more accurate LaBr$_3$(Ce) in this work for simplicity.

LaBr$_3$ and CeBr$_3$ scintillation detectors commonly offer a superb time resolution, slightly higher intrinsic FEP efficiencies and can also be operated at higher count rates. On the other hand, they usually have significantly worse relative energy resolutions of only a few percent and a non-linear energy response, which makes precise energy calibrations challenging, especially at high energies. Naturally, since the intrinsic efficiency of a detector depends on the size of its detection volume, the considerably smaller $2'' \times 2''$ CeBr$_3$ detectors have significantly lower efficiencies than their larger LaBr$_3$ counterparts.

The detectors were aimed[10] at the setup's target position and arranged in a close geometry around the target to maximize the solid-angle coverage and consequently the detection efficiency for γ rays originating from NRF reactions in the target. To reduce, in particular, the count rate of less-relevant, lower-energy ionizing photons, the front faces of all detectors were shielded with lead and copper plates, each a few mm thick, serving as radiation attenuators. These attenuators were secured in place by thin custom-made plastic holders fitted to the detectors' housings. The four LaBr$_3$ detectors were all mounted at a polar angle of $\theta = 90°$ with respect to the beam direction and at azimuthal angles of $\varphi \in \{0°, 90°, 180°, 270°\}$ with respect to the beam's polarization plane, i.e., at those angles best suited for the determination of the branching ratio of 2_1^+ Raman to ES of the GDR of ^{154}Sm from the angular distribution as shown in the previous section. This choice was made to capitalize on their high rate capabilities and efficiencies since the drawbacks of their worse energy resolution and non-linear energy response are not a significant issue for this work's experiment. The six HPGe clover detectors were placed at so-called backward angles with respect to the beam direction of $\theta \in \{125°, 135°\}$ and azimuthal angles $\varphi \in \{0°, 45°, 135°, 180°, 225°, 315°\}$. Finally, the ten CeBr$_3$ detectors were fit in the remaining space at various angles.

In addition to the so far elucidated setup, the UTR also features a coaxial HPGe detector mounted on a remote-controlled moveable platform, which allows to move this detector directly into the beamline downstream of the NRF and activation target positions. The purpose of this $\theta = 0°$ detector is to measure the profile of the photon beam directly. For this, the beam has to be significantly attenuated down to an intensity that the detector can handle though, and hence beam-profile measurements cannot be performed simultaneously to meaningful NRF and activation measurements.

---

[10]The normal vector through the center of the detector's face was aimed at the target position.
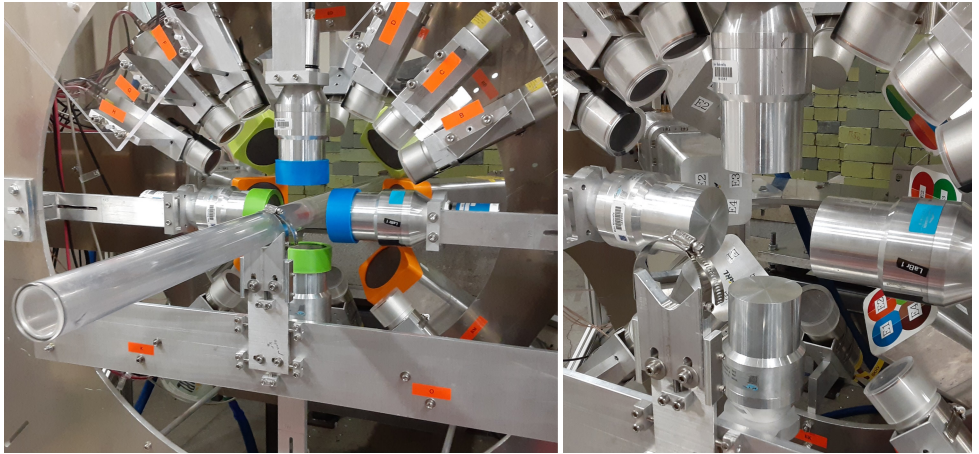
Figure 3.5.: Photographs of the Clover Array setup in the UTR during this work's experiment. Both photographs were taken from a position downstream of the beam. The left image shows the complete Clover Array setup, while the right image shows the same setup with the 50.8 mm outer-diameter acrylic-glass beam pipe and the detectors' attenuators removed. The activation target position and the 0° detector are situated further downstream of the Clover Array and are not visible in these images.

Instead, the beam profile is usually taken before or after the main measurements using remotely deployable beam attenuators and the moveable detector platform. Such beam-profile measurements were taken for all combinations of beam energy and polarization mode in this work's experiment.

The labels used for identification of all detectors in the UTR along with their type, position and attenuator configuration are given in Table 3.3. Two photographs of the Clover Array setup are shown in Fig. 3.5.

Table 3.3.: Detector configuration of the Clover Array setup as employed in this work's NRF experiment. The IDs are the detector identifiers for this specific setup and are used throughout this work and in the logbook of the experiment [109]. Note that they encode a detector's type (numbers with or without "L" prefix for LaBr$_3$ or clover detectors, respectively, and just letters for CeBr$_3$ detectors) and its approximate position in the setup (a "B" prefix for backward angles and ascending numbers or letters for increasing azimuthal angles). The serial or inventory numbers are permanent identifiers found on the detectors. The distances and positions use the usual spherical coordinate system centered at the target position with the polar angle θ and the azimuthal angle φ defined with respect to the beam direction and its polarization plane, respectively. Attenuators are copper and lead plates mounted onto the detectors' faces. The distances are given with respect to the detectors' faces, regardless of any attenuators.

| ID | Type | Serial or inventory number | Relative position | | Distance in mm | Attenuator thickness in mm | | Notes |
			θ	φ		Copper	Lead	
0°	Coaxial HPGe	Duke C120A	0.0°	0.0°	2743(26)	0	0	a b
L1	LaBr$_3$	Duke 166247	90.0°	0.0°	77.4(5)	2.07(2)	5.12(3)	
L3	LaBr$_3$	Duke 165051	90.0°	90.0°	70.4(5)	2.07(2)	5.12(3)	c
L5	LaBr$_3$	Duke 165050	90.0°	180.0°	63.4(5)	2.07(2)	5.12(3)	d
L7	LaBr$_3$	Duke 165052	90.0°	270.0°	65.4(5)	4.14(2)	5.12(3)	
B1	Clover	USNA 0016110391	135.0°	0.0°	203.2(15)	2.07(2)	2.32(3)	a e
B2	Clover	Duke 137367	125.3°	45.0°	203.2(15)	2.07(2)	2.56(3)	f
B4	Clover	Yale 154274	125.3°	135.0°	203.2(15)	2.07(2)	2.56(3)	a g
B5	Clover	ARL 4911I	135.0°	180.0°	203.2(15)	2.07(2)	2.56(3)	h
B6	Clover	ARL 4612I	125.3°	225.0°	203.2(15)	2.07(2)	2.32(3)	i
B8	Clover	Yale 142051	125.3°	315.0°	203.2(15)	2.07(2)	2.56(3)	j

3. Experimental approach and realization

Table 3.3: (Continued)

ID	Type	Serial or inventory number	Relative position		Distance in mm	Attenuator thickness in mm		Notes
			θ	φ		Copper	Lead	
B	CeBr$_3$	S2AB0346	90.0°	27.5°	203.2(15)	1.02(2)	1.16(3)	a
C	CeBr$_3$	S2AB0342	90.0°	45.0°	203.2(15)	1.02(2)	1.16(3)	a
D	CeBr$_3$	S2AB0343	90.0°	62.5°	203.2(15)	1.02(2)	1.16(3)	a
F	CeBr$_3$	S2AB0349	90.0°	117.5°	203.2(15)	1.02(2)	1.16(3)	a
G	CeBr$_3$	S2AB0351	90.0°	135.0°	203.2(15)	1.02(2)	1.16(3)	a
H	CeBr$_3$	S2AB0341	90.0°	152.5°	203.2(15)	1.02(2)	1.16(3)	a
K	CeBr$_3$	S2AB0350	90.0°	225.0°	203.2(15)	1.02(2)	1.16(3)	a
O	CeBr$_3$	S2AB0348	90.0°	315.0°	203.2(15)	1.02(2)	1.16(3)	a
BD	CeBr$_3$	S2AB0345	135.0°	90.0°	203.2(15)	1.02(2)	1.16(3)	a
BK	CeBr$_3$	S2AB0352	135.0°	270.0°	203.2(15)	1.02(2)	1.16(3)	a

a These detectors' data were ultimately not used in the data analysis, see text for details.

b The given position and distance refer to the case when the 0° detector is moved into the beamline. Furthermore, the 0° detector was aimed at the point $(r, \theta, \varphi) = (23(2)\,\text{mm}, 90°, 270°)$ instead of the target position. Thus, the beam hit the 0° detector 23(2) mm off its center axis. The detector suffered from severe electrical issues, which made a reliable energy calibration of its spectra impossible, see text for details.

c Detector L3 was slightly misaligned and aimed at the point $(r, \theta, \varphi) = (4(1)\,\text{mm}, 90°, 180°)$ instead of the target position, i.e., it is slightly too far left when standing in the UTR and viewing the setup from a $\theta = 0°$ downstream position.

d Detector L5 was slightly misaligned and aimed at the point $(r, \theta, \varphi) = (4(3)\,\text{mm}, 90°, 270°)$ instead of the target position, i.e., it is slightly too low when standing in the UTR and viewing the setup.

e Detector B1 was unable to measure photon energies above about 7 MeV.

f Detector B2 stopped working just before run 774. One leaf of detector B2 did not provide valid spectra for the measurements at 17.79 MeV. Another leaf exhibited an abnormally bad resolution in many runs hinting at an electrical issue with this leaf.

g Detector B4 broke down during run 734 and did not provide any valid spectra for photon energies above about 12 MeV.

h Two leaves of detector B5 did not provide valid spectra for the measurements at 17.79 MeV. Another leaf of detector B5 was not operational in many runs due to an electrical issue.

i One leaf of detector B6 did not provide valid spectra for the measurements at 17.79 MeV.

j One leaf of detector B8 did not provide valid spectra for the measurements at 17.79 MeV.

In the end, not all detectors were used in the analysis of the experiment. Due to the very low statistics[11] of the NRF signals in the $CeBr_3$ detectors' spectra in combination with their difficult and time-consuming energy and efficiency calibrations, it was not deemed worthwhile to include them in the analysis at all. For the clover detectors, it was found that many of their leaves showed various issues that made them unsuitable for the evaluation of some or even all of the measurements. The most common issue was a limited energy range, beyond which the detectors did not provide useful data. This affected at least one leaf of each clover detector at the highest energy investigated in the experiment. Since detector B1 did not provide any valid spectra for photon energies above about 7 MeV, it was completely disregarded in this work's analysis. Similarly, detector B4 was not considered in the analysis, as, in addition to having an energy range limited to about 12 MeV, it furthermore broke down already during run 734, i.e., in the early stage of the experiment. While detector B2 likewise stopped working just before run 774, it was still included in the data evaluation, since it was at least operational for the majority of the measurements. However, one of its leaves exhibited an abnormally bad resolution in many spectra hinting at an electrical issue with this leaf. Hence, the data of this leaf was dropped in the analysis. Similarly, one leaf of detector B5 was not operational in many runs due to an electrical issue and was therefore not further considered as well. Finally, the clover detectors B6 and B8 were fully operational in almost all measurements expect for those at the highest beam energy of 17.79 MeV, where, just as for all other clover detectors, some of their leaves suffered from an insufficient energy range. Certainly, malfunctioning leaves could have been excluded from the analysis on a run-by-run basis instead of a general exclusion, but this was simply not deemed worthwhile. After all, the remaining leaves still provided ample data and such a run-by-run exclusion would have unnecessarily complicated and thereby delayed the experiment's evaluation. As the single exception however, clover leaves which suffered from issues solely in the 17.79 MeV measurements were still considered in the analysis for all other beam energies. This issue affecting only four measurements was simply too widespread among the detectors to justify an exclusion of all affected leaves from the analysis. Ultimately though, the $LaBr_3$ detectors' data was sufficient to reach the goal of the experiment. The clover detectors mostly complemented the $LaBr_3$ detectors, providing additional information for the analysis, but were not essential for the experiment's objective anyway.

---

[11]The $LaBr_3$ detectors' spectra generally had more than one order of magnitude more counts than the $CeBr_3$ detectors' spectra in the energy regions of interest.

A more severe issue was raised by the behavior of the 0° detector used for the beam profile measurements. From calibration measurements using a ^{56}Co and a ^{152}Eu source, it was found that the detector's energy response was not even linear in the comparably narrow energy region from 0.3 to 4.9 MeV covered by these source measurements[12]. The residuals of a linear fit to the calibration data points showed significant structures with deviations of up to tens of keV to the known energies [111, 112] of the ^{56}Co and ^{152}Eu decay γ rays. Hence, an extrapolation of this non-linear energy response to the energy region of the beam profile measurements is not reliable and would introduce sizeable energy uncertainties to the beam profile[13]. Furthermore, the detector's energy resolution was found to be significantly worse than expected for a HPGe detector with peak FWHMs larger than 10 keV in multiple measurements and more than 6 keV even in the best cases. Many of its spectra also contained various unphysical, peak-like artifacts around 5, 7, and 10 MeV of high intensity. Finally, multiple beam-profile spectra taken at the same beam energies, but at different times were found to be shifted by up to hundreds of keV with respect to each other. These shifts must be attributed to the 0° detector and its electronics, as the spectra of the Clover Array detectors did not indicate significant beam-energy shifts during the NRF measurements, and such behavior of the HIγS facility's beam would also be highly unexpected.

From this plethora of issues, it had to be concluded that the 0° detector suffered from severe issues, which rendered its whole data unreliable. While unfortunate, in the end, the beam profile measurements made with the 0° detector were not essential for the analysis of the experiment. Since each γ-decay signal of the GDR is an image of the beam profile according to Eq. (3.4), the NRF spectra taken on ^{140}Ce and ^{154}Sm themselves allowed to determine the beam profile and, in particular, its energy with sufficient precision.

---

[12]Sum peaks, which stemmed from two γ rays emitted by the ^{56}Co decay simultaneously depositing their energy in the detector, yielded calibration data points up to 4.9 MeV.

[13]Unlike for the clover and LaBr$_3$ detectors' spectra, as will be discussed in Section 4.3, there were also no higher-energy background peaks present in the 0° detector's spectra, which could have been used for energy calibrations.

Data acquisition system

In this work's experiment the mvme [113, 114] data acquisition (DAQ) system was used for the readout and processing of the signals from the detectors. mvme is a DAQ software and system provided by mesytec GmbH & Co. KG for use with their DAQ hardware products. Hence, on the hardware side the employed DAQ consisted mainly of mesytec electronics. At the core this was a mesytec MVLC VME controller module to manage and read out the other modules as well as communicate with and send the acquired data to the mvme DAQ software running on a local server at TUNL. For the actual analog detector-signal readout and digitization, four mesytec MDPP-16 digitizer modules were used. One of these was used to process the signals of the scintillation detectors, while the other three were used for readout of the clover detectors and the 0° detector, with each being configured with optimized firmware[14] for their respective detector type. Furthermore, in addition to the detector signals, the DAQ system was also fed with an RF signal from the HIγS facility, whose time structure is directly related to the photon beam's time structure. Hence, the recorded RF signal's time information allows correlating detector signals with the beam pulses and thereby to investigate coincidences or anti-coincidences between the beam and the detector signals. Thus, separate spectra for the beam-on and the beam-off periods can be generated through time gating in the analysis using this RF signal.

The DAQ used a synchronous event mode where a trigger from a single channel of a digitizer causes the readout of all modules. To limit the trigger rate, threshold levels had to be set on the digitizers for each channel, which prohibit the generation of a DAQ trigger by signals below their individual energy threshold. However, these thresholds did not only prevent triggering by signals below them, but also the readout of such signals altogether, even when a trigger was generated by another channel. Unfortunately, the mvme DAQ system did not allow configuring two distinct thresholds for triggering and readout. Yet, it was desirable to read out any lower-energy signals of all clover leaves when one leaf observes a high-energy signal, as this is relevant for the generation of add-back spectra of the clover detectors. In add-back spectra, the energy-calibrated signals of all leaves of a clover detector in an event are summed up before being sorted into a single spectrum. This allows to treat a clover detector as a single detector with a higher FEP efficiency than just the sum of the FEP efficiencies

---

[14]The MDPP-16 modules used for the HPGe detectors ran mesytec's SCP firmware, while the one used for the scintillation detectors was configured with their QDC firmware.

of its individual leaves, since events in which the full photon energy was deposited across multiple leaves will still contribute to the add-back spectrum's FEP, unlike in a simple leave-sum spectrum, where the event will be split into multiple lower-energy events. Thus, through the add-back method, events in the single-escape peak (SEP), double-escape peak (DEP), and Compton continuum of a single leaf can be recombined into the FEP if the escaped energy was deposited in one or across multiple of the other leaves. Naturally, this is severely hindered though if lower-energy signals are not read out at all. Hence, to work around the issue of the single energy threshold for both triggering and readout imposed by the mvme DAQ system, the signals of the clover detectors were also fed into an analog Fan-In-Fan-Out module, which summed the analog signals of all leaves of a clover detector into a single signal[15]. These analog-sum signals were then connected to one of the MDPP-16 modules to generate readout triggers from the clover detectors with a high energy threshold, while the individual leaf signals were read out with a low energy threshold by two other MDPP-16 modules, which were simply configured to not generate triggers at all. This way, readout and triggering of the clover detectors were manually decoupled, allowing to read out low energy signals of the clover detectors, while still only generating triggers for high energy signals.

In the end though, no add-back spectra of the clover detectors were used in this work's analysis. This is because during the latter, it was found that the DAQ system was misconfigured in a way that severely hindered the generation of add-back spectra. The window of interest, during which the DAQ system waited for signals after being triggered, was set to a width of about 6000 ns for the clover detectors[16]. This was a very long time period for this purpose, much longer than necessary, as it could, for instance, cover up to 34 beam pulses of the HIγS facility. More importantly though, it was much longer than the time period the 16-bit time-to-digital converters of the MDPP-16 modules could cover. Since their resolution was set to about 0.0244 ns per time value, the 16-bits, corresponding to 65 536 distinct time values, could only cover a time period of about 1600 ns. For any signal arriving after this time period, but within the 6000 ns window of interest, the time-to-digital converter would overflow and not be able to assign a time value to the signal, though the signal's energy would still be recorded by the digitizer. This caused up to 45 % of all clover events in the

---

[15]Care was taken that all leaves of a clover detector have a similar energy response, so that this summed signal is approximately proportional to the total energy deposited across the leaves.

[16]The window of interest for the scintillation detectors was set to a reasonable value of 400 ns.

---

recorded data to not have a time stamp attached to them. Hence, when performing any time gating on the clover detectors' data, a significant number of events will be immediately lost, since without a time stamp they cannot fulfill any time-gate condition. Therefore, a creation of add-back spectra for the clover detectors with a time-gate on coincident signals among their leaves was out of the question. Now, usually one could just generate add-back spectra without explicit time-gating by simply considering all signals of a clover detector's leaves within the same event as coincident. However, this is severely hindered by the large window of interest as well, since it allows for a significant number of random coincidences between the leaves to be part of the same event which would be erroneously added up in such ungated add-back spectra. Hence, no meaningful add-back spectra could be generated from the clover detectors' data due to this misconfiguration of the DAQ system. Likewise, any beam-pulse gating on the clover detectors' data went along with a significant loss of statistics due to the missing time stamps. Therefore, such time-gated spectra were not used in the analysis either, except for the energy calibration step where only the overall quality of the spectra was of relevance, while the exact number of counts contained in them did not matter much.

Ultimately, the unavailability of time information for all events of the clover detectors did not significantly impact the evaluation of the experiment. Instead of evaluating add-back spectra, the energy-calibrated spectra of the leaves were simply summed up for each clover detector for the analysis. While this resulted in a reduced FEP efficiency in comparison to proper add-back spectra, this drawback loses much of its relevance when the events in the SEP, DEP, and Compton continuum are considered in the analysis as well, which is the case in this work.

4. Analysis of the experimental data

This chapter elaborates on the analysis of the ^{140}Ce and ^{154}Sm NRF data taken on the γ decay of their GDRs in the 2021 pilot experiment at the HIγS facility presented in Section 3.3. All steps of the analysis discussed here can be reproduced using the data publication [69] associated with this work, which is openly available in the TUdatalib repository of Technische Universität Darmstadt.

4.1. Analysis software

Naturally, the analysis relies heavily on modern computation technology for data storage, processing and visualization to handle the large amount of data produced by the experiment with state-of-the-art evaluation methods and tools. Almost all computer code produced specifically for this work was written in the Python programming language [115]. It was executed in the CPython reference implementation [116] of the language and made use of the plethora of software libraries available for Python, in particular those aimed at scientific computing. Without explicit inclusion of their individual dependencies, the employed libraries most central for this work were ArviZ [117, 118], Hist [119], ipywidgets [120], JupyterLab [121, 122], Matplotlib [123, 124], NumPy [125, 126], NumPyro [127–129], PyMC [130–132], SciPy [133, 134], uncertainties [135] and Uproot [136]. NumPy and SciPy were used throughout the entire analysis for the various algorithms and data structures these packages provide, especially for numerical computations. Likewise, the uncertainties package was employed throughout the analysis for its seamless implementation of the propagation of uncertainties. Uproot allowed for the interfacing with ROOT files [137, 138], while Hist was utilized for the generation of the spectra from the raw data. PyMC was the cornerstone packages for all performed Bayesian analyses

which were furthermore supported by NumPyro for efficient numerical sampling and ArviZ for handling of the results. Finally, the JupyterLab, ipywidgets and Matplotlib packages allowed for interactive data exploration and visualization. JupyterLab, in particular, introduces interactive notebook files [121] that can combine code, text, mathematical derivations, and visualizations in a single document, which enabled a thorough documentation of the analysis process and its results already during this process and in the same location as the analysis code itself. The Matplotlib package was also used to create all plots in this work.

In addition to the specifically developed analysis code and the aforementioned Python packages, the analysis also made use of the software packages HDTV and utr. The spectrum analysis software HDTV [139] was used to review experimental spectra and fit peaks within them for the energy and efficiency calibrations. For Monte-Carlo simulations of the detector response, the utr [140] software package was used, which itself is based on the GEANT4 simulation toolkit [141–143]. This furthermore required to implement the full geometry of this work's experimental setup in C++ code.

4.2. Generation of spectra from raw event data

The mvme DAQ system used in the NRF experiment recorded the raw event data of the detector signals in a custom binary file format. For easier handling of the raw data, it was first converted to the ROOT file format using a ROOT client shipped with the mvme software for this purpose [113, 114]. The ROOT file format [137, 138] is a binary file format widely used in particle and nuclear physics, which allows for efficient storage of and access to large amounts of data. Due to its wide adoption, it is supported by many software packages, including the Uproot [136] package for Python used in this work to interface with ROOT files. After this conversion the raw event data still needed to be processed into spectra for further analysis. For this purpose, a Python event-sorting code named mvmeRoot2Spec was written tailored to the specific ROOT file structure produced by the mvme ROOT client. Besides the generation of simple energy spectra, the program also allows for easy formation of more complex structures like difference, gated and arbitrary multidimensional coincidence spectra. In particular, the creation of add-back and beam-pulse-gated spectra was implemented in the program. While a one-size-fits-all event-sorting program is hardly feasible due to the variety of DAQ systems and their peculiarities, care was taken to implement

the code with a somewhat generic structure and ample documentation, so that it can be adapted to other DAQ systems with little effort or at least serve as a starting point for similar projects in the future. The mvmeRoot2Spec code is included in the data publication [69] belonging to this work.

During the generation of the spectra from the raw event data, using the mvme-Root2Spec program, the misconfiguration of the DAQ system discussed in Section 3.3.2 was uncovered. Consequently, multiple features implemented in the mvmeRoot2Spec code were not used for this work's evaluation after all, as this misconfiguration rendered the clover detectors' data unusable for these. Ultimately, only simple energy spectra without any coincidence conditions were considered in the main analysis of the ^{140}Ce and ^{154}Sm NRF data. In particular, no add-back or beam-pulse-gated spectra were utilized. In the case of the clover detectors, the energy-calibrated spectra of their individual leaves were simply summed to obtain one spectrum per detector which were evaluated instead of add-back spectra. For the LaBr$_3$ detectors, it was found that on-beam-pulse-gated spectra were not necessary for the NRF analysis as background radiation during the beam-off periods in the energy region of interest was negligible anyway. Therefore, there was simply no need for their usage. However, as already stated, off-beam-gated spectra were used for energy calibration purposes, as will be discussed in the following section.

4.3. Energy calibration of the spectra

The first analysis step after generating the spectra from the raw data was to energy calibrate them. Energy calibrations relate the channel numbers, which the DAQ system assigns to every signal produced by a detector when it observes an event, to the physical energy deposited in the detector by the event. They are necessary to convert the raw-channel-based spectra into calibrated ones, which use physical units and are suited for the further analysis. To conduct an energy calibration, peaks of already well-known energies are identified in the detectors' spectra and their corresponding mean channel numbers are determined. With these calibration pairs a mathematical relation between channel numbers and energies can then be established, which is the required energy calibration function for the detector [144, 145]. In most cases a polynomial of low order fitted to the calibration points suffices as an energy calibration function. For HPGe detectors, such as the clover detectors used in this work, commonly

a linear function is already sufficient for this purpose, while scintillation detectors, like the LaBr$_3$ detectors, often require a higher-order polynomial [145]. A good indicator whether a polynomial of a certain order is adequate for a calibration are its residuals for the calibration points. If they do not show any distinctive structure, the polynomial is likely sufficient and any higher-order polynomial would be overfitting the calibration points.

All energy calibrations in this work use polynomials. The peak positions in the uncalibrated spectra were determined by fitting Gaussian functions to them on a polynomial background. This was done using the HDTV software [139].

A first energy calibration of all detectors was obtained from the measurements with either the ^{56}Co, the ^{60}Co, or the ^{152}Eu radioactive source placed at the target position. During their radioactive decays, they emit γ rays of well-known energies [111, 112, 146], which were used for these calibrations. However, the energies of their observed γ rays and therefore the calibration region were limited to 3.548 MeV [111]. Hence, usage of these calibrations at the much higher energies of the GDR NRF measurements would have implied a tremendous extrapolation of the calibrations.

At the same time, the high energies of the employed HIγS photon beams, greater than 11 MeV, meant that their photons exceeded in energy the neutron separation thresholds of many nuclei contained in the setup materials, such as the NRF targets and the beam dump. Accordingly, a significant number of (γ,n) reactions in these materials were induced during beam operation, which produced free neutrons that were subsequently captured in (n,γ) reactions by other nuclei in the environment. This is apparent from an abundance of background peaks appearing only in the spectra taken with beam, which were identified to originate either directly from such (n,γ) reactions[1] or, in one case, from radioactive decay of ^{28}Al, the ^{27}Al(n,γ) reaction product. These background peaks span a wide energy range from 1.779 to 9.298 MeV and are superbly suited for energy calibrations of the detectors even on a measurement-by-measurement basis. The latter is of relevance, as the energy

---

[1] Since neutron capture excites the newly formed nucleus to an excited state around its neutron separation energy, it is commonly followed by the prompt de-excitation of this nucleus through the emission of one or more γ rays with respective, comparably high energies.

response[2] and, hence, the necessary energy calibration of a detector, can change from one measurement to another due to various reasons, such as event-rate dependencies or shifts in the amplifier gain. By calibrating each spectrum using its own background peaks, such changes can be accounted for and the best possible energy calibration for each spectrum is obtained.

First background peaks, their origins and, hence, precise energies according to literature databases had to be determined though. To search for background peaks, the off-beam gated spectra of the clover detectors were employed, using the initial energy calibration obtained from the radioactive source measurements. The clover detectors were chosen for this purpose because of their superior energy resolution and their highly linear energy response, which had already been confirmed by the source measurements. The latter allowed for the necessary extrapolation of this energy calibration to the significantly higher energies of the background peaks with sufficient precision. This would not have been trivial for highly non-linear energy responses as had been observed for the LaBr$_3$ detectors. The off-beam gated spectra were used since they featured a better peak-to-background ratio compared to the non-gated spectra[3], which allowed for better identification and fitting of the peaks. This advantage even outweighed the drawback of the substantially reduced statistics in the clover detectors' off-beam gated spectra, which was caused by the DAQ system's misconfiguration as discussed in Section 3.3.2. For the mapping of the observed background peaks to their respective origin, and therefore their nominal energies, the databases of Refs. [147, 148] were consulted. The results of this assignment are summarized in Table 4.1, while Fig. 4.1 shows typical spectra in the energy region of the most energetic observed background peaks. In order to exclude incorrect assignments, it was checked for each assigned reaction that its capturing nuclei were plausibly present in the setup's environment and that none of its other γ rays, which should have been observed based on their relative intensity and the background level at their respective energies, were missing in the spectra.

---

[2]Energy response refers to the relation between the energy actually deposited in a detector by an event and the signal produced by the detector in response to this. Not to be confused with the term detector response used in this work, which refers to the relationship between the energy of an incident photon and the probability distribution of the energy deposited in the detector by it.

[3]While these background peaks were also beam-induced, this peak-to-background enhancement through off-beam gating can be explained by the (n,γ) capture reactions being regularly slightly delayed in time, since it takes the neutrons some time to be captured, e.g., because they have to thermalize first. In comparison, most of the background continuum, which might be mainly detector response, seems to be produced in prompt reactions, such as photon scattering.
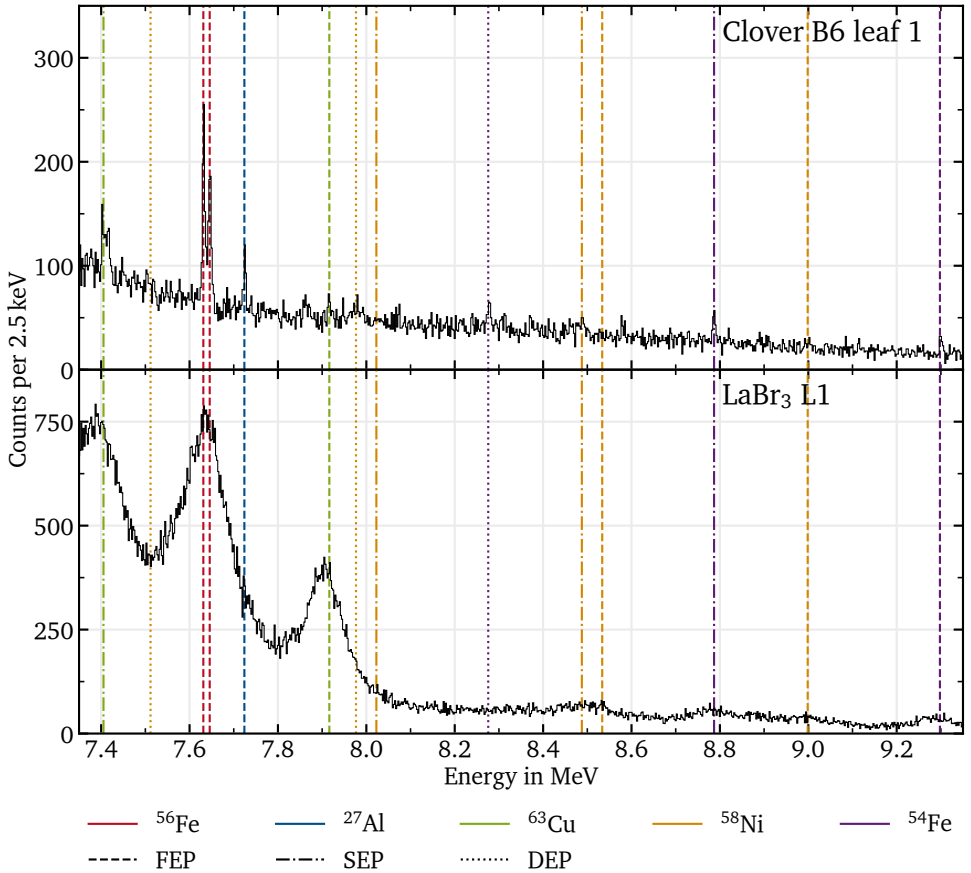

Figure 4.1.: Extracts of energy calibrated, off-beam gated spectra of the LaBr$_3$ detector L1 (bottom) and leaf 1 of the clover detector B6 (top) for run 754, in which ^{140}Ce was irradiated by a 16.18 MeV circularly polarized photon beam. Multiple background peaks stemming from (n,γ) reactions are observed in the spectra. Their energies according to Ref. [148] are marked by vertical lines. The lines' colors encode the nuclei capturing a neutron, while their styles distinguish FEPs (dashed), SEPs (dash-dotted), and DEPs (dotted).

Table 4.1.: Observed background γ rays stemming from (n,γ) reactions used for the energy calibration of the detectors. The listed nuclei are those capturing the neutrons. The intensities of the γ rays are relative to the most intensive γ ray produced in the same reaction. The data was taken from Ref. [148] unless stated otherwise.

Nucleus	γ-ray energy in keV	Relative intensity in %	Notes
^{27}Al	1778.99(2)	100.0	a
^{40}Ca	1942.61(17)	100.0	
^{1}H	2223.25	100.0	
^{28}Si	3538.98(4)	100(5)	
^{28}Si	4933.98(3)	94(5)	
^{139}La	5161.00(1)		b
^{56}Fe	5920.35(7)	33(7)	
^{56}Fe	6018.42(7)	34(7)	
^{40}Ca	6420.7(10)	49.15	
^{56}Fe	7278.82(9)	21(5)	
^{56}Fe	7631.18(10)	100(24)	
^{56}Fe	7645.58(10)	86(20)	
^{27}Al	7724.03(1)	96.06(36)	
^{63}Cu	7916.26(8)	100.0(26)	
^{58}Ni	8533.71(7)	48(1)	
^{58}Ni	8998.63(7)	100(2)	
^{54}Fe	9297.8(10)	100(9)	

[a] This γ ray is not directly emitted in the ^{27}Al(n,γ)^{28}Al reaction, but by the subsequent β decay of ^{28}Al to ^{28}Si with a lifetime of 2.245(2) min. The data was taken from Ref. [102].

[b] Only observed in the LaBr$_3$ detectors. Caused by ^{139}La, which is abundant in the LaBr$_3$-detector crystals [103], capturing a neutron and forming ^{140}La in its 5161.00(1) keV excited state [99]. While this excited state can decay via a multitude of γ-ray cascades with significant intensities [99], no such additional peaks were observed. This is, however, easily explained by the fact that these γ rays originate from within the detector crystals, which makes it very likely that they all deposit their energy within it. This causes the observed sum peak at the state's excitation energy, which is apparently by far the likeliest outcome of this decay.

With the origin of the background peaks and, hence, their nominal energies determined, linear energy calibrations were performed for the spectra of each clover-detector leaf in each NRF measurement. While these mainly relied on the (n,γ) background peaks listed in Table 4.1, they also used a few well-known lower-energy natural background peaks, such as the electron-positron-annihilation peak at 511.00 keV, the ^{40}K decay peak at 1460.82(1) keV [149], and the ^{208}Tl and ^{208}Bi decay peak at 2614.51(1) keV [150]. To increase the number of calibration points further, in addition to the FEPs, SEPs and DEPs were also included in the calibration data sets. The adequacy of the obtained linear energy calibrations was confirmed by their residuals not showing any noticeable structures. Furthermore, their expectable accuracy was investigated by examining the energy values assigned by the calibrations of the ^{12}C and ^{28}Si spectra to the NRF peaks of these nuclei, which were not used for the calibrations of the clover leaf spectra. Though this required a substantial extrapolation of the calibrations to these peaks' energies around 15.1 MeV [101] and 11.4 MeV [102], respectively, the obtained values deviated by only a few keV from the literature values [101, 102] after recoil correction according to Eq. (2.7). Figure 4.2 illustrates this on the example of a leaf of the clover detector B6. This accuracy is more than sufficient for the purposes of this work, concluding the energy calibration of the clover detectors.

The energy calibration of the LaBr$_3$ detectors was more challenging due to their strongly non-linear energy responses. The base of the calibration data set was again formed by the (n,γ) background lines of Table 4.1 and the aforementioned natural background lines. As for the clover detectors, their FEPs, SEPs and DEPs were fitted in off-beam gated spectra to obtain calibration points. This data already showed a clear non-linearity in the energy responses of all LaBr$_3$ detectors. While it would have been trivial to fit a higher-degree polynomial to the data to energy-calibrate the LaBr$_3$ detectors' spectra in the energy region covered by the calibration points reasonably well, the actual goal was to obtain calibrations suitable for the full energy range covered by the NRF measurements on the GDRs of ^{140}Ce and ^{154}Sm. However, no single polynomial of any order, fitted to just this calibration data, extrapolated well to these much higher energies for any of the LaBr$_3$ detectors. This was proven by the spectra of the ^{12}C and ^{28}Si calibration measurements, since the expected positions of their NRF peaks could not be reproduced by such calibrations obtained from just the background peaks. The observed deviations to the nominal value for the ^{12}C NRF peak around 15.1 MeV, for example, were of the order of few hundreds
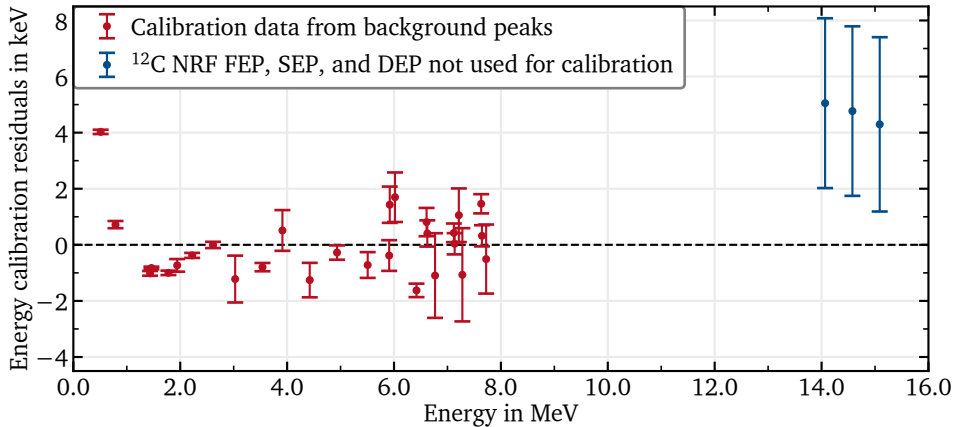
Figure 4.2.: Energy calibration residuals of leaf 1 of the clover detector B6 for the ^{12}C measurement taken with a 15.35 MeV linearly polarized photon beam. The linear energy calibration was constructed based on background peaks, whose calibration residuals are shown in red. Since no structure is apparent in these residuals, the linear calibration is considered adequate. The FEP, SEP and DEP from NRF on ^{12}C were not used for the calibration and thus provide an independent test of its accuracy. Their calibration residuals are shown in blue and are of the order of a few keV, which is a sufficient accuracy for the purposes of this work.

of keV. Furthermore, not even the relative energy distances of 511 keV separating the FEPs, SEPs and DEPs could be reproduced correctly by such calibrations with deviations of up to 100 keV to the correct 511 keV distances in many cases. The latter is especially problematic for here-aspired detector-response deconvolutions, which require a correct spacing of these peaks, while the absolute energy scale is less critical for this purpose.

To alleviate this issue and obtain more reliable energy calibrations for the higher energies of the GDR NRF measurements, the calibration approach was modified in comparison to the clover detectors. Instead of only relying on the lower-energy background peaks, the FEPs, SEPs and DEPs of the ^{12}C and ^{28}Si ground-state-decay NRF signals were included in the calibration data set. For this, they were fitted in the non-gated spectra of the respective measurements taken with circularly polarized

photon beams. Since these peaks were, however, part of two different measurements, in between which the energy response of at least detector L3 noticeably changed, channel-to-channel recalibrations were performed using the background peaks contained in both measurements. Essentially, a mapping between the channel numbers of the two spectra corresponding to the same energies was constructed by fitting a linear function to the respective channel pairs of the background peaks for each detector. A linear function was chosen for this purpose since changes in the energy response of the detectors were relatively small and a robust extrapolation behavior of this recalibration was crucial. Using these recalibration functions, the fitted channel numbers of the ^{28}Si NRF peaks were mapped to the channel numbers they were expected to have had in the ^{12}C spectra. This allowed for the combination of the ^{12}C and ^{28}Si calibration points from their NRF reactions, along with the background peaks observed in the ^{12}C measurement, into one data set for each detector. This data set was then used to fit a fourth-degree polynomial as the calibration function of this detector for its spectrum taken on ^{12}C with the circularly polarized photon beam in run 751. A fourth-degree polynomial was chosen since all fits of lower-degree polynomials showed a noticeable structure in their residuals for the calibration points, while the fourth-degree polynomial did not. Finally, to address potential energy-response shifts between this ^{12}C measurement, which now provided the energy-calibration functions $E(c)$, and all other measurements, linear channel-to-channel recalibrations $c(c')$ were constructed for each of the latter using the background peaks just as before. These recalibrations were then composed with the respective calibration function to obtain the final energy calibrations $E(c') = E(c(c'))$ for each of the LaBr$_3$ detectors and each of their spectra. With this approach all LaBr$_3$ detector spectra were energy-calibrated as accurately as possible.

Still, these obtained calibrations were not perfect. This was evident by deviations of the ^{12}C NRF peaks from their expected positions in the LaBr$_3$ spectra taken with the linearly polarized photon beam on ^{12}C. Although the discrepancies were significantly reduced compared to those observed with calibrations based solely on background peaks, they were still on the order of tens of keV for detectors L1 and L3 and around 100 keV for detectors L5 and L7. The origin of these remaining deviations are shifts in the energy response of the LaBr$_3$ detectors between the measurements, which could not be fully accounted for by the performed linear recalibrations. Such shifts are clearly visible in a comparison of the LaBr$_3$ detectors' uncalibrated spectra for the ^{12}C measurements taken with circularly or linearly polarized beams, where the ^{12}C

NRF peaks' positions do not coincide between the two measurements. While the full cause of these shifts is unclear, at least one contributing factor was already identified during the experiment. In a brief test measurement on ^{12}C in which the photon-beam intensity was slowly increased, a shifting of the ^{12}C NRF peaks in the LaBr$_3$ spectra was observed in real time. Hence, changes of the event rate of the LaBr$_3$ detectors clearly contribute to such shifts in their energy response. However, in the interest of time, this issue was not further investigated in this work. After all, at least the relative energy distances of 511 keV between the FEPs, SEPs and DEPs in all ^{12}C and ^{28}Si spectra were now reproduced much more accurately, with deviations of only a few keV, if any. As mentioned earlier, this was the more relevant factor for the planned detector-response deconvolutions, while correct absolute energies could be obtained from the clover detectors' spectra. Thus, whenever necessary, the LaBr$_3$ detectors' spectra were simply shifted to match the clover detectors' spectra in the energy region of interest.

For illustrative purposes, Fig. 4.3 shows spectra taken during the irradiation of ^{12}C by linearly and circularly polarized photon beams, while Fig. 4.4 shows the same for ^{28}Si.

4.4. GEANT4 simulations of the detector responses

For the evaluation of the NRF data taken on the GDR, the detector efficiencies with respect to the NRF target position in the energy region covered by these measurements has to be known. While experimental values for FEP detector efficiencies with respect to the target position are easily obtainable from source measurements, just as for the energy calibrations, they can only cover a limited energy range. With the ^{56}Co, ^{60}Co, and ^{152}Eu source measurements performed in this work's experiment, the upper end of this range was 3.548 MeV [111]. Unlike for the energy calibrations, the observed (n,γ) background peaks cannot be used for efficiency calibrations, since they do not originate from the target position and, hence, do not provide the necessary efficiency values with respect to it. However, simply fitting an empirical model to the experimental low-energy efficiency data obtained from source measurements and extrapolating it to the higher energies of the GDR NRF measurements would be highly unreliable and therefore unfeasible, just as discussed for the energy calibrations.
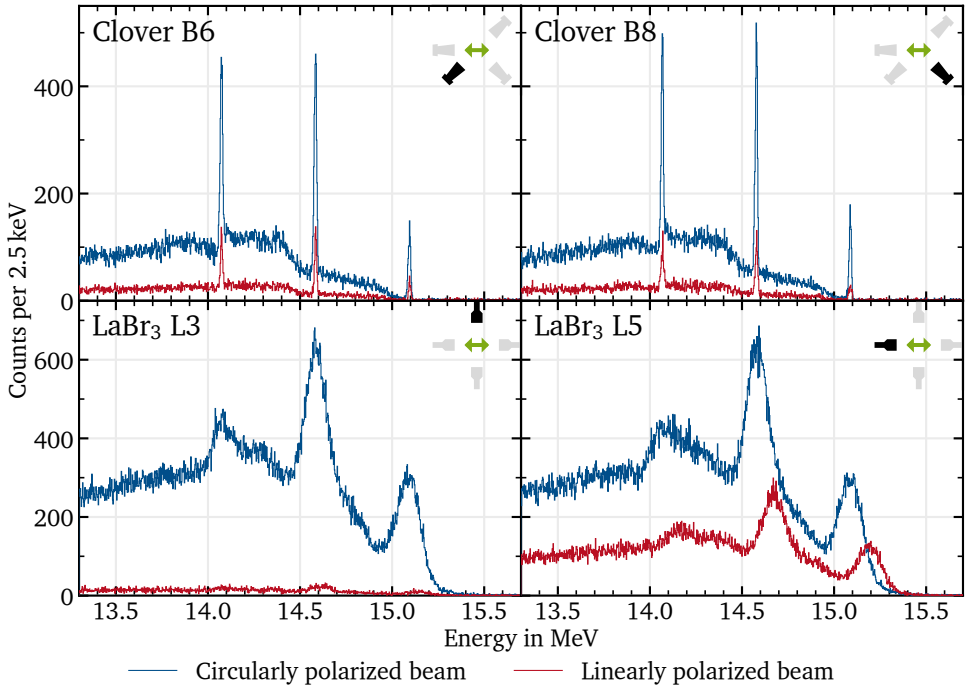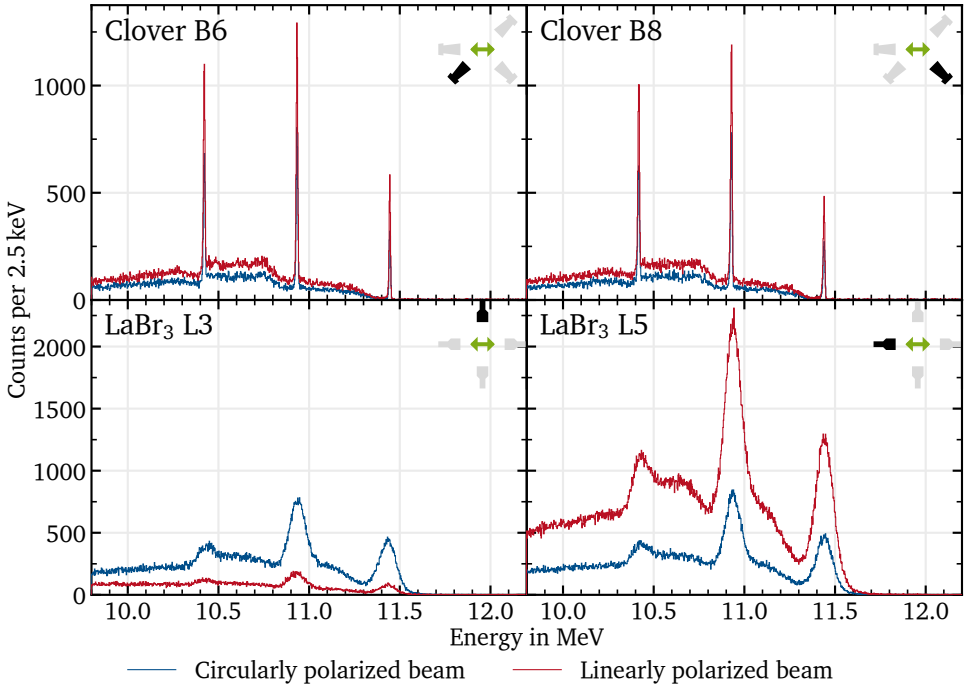
Figure 4.3.: Spectra of the LaBr$_3$ detectors L3 and L5 (bottom left and right, respectively) and the clover detectors B6 and B8 (top left and right, respectively) taken during irradiation of ^{12}C by 15.35 MeV circularly (blue) and linearly (red) polarized photon beams for calibration purposes. The positions of the detectors (black), relative to the beam polarization plane (green arrow) and the other LaBr$_3$ detectors (light gray), are indicated in the top right of each panel. Elastic NRF on the 1^+ state of ^{12}C at 15.110(3) MeV [101] produced the observed, prominent FEPs, SEPs, and DEPs. The two beam polarizations furthermore resulted in distinct angular distributions of this reaction, leading to a notably weaker NRF signal in the spectrum of detector L3 taken with the linearly polarized beam. The reliability issues with the energy calibrations of the LaBr$_3$ detectors are evident from the unphysical shift between the two spectra of detector L5.

Figure 4.4.: Spectra of the LaBr$_3$ detectors L3 and L5 (bottom left and right, respectively) and the clover detectors B6 and B8 (top left and right, respectively) taken during irradiation of ^{28}Si by 11.45 MeV circularly (blue) and 11.37 MeV linearly (red) polarized photon beams for calibration purposes. The positions of the detectors (black), relative to the beam polarization plane (green arrow) and the other LaBr$_3$ detectors (light gray), are indicated in the top right of each panel. Elastic NRF on the 1$^+$ state of ^{28}Si at 11.4460(2) MeV [102] produced the observed, prominent FEPs, SEPs, and DEPs. The two beam polarizations furthermore resulted in distinct angular distributions of this reaction, leading to a notably weaker NRF signal in the spectrum of detector L3 taken with the linearly polarized beam.

The high photon energies investigated in the GDR NRF measurements, furthermore, introduce another challenge. The detector response to such high-energy photons is not mainly governed by the photoelectric effect anymore, but by the Compton effect and pair production. This results in spectra featuring strong SEPs, DEPs and Compton-escape continua, which usually even surpass the FEPs in intensity. Since the GDR NRF signals furthermore have a broad spectral distribution as explained in Section 3.2, these parts of their detector response overlap in the spectra and, hence, cannot be disentangled by simple peak fitting anymore. The issue is exemplified by Fig. 4.5. Consequently, the detector response has to be explicitly taken into account for the evaluation of the NRF data. For this, it has to be known though.

The main fundamental processes, namely the photoelectric effect, the Compton effect and pair production, governing the interaction of ionizing photons with matter and thus the detector response, are, however, well-known [87, 144, 145]. Consequently, the detector response, which includes the efficiency, can be determined by simply simulating the interaction of photons originating from the target position with the detectors and the overall experimental setup [151]. For such computer simulations, the GEANT4 toolkit [141–143] is available, which is widely used in particle and nuclear physics. It provides the necessary framework to simulate the passage of particles through matter in complex geometries using a Monte-Carlo approach based on an extensive data set on electromagnetic, strong and weak interaction processes of particles in matter.

Therefore, both discussed issues were addressed by GEANT4 simulations of the detector response in this work. Now while GEANT4 implements all the necessary code to simulate the interaction of particles with matter, it is still only a toolkit and not an executable application. Its usage requires user code, which interfaces with GEANT4 and defines the quantities of interest to be recorded during the simulation, specifies the geometry of the setup, etc. and finally executes the simulation. To facilitate this, the utr software package [140] was used, which is specifically designed for simulations of detector responses and already implements most of the necessary additional code to set up and execute GEANT4 simulations for this purpose. With utr, the only remaining task was to digitally replicate the geometry of the experimental setup in C++ code, including not only the detectors but also the NRF targets, the beam pipe, and other components. A copy of utr, including the code added for this work, is included in the data publication associated with this work [69].

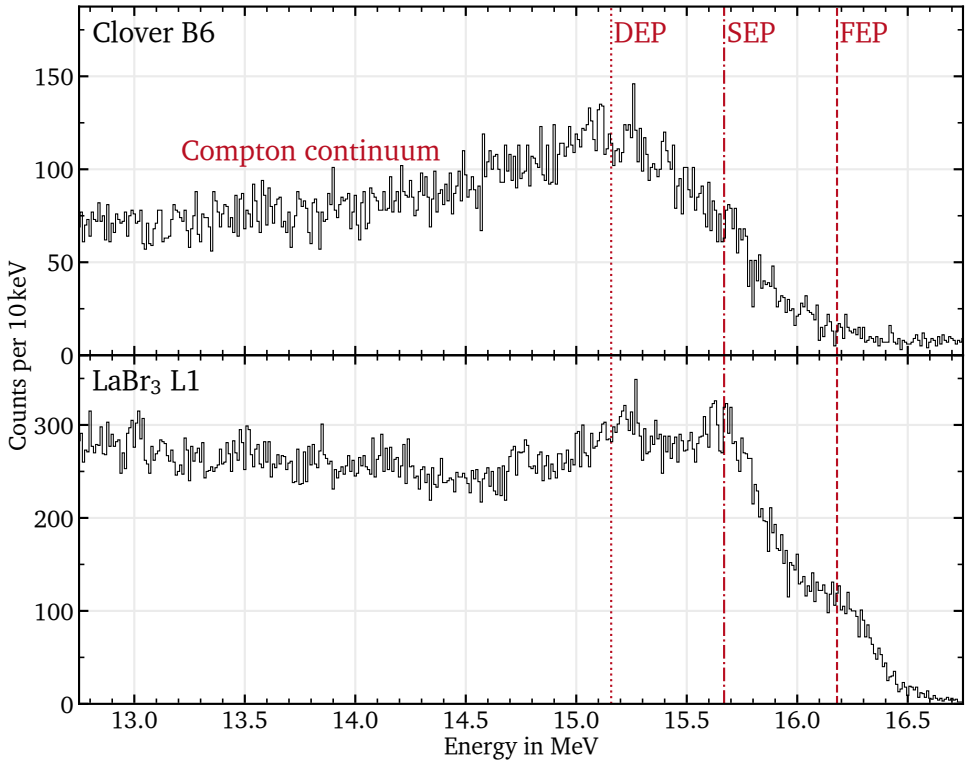Simulations were performed for every γ-ray signal relevant to this work. For the

Figure 4.5.: Spectra of the LaBr$_3$ detector L1 (bottom) and the clover detector B6 (top) taken during irradiation of ^{140}Ce by a 16.18 MeV circularly polarized photon beam. While both detectors observe a significant γ signal from ES on the GDR of ^{140}Ce, this signal does not emerge through well-defined peaks in the spectra, with the expected peak positions indicated by red vertical lines. This is due to an overlap of FEP, SEP, DEP, and Compton-escape continuum in each spectrum, requiring explicit consideration of these components of the detector response for accurate evaluation of the NRF data.

source measurements an isotropic point source at the target position was simulated, while for the NRF measurements the irradiated portion[4] of the respective NRF target material emitting γ rays with the known angular distributions for photon scattering were simulated once for each of their relevant angular distributions. For example, for the ^{154}Sm measurements four simulations were conducted to account for the four angular distributions of its photon-scattering processes relevant to this work, which are the $0^+ \rightarrow 1^- \rightarrow 0^+$ ES and $0^+ \rightarrow 1^- \rightarrow 2^+$ Raman scattering cascades being induced by either a linearly or a circularly polarized photon beam. Since the simulations take the measurements' geometries and the angular distributions of the emitted γ rays into account, the detector responses obtained from them are directly applicable to the evaluation of the NRF data. In particular, all geometry- and angular-distribution-related effects, such as the detectors' finite solid-angle coverage, are inherently included in the simulations.

Each simulation considered multiple energies of the emitted photons ranging from 0.1 to 19 MeV in steps of 0.1 MeV up to 3.6 MeV and in steps of 0.6 MeV from 4 MeV onward. With this approach, the full energy range relevant to this work was covered. For each of these energies the emission of $5 \cdot 10^8$ photons was simulated.

To extract the detector responses from the simulations, energy-deposition spectra were constructed across the $5 \cdot 10^8$ events for each combination of detector, emission energy and simulation using a 1 keV binning. One of these spectra is shown in Fig. 4.6 for illustration purposes. By subsequent division of all bin counts by the total number of simulated photons, i.e., $5 \cdot 10^8$, these normalized spectra directly represent the detector responses to the respective emission energies and with respect to the target geometry and angular distribution considered in the respective simulation.

To obtain the detector responses for photon energies between the simulated values, linear interpolation of the normalized spectra was performed. This involved shifting the spectra of the next lower and higher simulated incident energies along their observed-energy-deposition axis by their difference in incident energy to the target value and then averaging the shifted spectra, weighted by this energy distance. This

---

[4]With the collimator of 8 mm aperture diameter used in the experiment, the NRF target materials with diameters of 12 mm or more were only partially irradiated by the photon beam. Since photon scattering can only occur in these irradiated regions, the simulations accounted for this by solely emitting γ rays from these parts of the targets.
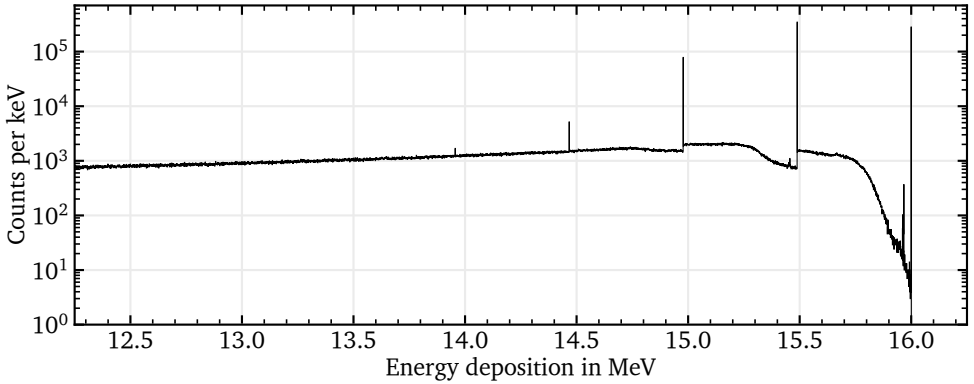
Figure 4.6.: Simulated spectrum of detector L1 for isotropic emission of $5 \cdot 10^8$ photons with an energy of 16 MeV from a point source located at the NRF target position of the experimental setup. Normalizing the spectrum by dividing all bin counts by $5 \cdot 10^8$ yields the detector's response to such photons. In particular, the FEP, SEP and DEP efficiencies, each part of the detector response, are given by the normalized counts of the corresponding peaks in the spectrum. Since GEANT4 simulations account only for energy depositions in the detector crystals, resolution effects are not reproduced and also not considered part of the detector response in this work.

method effectively aligned the FEPs, SEPs and DEPs to their correct positions before averaging[5].

Since the detector responses were obtained from spectra, each mathematically has the structure of a matrix corresponding to a two-dimensional histogram. Thus, energy values are not used directly. Instead, they must be mapped to bin numbers to access the respective response values. For simplicity, the same 1 keV binning was used for both axes, resulting in square matrices. The rows of these matrices correspond to the deposited and thus observed energies in the detector, while the columns correspond to the energies of emitted photons. The matrix elements are the absolute probabilities of observing events in the respective bin of the energy-deposition axis when photons belonging to the respective bin of the emitted-energy axis are emitted from the target

---

[5]Of course, this shifting creates unphysical artifacts at lower energies, for example when the 511 keV background peak from electron-positron annihilation is shifted to lower or higher energies. However, since the detector responses are only considered at higher energies, this is not an issue.

---

position. Hence, a detector's observed spectrum $\vec{o}$ expected for a spectrum of emitted photons $\vec{y}$ is obtained by the matrix-vector multiplication

$$\vec{o} = \mathcal{R} \cdot \vec{y} \tag{4.1}$$

from the detector-response matrix $\mathcal{R}$ for this emission process, where both $\vec{o}$ and $\vec{y}$ are represented by vectors and are required to use the same binning as the detector-response matrix along its respective axis.

Since the GEANT4 simulations only account for the energy depositions in the detector crystals, without considering the subsequent processing of the detectors' signals from these depositions, the simulations do not factor in the limited energy resolution of the detectors. Consequently, the detector responses are represented not only by square matrices but by triangular ones, because the conservation of energy precludes energy depositions exceeding the energy of the emitted photons.

In this matrix formulation, the columns of the detector-response matrix belonging to simulated energies are simply the normalized spectra directly obtained from the simulations, while the elements $\mathcal{R}_{o,e}$ of linearly interpolated columns were obtained according to

$$\mathcal{R}_{o,e} = \frac{1}{\frac{1}{e-l} + \frac{1}{u-e}} \left(\frac{1}{e-l} \mathcal{R}_{o-e+l,l} + \frac{1}{u-e} \mathcal{R}_{o-e+u,u} \right) \tag{4.2}$$

from those directly simulated elements in the l-th and u-th columns nearest below and above, respectively, to the interpolated column e.

With this a set of detector-response matrices was obtained for each detector and each simulated combination of target geometry and angular distribution as required for the evaluation of the NRF data. For illustration, Fig. 4.7 shows a section of one of these matrices for detector L1.
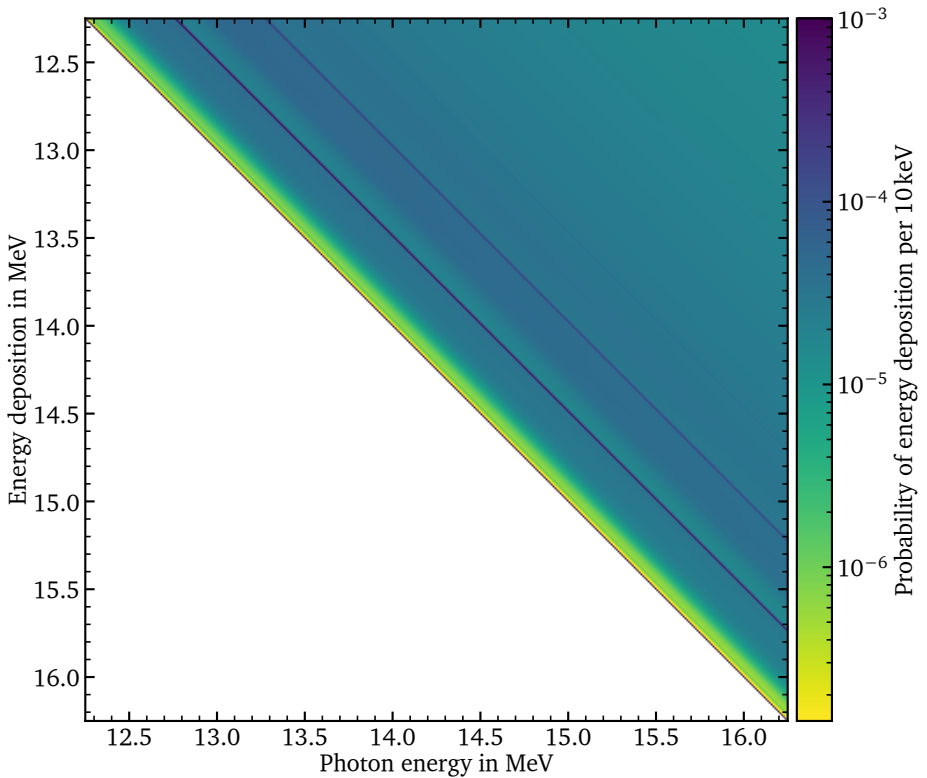
Figure 4.7.: Cutout of the response matrix of detector L1 for isotropic photon emission from the NRF target position. The matrix was constructed from simulated spectra, including that of Fig. 4.6, and rebinned to 10 keV wide bins along both axes. Each element of the matrix is color-coded and represents the probability of depositing an energy amount corresponding to the respective y-axis bin in the detector's crystal when a photon with energy in the corresponding x-axis bin is emitted isotropically from the target position. Thus, the diagonal elements of the matrix represent the simulated FEP efficiencies of the detector for isotropic photon emission from the target position and the columns the respective detector responses as obtained from the normalized simulated spectra. Due to energy conservation, the matrix is triangular with zero probabilities for energy depositions exceeding the energy of the emitted photons.

4.5. Efficiency calibration of the detectors

If all details of the experimental setup were perfectly known and replicated in the Geant4 simulations, such simulated detector responses are expected to be accurate replications of the actual responses of the detectors in the experiment [152–154]. However, it is virtually impossible to perfectly simulate the complex detector setup in every detail. Besides inevitable uncertainties in the measured geometry of the setup, the detector crystals might have developed dead layers or other defects during their lifetime [155], which are not accounted for in the simulations, or their precise geometry might not be known in the first place [153, 156]. Therefore, the simulated detector responses are only expected to be sufficiently accurate on a relative probability scale and may require rescaling to match the actual experimental detector responses.

This rescaling can be achieved by comparing the simulated FEP efficiencies, contained in the diagonal elements of the detector-response matrices, to experimental FEP efficiencies obtainable from source measurements. To determine experimental FEP efficiency values, the FEPs in the ^{56}Co, ^{60}Co, and ^{152}Eu source-measurement spectra, stemming from γ rays emitted during the radioactive decay of these nuclei, were fitted using HDTV [139] to obtain their counts A above the background level. The FEP efficiencies ϵ_{Iso} at the respective γ-ray energies E_γ for isotropic photon emission from the target position were then obtained, according to Eq. (2.67), by simply dividing these counts A by the known number of respective γ rays Y_{Source} emitted by the source during the measurement. The latter was calculated from the known activities and lifetimes of the sources, the durations of the measurements, and the known absolute emission probabilities of each γ ray per decay of the source nucleus [111, 112, 146]. Using these experimental FEP efficiency data points, rescaling factors for the detector-response matrices were obtained for each detector by averaging the ratios of the experimental FEP efficiencies to the simulated efficiencies for the same energy and isotropic emission from a point source. This yielded a single rescaling factor for each detector, which was then applied to all elements of all respective detector-response matrices. The data points and rescaled simulated efficiency curves are shown in Fig. 4.8, which also allows to visually confirm the reproduction of the relative experimental FEP efficiency curve-shape by the simulation. All fitted scaling factors ranged from 0.778 to 0.941, meaning that the simulated FEP efficiencies deviated at most by 22.2 % from the absolute experimental values, which is a satisfactory reproduction considering that the simulations were only required to be accurate in

their relative evolution with energy.

Unfortunately, a cross-check of the extrapolation of the rescaled simulated FEP efficiencies to the much higher energies of the ^{12}C and ^{28}Si measurements revealed an unphysical discrepancy among the detectors when using these rescaling factors. The efficiency-corrected intensities of the ^{12}C and ^{28}Si NRF FEPs significantly deviated among the detectors for all four measurements. This discrepancy should not have occurred, as the rescaled simulated efficiencies for the specific NRF reactions were used in this comparison, which already accounted for the respective angular distribution. More precisely, the detectors split into two groups, each yielding compatible intensity values within the group. The LaBr$_3$ detectors formed one group, and the clover detectors formed the other, with the latter reporting lower intensities than the former for the ^{12}C and ^{28}Si NRF γ-ray signals.

It was concluded that the issue must be attributed to an incorrect representation of the clover detectors in the simulations, which hindered the extrapolation and led to an overestimation of the clover detectors' efficiencies at higher energies, based on two correlated factors. Firstly, the LaBr$_3$ detectors' responses were better reproduced in the simulations than those of the clover detectors on an absolute scale, requiring less rescaling on average than the clover detectors. Secondly, the LaBr$_3$ detectors have simple cylindrical crystals, whereas the clover detectors have much more complex geometries. These complex geometries are not known in detail, necessitating some assumptions in the simulations in the first place [153, 156].

Therefore, it was decided to use the ^{12}C and ^{28}Si NRF reaction counts measured by the LaBr$_3$ detectors to determine absolute FEP efficiency data points for the clover detectors and, consequently, new simulation-scaling factors for them at these higher energies. These new scaling factors were 14 to 21 % smaller compared to those based on the source measurements. They were then applied to the detector-response matrices of the clover detectors, which, naturally, now yielded compatible NRF reaction counts for the ^{12}C and ^{28}Si measurements among all detectors. The correspondingly rescaled FEP efficiency curves of all detectors for detection of γ rays emitted isotropically by a point source are shown in Fig. 4.9.
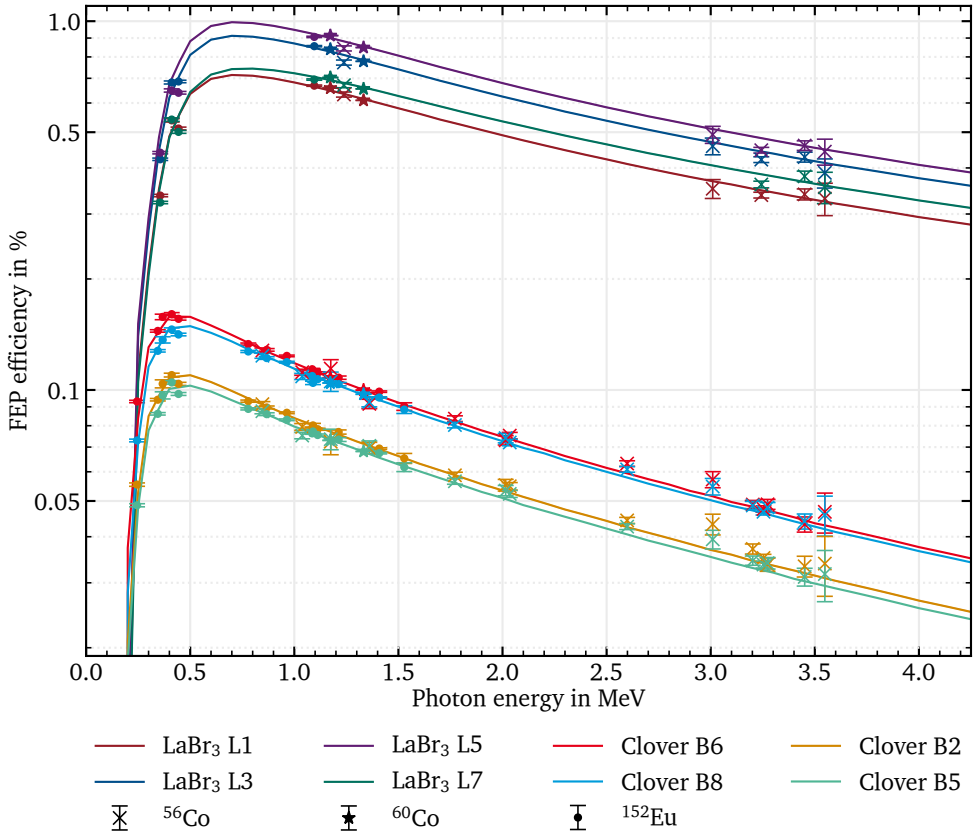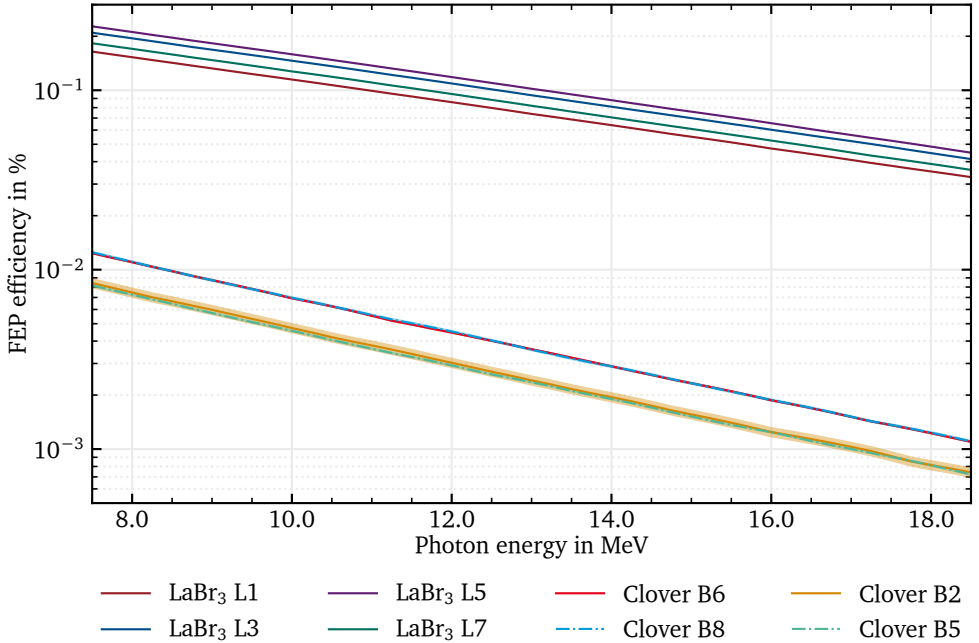
Figure 4.8.: FEP efficiencies of all detectors (color-coded) for isotropic photon emission from the target position. The experimental data points were obtained from the ^{56}Co (crosses), ^{60}Co (stars), and ^{152}Eu (points) source measurements, while the curves were obtained from GEANT4 simulations and rescaled in their absolute magnitude to match the experimental data. A good agreement between the experimental data and the rescaled simulated efficiencies is visible, confirming the accuracy of the simulations on a relative scale.

Figure 4.9.: FEP efficiencies of all detectors (color-coded) for isotropic photon emission from the target position in the energy region of the GDR NRF measurements. The curves shown for the LaBr$_3$ detectors are the same as in Fig. 4.8, while those for the clover detectors have been slightly rescaled once more to match the LaBr$_3$ detectors' efficiencies in the ^{12}C and ^{28}Si calibration measurements.

4.6. Analysis of the NRF spectra

As already stated, the high photon energies investigated in the GDR NRF measurements resulted in significant SEPs, DEPs, and Compton-escape continua in the spectra accompanying the FEPs. Due to the broad spectral distribution of the GDR NRF γ rays, these components of the detector responses overlap in the spectra and cannot be disentangled by simple peak fitting. Instead, the detector responses had to be explicitly considered in the evaluation of the NRF data, which aimed to extract the individual scattering reaction counts and the branching ratios of these reactions. While the detector responses had been obtained from the performed GEANT4 simulations, it was now necessary to develop a method to extract the desired information from the measured spectra using these detector-response matrices. Such analysis steps, which account for the convolution[6] of the γ-emission spectra with the detector response, are often referred to as deconvolutions [157–159]. In these procedures, either as a byproduct or as the main objective, the incident γ-ray spectra before convolution with the detector response are typically reconstructed, which is why the term deconvolution is used. However, because the detector resolution is commonly not considered in such deconvolutions, the obtained spectra are not the true γ-emission spectra, but rather those still convolved with the detector resolution. Nevertheless, as this detail seldomly matters for the purpose of the analysis, it is often disregarded in the following for brevity.

Given that the measured spectra and detector-response matrices are all binned, deconvolutions primarily involve solving linear matrix problems. Naturally, all binnings have to match for this purpose, which usually requires rebinning. Since the detector-response matrices already had a common uniform binning of 1 keV along both axes, the measured spectra were rebinned to match this binning. This was achieved by effectively[7] generating a random number for every count of a spectrum from a uniform distribution over the energy interval of the bin the count belonged to, and sorting

---

[6]Technically, one could argue that this is not truly a convolution since the detector response also depends on the energies of the incident photons, which is not the case for convolutions in the mathematical definition. Nevertheless, the term convolution is commonly used in this context and the detector response usually does not change significantly over the energy range of deconvolutions anyway.

[7]Actually, a more complex, mathematically equivalent, but computationally more efficient method was used, which distributed the number of counts in each bin of the original spectrum directly to those of the rebinned spectrum using the multinomial distribution.

these random numbers into a new spectrum of the desired binning. This resampling method kept the total statistics of the spectra intact, while also preserving the statistical properties of the counts as much as possible.

4.6.1. Introduction to detector-response deconvolutions: The top-down method

A simple approach to detector-response deconvolutions is the so-called top-down deconvolution. In this method, Eq. (4.1) is solved for the emitted spectrum $\vec{y}$ by inverting the detector-response matrix $\mathscr{R}$, i.e., $\vec{y} = \mathscr{R}^{-1} \cdot \vec{o}$. Since the detector-response matrix is a triangular matrix if it does not include resolution effects, it is always invertible, leading to a unique solution in all cases. In accordance with the Gaussian elimination method for matrix inversion, the top-down deconvolution can also be visualized as an iterative subtraction of detector-response spectra, contained in the columns of the matrix, from the measured spectrum. The iterative process starts at the highest-energy bin of the measured spectrum and proceeds to lower energies, hence the name top-down deconvolution. In each iteration step, the respective response spectrum is scaled in its bin heights to fully subtract the (remaining) FEP counts at the iteration step's energy in the measured spectrum. The deconvolved spectrum is then simply given by the scaling factors of the detector-response spectra used in each iteration step. While this method is simple and thus serves as a good starting point for understanding the concept of deconvolutions, it has several drawbacks.

One major drawback of top-down deconvolutions is their inability to consider the physical fact that the emission spectrum must be non-negative. In a perfect scenario, where the measured spectrum is exactly the linear transformation of the emission spectrum, this would of course not be an issue. However, such an exact correspondence is extremely unlikely and can be considered practically impossible due to at least two factors. Firstly, the statistical nature of the measured spectra introduces fluctuations in its counts. Secondly, it is unlikely that the used detector-response matrix perfectly represents the actual detector response. Both factors break the exact correspondence of measured and emitted spectra required for a perfect deconvolution and cannot be easily accounted for in the simple top-down approach. Since the method effectively starts at the FEPs of the highest-energy bins of the measured spectrum and fully subtracts their expected detector response, any statistical or systematic deviations

from the actual detector response accumulate at the lower-energy bins. This can easily lead to over- or under-subtraction of counts at these lower energies, often resulting in unphysical negative bin heights in the deconvolved spectrum. Significant negative bin heights are a clear indication of an unsuccessful deconvolution. This issue can be mitigated by introducing a positivity constraint in the deconvolution process as a priori knowledge. Under this constraint, the deconvolution would have to find the emission spectrum that best fits the measured spectrum while remaining non-negative. This leads to more sophisticated fit-based approaches, which do not yield an exact analytical and potentially unphysical solution but rather an approximate solution that considers actual physical constraints. They are thus more robust against statistical fluctuations in the measured spectrum and systematic deviations in the detector-response matrix.

Another drawback of top-down deconvolution is its inability to handle spectra originating from multiple radiation sources with different detector responses. In this case, the matrix equation

$$\vec{o} = \sum_k \mathscr{R}_k \cdot \vec{y}_k, \tag{4.3}$$

which needs to be solved for the emitted spectra $\vec{y}_k$ with their respective detector-response matrices $\mathscr{R}_k$, is underdetermined, allowing arbitrary unphysical solutions. However, such spectra, stemming from multiple radiation sources with different detector responses, occur in the GDR NRF measurements. The ES and 2_1^+ Raman scattering signals contribute to the spectra with different detector responses due to their different angular distributions. The latter cause not only different absolute intensities but also different shapes of the detector response. This can be easily understood by considering that single escape events are more likely to occur if photons are predominantly emitted towards the edge regions of a detector rather than its center, which is possible with strongly anisotropic angular distributions, such as the one of ES of a linearly polarized photon beam. Figure 4.10 illustrates this effect. Likewise, the top-down deconvolution is unable to handle the deconvolution of multiple detectors' spectra $\vec{o}^{(d)}$ simultaneously, since, in this case, the equation system

$$\vec{o}^{(d)} = \sum_k \mathscr{R}_k^{(d)} \cdot \vec{y}_k, \tag{4.4}$$

which needs to be solved, is overdetermined and very likely not analytically solvable, even though physically all spectra should be consistent with each other.
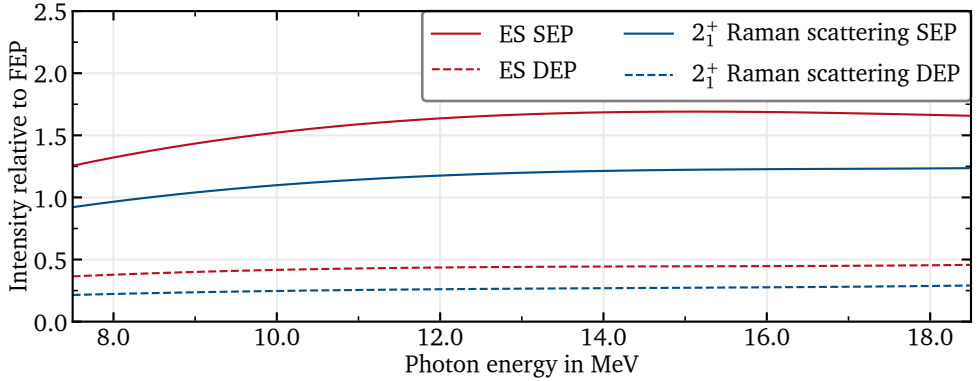
Figure 4.10.: Relative intensities of the SEP (solid) and DEP (dashed) compared to the FEP for pure ES (red) or 2_1^+ Raman scattering (blue) on the GDR induced by a linearly polarized photon beam, as observed in simulated spectra of the LaBr$_3$ detector L1. The distinct angular distributions of these two scattering reactions result in different detector-response shapes. This is evident by the escape peaks' relative intensities being greater here for ES than for 2_1^+ Raman scattering.

Finally, top-down deconvolutions yield only deconvolved spectra and therefore always require additional spectrum-analysis steps to obtain the actual quantities of interest, which here are the counts of the ES and 2_1^+ Raman scattering reactions and their branching ratios.

These drawbacks of the top-down deconvolution method can be addressed using more sophisticated fit-based approaches. For this work, a Bayesian inference fitting approach was applied.

4.6.2. Bayesian inference basics

The goal of Bayesian data analyses is to assign a conditional probability distribution $P_M(\vec{\theta}\,|\,\vec{D})$ to the parameters of interest $\vec{\theta}$, which are not directly observed, considering observed data $\vec{D}$ linked to them through some assumed model M. This so-called posterior distribution $P_M(\vec{\theta}\,|\,\vec{D})$ then allows to fully quantify the likelihood of the

parameters' values. To achieve this, Bayes' theorem

$$P_M(\vec{\theta}\,|\,\vec{D}) = \frac{P_M(\vec{D}\,|\,\vec{\theta})\,P_M(\vec{\theta})}{P_M(\vec{D})} \propto P_M(\vec{D}\,|\,\vec{\theta})\,P_M(\vec{\theta}) \tag{4.5}$$

is simply applied to the case of interest [160]. Here, $P_M(\vec{\theta})$ is commonly referred to as the prior distribution and is merely assumed based on previous knowledge or information about the parameters $\vec{\theta}$ already available before observing the data $\vec{D}$. Boundary conditions of parameters can, for example, be easily incorporated through the prior by a probability distribution yielding 0 outside the boundaries, such as the uniform distribution. For simplicity, the assumed priors are considered as part of the model M here and, hence, $P_M(\vec{\theta})$ depends on M. Such a dependency on the model is the case for all probabilities P_M in Eq. (4.5) and explicitly expressed by the index M. The probability of the observed data given the parameters $P_M(\vec{D}\,|\,\vec{\theta})$, known as the likelihood, is a function solely of $\vec{\theta}$ since $\vec{D}$ is fixed through its observation here. It is obtained from the model M. For example, the model could assume normal distributions $\mathcal{N}(\vec{\mu}_k(\vec{\theta}), \vec{\Delta D}_k^2)$ for each data point k in $\vec{D}$ with their means $\vec{\mu}_k$ predicted through the parameters $\vec{\theta}$ and their variances given by the uncertainties $\vec{\Delta D}_k$ of the data points. In this example, the product of the probabilities of all data points according to these normal distributions

$$P_M(\vec{D}\,|\,\vec{\theta}) = \prod_k P_{\mathcal{N}}(\vec{D}_k\,|\,\vec{\mu}_k(\vec{\theta}), \vec{\Delta D}_k^2) \tag{4.6}$$

would be the likelihood. Finally, the denominator

$$P_M(\vec{D}) = \int P_M(\vec{D}\,|\,\vec{\theta})\,P_M(\vec{\theta})\,\mathrm{d}\vec{\theta} \tag{4.7}$$

of Eq. (4.5) is a constant here, which is usually difficult or impossible to compute. However, it does not need to be further considered, since the posterior distribution has to be normalized by definition with

$$\int P_M(\vec{\theta}\,|\,\vec{D})\,\mathrm{d}\vec{\theta} = 1, \tag{4.8}$$

allowing to initially drop all constant factors for its determination, since their product can be recovered by this normalization condition. Furthermore, this also allows for

the use of improper prior distributions, which cannot be normalized, such as uniform distributions over the entire set of real numbers $\mathbb{R}$ or the positive real numbers $\mathbb{R}^+$, when little prior information is available.

Hence, by developing a model M and constructing the likelihood $P_M(\vec{D}|\vec{\theta})$ and prior $P_M(\vec{\theta})$ accordingly, the unnormalized posterior distribution $P_M(\vec{\theta}|\vec{D})$ to the data $\vec{D}$ is, in principle, trivially obtained from Eq. (4.5), no matter the number of parameters or complexity of the model. However, usually it is not feasible to normalize or even just directly explore[8] the unnormalized posterior distribution obtained this way, since the parameter space can be very large. One solution to this problem is simply sampling values for $\vec{\theta}$ from the unnormalized posterior distribution. This is for example possible with Markov chain Monte Carlo (MCMC) methods [161]. State-of-the-art MCMC algorithms and modern computer technology allow generating large samples of $\vec{\theta}$ in reasonable time periods even for complex models of many parameters. With sufficiently large samples the relevant parts of the normalized posterior distribution, containing the bulk of the probability mass, can then be simply investigated through a standard probability density estimation from the sample.

4.6.3. Bayesian inference fits to the spectra

Using a Bayesian inference approach for the analysis of the GDR NRF spectra has multiple advantages. These include:

- Simultaneously fitting the spectra of all detectors in a measurement using a mix of common and individual parameters is straightforward.

- The quantities of interest can be parameterized directly within the model, allowing for the inferred values to be obtained without additional processing of the spectra.

- Quantifying statistical uncertainties and correlations of the quantities of interest is trivial, as their full probability densities are available after inference.

- Constructing and fitting the complex model of the NRF reactions that produce the observed spectra is relatively simple.

---

[8]For example, to find the region containing most of the probability mass or study correlations of parameters

- Incorporating prior knowledge and physical boundary conditions on the parameters is not just trivial, but a cornerstone of Bayesian inference.

- Even the fact that the spectra's bins follow Poisson statistics can be explicitly taken into account.

Basic structure of the fit model

As the first step of Bayesian inference analysis of the GDR NRF spectra, the fit model to the observed spectra had to be constructed. This was simply based on the physical processes underlying the observed spectra.

The photon beam profiles were assumed to have slightly asymmetric Gaussian shapes with the beams' spectral densities being given by

$$\frac{d\Phi(E)}{dE} = \Phi \, \frac{2}{\Delta_l + \Delta_u} \begin{cases} \Delta_l \, \mathcal{N}(E, E_{\text{Beam}}, \Delta_l^2) & \text{for } E < E_{\text{Beam}} \\ \Delta_u \, \mathcal{N}(E, E_{\text{Beam}}, \Delta_u^2) & \text{for } E \geq E_{\text{Beam}}, \end{cases} \tag{4.9}$$

where E is the photon energy, Φ is the total number of beam photons which passed the target position during a measurement,

$$\mathcal{N}(E, E_{\text{Beam}}, \Delta^2) = \frac{1}{\sqrt{2\pi}\,\Delta} \exp\left(-\frac{1}{2} \left(\frac{E - E_{\text{Beam}}}{\Delta} \right)^2 \right) \tag{4.10}$$

is the PDF of the normal distribution, E_{Beam} is the beam energy and Δ_l and Δ_u are the widths of the lower and upper beam flank, respectively. Note that $\frac{d\Phi(E)}{dE}$ is continuous in E, that $\Phi = \int \frac{d\Phi(E)}{dE} \, dE$ indeed holds and that the beam energy E_{Beam} by this definition is the energy at which the spectral density of the photon beam is maximal. As the beam profile measurements performed with the $0°$ detector were unusable, as discussed in Section 3.3.2, the beam parameters were unknown at this point and had to be inferred from the NRF spectra.

In the following the relative shape primarily matters. So the normalized beam profile

$$s(E) = \frac{1}{\Phi} \frac{d\Phi(E)}{dE} = \frac{2}{\Delta_l + \Delta_u} \begin{cases} \Delta_l \, \mathcal{N}(E, E_{\text{Beam}}, \Delta_l) & \text{for } E < E_{\text{Beam}} \\ \Delta_u \, \mathcal{N}(E, E_{\text{Beam}}, \Delta_u) & \text{for } E \geq E_{\text{Beam}} \end{cases} \tag{4.11}$$

with

$$\int s(E)\,\mathrm{d}E = 1 \tag{4.12}$$

is introduced here.

As shown by Eq. (3.4), the spectral distributions $\frac{\mathrm{d}Y_f(E)}{\mathrm{d}E}$ of γ rays emitted by ES and 2^+_1 Raman scattering on the GDR both share the shape of the beam profile. In the case of 2^+_1 Raman scattering, its γ spectrum is additionally shifted down in energy by the excitation energy $E_{2^+_1}$ of the 2^+_1 state, while the ES γ spectrum is unshifted. In addition to these γ rays from scattering reactions on the GDR, there might also be some background spectrum $\frac{\mathrm{d}Y_{\mathrm{BG}}(E)}{\mathrm{d}E}$ present in the measurement, whose precise modeling will be discussed later. Hence, the full γ-emission spectrum was modeled as the sum

$$
\begin{aligned}
\frac{\mathrm{d}Y(E)}{\mathrm{d}E} &= \frac{\mathrm{d}Y_{\mathrm{ES}}(E)}{\mathrm{d}E} + \frac{\mathrm{d}Y_{2^+_1}(E)}{\mathrm{d}E} + \frac{\mathrm{d}Y_{\mathrm{BG}}(E)}{\mathrm{d}E} \\
&= Y_{\mathrm{ES}}\, s(E) + Y_{2^+_1}\, s(E + E_{2^+_1}) + \frac{\mathrm{d}Y_{\mathrm{BG}}(E)}{\mathrm{d}E},
\end{aligned}
\tag{4.13}
$$

where the Y_f are the total numbers of respective scattering reactions f that occurred during a measurement. Other potential γ-decay channels of the GDR were not considered here, as no indications of their presence were found in the experimental spectra.

By convolving each part of this model with its corresponding detector response, which includes the angular-distribution effects and detector efficiency, the expected observed spectra can be modeled for every detector. However, the observed spectra and simulated detector-response matrices are not continuous functions, but discretely binned entities. Hence, before convolution with the detector response, the parts of the emission model had to be discretized as well using the same binning as the detector-response matrices. The required discretized values $\vec{y}_f$ of $\frac{\mathrm{d}Y_f(E)}{\mathrm{d}E}$ were obtained by the integrals

$$\left(\vec{y}_f\right)_k = \int_{l_k}^{u_k} \frac{\mathrm{d}Y_f(E)}{\mathrm{d}E}\,\mathrm{d}E \tag{4.14}$$

for every energy bin k with lower bin edge l_k and upper bin edge u_k. Using the well-known cumulative distribution function of the normal distribution, the integrals over $s(E)$ appearing for the components of $\vec{y}_{\mathrm{ES}}$ and $\vec{y}_{2^+_1}$ are analytically computable.

The discretized model of the γ-emission spectrum is then

$$
\begin{aligned}
\vec{y}_k &= \quad (\vec{y}_{\text{ES}})_k \quad + \quad \left(\vec{y}_{2_1^+}\right)_k \quad + \quad (\vec{y}_{\text{BG}})_k \\
&= \int_{l_k}^{u_k} Y_{\text{ES}} \, s(E) \, dE + \int_{l_k}^{u_k} Y_{2_1^+} \, s(E + E_{2_1^+}) \, dE + \int_{l_k}^{u_k} \frac{dY_{\text{BG}}(E)}{dE} \, dE
\end{aligned}
\tag{4.15}
$$

analogous to Eq. (4.13). Its parts f could now be convolved with their simulated detector-response matrices[9] $\mathscr{R}_f^{(d)}$ for each detector d through matrix-vector multiplication. This yields the model for the observed spectra

$$
\vec{o}_M^{(d)} = \mathscr{R}_{\text{ES}}^{(d)} \cdot \vec{y}_{\text{ES}} + \mathscr{R}_{2_1^+}^{(d)} \cdot \vec{y}_{2_1^+} + \mathscr{R}_{\text{BG}}^{(d)} \cdot \vec{y}_{\text{BG}}
\tag{4.16}
$$

for every detector d in the same binning as the detector-response matrices, which can be fitted to the rebinned observed NRF spectra. The fit parameters are the reaction counts Y_{ES} and $Y_{2_1^+}$, the photon beam parameters E_{Beam}, Δ_l and Δ_u and those of the background model $\vec{y}_{\text{BG}}$ skipped for the moment.

In the chosen Bayesian inference approach, fitting this model is achieved by considering each predicted k-th bin height $\left(\vec{o}_M^{(d)}\right)_k$ of the spectrum of detector d as the mean μ of a Poisson distribution. Each bin height $\left(\vec{o}_{\text{Exp}}^{(d)}\right)_k$ in the experimentally observed spectra is then considered a sample of its respective Poisson distribution. Hence, the probability of observing this bin height when assuming the respective Poisson distribution can be calculated from the probability mass function

$$
P_{\text{Pois}}(x \,|\, \mu) = \frac{\mu^x \exp(-\mu)}{x!}
\tag{4.17}
$$

of the Poisson distribution with mean μ. Plugging in the actual quantities thus yields

$$
P_{\text{Pois}}\left(\left(\vec{o}_{\text{Exp}}^{(d)}\right)_k \,\middle|\, \left(\vec{o}_M^{(d)}\right)_k\right) = \frac{\left(\vec{o}_M^{(d)}\right)_k^{\left(\vec{o}_{\text{Exp}}^{(d)}\right)_k} \exp\left(-\left(\vec{o}_M^{(d)}\right)_k\right)}{\left(\vec{o}_{\text{Exp}}^{(d)}\right)_k!}
\tag{4.18}
$$

---

[9] While not explicitly indicated here, besides the detector d and γ-ray origin f, the concrete detector-response matrices to use also depend on the target and beam polarization mode of the measurement whose spectra are to be described.

for the probability of a single experimentally observed bin height according to the model. Since probabilities are multiplicative, the likelihood for the full model and data is therefore

$$P_M(\vec{D}\,|\,\vec{\theta}) = \prod_d \prod_k P_{\text{Pois}}\left(\left(\vec{\sigma}_{\text{Exp}}^{(d)}\right)_k \,\middle|\, \left(\vec{\sigma}_M^{(d)}\right)_k\right) \qquad (4.19)$$

when fitting the model to the spectra of all detectors simultaneously.

Hence, after setting up prior distributions $P_M(\vec{\theta})$ on the fit parameters[10] as well, which in particular should exclude any non-physical values, the inference fit can be performed by sampling the unnormalized posterior distribution and investigating the density estimations of the fit parameters based on their samples.

At this point it is worthwhile to briefly discuss how this fit model allows to determine the branching ratio of 2_1^+ Raman to ES on the GDR of ^{154}Sm from the spectra taken with the linearly polarized photon beams. In Section 3.2 Eq. (3.12) was introduced to explicitly show how this branching ratio can be determined from the azimuthal asymmetry of the doublet γ signal observed in this case. However, the fit model does not explicitly consider this azimuthal asymmetry of the overall γ signal. This is because it is simply not necessary here, since the distinct angular distributions of ES and 2_1^+ Raman scattering are already implicitly considered through the detector-response matrices in the model. Hence, when fitting the model to the spectra of the relevant detectors simultaneously, the branching ratio[11] has to be reproduced by the fit, since it is otherwise just not possible to describe the spectra in such a global fit. This is a clear advantage of the chosen simultaneous Bayesian inference approach: the quantities of interest are directly inferred from the data without the need for additional processing steps. Naturally, it is also possible to fit the ^{154}Sm spectra taken with the circularly polarized photon beams in the same way. However, one cannot expect the fit to reliably determine the branching ratio in this case, since without an azimuthal asymmetry to implicitly exploit, the two reaction-count parameters are virtually degenerate. Nevertheless, the model still has to be able to describe the spectra of all detectors simultaneously, which allows for a cross-check of the fit method.

---

[10]For the reaction counts Y_{ES} and $Y_{2_1^+}$ uniform distributions on the non-negative real numbers were used, while for the beam parameters E_{Beam}, Δ_l and Δ_u normal distributions centered around their roughly expected values were employed, which were furthermore truncated to the positive real numbers.

[11]While the branching ratio is not directly a fit parameter here, the fitted reaction counts of the two reactions yield the branching ratio trivially through Eq. (3.15)

Details of the fit model

While the so far elucidated model is close to the one actually used, some details were left out so far.

Firstly, the model for the background spectrum $\vec{y}_{BG}$ was not discussed yet. At the here-considered photon energies, natural background is negligible, and the observed background must have been induced by the photon beam itself. However, the full origin of the observed background is unknown. Consequently, it was impossible to explicitly simulate the detector responses to it, and instead the detector-response matrices to an isotropic source at the target position $\mathscr{R}_{Iso}$ were used as a proxy. One likely source of background is small-angle Compton scattering of beam photons directly into the detectors, which must have occurred upstream of the target position. Hence, the background was expected to significantly differ between the two detector types, which were positioned at very different distances and polar angles to the target position. Therefore, two independent background models $\vec{y}_{BG\,LaBr_3}$ and $\vec{y}_{BG\,clover}$ were used for the LaBr$_3$ and clover detectors, respectively. As moreover the overall intensity of the background was expected to vary between the detectors, detector-specific background scaling factors $s_{BG}^{(d)}$ were additionally introduced. With this, the overall detector-specific background model was

$$\vec{y}_{BG}^{(d)} = s_{BG}^{(d)} \begin{cases} \vec{y}_{BG\,LaBr_3} & \text{if } d \text{ is a LaBr}_3 \text{ detector} \\ \vec{y}_{BG\,clover} & \text{if } d \text{ is a clover detector} \end{cases} \tag{4.20}$$

for each detector d. To keep these models simple and extremely flexible at the same time, no rigid overall model for the backgrounds was assumed. Instead, every bin height of each of the two background spectra $\vec{y}_{BG\,LaBr_3}$ and $\vec{y}_{BG\,clover}$ was considered a free parameter of the model. These were fitted to the data, alongside the scaling factors $s_{BG}^{(d)}$. This effectively allowed the background to be modeled by the data itself, and thus to also account for the (n,γ) peaks occurring in the spectra without having to explicitly model them. To prevent fitting the full spectra using background only, it was strongly regularized by using exponential distributions as the priors of the background spectra's bin heights and narrow normal distributions of mean 1 as the prior on the scaling factors $s_{BG}^{(d)}$. These priors effectively penalized large bin heights while also preventing negative values. Since no background was expected in vicinity of the beam energy, the background models were furthermore cut off at 99 % of the beam energy,

which corresponds to the lower half-maximum energy of the beam profile assuming a 2 % beam resolution. To obtain a smooth transition of the background models to this cutoff, the regularization through the exponential priors was made progressively stronger towards the beam energy, slowly forcing the background bin heights to zero. This was achieved by using a logistic function to continuously lower the means of the exponential priors towards the cutoff point. This overall flexibility of the background model combined with its regularization and the full cutoff in the region of the ES FEP made it well suited for the analysis of the NRF spectra taken on ^{154}Sm, where it could not interfere with fitting of the GDR scattering signals. However, for the ^{140}Ce spectra the background model competed with the 2_1^+ Raman scattering signal located about 1.6 MeV below the beam energy in this case. This could lead to an overestimation of the 2_1^+ Raman scattering counts since the regularization favored no background if possible, an issue which could be addressed in future analyses by using a more complex and rigid background model. Nonetheless, for this work this potential issue did not arise, since both the background and the 2_1^+ Raman scattering signal were of such low intensities that only low upper limits on the 2_1^+ Raman scattering counts were obtained.

Besides the just discussed photon background, a quasi-constant background noise appearing in all spectra also had to be accounted for in the overall fit model. Since this noise exhibited no detector response or structure, it was treated separately from the photon background model, which gets convolved with the detector response. Instead, it was simply represented through detector-specific, scalar, positive offset parameters $o_{\text{Noise}}^{(d)}$ in the model of the observed γ spectrum, resulting in

$$\vec{o}_M^{(d)} = \mathscr{R}_{\text{ES}}^{(d)} \cdot \vec{y}_{\text{ES}} + \mathscr{R}_{2_1^+}^{(d)} \cdot \vec{y}_{2_1^+} + \mathscr{R}_{\text{Iso}}^{(d)} \cdot \vec{y}_{\text{BG}}^{(d)} + o_{\text{Noise}}^{(d)} \tag{4.21}$$

as the updated form of Eq. (4.16). As the priors on these noise-offset parameters normal distributions were used, whose means and variances were estimated before fitting the model from the spectra themselves, specifically in regions above the beam energy where no other signal was present.

To take the uncertainties of the rescaling factors into account, which rescaled the simulated detector-response matrices to reproduce experimental efficiency values as discussed in Section 4.5, these factors were included as parameters of the model. Their priors were chosen as normal distributions with means and variances corresponding to their nominal values and uncertainties, respectively. This allowed variations of

the rescaling factors within their uncertainties during the fits, therefore effectively incorporating these uncertainties into the fits.

Another aspect that the fit model needed to account for was the possibility of imperfect energy calibrations of the detectors, particularly known to be the case for the $LaBr_3$ detectors. Such calibration imperfections can cause the spectra to appear shifted in energy relative to one another, a discrepancy not yet accommodated by the model, which so far assumed identical peak positions for all detectors based on the common beam energy E_{Beam} contained in $s(E)$ of Eq. (4.11). Hence, to account for imperfect energy calibrations, the model parameter was simply replaced by a detector-specific beam energy $E_{\mathrm{Beam}}^{(d)}$ to be fitted for each detector d.

Likewise, the fit model had to consider the different energy resolutions of the $LaBr_3$ and clover detectors. With the $LaBr_3$ detectors' limited energy resolutions of about 1 % in the energy range of the NRF measurements, they still moderately broadened the GDR's γ-ray peaks of about 2 % resolution. As the detector resolution was not considered in the detector-response matrices, the model had to explicitly take this effect into account. Similarly to the detector-specific beam energies, this was achieved by simply replacing the width parameters Δ_l and Δ_u in the normalized beam-profile model $s(E)$ by larger widths $\tilde{\Delta}_l$ and $\tilde{\Delta}_u$ for the $LaBr_3$ detectors. Unlike the beam-energy parameters, the two widths were, however, shared by all $LaBr_3$ detectors, as individual parameters were not expected to be necessary. After all, the γ-signals' widths were still dominated by the beam resolution and only slightly broadened by the detector's individual resolutions, which were similar enough among the $LaBr_3$ detectors to be considered the same in this context. For the clover detectors, resolution effects were negligible when fitting the GDR's γ-ray signals due to their much better energy resolution of less than 0.1 % in the relevant energy range. Hence, no modification of the normalized beam-profile model $s(E)$ was necessary for them, which allowed to directly determine the beam parameters Δ_l and Δ_u from the clover spectra.

In addition to evaluating the GDR NRF spectra of ^{140}Ce and ^{154}Sm using this fit model, it was also desirable to apply this analysis approach to the spectra of the ^{12}C and ^{28}Si calibration measurements. This would yield an additional benchmark for both the fit model and the fitting procedure. However, the narrow NRF peaks of these nuclides naturally required slight modifications to the model. Obviously, the GDR scattering signals had to be replaced by a single ENRF signal in the model with corresponding reaction count Y_{ENRF} and response matrix $\mathscr{R}_{\mathrm{ENRF}}^{(d)}$. As the employed detector-response

matrices in any case always implicitly depend on the measurement to be fitted, since they each specifically consider the target material and the beam polarization of the measurement, this was merely a change of labels and number of terms in the model so far. The important difference to the GDR measurements, that had to be considered by the model, is rooted in the narrow spectral distributions of the ^{12}C and ^{28}Si NRF γ rays. Hence, the observed widths of the NRF peaks were governed by the detectors' individual energy resolutions and do not follow the normalized beam-profile model $s(E)$. Similar to before, to account for this, the normalized beam-profile model $s(E)$ was simply modified using detector-specific widths. Since the NRF peaks were expected to be symmetric, the model was replaced by a symmetric Gaussian

$$s_{\mathrm{ENRF}}^{(d)}(E) = \mathcal{N}(E, E_{\mathrm{ENRF}}^{(d)}, \Delta^{(d)}) \tag{4.22}$$

when fitting the ^{12}C and ^{28}Si measurements with detector-specific widths $\Delta^{(d)}$ and detector-specific peak positions $E_{\mathrm{ENRF}}^{(d)}$, as before to compensate for possible energy calibration offsets. Now while the underlying physics are different here and $s(E)$ does not represent the beam profile in this case, with this modification of $s(E)$ the overall fit model could still be used just as for the GDR spectra.

Another detail which has to be discussed was specific to the ^{140}Ce and ^{154}Sm measurements performed at 15.35 MeV photon-beam energy. Since the ^{140}Ce and ^{154}Sm target-container materials contained ^{12}C, the ENRF signal from its 15.110(3) MeV 1^+ state [101] was present in the spectra, overlapping with the GDR scattering signals. Hence, it had to be included in the model as well for the analyses of these measurements. In principle, the just discussed model term for narrow NRF signals simply had to be added to the model for the GDR scattering signals. However, without modifications, two energy parameters $E_{\mathrm{Beam}}^{(d)}$ and $E_{\mathrm{ENRF}}^{(d)}$ would have been included per detector d to account for imperfect energy calibrations, which was unnecessary. Therefore, the ^{12}C ENRF signal's energy position was defined here via

$$E_{\mathrm{ENRF}}^{(d)} := E_{\mathrm{Beam}}^{(d)} + \Delta E_{\mathrm{ENRF}} \tag{4.23}$$

relative to the GDR ES signal located at the detector-specific fitted beam energy $E_{\mathrm{Beam}}^{(d)}$. With this only a single additional energy parameter ΔE_{ENRF} was introduced, which encodes the physical energy difference between the GDR ES and the ^{12}C ENRF signals,

which was approximately equal for all detectors[12].

The final detail likewise concerns exclusively the measurements performed at a single beam energy, namely 17.79 MeV. As elaborated in Section 3.3.2, at least one of the leaves of each of the four clover detectors considered in the analysis was non-operational at this beam energy, while working fine in all other measurements. Therefore, the decision had been made to include the five affected leaves in the analysis for all other measurements, and the so-far employed detector-response matrices thus accounted for them accordingly. Consequently, for fitting the spectra taken at 17.79 MeV the detector-response matrices had to be modified to exclude the non-operational leaves. As it was not deemed worthwhile to create separate detector-response matrices solely for these measurements from scratch, the options were either to exclude the clover detectors' spectra altogether from the fit or to simply rescale their detector-response matrices by the fraction of remaining operational leaves. The latter approach effectively assumes that the detector responses are identical for each leaf of a clover detector. While this is not entirely accurate, for example due to their slightly different positions in the setup, it was expected to be a reasonable approximation for the purpose of this work. Ultimately, both approaches were tested and found to yield identical results for the GDR's γ-decay properties within their uncertainties. Thus, including the clover detectors' spectra in the fits in this manner was confirmed not to skew the results, while allowing to benefit from their additional statistics and superior energy calibration.

Fitting the model

With this, a fairly complex model of many parameters had been developed, which covered all relevant aspects of this work's NRF spectra and should allow to describe the spectra of all detectors in a measurement simultaneously. To fit this model in a Bayesian inference approach to the observed spectra, the Python package PyMC [130–132] was used. PyMC is a probabilistic programming library that allowed to implement the fit model in Python code using a simple and intuitive syntax and provided the necessary tools to fit it by sampling its posterior distribution with respect to the observed spectra using MCMC methods. The additional Python code specifically written as part of this

---

[12]The dependence of this energy difference on the detectors' polar angles due to the nuclear recoil was neglected here. Likewise, imperfections in the energy calibration of the detectors were assumed to not significantly affect this energy difference, but only the absolute energy positions of the signals.

work for the whole fit procedure and subsequent handling and investigation of the fit results was implemented in its own package called devonvolutionlib. This Python package is published as part of this work's data publication [69] and the core fit code containing the full model with all its details is contained in its `core.deconvolve()` function. As always, care was taken to implement all code in a modular structure with ample documentation so that it can be understood and adapted to future analyses with as little effort as possible. In addition to PyMC, the Python packages ArviZ [117, 118] and NumPyro [127–129] supported the fit procedure and the subsequent analysis of the fit results. ArviZ provided a file format for storing the MCMC samples and a wide range of diagnostic tools to investigate their statistical properties, while NumPyro provided an optimized MCMC backend for PyMC, which allowed to perform the computationally expensive sampling of the posterior distribution in reasonable time.

For the Bayesian inference fits all spectra and detector-response matrices were cut down to 4 MeV wide fit regions and rebinned to 10 keV wide bins, striking a balance between the range and resolution of the spectra and the computational demands of the inference. This led to a total of 3200 bins to consider for a single measurement when the spectra of the up to 8 usable detectors were fitted simultaneously. Except for those on the empty target container and no target at all, the spectra from all 26 remaining beam measurements were fitted. For each fit 20 000 samples across 8 separate MCMC chains were drawn from the posterior distribution after an MCMC sampler tuning phase of 20 000 discarded samples. Since the sampled fit parameters included the GDR NRF reaction counts Y_{ES} and $Y_{2_1^+}$, and the beam parameters $E_{Beam}^{(d)}$, Δ_l and Δ_u, the full posterior distribution of these quantities were obtained through a standard probability density estimation from the samples. By calculating the branching ratio of 2_1^+ Raman to ES according to Eq. (3.15) for each sample, the full posterior distribution of this quantity was obtained as well.

Viewing the fit results

Naturally, before proceeding to the final analysis steps using these fit results on the GDR's γ decay, it was imperative to first investigate the overall quality of the fits and therefore the reliability of the inferred quantities besides their statistical uncertainties. After all, if any part of the fit model, for instance the detector-response matrices containing the angular-distribution effects and detector efficiencies, would

not adequately reflect the true physical processes underlying the observed spectra, the results of the fits would be skewed and unreliable. However, in such a case it would also be impossible to simultaneously describe all detectors' spectra well across all measurements using the same fit procedure. Especially the ^{140}Ce, ^{12}C, and ^{28}Si measurements performed with both linearly and circularly polarized photon beams produced well-understood spectra of isolated γ-ray signals, for which the fit had little chance to conceal any critical inadequacies, making them ideal for an assessment of the quality of the fits.

The straightforward way to judge the overall quality of the fits is to compare the predicted to the observed spectra. However, due to its statistical sampling nature, the fit procedure does not predict a single spectrum for each detector, but a full probability distribution for each bin height of the spectra from their 20 000 samples. Since it is unfeasible to compare 3200 probability distributions to the observed spectra manually, they had to be summarized in some way.

For this work the choice was made to summarize samples by their median and 68.3 % highest density interval (HDI)[13] and use them as the point estimate and uncertainty band, respectively. The median was chosen as the point estimate since it is usually more robust against outliers than the mean, while being trivial to extract from samples, unlike the mode. Hence, the medians of the samples for each bin height were used to construct a single predicted spectrum for each detector, while the 68.3 % HDIs of the samples were used to generate uncertainty bands around these predictions. This reduction allowed a visual comparison of the predicted to the observed spectra and thus a judgement on the quality of the fits.

However, it must be stressed at this point that reducing full posterior distributions to a single point estimate and uncertainty band induces information loss, which can lead to false conclusions if not kept in mind. For this work, this has to be considered, in particular, when viewing the fitted incident background $\vec{y}_{\mathrm{BG}}^{(d)}$ in terms of its median bin heights before convolution with the detector response. Since bin heights are non-negative quantities in the model, their posterior distributions are cut off at zero. In combination with the usually low intensity of the background, this commonly leads to the fitted background bin heights roughly following exponential distributions. For such distributions the median is skewed towards higher values, for example in

---

[13]For a normal distribution the 68.3 % HDI corresponds to the commonly used 1-σ interval, hence this percentage was chosen here.

comparison to the mode which is the most probable value located at zero in this case. Hence, focusing solely on the medians of the background bin heights can lead to one overestimating the actually fitted background level. Consequently, it is important to always consider the uncertainty bands given by the 68.3 % HDIs as well, which provide a more realistic view of the fitted background. If a bin height, for example, indeed follows exactly an exponential distribution, the 68.3 % HDI corresponds to the interval from zero to 1.66 times the median, indicating a compatibility with no background, no matter the median value.

The measured spectra for all 26 measurements along with their fits[14] are shown in Appendix A, while in this section Figs. 4.11 and 4.12 show and discuss fits for two ^{140}Ce and two ^{154}Sm measurements, respectively, for illustration purposes. The fits are of high quality in all cases with the fitted spectra closely following the observed spectra within their uncertainties. Thus, the reliability of the inferred quantities was confirmed. Again, one has to stress that for each measurement a single, common fit to all its spectra simultaneously was made. In these, the spectra of all detectors were primarily constructed from a common count of emitted γ rays for each reaction and the detectors' individual detector-response matrices, which contained the angular-distribution effects and detector efficiencies. Hence, the fits indeed being capable of describing all detectors' spectra simultaneously across all measurements proves that the model accurately captured the underlying physics of the observed spectra including the angular-distribution effects and detector efficiencies. As already stated, otherwise it would simply not have been possible to describe, in particular, the ^{140}Ce, ^{12}C, and ^{28}Si spectra taken in both beam polarization modes this well.

As just hinted at, the fitted γ-ray background levels are generally low compared to the NRF signals, and in many cases, they are even compatible with zero within their 68.3 % HDIs. This confirms that no overfitting occurred from the relatively flexible background model. Likewise, the constant noise background is largely negligible relative to the NRF signals. Especially for the clover detectors' spectra, beam-induced background is virtually absent. This is not surprising considering they were positioned at backward angles and large distances to the target position, where beam-induced background is expected to be significantly lower than for the LaBr$_3$ detectors positioned

---

[14]The fits shown in Appendix A for the ^{140}Ce measurements performed with linearly polarized photon beams actually already include a slight extension of the so-far presented model to incorporate a magnetic dipole term, which is discussed further below. Since including this term did not noticeably affect the fits, the results without it are not shown here, as they would effectively look identical anyway.
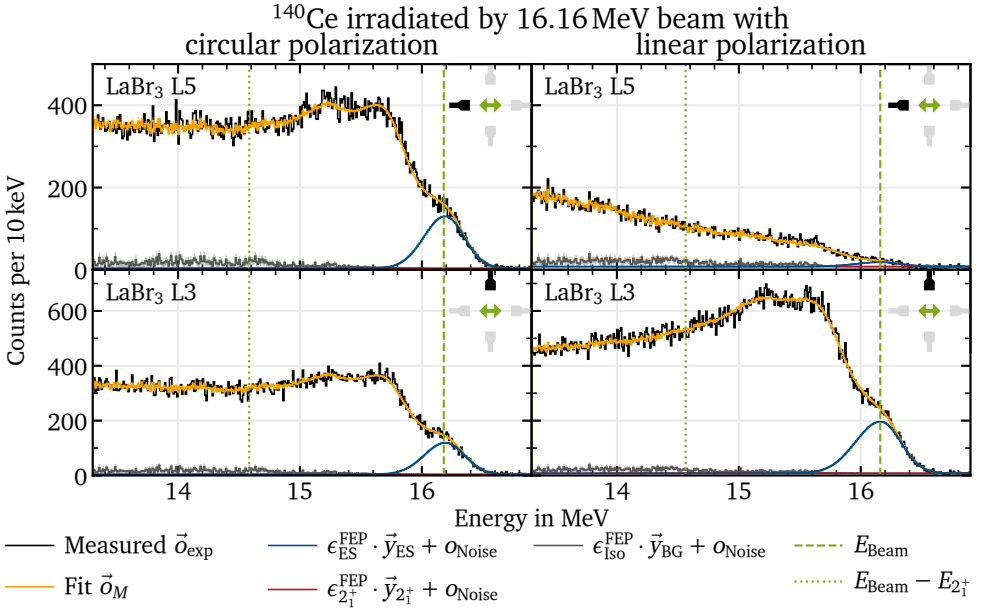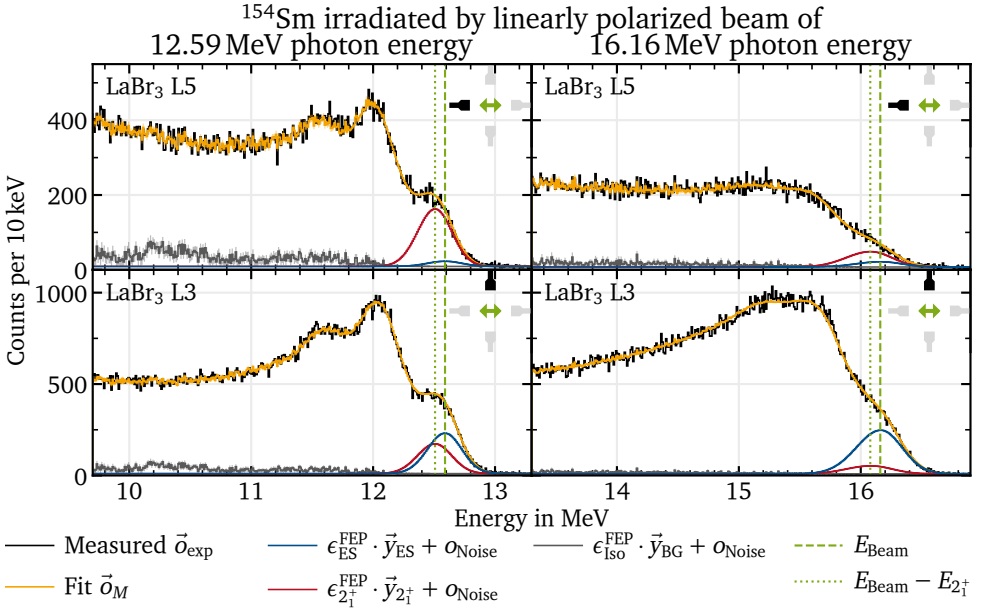
Figure 4.11.: Experimental spectra (black) of the LaBr$_3$ detectors L3 (bottom) and L5 (top) taken during irradiation of ^{140}Ce with 16.18 MeV circularly (left) and 16.16 MeV linearly (right) polarized photon beams, along with their fits (orange). The positions of the detectors (black), relative to the beam polarization plane (green arrow) and the other LaBr$_3$ detectors (light gray), are indicated in the top right of each panel. The two beam polarizations result in distinct angular distributions, and consequently azimuthal asymmetries, of the ES signal (compare top vs. bottom for left and right). The fits' ability to describe the spectra well in both cases confirms that the detector efficiencies and angular-distribution effects, as well as the overall shape of the detector response itself (shape of spectra), are accurately captured by the detector-response matrices used by the fit model. Additionally, the individual components of the fit model from Eq. (4.21), before convolution with the detector-response matrices, are shown (blue, red and gray), scaled by their FEP efficiencies and offset by the quasi-constant background noise, i.e., as they would appear in a detector with only FEP response. While a strong γ-signal from ES on the GDR of ^{140}Ce is present in the spectra at the beam energy (vertical dashed green line), 2_1^+ Raman scattering is not observed at its expected energy (vertical dotted green line).

Figure 4.12.: Experimental spectra (black) of the LaBr$_3$ detectors L3 (bottom) and L5 (top) taken during irradiation of ^{154}Sm with 12.59 MeV (left) and 16.16 MeV (right) linearly polarized photon beams, along with their fits (orange). The positions of the detectors (black), relative to the beam polarization plane (green arrow) and the other LaBr$_3$ detectors (light gray), are indicated in the top right of each panel. The individual components of the fit model from Eq. (4.21), before convolution with the detector-response matrices, are shown (blue, red and gray), scaled by their FEP efficiencies and offset by the quasi-constant background noise, i.e., as they would appear in a detector with only FEP response. The distinct azimuthal asymmetries (top vs. bottom) of ES (blue, asymmetric) and 2_1^+ Raman scattering (red, quasi-symmetric) of linearly polarized photon beams on the GDR of ^{154}Sm allow to disentangle the two energetically overlapping signals in each measurement. Thus, by fitting all observed spectra (top and bottom) of a measurement simultaneously, the 2_1^+ Raman to ES branching ratio of the GDR is effectively determined from the indirectly fitted azimuthal asymmetries of the spectra. Since the azimuthal asymmetry at 12.59 MeV is lower than at 16.16 MeV, the branching ratio must be higher at the lower energy, which is consistent with the fit results.

much closer to the target.

A detail warranting brief discussion is the unreliable energy calibration of the LaBr$_3$ detectors, as already elaborated on in Section 4.3. Simply by comparing the calibrated spectra, it was evident that the energy calibrations for the LaBr$_3$ detectors were unreliable on an absolute scale, as their spectra often did not align with each other or with those of the clover detectors. While the fit model could accommodate these discrepancies through detector-specific energy parameters, it was still desirable to align the spectra in energy to enable meaningful comparisons of the fits across detectors. This was accomplished by simply shifting the calibrated spectra of the LaBr$_3$ detectors in energy until their fitted peak energies agreed with those of the clover detectors within their uncertainties. The necessary shifts measured up to 500 keV, with the largest adjustments required at the highest energies, where the calibration was most unreliable due to significant extrapolation. Additionally, in a few cases, the LaBr$_3$ detectors' spectra were also manually stretched or compressed in energy by a few percent to correct slight deviations in their relative energy scales. These adjustments were necessary when the FEPs, SEPs and DEPs were not reproduced with their correct energy spacing of 511 keV, which would hamper the detector response fit.

Adding a magnetic dipole term to the model

So far it was assumed that in the energy region of the GDR no other nuclear dipole excitations exist for heavy nuclei like ^{140}Ce and ^{154}Sm. This is a reasonable assumption since no magnetic dipole excitations are known to occur in this region for such nuclei. It is also supported by the absence of any significant M1 strength in the spectra of the ^{140}Ce measurements, as it would have prevented to fit the spectra with the employed model, which did not include an M1 term. Ultimately, it was still desirable though to estimate upper limits on the M1 strength in the GDR region. Hence, an additional term for $0_1^+ \rightarrow 1^+ \rightarrow 0_1^+$ M1 ENRF reactions was added to the fit model. Since the physics of such reactions are very similar to ES on the GDR, this term was constructed analogously to the ES term. Effectively it was a copy of the GDR ES term, sharing its position and shape, but using a different reaction count Y_{M1} and different response matrices $\mathscr{R}_{M1}^{(d)}$. As always, the latter in particular encapsulated the angular distribution of the M1 ENRF signal, which is given by Eq. (2.65) with the positive sign for the measurements using the linear polarization mode of the photon beam. In case of photoexcitation by a circularly polarized beam, the angular distributions of M1 ENRF

and ES on the GDR are identical. Hence, the two are indistinguishable in this case and the M1 term was not included in the fit model for these measurements.

As expected, including the M1 term to the fit model for the ^{140}Ce measurements performed with linearly polarized photon beams did not noticeably affect the fits. All other quantities of interest remained unchanged within their uncertainties to their previous values obtained without the M1 term. In fact their predicted spectra looked effectively the same as before, which is why only those including the M1 term are shown in Appendix A. While a small number of M1 reaction counts were fitted, it is likely that these are overestimated due to systematic uncertainties, which in particular are expected to affect the ^{140}Ce measurements. The amount of ^{140}Ce nuclei irradiated by the beam was less than a third of that for ^{154}Sm, which leads to a much worse peak-to-background ratio in the spectra in addition to lower statistics. This makes it more likely that background is fitted by the M1 term, especially considering the at best weakly observed GDR ES signals in the spectra of the LaBr$_3$ detectors placed in the beam's polarization plane. In combination with the unreliable energy calibration of the LaBr$_3$ detectors, this can lead to the M1 term being fitted into the background starting below its physical peak energy, whose precise position in the spectra is simply not known due to the unreliable energy calibrations. Indeed, the by-far strongest relative M1 intensities were fitted for the measurement at 11.37 MeV, where the peak-to-background ratio was the worst, and the 15.35 MeV measurement, where a strong M1 contamination by the ^{12}C ENRF signal was present. While the fitted ratios of M1 to GDR ES reaction counts were at most 1.7(6) % for all other measurements, they were 13.3(12) % for the 11.37 MeV measurement and 6.5(7) % for the 15.35 MeV measurement.

To roughly estimate the systematic uncertainties of the fitted M1 reaction counts, the ^{12}C and ^{28}Si spectra taken with linearly polarized photon beams were fitted similarly to the ^{140}Ce spectra. For this, an E1 term was included in the model as the analog to the M1 term for ^{140}Ce, since no E1 strength is expected for ^{12}C and ^{28}Si at the energies of their measurements, at which they feature their strong M1 ENRF signals. Hence, this was basically the flipped situation to the ^{140}Ce measurements and thus comparable. To make the ^{12}C and ^{28}Si spectra, containing narrow NRF peaks, similar to the ^{140}Ce GDR spectra of wide ES peaks, they were artificially blurred through convolution with a normal distribution with a FWHM of 235 keV before fitting, so that the individual detector resolutions did not have to be considered here as well. This allowed to fit the ^{12}C and ^{28}Si spectra with basically the same model as the ^{140}Ce

spectra. The result were E1 to M1 reaction-count ratios of 2.18(12) % for the ^{12}C measurement and 0.982(6) % for the ^{28}Si measurement. Taking these values as a rough estimate for the systematic uncertainties of the M1 reaction counts, relative to the GDR ES reaction counts, fitted in the ^{140}Ce measurements meant that no significant M1 strength was observed in the ^{140}Ce spectra, except for the 11.37 and 15.35 MeV measurements, judging by the fitted ratios alone. For the latter two measurements, however, the M1 strength was likely overestimated due to the reasons discussed above. Therefore, all fitted M1 reaction counts were ultimately considered upper limits.

4.6.4. Determination of the photon beam properties

Before turning to the obtained γ-decay properties of the GDRs of ^{140}Ce and ^{154}Sm, it was still necessary to determine the properties of the photon beams with which they had been measured.

Energies and shapes of the photon beams

Usually, the energies and shapes of the photon beams would have been extracted from the direct measurements of the beam profile performed using the 0° detector. However, due to the issues with the 0° detector discussed in Section 3.3.2, this was not possible for this work's measurements. Nevertheless, this did not pose a problem, since the beam energies and shape parameters could instead be determined from the fits to the ^{140}Ce and ^{154}Sm spectra themselves. After all, according to Eq. (3.4) the fitted GDR ES signals are direct images of the respective beam profile. Now while the LaBr$_3$ detectors' energy calibrations were unreliable, this was not the case for the clover detectors. As discussed in Section 4.3, the clover detectors' energy calibrations were found to be reliable up to a few keV in the relevant energy range. Therefore, the fits to the clover detectors' spectra on ^{140}Ce and ^{154}Sm were well suited for a determination of the beam profile parameters. While the beam energy, unlike the shape parameters, had been fitted individually for each detector, the results from the clover detectors indeed agreed within their uncertainties for each measurement. Thus, they were averaged to obtain a single value for the beam energy per measurement. Since from experience the HIγS beam profile is known to be very stable, it was furthermore expected that all measurements taken with the same requested beam energy and

polarization mode would share the same beam profile. This was indeed confirmed by the fits to the ^{140}Ce and ^{154}Sm spectra, which yielded consistent beam parameters for each measurement pair taken with the same beam setting. Hence, the beam parameters extracted from the ^{140}Ce and ^{154}Sm spectra were considered reliable, averaged over the measurement pairs and used for the subsequent analysis of the GDR data. The obtained values are listed in Table 4.2. It is interesting to note that, while the requested relative resolutions of the photon beams of about 2 % were overall achieved, the obtained beam energies are found to be significantly higher than their target values in all measurements. These energy deviations range from 0.15(1) to 0.34(1) MeV. Still, the energies of all photon beam pairs of same requested energy but different polarizations are found to match closely, with a maximum difference of 0.08(2) MeV and an average difference of 0.05(1) MeV. Given that these differences are negligible in the context of this work, the energies of the linearly polarized beams are also commonly used when referring to the corresponding circularly polarized beams throughout this work.

Fluxes of the photon beams

As stated in Section 3.3.1, photoactivations were performed in parallel to those NRF measurements on ^{140}Ce and ^{154}Sm, which used linearly polarized photon beams. In these either a ^{140}Ce or a ^{154}Sm activation target was irradiated, matching the target of the respective NRF measurement, in addition to one of the ^{197}Au activation targets, which were always included in the photoactivations. The irradiations by the photon beam activated the targets as the radioactive nuclei ^{196}Au, ^{139}Ce, and ^{153}Sm were produced through photodisintegration reactions in the ^{197}Au, ^{140}Ce, and ^{154}Sm targets, respectively. After irradiation, the activities of these nuclei in the targets was measured through γ spectroscopy, using the well-known properties [104–106] of their radioactive decays, which then allowed to determine the number of beam-induced photodisintegration reactions, which had produced the respective radioactive nuclei. The analysis of this activation data, yielding these reaction counts, was performed by K. Prifti in the scope of her master's thesis [107, 108].

Since all measured radioactive nuclei are (γ,n) reaction products of their respective targets, one might assume that the activation data analysis yielded the reaction counts of these (γ,n) reactions. While this was indeed the case for ^{197}Au and ^{140}Ce, it was not for the ^{154}Sm. This is due to the ^{154}Sm(γ,p) daughter nucleus, ^{153}Pm, being

Table 4.2.: Beam-profile parameters of this work's measurements extracted from the fits to the ^{140}Ce and ^{154}Sm NRF spectra. See Eq. (4.9) for the definition of the beam-profile model, whose parameters are given here. Comparison of the first and third column shows that the physical beam energies given in the third column are found to be consistently higher than those originally requested from the HIγS facility given in the first column.

Requested E_{Beam} in MeV	Polarization mode	E_{Beam} in MeV	Δ_l in keV	Δ_u in keV	FWHM in keV	$\frac{\mathrm{FWHM}}{E_{\mathrm{Beam}}}$ in %
11.22	Circular	11.45(1)	117(7)	97(4)	253(7)	2.21(6)
11.22	Linear	11.37(1)	170(5)	111(4)	331(10)	2.91(9)
12.4	Circular	12.66(1)	104(5)	98(4)	238(7)	1.88(6)
12.4	Linear	12.59(1)	117(9)	116(14)	274(27)	2.17(21)
14.0	Circular	14.25(1)	118(4)	122(6)	283(7)	1.98(5)
14.0	Linear	14.27(1)	130(5)	112(4)	284(8)	1.99(5)
15.11	Linear	15.35(1)	143(6)	126(5)	317(8)	2.06(5)
15.9	Circular	16.18(1)	136(5)	115(4)	295(7)	1.82(5)
15.9	Linear	16.16(1)	158(5)	127(4)	336(8)	2.08(5)
17.5	Circular	17.84(1)	145(7)	157(10)	356(19)	1.99(10)
17.5	Linear	17.79(1)	193(6)	155(5)	410(10)	2.30(5)

radioactive as well and undergoing β^- decay to ^{153}Sm, the ^{154}Sm(γ,n) daughter nucleus, with a lifetime of 454.4(17) s [104]. This lifetime is short compared to all other relevant timescales in the experiment, namely the irradiation time, the time between irradiation and activation counting, and the counting time. So for the purpose of the analysis, the decay can be considered instantaneous. As a result, both reaction channels populate ^{153}Sm whose radioactive decay was the sole observable in the ^{154}Sm activation measurements. Consequently, the activation data analysis could not distinguish between (γ,n) and (γ,p) reactions for ^{154}Sm, and only the sum of their reaction counts $Y_n + Y_p$ was obtained for ^{154}Sm from the activity of ^{153}Sm.

With the precise photon-beam energies now known from the fits to the ^{140}Ce and ^{154}Sm

spectra, the activation-analysis results[15] of K. Prifti [107, 108] could now be used to determine the total photon fluxes Φ of the ^{140}Ce and ^{154}Sm measurements, which employed linearly polarized photon beams. This was possible through Eq. (3.17), provided that the cross sections of the observed photodisintegration reactions at the relevant photon-beam energies were available in the literature. Strictly speaking, there was, however, no direct literature data published on the ^{197}Au(γ,n), ^{140}Ce(γ,n), ^{154}Sm(γ,n), and ^{154}Sm(γ,p) reactions measured in this work [22, 23]. Yet, values from photoneutron measurements were available for ^{197}Au, ^{140}Ce, and ^{154}Sm in the literature [21, 98, 162]. In these experiments, neutrons emitted in photodisintegration reactions of ^{197}Au, ^{140}Ce, and ^{154}Sm were measured with the ability to determine the neutron multiplicity of each observed reaction. Hence, (γ,n) and (γ,2n) reactions could be distinguished. However, since only neutrons were detected in these experiments, they could not discriminate (γ,n) and (γ,n+X) reactions, where X denotes any particle or combination of particles not including neutrons. Consequently, they only provided data for the sum of the cross sections of (γ,n) and all (γ,n + X) reactions. Neglecting unlikely photoalpha or photofission reactions, the only photodisintegration reactions energetically possible up to the highest photon-beam energy of 17.79 MeV used in this work were (γ,n), (γ,np), (γ,2n), (γ,p), and (γ,2p) for ^{197}Au, ^{140}Ce and ^{154}Sm, given their particle separation energies [163, 164]. Furthermore, (γ,np) reactions were energetically only possible for the highest photon-beam energy of 17.79 MeV for ^{140}Ce and ^{154}Sm, while for ^{197}Au the reaction channel was open starting from the 14.27 MeV measurement. Therefore, the available single-photoneutron cross sections gave the sum of the (γ,n) and (γ,np) cross sections or solely the (γ,n) cross section depending on the photon-beam energy and nucleus for the nuclei and photon energies of interest in this work. Still even in the former case, the (γ,np) cross sections σ_{np} were expected to be negligible compared to the (γ,n) cross sections σ_n as the (γ,np) reactions' phase spaces were much smaller due to their much higher threshold energies compared to the (γ,n) reactions and as the protons also had to overcome the Coulomb barrier of their respective nuclei for the (γ,np) reactions to occur. Hence, the approximation

$$\sigma_n \approx \sigma_n + \sigma_{np} \tag{4.24}$$

was made for the purpose of this work, and the available single-photoneutron cross sections were considered to be the (γ,n) cross sections of the reactions measured in

---

[15]This work uses results from a revised activation analysis by K. Prifti [108], which corrected minor errors in the original analysis [107]. These revised results are accessible through the data publication associated with this work [69].

this work, irrespective of whether they were actually the sum of (γ,n) and (γ,np) cross sections or not.

With this slight approximation, the total photon flux determination was after all possible using the literature cross sections of single-photoneutron reactions on ^{197}Au [162] and ^{140}Ce [98], which were retrieved in tabulated form from the EXFOR database [22, 23]. Unfortunately, the ^{154}Sm activation data could not be used for this purpose, since no (γ,p) cross-section data was available for ^{154}Sm, which would have been necessary as elucidated above. Still the total photon flux of the ^{154}Sm measurements could be determined from the literature (γ,n) cross sections of ^{197}Au and ^{140}Ce. For ^{197}Au this was directly possible[16] using Eq. (3.17), since a ^{197}Au activation target was irradiated in every ^{154}Sm measurement performed with linear beam polarization. To determine the total photon flux Φ of the ^{154}Sm measurements from the ^{140}Ce(γ,n) cross section as well, although no ^{140}Ce activation targets were irradiated in these measurements, a two-step procedure was employed for each measurement. First, the ^{140}Ce measurement at the same beam energy was effectively used to determine the ^{197}Au(γ,n) cross section at this energy from the ^{140}Ce(γ,n) literature cross section. Then this ^{197}Au(γ,n) cross section was used to determine the total photon flux Φ of the respective ^{154}Sm measurement. All steps again simply employed Eq. (3.17). With this, two photon-flux values based on distinct (γ,n) cross-section data sets were obtained for each measurement. A comparison of these values showed that they agreed within their uncertainties, which confirmed the reliability of the determined photon fluxes. Finally, each pair of values were averaged, weighted by their uncertainties, to obtain a single value for the total photon flux Φ of each measurement performed on ^{140}Ce and ^{154}Sm with linearly polarized photon beams. The determined photon-flux values are listed in Table 4.3.

---

[16]Whenever necessary, cross-sections values and their uncertainties were interpolated in energy between the available data points.

Table 4.3.: Photon-flux values of this work's measurements on ^{154}Sm and ^{140}Ce performed with linearly polarized photon beams. The values were determined from the ^{197}Au and ^{140}Ce activation data analyzed by K. Prifti [107, 108] and the literature single-photoneutron cross sections of ^{197}Au [162] and ^{140}Ce [98]. $\Phi_{^{197}\text{Au}(\gamma,n)}$ and $\Phi_{^{140}\text{Ce}(\gamma,n)}$ are the total photon fluxes determined using the literature single-photoneutron cross sections of ^{197}Au and ^{140}Ce, respectively and $\langle\Phi\rangle$ is their uncertainty weighted average. Additionally temporal, and temporal and areal photon-flux densities are given, based on the irradiation times and the beam collimator diameter.

Target nucleus	E_{Beam} in MeV	$\Phi_{^{197}\text{Au}(\gamma,n)}$ in $10^{11}\,\gamma$	$\Phi_{^{140}\text{Ce}(\gamma,n)}$ in $10^{11}\,\gamma$	$\langle\Phi\rangle$ in $10^{11}\,\gamma$	$\frac{\mathrm{d}\langle\Phi\rangle}{\mathrm{d}t}$ in $10^7\,\frac{\gamma}{\mathrm{s}}$	$\frac{\mathrm{d}^3\langle\Phi\rangle}{\mathrm{d}t\,\mathrm{d}x\,\mathrm{d}y}$ in $10^7\,\frac{\gamma}{\mathrm{s\,cm^2}}$
	11.37(1)	6.2(5)	5.3(4)	5.6(5)	2.43(20)	4.8(4)
	12.59(1)	9.5(6)	9.4(5)	9.4(4)	3.97(16)	7.90(31)
^{140}Ce	14.27(1)	2.09(12)	2.13(8)	2.12(7)	2.44(8)	4.86(15)
	15.35(1)	2.58(23)	2.82(10)	2.78(9)	2.99(10)	5.95(20)
	16.16(1)	10.3(12)	9.7(4)	9.71(35)	4.47(16)	8.90(32)
	17.79(1)	33(43)	12.2(9)	12.2(9)	6.0(5)	12.0(9)
	11.37(1)	4.35(35)	3.67(30)	3.95(35)	1.70(15)	3.38(30)
	12.59(1)	4.61(28)	4.56(29)	4.58(22)	1.99(9)	3.95(19)
^{154}Sm	14.27(1)	2.19(13)	2.23(12)	2.21(10)	1.43(6)	2.85(12)
	15.35(1)	1.87(17)	2.05(11)	2.00(10)	1.79(9)	3.57(17)
	16.16(1)	5.8(7)	5.47(29)	5.53(28)	2.47(12)	4.91(25)
	17.79(1)	22(29)	8.3(7)	8.3(7)	4.01(34)	8.0(7)

5. Results on the decay behavior of the giant dipole resonances of ^{140}Ce and ^{154}Sm

This chapter presents the results of this work's experiment on the decay behavior of the GDRs of ^{140}Ce and ^{154}Sm. They are obtained by combining the intermediate results of the NRF-data analysis, presented in Chapter 4, with those of the activation-data analysis. The activation measurements were performed in parallel to those NRF measurements on ^{140}Ce and ^{154}Sm which used linearly polarized photon beams and their data was analyzed by K. Prifti[1] in the scope of her master's thesis [107, 108].

To obtain the results presented in this chapter, the posterior distributions of the Bayesian inference fits to the NRF spectra were reduced to a point estimate and a symmetric uncertainty for each parameter of interest. The median of a posterior distribution was again used as the point estimate, while the uncertainty was determined as the greater of the two distances from the median to the endpoints of the 68.3 % HDI. For parameters that are perfectly normally distributed, this method corresponds exactly to using the mean and standard deviation. Yet, in cases where distributions are non-normal, this approach is more robust against outliers and skewness than using the mean and standard deviation. Since most of the posterior distributions of interest were unimodal and quasi-symmetric, often even close to normal distributions, this simplification was considered acceptable. However, some posterior distributions

---

[1]This work uses results from a revised activation analysis by K. Prifti [108], which corrected minor errors in the original analysis [107]. These revised results are accessible through the data publication associated with this work [69].

instead resembled exponential distributions, necessitating a different reduction approach. In these cases[2], the quantities are reported as upper limits, with the point estimate being the median of the posterior distribution and the uncertainty being the distance from the median to the upper endpoint of the 68.3 % HDI.

5.1. Branching ratios of 2_1^+ Raman to elastic scattering

The obtained results on the branching ratio of 2_1^+ Raman to ES $\frac{\sigma_{2_1^+}}{\sigma_{\mathrm{ES}}}$ are presented in Table 5.1 and visualized in Fig. 5.1. They are directly based on the posterior distributions of the Bayesian inference fits to the NRF spectra. While this branching ratio was not directly a fit parameter, the fitted reaction counts of the two scattering processes yielded it immediately through Eq. (3.15) and since it could be calculated for each sample individually, the full posterior distribution of this branching ratio was nevertheless obtained as well for each measurement.

For ^{154}Sm the reported values are solely based on the measurements with linearly polarized photon beams. This is because the ^{154}Sm measurements using circularly polarized beams lacked a significant sensitivity to this branching ratio due to the, in this case, rather similar angular distributions of 2_1^+ Raman and ES, which did not allow for a clear disentanglement of the two processes from their observed doublet γ-ray signal.

For ^{140}Ce the two scattering processes did not overlap in energy and their branching ratio could be extracted from the NRF spectra regardless of whether their angular distributions were similar or not. Hence, the branching ratios obtained from the pairs of ^{140}Ce measurements at the same beam energy but with different beam polarizations were averaged to obtain the final values presented in Table 5.1. Since in all cases except for the 11.37 MeV measurements the posterior distributions of the branching ratio resembled exponential distributions, only upper limits are obtained. Finally, while for the 11.37 MeV measurements the posterior distribution of the branching ratio was quasi-symmetric around a finite value, this value is still reported as an upper

---

[2]There are also instances where the posterior distribution does not resemble an exponential distribution, but the fitted value is still reported as an upper limit due to other factors. In these cases, the uncertainty of the upper limit was also determined as the distance from the median to the upper endpoint of the 68.3 % HDI.

limit. The reason for this is that the large level of background in the NRF spectrum at this energy competed with the 2_1^+ Raman signal. With the flexible background model used in the Bayesian inference fits, which additionally was regularized towards zero by its prior, the 2_1^+ Raman signal, and hence the branching ratio, was very likely overestimated, since the fit considered what was likely background as part of this signal.

5.2. Branching ratios of elastic scattering to photodisintegration reactions

By forming the ratio of Eq. (3.17) for ES and (γ,n) reactions the respective branching ratio

$$\frac{\sigma_{\text{ES}}}{\sigma_{\text{n}}} = \frac{Y_{\text{ES}}}{Y_{\text{n}}} \frac{\left(\frac{\text{d}^2 N_{\text{T}}}{\text{d}x\,\text{d}y}\right)_{\text{Activation}}}{\left(\frac{\text{d}^2 N_{\text{T}}}{\text{d}x\,\text{d}y}\right)_{\text{NRF}}} \tag{5.1}$$

of the two processes was determined for ^{140}Ce from their reaction counts Y_f, obtained in the NRF- and activation-data analyses, and the targets' areal densities $\frac{\text{d}^2 N_{\text{T}}}{\text{d}x\,\text{d}y}$. Likewise, for ^{154}Sm the branching ratio

$$\frac{\sigma_{\text{ES}}}{\sigma_{\text{n}} + \sigma_{\text{p}}} = \frac{Y_{\text{ES}}}{Y_{\text{n}} + Y_{\text{p}}} \frac{\left(\frac{\text{d}^2 N_{\text{T}}}{\text{d}x\,\text{d}y}\right)_{\text{Activation}}}{\left(\frac{\text{d}^2 N_{\text{T}}}{\text{d}x\,\text{d}y}\right)_{\text{NRF}}} \tag{5.2}$$

was obtained, taking into account that the activation-data analysis could not distinguish between (γ,n) and (γ,p) reactions for ^{154}Sm as elucidated in Section 4.6.4. The results on these branching ratios are presented in Table 5.1.

5.3. Absolute cross sections relative to literature data

The total photon fluxes Φ of those ^{140}Ce and ^{154}Sm measurements which had been performed with linearly polarized beams, were determined in Section 4.6.4 using

literature cross-section values for single-photoneutron reactions on ^{197}Au and ^{140}Ce. Through Eq. (3.17), these values could be used to determine the total cross sections of any other reaction for which the reaction count Y_f had been measured. The cross sections of ES and 2_1^+ Raman scattering on the GDRs of ^{140}Ce and ^{154}Sm were determined using the NRF-analysis results in this way. For the same reasons discussed in Section 5.1, the cross sections of 2_1^+ Raman scattering are upper limits for ^{140}Ce. Furthermore, the sum of the cross sections of the ^{154}Sm(γ,n) and ^{154}Sm(γ,p) reactions was calculated using the activation-data-analysis results. By using the single-photoneutron cross section of ^{154}Sm, for which literature values were available [21], as the ^{154}Sm(γ,n) cross section[3], the cross section of the ^{154}Sm(γ,p) reaction was determined by the cross-section difference as well. Finally, using the total photon-flux values calculated solely relative to the literature ^{197}Au(γ,n) cross section [162], instead of the weighted average value, the ^{140}Ce(γ,n) cross section was determined as well to provide a comparison to literature values. All obtained cross sections are presented in Tables 5.3 and 5.4 for ^{140}Ce and ^{154}Sm, respectively, along with interpolated literature values on single and total photoneutron cross sections [21, 98] for comparison. Furthermore, the ES cross sections are visualized in Fig. 5.1, while the photodisintegration cross sections are shown in Fig. 5.2.

5.4. Branching ratios of elastic scattering to photoabsorption reactions

By neglecting unlikely $(\gamma,2p)$, photoalpha and photofission reactions as well as other unobserved (γ,γ') reactions, the photoabsorption cross section of the GDR of ^{154}Sm was approximated as

$$\sigma_{\text{Abs}} \overset{\text{For }^{154}\text{Sm}}{\approx} \sigma_{\text{ES}} + \sigma_{2_1^+} + \sigma_{\text{n}} + \sigma_{\text{np}} + \sigma_{2\text{n}} + \sigma_{\text{p}} \tag{5.3}$$

for a determination of the branching ratio $\frac{\sigma_{\text{ES}}}{\sigma_{\text{Abs}}}$ of ES on its GDR to this approximated photoabsorption cross section at the six measurement energies of this work. To

---

[3]This is an approximation for the 17.79 MeV measurement where the ^{154}Sm(γ,np) reaction could have contributed to its single-photoneutron cross section, but was assumed to be negligible. For all other measurement energies, the ^{154}Sm single-photoneutron cross section was exactly equal to the ^{154}Sm(γ,n) cross section, since the ^{154}Sm(γ,np) reaction was energetically forbidden.

calculate the same branching ratio for ^{140}Ce the approximation

$$\sigma_{\text{Abs}} \overset{\text{For }^{140}\text{Ce}}{\approx} \sigma_{\text{ES}} + \sigma_{2_1^+} + \sigma_{\text{n}} + \sigma_{\text{np}} + \sigma_{2\text{n}} \tag{5.4}$$

was used, which additionally neglects (γ,p) reactions for which no cross-section data was available, as well as $(\gamma,\gamma_{2_1^+})$ reactions for which only upper limits were obtained. The results on these branching ratios are presented in Table 5.1 and visualized in Fig. 5.1. Below the threshold energies of the $(\gamma,2\text{n})$ and (γ,np) reactions, they were calculated via

$$\frac{\sigma_{\text{ES}}}{\sigma_{\text{Abs}}} \approx \frac{\sigma_{\text{ES}}}{\sigma_{\text{ES}} + \sigma_{2_1^+} + \sigma_{\text{n}} + \sigma_{\text{p}}}$$
$$= \frac{1}{1 + \frac{\sigma_{2_1^+}}{\sigma_{\text{ES}}} + \left(\frac{\sigma_{\text{ES}}}{\sigma_{\text{n}} + \sigma_{\text{p}}} \right)^{-1}} \tag{5.5}$$

for ^{154}Sm, and likewise for ^{140}Ce by omission of the σ_{p} and $\frac{\sigma_{2_1^+}}{\sigma_{\text{ES}}}$ summands. Since these calculations did not require any literature data, the uncertainties of these branching ratios are lower below the threshold energies of the $(\gamma,2\text{n})$ and (γ,np) reactions than above, where literature data had to be used.

5.5. Upper limits on magnetic dipole strength in ^{140}Ce

As elaborated at the end of Section 4.6.3, upper limits on M1 strength from $0_1^+ \rightarrow 1^+ \rightarrow 0_1^+$ NRF reactions were determined for ^{140}Ce at the six measurement energies. The upper limits are presented in Table 5.2 in the form of absolute cross sections σ_{M1} and as the cross-section ratio $\frac{\sigma_{\text{M1}}}{\sigma_{\text{ES}}}$ to ES on the GDR of ^{140}Ce.

Table 5.1.: Results of this work on γ-decay branching ratios of the GDRs of ^{140}Ce and ^{154}Sm.

Nucleus	E_{Beam} in MeV	$\dfrac{\sigma_{2_1^+}}{\sigma_{\text{ES}}}$ in %	$\dfrac{\sigma_{\text{ES}}}{\sigma_{\text{n}}}$ in %	$\dfrac{\sigma_{\text{ES}}}{\sigma_{\text{n}}+\sigma_{\text{p}}}$ in %	$\dfrac{\sigma_{\text{ES}}}{\sigma_{\text{Abs}}}$ in %
^{140}Ce	11.37(1)	≤53(41)	0.614(23)		0.610(22)
	12.59(1)	≤0.34(16)	0.285(11)		0.284(11)
	14.27(1)	≤0.10(5)	0.904(33)		0.896(33)
	15.35(1)	≤0.07(5)	1.40(5)		1.38(5)
	16.16(1)	≤0.09(4)	1.47(5)		1.45(5)
	17.79(1)	≤0.19(9)	2.06(7)		1.31(13)
^{154}Sm	11.37(1)	97.8(23)		0.360(16)	0.357(16)
	12.59(1)	101.7(15)		0.516(22)	0.511(22)
	14.27(1)	87.8(17)		0.645(29)	0.596(30)
	15.35(1)	43.6(34)		1.93(9)	1.06(6)
	16.16(1)	25.5(4)		3.09(14)	1.10(6)
	17.79(1)	9.64(32)		6.12(26)	1.24(11)

Table 5.2.: Results of this work on upper limits on M1 strength from $0_1^+ \rightarrow 1^+ \rightarrow 0_1^+$ NRF reactions on ^{140}Ce.

E_{Beam} in MeV	$\dfrac{\sigma_{\text{M1}}}{\sigma_{\text{ES}}}$ in %	σ_{M1} in mb
11.37(1)	≤13.3(12)	≤0.072(9)
12.59(1)	≤ 1.7(6)	≤0.0072(25)
14.27(1)	≤ 1.6(4)	≤0.049(12)
15.35(1)	≤ 6.5(7)	≤0.35(4)
16.16(1)	≤ 1.18(17)	≤0.052(8)
17.79(1)	≤ 0.10(10)	≤0.0022(22)

Table 5.3.: Results of this work on absolute cross sections of the GDR of ^{140}Ce along with interpolated literature values for comparison. As usual in this work, $\sigma_{\Sigma n} = \sigma_n + \sigma_{np} + \sigma_{2n}$ denotes the total photoneutron cross section.

E_{Beam} in MeV	σ_{ES} in mb	$\sigma_{2_1^+}$ in mb	σ_n in mb	$\sigma_n + \sigma_{np}$ in mb[a][b]	$\sigma_{\Sigma n}$ in mb[a]
11.37(1)	0.54(5)	≤0.58(10)	79(7)	94(6)	94(6)
12.59(1)	0.433(20)	≤0.0017(11)	151(10)	153(7)	153(7)
14.27(1)	3.08(12)	≤0.0032(21)	345(23)	338(7)	338(7)
15.35(1)	5.44(21)	≤0.0038(25)	419(39)	383(7)	383(7)
16.16(1)	4.45(18)	≤0.0041(28)	284(35)	304(7)	304(9)
17.79(1)	2.11(17)	≤0.0038(24)	38(49)	103(8)	159(9)

[a] These values were interpolated from data measured by Leprêtre *et al.* [98] and retrieved from the EXFOR database [22, 23].
[b] Equal to σ_n for all measurement energies except 17.79 MeV, since they are below the threshold energy of the ^{140}Ce(γ,np) reaction.

Table 5.4.: Results of this work on absolute cross sections of the GDR of ^{154}Sm along with interpolated literature values for comparison. As usual in this work, $\sigma_{\Sigma n} = \sigma_n + \sigma_{np} + \sigma_{2n}$ denotes the total photoneutron cross section.

E_{Beam} in MeV	σ_{ES} in mb	$\sigma_{2_1^+}$ in mb	$\sigma_n + \sigma_p$ in mb	σ_p in mb	$\sigma_n + \sigma_{np}$ in mb[a][b]	$\sigma_{\Sigma n}$ in mb[a]
11.37(1)	0.70(7)	0.69(7)	195(18)	21(19)	175(4)	175(4)
12.59(1)	1.49(9)	1.52(9)	289(16)	40(16)	249(4)	249(4)
14.27(1)	1.61(9)	1.41(8)	249(13)	40(14)	209(4)	227(5)
15.35(1)	2.80(17)	1.22(10)	145(8)	17(9)	128(5)	243(5)
16.16(1)	3.01(18)	0.77(5)	97(6)	22(7)	75(5)	247(5)
17.79(1)	2.24(20)	0.216(21)	36.7(33)	0(6)	36(5)	179(6)

[a] These values were interpolated from data measured by Carlos *et al.* [21] and retrieved from the EXFOR database [22, 23].
[b] Equal to σ_n for all measurement energies except 17.79 MeV, since they are below the threshold energy of the ^{154}Sm(γ,np) reaction.
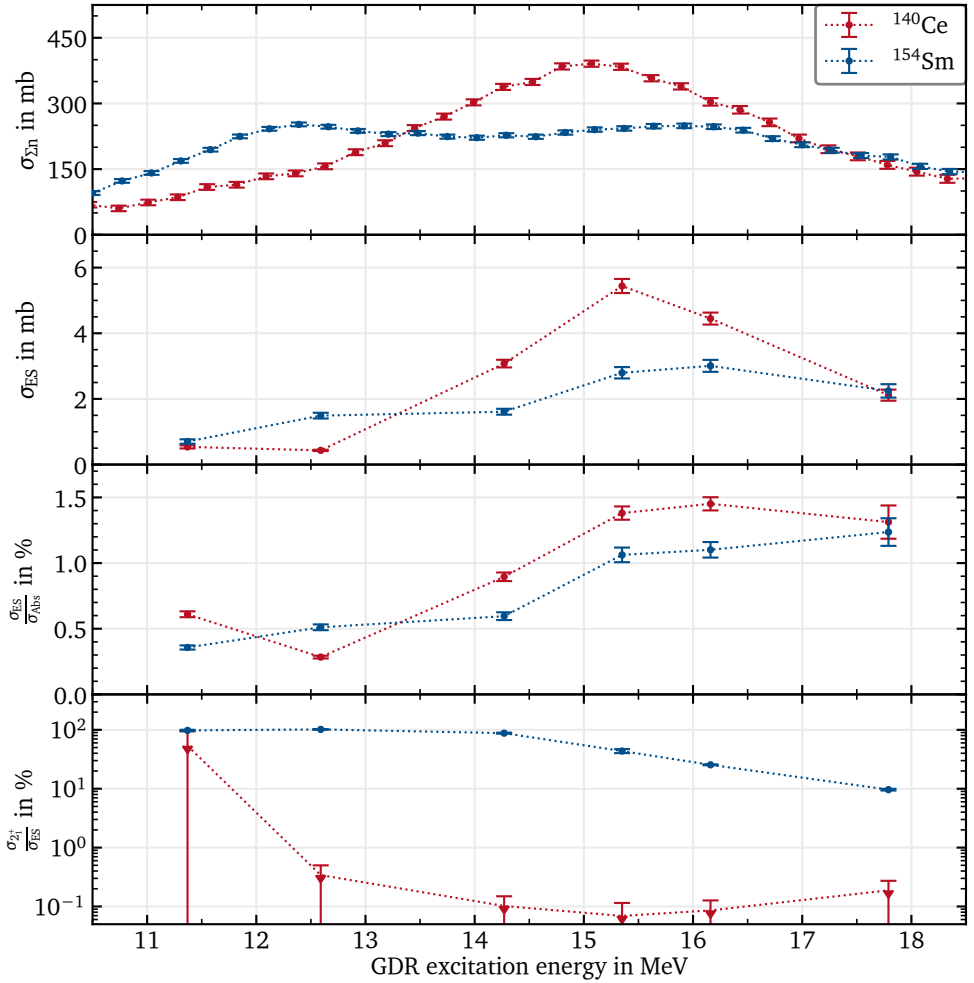
Figure 5.1.: Results of this work on the γ-decay behavior of the GDRs of ^{140}Ce (blue) and ^{154}Sm (red) in the lower three panels. The top panel shows their total photoneutron cross sections measured by Leprêtre *et al.* [98] on ^{140}Ce and Carlos *et al.* [21] on ^{154}Sm, which were retrieved from the EXFOR database [22, 23] and illustrate the shapes of the GDRs.
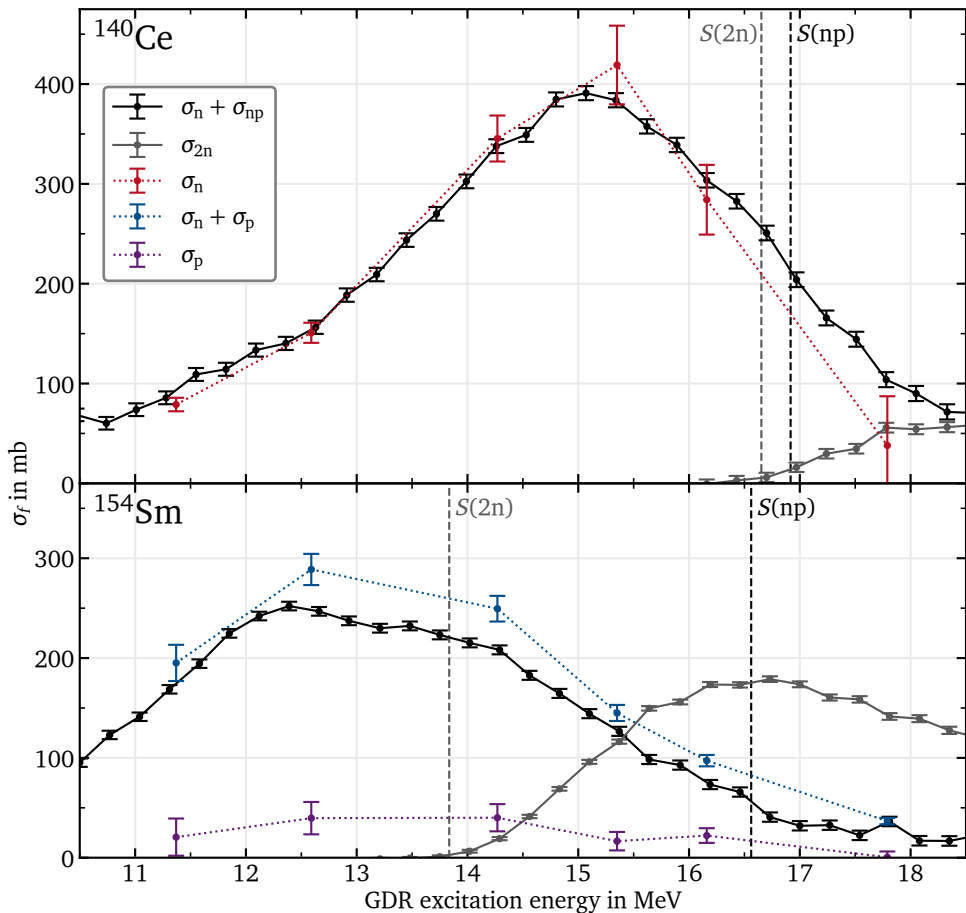
Figure 5.2.: Results of this work (red, blue, and purple) on photodisintegration cross sections of the GDRs of ^{140}Ce (top) and ^{154}Sm (bottom) in comparison to literature values (black and gray). Vertical dashed lines indicate the threshold energies of the (γ,2n) (gray) and (γ,np) (black) reactions. The ^{140}Ce and ^{154}Sm literature values were measured by Leprêtre *et al.* [98] and Carlos *et al.* [21], respectively, and were retrieved from the EXFOR database [22, 23].

6. Discussion and interpretation of the experimental results

In the following the results on the γ decay of the GDRs of ^{140}Ce and ^{154}Sm are discussed and interpreted. Specifically, the novel data is compared with the expectations based on the geometrical as well as the microscopical model of the GDR. Finally, the implications of the results for the nature of the GDR and the nuclei themselves are discussed.

6.1. General remarks on the experimental results

Before going into the details of the models and their comparison to the data, some general observations on the results are appropriate. First of all, it should be explicitly stated that the experiment and the subsequent analysis of its data were successful in achieving the goals set out in the introduction. The newly developed experimental technique for investigating γ decay of the GDR via NRF reactions induced by state-of-the-art LCB photon sources was successfully applied for the first time to the GDRs of ^{140}Ce and ^{154}Sm. Their GDRs' γ decay after energy-resolved photoexcitation was observed in the experiment with overall high statistics and its evolution with excitation energy was quantitatively determined across the full energy range of the two GDRs using six distinct measurement energies. In particular, the GDR's 2_1^+ Raman scattering cross section was successfully disentangled from its ES cross section for ^{154}Sm, which allowed to study its evolution with energy for a deformed nucleus for the first time. The activation measurements performed simultaneously to the NRF measurements allowed for the determination of absolute cross sections of the GDR's γ-decay processes.

For both ^{140}Ce and ^{154}Sm, an absolute branching ratio of γ decay of around 1 % was observed for their GDRs relative to photoabsorption. This finding is consistent with previous studies on the GDRs of heavy nuclei [35–42]. However, the exact value of this branching ratio is neither constant nor does it exhibit a fine structure as it is found to smoothly evolve with excitation energy. Interestingly, the branching ratio of ES to photoabsorption is found to increase with excitation energy for both nuclei. From a pure phase-space argument, one may have expected the branching ratio of ES to photoabsorption to decrease with excitation energy, as the phase space for ES should increase slower with excitation energy than the phase space for particle decay, which grows rapidly above the particle separation thresholds. However, the experimentally observed behavior is indeed in agreement with the scattering-theory considerations presented in Section 2.9.1, and in particular Eq. (2.88), as will be discussed in the following.

The 2_1^+ Raman scattering cross sections of the GDRs of ^{140}Ce and ^{154}Sm are found to differ significantly. For the spherical ^{140}Ce, no 2_1^+ Raman scattering on its GDR was observed. Respectively determined upper limits of around 0.1 % of the ES cross section place strong constraints on the potential presence of this decay channel of the GDR for ^{140}Ce. This contrasts with the findings of V. Yu. Ponomarev and A. Krasznahorkay [165], who reported significant γ decay of the GDRs of the spherical nuclei ^{116}Sn and ^{124}Sn to the 2_1^+ states in (α,α′γ) experiments. They provide branching ratios of this decay, relative to ground-state γ decay, of 1.5(5) for ^{116}Sn and 1.1(3) for ^{124}Sn. However, their distinction between 2_1^+ and 0_1^+ γ decay relies solely on fitting two Gaussian peaks to an assumed doublet γ signal, as the experiment's energy resolution was insufficient to resolve the two decay channels directly. Given the data's low resolution and limited statistics, the reliability of these results may thus be questioned.

For the deformed ^{154}Sm, the 2_1^+ Raman scattering cross section is found to be roughly equal to the ES cross section of the GDR around its lower resonance energy. It then decreases smoothly and significantly with increasing excitation energy, dropping to about 10 % of the ES cross section at the higher-energy tail of the GDR. Therefore, neither a fine structure nor a completely featureless behavior of the 2_1^+ Raman scattering cross section was observed for the GDR of ^{154}Sm. Finally, for both nuclei, no significant γ decays of their GDRs to other states were detected in the present data.

6.2. Test of the geometrical model of the giant dipole resonance via its γ-decay predictions

6.2.1. The geometrical model and its γ-decay predictions

To briefly recapitulate, in the geometrical model the GDR is pictured as an isovector oscillation of protons against neutrons. Since nuclei have three principal axes in a geometrical view, such oscillations can occur along any of these axes. Consequently, the GDR encompasses these three fundamental resonances as well as their interplay in this picture. With the photoabsorption cross section of each of these oscillations being described by an SLO, the photoabsorption cross section of the GDR is given by the sum

$$\sigma_{\text{Abs}}(E) = \sum_{k=1}^{3} \sigma_k^{\text{SLO}}(E) = \sum_{k=1}^{3} \frac{\widehat{\sigma}_k}{1 + \left(\frac{E^2 - \widehat{E}_k^2}{E \Gamma_k}\right)^2} \tag{6.1}$$

of these three SLOs in the geometrical model. As before $\widehat{E}_k$, Γ_k and $\widehat{\sigma}_k$ are the SLO parameters of the respective sub-resonances, which give the resonance energy, the FWHM, and the on-resonance photoabsorption cross section of the sub-resonances, respectively. Naturally, two or all three sub-resonances can be degenerate, which is the case for axially symmetric and spherical nuclei, respectively, making their SLO parameters degenerate as well.

As shown in Section 2.9.1, this parametrization of the GDR's photoabsorption cross section requires Eq. (2.93) to hold for nuclei with ground-state spin $J_{GS} = 0$. Hence, the ES cross sections of the GDRs of ^{140}Ce and ^{154}Sm should be, just like their photoabsorption cross sections, fully described by their SLO parameters. Furthermore, as discussed in Section 2.9.2, the geometrical model also provides an explicit prediction for the GDR's 2_1^+ Raman scattering cross section through Eq. (2.96) for these nuclei, which again is based solely on the GDR's SLO parameters. Consequently, also the GDR's branching ratio of 2_1^+ Raman to ES is predicted according to Eq. (2.97) by the geometrical model.

While it is textbook knowledge [12, 19] that the geometrical model can describe measured GDR photoneutron data well for nearly all nuclei, its just discussed predictions for the γ decay of the GDR have yet to be thoroughly tested. This is due to the

lack of necessary experimental data until now. The few pioneering experiments on γ decay of the GDR of the 1960s to 1980s, limited by the technology of their time, could either only cover low GDR excitation energies [37–39] or faced limitations due to low resolution and statistics [40–42], hindering a comprehensive test of the γ-decay predictions of the geometrical model. These predictions provide, however, a particularly rigorous and thus important test of the model as they are effectively parameter-free. Although they depend on the SLO parameters of the GDR, no additional parameters are introduced. Thus, when requiring the model to simultaneously describe both the photoabsorption cross section and the γ-decay behavior of the GDR, it has no additional flexibility to adjust to the data beyond what is available when considering only the photoneutron data.

6.2.2. Bayesian inference fits of the geometrical model to the GDRs of ^{140}Ce and ^{154}Sm

Consequently, testing the simultaneous descriptive power of the geometrical model is the next logical step in assessing the model's validity. It can now be taken with the newly obtained data on the GDR's γ decay for ^{140}Ce and ^{154}Sm. For this purpose, two independent Bayesian inference fits of the GDR's SLO parameters were performed for each nucleus. In the first fit, the photoabsorption cross section and the branching ratio of 2_1^+ Raman to ES of the GDR were simultaneously fitted to the respective experimental data sets. For comparison, a second fit was performed using only the previously available photoabsorption-cross-section data.

Since no direct experimental data on the GDR's photoabsorption cross section was available for ^{140}Ce and ^{154}Sm [22, 23], it was approximated by the total photoneutron cross sections of these nuclei [21, 98] as common practice in the literature [19]. Taking into account the particle separation energies [163, 164] of both nuclei, in the GDR's energy domain they are given by the sum

$$\sigma_{\Sigma n}(E) := \sigma_n(E) + \sigma_{np}(E) + \sigma_{2n}(E) \tag{6.2}$$

of the (γ,n), (γ,np) and (γ,2n) cross sections σ_n, σ_{np}, and σ_{2n}, respectively. As before, the literature photoneutron cross-section values were retrieved in tabulated form from the EXFOR database [22, 23].

Instead of the photoabsorption model $\sigma_{\text{Abs}}(E)$ of Eq. (6.1), the easily computable quantity

$$\sigma_{\text{Abs}}(E) - \sigma_{\text{ES}}(E) - \sigma_{2_1^+}(E) \approx \sigma_{\Sigma\text{n}}(E) \tag{6.3}$$

was fitted to the experimental total photoneutron cross sections $\sigma_{\Sigma\text{n}}$. This way, at least the contributions of ES and 2_1^+ Raman scattering to the GDR's photoabsorption cross section, not included in $\sigma_{\Sigma\text{n}}$, were explicitly taken into account.

As for ^{154}Sm concrete experimental values for its GDR's branching ratio of 2_1^+ Raman to ES had been obtained, the likelihood function for its Bayesian inference fit could be constructed using normal distributions similar to Eq. (4.6). For ^{140}Ce, though, only upper limits on this branching ratio had been obtained. However, these upper limits are rather strong as they reach down to per-mille level. Thus, to still include this valuable information in the Bayesian inference fit, the more complex likelihood function[1] for the branching ratio of 2_1^+ Raman to ES

$$P_M(\vec{D}|\vec{\theta}) = \prod_k \begin{cases} 1 & \text{for } 0 \leq \vec{\mu}_k(\vec{\theta}) < \vec{D}_k \\ 1 - \dfrac{\vec{\mu}_k(\vec{\theta}) - \vec{D}_k}{\Delta\vec{D}_k} & \text{for } 0 \leq \vec{D}_k \leq \vec{\mu}_k(\vec{\theta}) < \vec{D}_k + \Delta\vec{D}_k \\ 0 & \text{otherwise} \end{cases} \tag{6.4}$$

was used. Here, the index k runs over the six measurement energies, $\vec{D}$ represents the obtained upper limits on the GDR's branching ratio of 2_1^+ Raman to ES, $\vec{\Delta D}$ their uncertainties,

$$\vec{\theta} = \begin{pmatrix} \hat{E}_1 & \hat{\sigma}_1 & \Gamma_1 & \hat{E}_2 & \hat{\sigma}_2 & \Gamma_2 & \hat{E}_3 & \hat{\sigma}_3 & \Gamma_3 \end{pmatrix} \tag{6.5}$$

the SLO parameters of the GDR to be fitted, and $\vec{\mu}_k(\vec{\theta})$ the geometrical model's respective prediction on this branching ratio for the k-th measurement energy according to Eq. (2.97). This likelihood function effectively constrained the predicted branching ratios to be below the measured upper limits within their uncertainties by assigning the same likelihood to all predicted values below an upper limit and from there on linearly decreasing the likelihood to 0 beyond a limit's uncertainty range. The

---

[1]It should be acknowledged that the likelihood function of Eq. (6.4) is not actually a proper PDF of $\vec{D}$, as it does not integrate to unity. However, similar to improper priors, this is not an issue for the Bayesian inference fit performed here.

linear decrease was mainly introduced for improved numerical stability of the MCMC sampling used in the Bayesian inference fit.

Finally, since ^{140}Ce is known to be at least approximately spherical, using a triaxial geometry for fitting the data of its GDR would have over-parametrized the model. Therefore, for ^{140}Ce an axially symmetric geometry was assumed in the Bayesian inference fits. This meant that the SLO parameters of the second and third sub-resonances were fixed to be degenerate, i.e., $\hat{E}_2 = \hat{E}_3$, $\hat{\sigma}_2 = \hat{\sigma}_3$, and $\Gamma_2 = \Gamma_3$.

Just as for the analysis of the NRF spectra described in Section 4.6.3, the Bayesian inference fits were performed by sampling the posterior distributions using MCMC methods. All prior distributions were chosen to be uniform over a sufficiently large range to not bias the results. Through a simple reparametrization of the SLO resonance energies, it was ensured that they were sorted in ascending order $\hat{E}_1 \leq \hat{E}_2 \leq \hat{E}_3$ during the MCMC sampling. Once more, the Python packages PyMC [130–132], ArviZ [117, 118] and NumPyro [127–129] were used for MCMC sampling and analysis of the results. For each fit 32 000 samples across 8 separate MCMC chains were drawn from the posterior distribution after an MCMC sampler tuning phase of 32 000 discarded samples. As before, all samples, and hence the posterior distributions they represent, were summarized by their medians and 68.3 % HDIs as point estimate and uncertainty band, respectively. Furthermore, for quantitative presentations of results the uncertainty bands were reduced to a symmetric uncertainty in those cases where the median was located close to the midpoint of the 68.3 % HDI by taking the greater of the two distances from the median to its endpoints as the uncertainty value.

6.2.3. Discussion of the geometrical model fit results

For the GDR of ^{154}Sm, regardless of whether solely its photoneutron data $\sigma_{\Sigma n}$ or simultaneously both, its photoneutron data and its branching ratio of 2_1^+ Raman to ES $\frac{\sigma_{2_1^+}}{\sigma_{ES}}$ were fitted, the fits are in overall excellent agreement with its experimental photoneutron data. Likewise, both fits are able to describe its ES cross section σ_{ES}, although this was not explicitly considered by either fit. For the branching ratio of 2_1^+ Raman to ES, however, the descriptive power of the fits differs. While fitting only the photoneutron data still allows to describe the overall evolution of this branching ratio with excitation energy on a qualitative level, the quantitative reproduction of the

experimental data is not satisfactory. Fitting simultaneously both, the photoneutron data and the branching ratio of 2_1^+ Raman to ES, on the other hand, allows for a superb quantitative description of the branching ratio as well. As stated, this does not come at the cost of a noticeably worse description of the photoneutron or ES data, as they are still well reproduced by this fit. The two fits along with the data on the GDR of ^{154}Sm are shown in Fig. 6.1.

While the two, axial-symmetry-assuming fits to the GDR data of ^{140}Ce, shown in Fig. 6.2, are completely different from those performed for ^{154}Sm due to very different experimental data, the observations that can be made for them are still similar. Again, both fits are able to describe the photoneutron data of the GDR of ^{140}Ce well. Likewise, its ES cross section is fairly well reproduced by both fits, despite neither explicitly considering it. While the reproduction of the experimental data points on the quantitative level is certainly worse than for ^{154}Sm, it is unclear whether this is due to the model's limitations or possibly underestimated uncertainties of the experimental data. In this context, it should be noted that the deviating data points at 11.37 and 12.59 MeV stem from NRF measurements with rather low peak-to-background ratios as can be seen in Figs. A.1 and A.5 in Appendix A. Nevertheless, considering the simplicity of the model for the GDR's ES cross section and the fact that this experimental data was not explicitly fitted, the overall agreement with the data within a factor of at most 2.2 is still satisfactory, in particular, since the overall evolution of the ES cross section with excitation energy is fairly well described by the model. Finally, the experimental upper limits on the GDR's branching ratio of 2_1^+ Raman to ES are only in agreement with the fit which considered them explicitly and simultaneously with the photoneutron data. The second fit using exclusively the photoneutron data predicts branching ratios significantly above all measured upper limits, except for the weakest limit obtained at 11.37 MeV.

Thus, when its SLO parameters are appropriately fitted, the geometrical model is able to simultaneously describe the photoabsorption/photoneutron cross section, the ES cross section, and the branching ratio of 2_1^+ Raman to ES of the GDRs of both the deformed nucleus ^{154}Sm and the virtually spherical nucleus ^{140}Ce with overall high accuracy. The combination of the two latter observables naturally also implies a good description of the 2_1^+ Raman cross section itself too. Hence, the present data confirm the applicability of the geometrical model of the GDR even for its γ decay and so-far regardless of the nuclear shape. Its high descriptive power on all three data sets simultaneously is a novel, compelling argument for the model's validity including
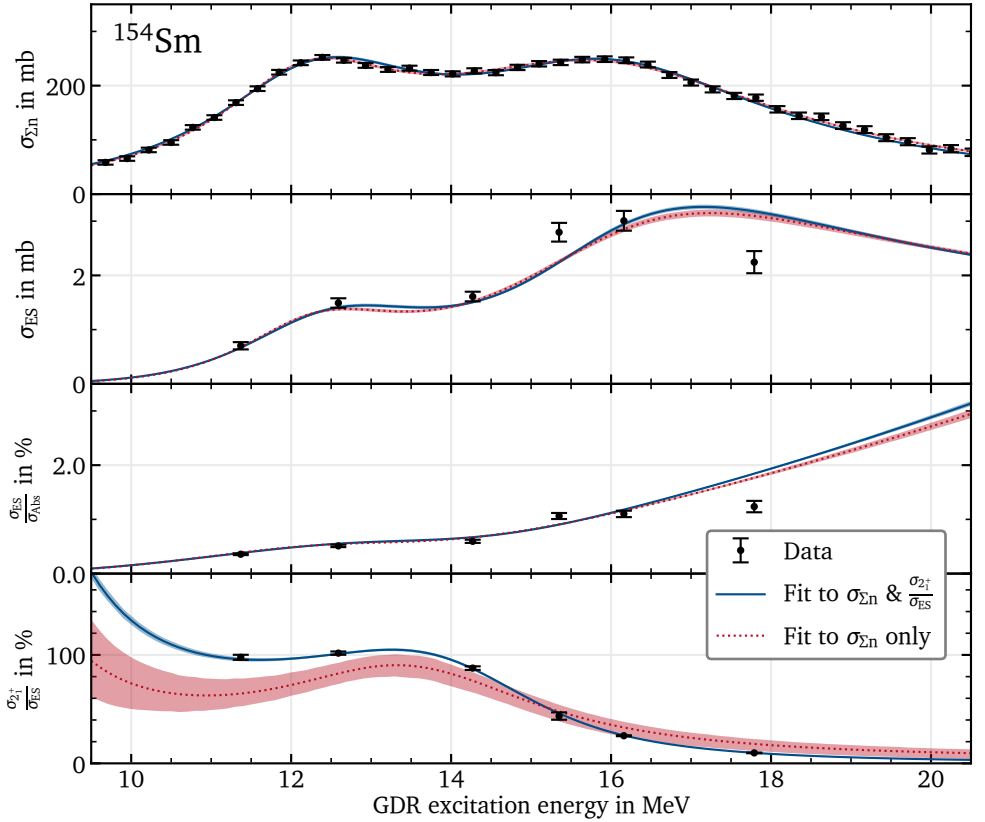
Figure 6.1.: Geometrical model fits (solid blue and dotted red) of the GDR SLO parameters to experimental data (black) on the GDR of ^{154}Sm. The total photoneutron cross section $\sigma_{\Sigma n}$ shown in the top panel, which was measured by Carlos *et al.* [21] and retrieved from the EXFOR database [22, 23], is considered and equally well described by both fits. The solid blue fit additionally considers the branching ratio of 2_1^+ Raman to ES $\frac{\sigma_{2_1^+}}{\sigma_{ES}}$ (bottom panel) measured in this work, allowing for a simultaneous quantitative description of this observable, not achieved by the red fit. Neither fit explicitly considers this work's ES cross section σ_{ES} data or its branching ratio $\frac{\sigma_{ES}}{\sigma_{Abs}}$ (middle panels) which are still well reproduced by both fits.
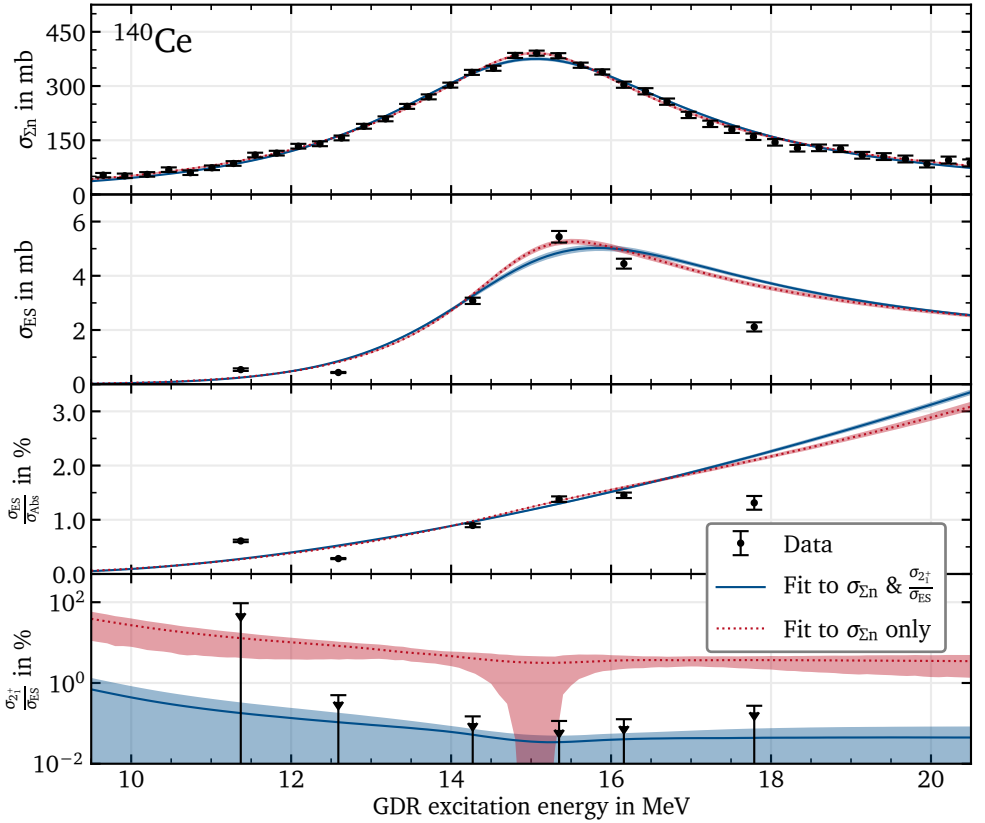
Figure 6.2.: Geometrical model fits (solid blue and dotted red) of the GDR SLO parameters to experimental data (black) on the GDR of ^{140}Ce. The total photoneutron cross section $\sigma_{\Sigma n}$ shown in the top panel, which was measured by Leprêtre *et al.* [98] and retrieved from the EXFOR database [22, 23], is considered and equally well described by both fits. The solid blue fit additionally considers the strong upper limits on the branching ratio of 2_1^+ Raman to ES $\frac{\sigma_{2_1^+}}{\sigma_{ES}}$ (bottom panel) measured in this work, allowing for a simultaneous quantitative description of this observable, not achieved by the red fit. Neither fit explicitly considers this work's ES cross section σ_{ES} data or its branching ratio $\frac{\sigma_{ES}}{\sigma_{Abs}}$ (middle panels) which are still fairly well reproduced by both fits.

its picture of the GDR as just three orthogonal and yet interrelated oscillators in the nucleus.

Furthermore, since a quantitative description of the γ-decay data requires explicit fitting, and since these simultaneous fits do not degrade the description of the photoneutron or ES data, this demonstrates a high sensitivity of the γ decay to the SLO parameters, and thus to the structure of the GDR. The finding suggests that the γ-decay behavior of the GDR is sensitive to details of its structure that cannot be discerned from the photoneutron or ES data alone. While this is a novel insight, it aligns with expectations based on the functional form of the geometrical model's prediction for the GDR's 2_1^+ Raman-scattering cross section given by Eq. (2.96). From this equation, it was to be expected that 2_1^+ Raman scattering is sensitive to small differences among the SLO parameters of the three sub-resonances, which, however, have minimal impact on the photoabsorption/photoneutron or ES cross sections.

This difference in sensitivity is also directly reflected in the SLO parameter sets inferred by the fits. They are listed in Table 6.1 and their posterior distributions are shown in Figs. 6.3 and 6.4 for ^{154}Sm and ^{140}Ce, respectively.

For the GDR of ^{154}Sm the fit to its photoneutron data alone yields rather broad posterior distributions for its SLO parameters. In particular, this fit fails to properly constrain the SLO parameters of its second and third sub-resonances. This is especially apparent for their on-resonance photoabsorption cross sections $\hat{\sigma}_2$ and $\hat{\sigma}_3$. They exhibit very broad and almost flat posterior distributions, constrained mainly by the chosen prior boundaries instead of the data. A strong anti-correlation between them hints to only their sum being constrained by the photoneutron data alone. Meanwhile, for the simultaneous fit to both ^{154}Sm GDR data sets the situation is entirely different. Here, the posterior distributions of the SLO parameters are significantly more constrained. In particular, the γ-decay data allows the fit to disentangle the SLO parameters of the second and third sub-resonances. However, it should also be noted that the results $\Gamma_2 = 4.25(19)\,\mathrm{MeV}$ and $\Gamma_3 = 5.95(32)\,\mathrm{MeV}$ of the simultaneous fit on the FWHMs of the second and third sub-resonances are unexpectedly distinct. Given the fitted resonance energies $\hat{E}_2$ and $\hat{E}_3$ differ by only 3.0(7) %, this is somewhat surprising and might hint to a possible slight overfitting of the FWHMs occurring in the simultaneous fit.

For ^{140}Ce considering its GDR's γ-decay behavior likewise allows for a much more
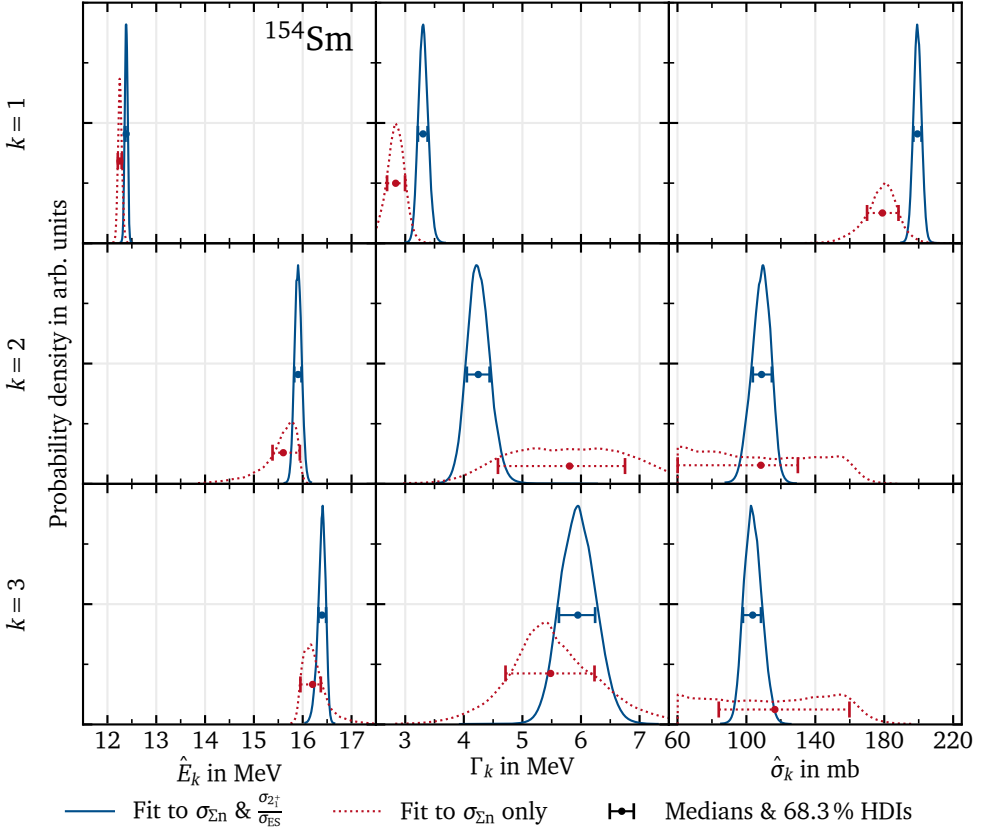
Figure 6.3.: Posterior distributions of the SLO parameters of the GDR of ^{154}Sm obtained from the two Bayesian inference fits of the geometrical model shown in Fig. 6.1 to its experimental data. Fitting simultaneously both the photoneutron data and the branching ratio of 2_1^+ Raman to ES yields significantly more constrained posterior distributions of the SLO parameters (solid blue) than fitting only the photoneutron data (dotted red). In particular, the SLO parameters of the second (middle row) and third (bottom row) sub-resonances are disentangled by the simultaneous fit, which is not possible when fitting only the photoneutron data. The uncertainty bars illustrate the medians and 68.3 % HDIs of the posterior distributions.
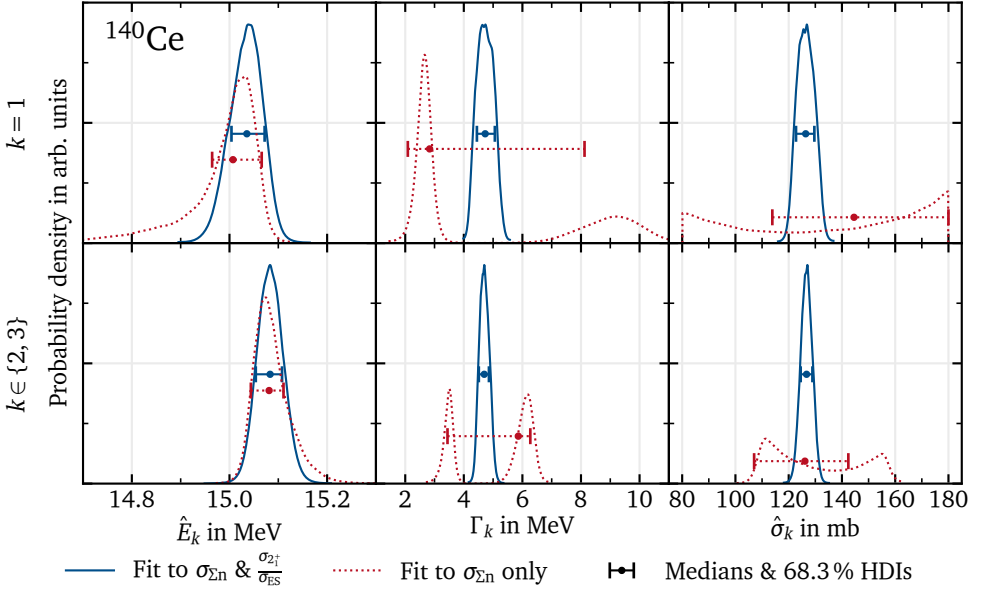
Figure 6.4.: Posterior distributions of the SLO parameters of the GDR of ^{140}Ce obtained from the two Bayesian inference fits of the geometrical model shown in Fig. 6.2 to its experimental data. Since ^{140}Ce is known to be at least approximately spherical, an axially symmetric nuclear shape was assumed for the fits, fixing the SLO parameters of the second and third sub-resonances (bottom row) to be degenerate. Fitting simultaneously both the photoneutron data and the strong upper limits on the branching ratio of 2_1^+ Raman to ES allows to constrain all SLO parameters (solid blue). In contrast, this is not possible when fitting only the photoneutron data (dotted red), where bimodal posterior distributions are obtained for the FWHMs (middle column) and on-resonance photoabsorption cross sections (right column). The uncertainty bars illustrate the medians and 68.3 % HDIs of the posterior distributions.

Table 6.1.: SLO parameters of the GDRs of ^{154}Sm and ^{140}Ce obtained from the Bayesian inference fits of the geometrical model shown in Figs. 6.1 and 6.2, respectively, to their experimental data. The given values are the medians of the posterior distributions shown in Figs. 6.3 and 6.4 and the uncertainties are based on their 68.3 % HDIs.

Nucleus	Fitted data		k	$\hat{E}_k$ in MeV	Γ_k in MeV	$\hat{\sigma}_k$ in mb
^{140}Ce	$\sigma_{\Sigma n}$ & $\dfrac{\sigma_{2_1^+}}{\sigma_{ES}}$		1	15.04(4)	4.73(33)	126(4)
			2, 3	15.083(29)	4.70(19)	126.7(22)
	$\sigma_{\Sigma n}$		1	$15.02^{+0.06}_{-0.04}$	$2.8^{+5.3}_{-0.7}$ [a]	145(35) [ab]
			2, 3	$15.081^{+0.030}_{-0.037}$	$5.9^{+0.4}_{-2.4}$ [a]	126(19) [a]
^{154}Sm	$\sigma_{\Sigma n}$ & $\dfrac{\sigma_{2_1^+}}{\sigma_{ES}}$		1	12.384(29)	3.30(9)	199.3(24)
			2	15.91(8)	4.25(19) [c]	109(6)
			3	16.39(8)	5.95(32) [c]	104(6)
	$\sigma_{\Sigma n}$		1	12.26(4)	2.84(16)	179(9)
			2	$15.60^{+0.34}_{-0.22}$	$5.8^{+0.9}_{-1.2}$	108^{+21}_{-48} [b]
			3	$16.20^{+0.17}_{-0.25}$	5.5(8)	117^{+43}_{-33} [b]

[a] This parameter's posterior distribution is multimodal and thus the given value is not fully representative of the distribution.
[b] This parameter's posterior distribution and thus the given value is mainly constrained by the prior boundaries.
[c] This parameter might be slightly overfitted.

reliable fit[2] of the SLO parameters of its GDR. Without usage of the γ-branching limits, the posterior distributions of the on-resonance photoabsorption cross sections $\hat{\sigma}_k$ are again rather broad and mainly constrained by the prior boundaries instead of the data. For the FWHMs Γ_k bimodal posterior distributions are obtained. Once more, a strong anti-correlation between the parameter pairs hints to them being arbitrarily interchangeable in this fit without affecting the model's descriptive power on the photoneutron data. In contrast, the simultaneous fit to both data sets provides significantly more constrained posterior distributions of the SLO parameters, which

---

[2]This requires the applicability of Eq. (2.96) for a non-rotational nucleus, such as ^{140}Ce, though, which is discussed in more detail further below.

single out a clear value for each parameter. Hence, just as for ^{154}Sm, considering the γ-decay behavior in addition to the photoabsorption allows separating otherwise entangled SLO parameters of the GDR of ^{140}Ce.

Consequently, these results establish the γ decay of the GDR as a novel, previously untapped observable highly sensitive to the structure of the resonance. This sensitivity is not only of theoretical interest, but also of practical relevance. For example, recent remeasurements of photoneutron data for ^{150}Nd and ^{152}Sm question not only the prior existing data, but also the presumed splitting of the GDR of these nuclei altogether [166]. Study of the GDR's γ decay behavior as an independent and yet untapped observable could provide new insights to these cases of disputed GDR structure.

Finally, while 9 independent parameters were fitted here for the GDR of ^{154}Sm, in accordance with a possibly triaxial shape of the nucleus, it is noteworthy that the fitted SLO parameters of the second and third sub-resonances are actually rather similar. Only their FWHMs, Γ_2 and Γ_3, differ significantly for the simultaneous fit to both data sets as evident in Table 6.1. Hence, for comparison, a simultaneous fit to both data sets based on an axially symmetric nuclear shape was performed as well, where the SLO parameters of the second and third sub-resonances were, consequently, fixed to be degenerate. Even with this substantial reduction of fitted parameters down to just 6, the results of this fit were still found to be in good agreement with the experimental data. This confirms the robustness of the results, and shows, in particular, that the conclusions drawn from the fits allowing triaxiality are not skewed by over-parametrization of the model. Indeed, the SLO parameters obtained in this case match those of the triaxial fit overall well. The sole exception are of course the now necessarily degenerate FWHMs Γ_2 and Γ_3, which attain a common value in between the respective values of the triaxial fit. As this still allows for a good description of the data, slight overfitting of these two parameters in the triaxial model is indeed likely, but not severe.

Likewise, for ^{140}Ce it is also possible to reproduce its GDR data when assuming a perfectly spherical shape, which corresponds to all three sub-resonances being degenerate and only 3 SLO parameters to be fitted. After all, the simultaneous fit to both its GDR data sets, which allowed for axially symmetric deformation, already favored degenerate SLO parameters of all three sub-resonances as apparent in Table 6.1. For spherical nuclei 2_1^+ Raman scattering on the GDR is forbidden according to Eq. (2.96), as it yields a vanishing cross section in this case. Hence, the experimental upper limits

on the GDR's branching ratio of 2_1^+ Raman to ES are trivially fulfilled by assuming a spherical shape. On the other hand, this implies that any observation of 2_1^+ Raman scattering on the GDR would be strong indication for at least slight deformation of the nucleus.

However, the question remains, whether the geometrical model's prediction for the GDR's 2_1^+ Raman scattering cross section is applicable to spherical nuclei in the first place. After all, its derivation is based on the coupling of the GDR to the rotational motion of the 2_1^+ state [40, 44, 45], but in spherical nuclei the 2_1^+ state is not a rotational excitation of the ground state. So this derivation of Eq. (2.96) should not be applicable to spherical nuclei. Still, the model's prediction for the 2_1^+ Raman scattering cross section is in excellent agreement with the strong experimental upper limits on ^{140}Ce. It is unclear whether this is just a coincidence or whether the model's prediction, Eq. (2.96), is indeed valid for spherical nuclei as well, raising the question if Eq. (2.96) can be derived in a more general approach applicable to all nuclear shapes after all.

As already discussed in Section 2.9.2, from a simple phonon model, for example, one may indeed expect the 2_1^+ Raman scattering cross section to vanish for spherical nuclei just as predicted by Eq. (2.96). The 2_1^+ state is understood as a one-phonon vibrational excitation of the ground state in spherical nuclei. Since the GDR itself is also considered a one-phonon vibrational excitation of the ground state, the 2_1^+ state should not be populated by γ decay of the GDR in spherical nuclei, as this would require simultaneous destruction of one phonon and creation of another one in a single process.

Still even this phonon model comes with a caveat. One may expect a two-phonon GDR built on top of the 2_1^+ state to be present in spherical nuclei, similar to how the GDR is pictured as a one-phonon excitation of the ground state. Its excitation energy should be roughly the sum of the GDR's and the 2_1^+ state's excitation energies. Hence, due to the large width of the GDR in comparison to typical excitation energies of the 2_1^+ state, such a two-phonon GDR should overlap with the GDR itself, allowing for a mixing of the two. Thus, the physically observed GDR, photoexcitable from the ground state, could be the result of such a mixing and consequently contain components from both the one-phonon GDR and the two-phonon GDR. In this scenario, this mixed GDR is expected to significantly decay into the 2_1^+ state, i.e., exhibit a 2_1^+ Raman scattering cross section, as the 2_1^+ state is part of its fundamental structure. This is, however, in contradiction to the observed behavior of the GDR of ^{140}Ce, which does

not exhibit substantial 2_1^+ Raman scattering if any at all. Therefore, the obtained data on ^{140}Ce can also be taken as strong evidence of one-phonon pureness of the GDR of this nucleus.

6.3. Comparison to the microscopical model of the giant dipole resonance

In the microscopical picture, the GDR is understood as the product of collective particle-hole excitations of the nucleus involving all nucleons, i.e., constructively coherent superpositions of all possible electric dipole particle-hole excitations [12–14]. In first order, the GDR is modeled as a collective one-particle-one-hole (1p-1h) excitation of the ground state. This ansatz already allows to roughly describe the experimentally observed resonance energies and the ground-state excitation strengths, i.e., the integrated photoabsorption cross sections, of the GDR. However, its widths cannot be reproduced by this simple approach, being too narrow compared to the experimental observations [13, 167]. This discrepancy is commonly explained by mixing of the 1p-1h excitations with more complex configurations taking place. Thus, the next step in the microscopical description of the GDR is to consider strong mixing of 1p-1h excitations with two-particle-two-hole (2p-2h) excitations [14], also referred to as doorway states [53, 91]. This results in a fragmentation of the GDR's strength over many states spread across a wider energy range, allowing for a much better description of the observed GDR widths. Naturally, this mixing is expected to continue with even more complex n-particle-n-hole (np-nh) configurations [91] resulting in the GDR being microscopically pictured as fragmented over a myriad of states.

In the microscopical view the GDR's width Γ is commonly broken down according to

$$\Gamma = \Delta\Gamma + \Gamma^{\downarrow} + \Gamma^{\uparrow} \tag{6.6}$$

into three components [12, 14, 168]. The first component $\Delta\Gamma$, referred to as Landau damping, encompasses fragmentation of the single intrinsic collective 1p-1h state into multiple 1p-1h states [14, 168]. In realistic microscopical calculations such fragmentation occurs due to coupling of the collective 1p-1h state to non-collective 1p-1h states [12]. The next term $\Gamma^{\downarrow}$ is referred to as the spreading width [12] or collisional damping [53]. It represents the already discussed width contribution

due to the mixing of the simple 1p-1h states with numerous more complex np-nh states [14, 91] and gives the by-far largest contribution to the GDR's width for heavy nuclei [12]. The last component $\Gamma^\uparrow$ is called the escape width and is due to the coupling of the 1p-1h states to the continuum [14, 91]. Since in general it is located well above the nucleon separation thresholds, the collective 1p-1h state acquires this width contribution $\Gamma^\uparrow$ by direct particle emission [12, 168]. It must be stressed that the escape width $\Gamma^\uparrow$ only refers to direct particle emission from the 1p-1h states. After mixing with more complex configurations, particle emission is also possible, but the associated width[3] is then considered part of the spreading width $\Gamma^\downarrow$ and not the escape width $\Gamma^\uparrow$ [12, 91]. Direct particle emission from the 1p-1h states is expected to result in highly energetic particles and population of simple 1h states in the daughter nucleus [91], while particle emission after mixing with more complex configurations is expected to result in lower-energy particles and population of more complex states of higher excitation energies [91].

However, this segmentation of the GDR's width into different components does not directly translate to any quantitative predictions of the GDR's observable decay behavior. In particular, no predictions for the γ-decay behavior of the GDR and its evolution with excitation energy based on the microscopical picture are available to compare to the experimental data of this work. It is also unclear how the smooth evolution of the GDR's γ-decay behavior with energy observed for ^{140}Ce and ^{154}Sm could even be reproduced by microscopical models. Since the GDR is understood as a myriad of states resulting from chaotic mixing with complex np-nh configurations in the microscopical picture, naively one may either expect a fine structure or completely structureless, statistical chaos in its γ decay governed by the individual states' properties, but not in an obvious way the observed smooth evolution across the whole resonance.

The issue becomes more apparent when Eq. (2.93), which predicts the ES cross section of a GDR built from just three resonances, is considered once again. Its derivation is solely based on the optical theorem and the dispersion relation [90] as well as the well-known angular distributions of Thomson and elastic electric dipole scattering on nuclei with a ground-state spin $J_{GS} = 0$. The number and properties of the resonances forming the GDR only enter as a summation over their forward ES amplitudes given by Eq. (2.86), which solely assumes the individual resonances to be Lorentzians. Hence, by adapting its summation limits Eq. (2.93) should hold for the countless states forming the GDR in the microscopical picture as well. It is, however, not intuitive how

---

[3]The symbol $\Gamma^{\downarrow\uparrow}$ is sometimes used in the literature to refer to this part of the spreading width $\Gamma^\downarrow$ [12].

the intricate interference of their ES amplitudes following Eq. (2.94) may reproduce the GDR's ES data simultaneously with its photoabsorption cross section, as achieved by the simple geometrical model of the GDR assuming three broad Lorentzians.

In conclusion, no current microscopic theory of the GDR is capable of reproducing the GDR's γ-decay behavior as observed in this work. Achieving this will undoubtedly require significant and challenging theoretical efforts. Such efforts are currently underway [169] and the findings of this work may provide valuable input for these developments.

6.4. Implications on the structure and the lifetime of the giant dipole resonance

Referring to the width of the GDR is commonly understood as referring to the width of its photoabsorption cross-section distribution. For isolated resonances, this distribution width is also the natural width, which is directly related to the decay behavior and lifetime of the resonance according to Eqs. (2.27), (2.30) and (2.31). For the GDR, however, it is not clear whether its distribution width is to be understood as its natural width as well. After all, microscopically the GDR is conceived as a myriad of states resulting from strong mixing of a collective 1p-1h state with np-nh configurations. In this picture, each of these states has its own natural width and may exhibit an individual decay behavior. Furthermore, the sum of their natural widths may be smaller than the observed distribution width of the GDR, as it may be dominated by the actual distribution of states over energy instead of their natural widths. In particular, Eq. (6.6) may yield this impression, since the spreading width $\Gamma^{\downarrow}$ is argued to be the dominant contribution to the GDR's width for heavy nuclei. It is mainly discussed as being due to a fragmentation of the GDR's strength over many states spread across a wider energy range, while the effect of this mixing on the individual states' natural widths is rarely elaborated on.

On the other hand, the geometrical model of the GDR assumes the GDR to consist of at most three sub-resonances. For spherical nuclei, the GDR is even pictured as a single resonance, whose photoabsorption cross section is described by the SLO model of Eq. (2.26). As shown in Section 2.9.1 the elastic NRF cross section of such a

single Lorentzian resonance has to meet[4] Eq. (2.88). Hence, if a single Lorentzian resonance, for which the distribution width is the natural width, is able to describe the GDR's photoabsorption cross section and its decay behavior, that is its elastic NRF cross section, simultaneously, this would be a strong argument for the GDR indeed being one coherent excitation mode.

Yet, this is exactly what was observed for the GDR of ^{140}Ce in this work, as discussed in Section 6.2.3. Both the photoabsorption cross section and the elastic NRF cross section of its GDR are indeed well described by assuming just a single Lorentzian resonance across the whole energy range of the GDR. Thus, this can be taken as strong circumstantial evidence that the observed width of the GDR of ^{140}Ce of $\Gamma = 4.71(10)$ MeV is its natural width after all and corresponds to its lifetime, yielding a value of $\tau = 0.1397(30)$ zs according to Eq. (2.31) for the latter. Consequently, the GDR of ^{140}Ce is expected to oscillate only 0.509(11) times on average before decaying when it was photoexcited at its resonance energy of $\hat{E} = 15.067(24)$ MeV, i.e., by absorption of a photon with a corresponding frequency of 3.643(6) ZHz and a wavelength of 82.29(13) fm.

It should be stressed, however, that a decay of the GDR with a lifetime corresponding to its width does not necessarily imply that particle emission from the nucleus must occur exclusively on this timescale after excitation of the GDR. The main contribution to the GDR's natural width may just be due to (unobservable) internal transitions of the broad GDR to other nuclear configurations at the same excitation energy but with longer lifetimes, which then decay exclusively by particle emission and are not directly excitable themselves by photoabsorption. In this scenario, only the γ decay (and potentially occurring direct particle decay) of the GDR may be expected to occur on the timescale set by the GDR's natural width and with the decay behavior observed here, while subsequent particle decay of the configurations otherwise populated by the GDR's internal decay may delay particle emission due to their longer lifetimes. This notion of internal transitions may offer a path to reconciliation between the geometrical and the microscopical view of the GDR, envisioning the photoexcited GDR as one coherent excitation mode that promptly decays either directly via γ or particle emission or through (unobservable) internal transitions to countless other configurations, which subsequently decay exclusively by particle emission.

---

[4]The interference with Thomson scattering and assumed spins of the ground state and the resonance are neglected here for simplicity.

Finally, while this work's data on the GDR of ^{140}Ce provides a novel, strong argument for the width of the GDR corresponding to its lifetime, only direct lifetime measurements can give a definitive answer. Such measurements are, however, very challenging due to the extremely short lifetimes expected and require significant advances in experimental techniques. Until they become feasible, questions regarding the GDR's lifetime will likely remain open. In particular, it is still completely unclear, what is to be expected for the GDR's lifetime in deformed nuclei, where the GDR splits into two or three sub-resonances with differing widths as observed for ^{154}Sm.

6.5. Constraints on nuclear shapes from γ decay of the giant dipole resonance

The study of nuclear deformation, nuclei deviating from a perfectly spherical form, is of fundamental interest [170, 171]. As already stated numerous times, the GDR is known to be sensitive to the nuclear deformation as it splits into two or three sub-resonances in deformed nuclei [12, 19]. The following demonstrates how the just confirmed geometrical model of the GDR, combined with the newly established experimental method for measuring its γ decay, offers a novel and powerful tool for studying nuclear shapes.

6.5.1. A brief overview on quadrupole deformation

The simplest and most common form of nuclear deformation is quadrupole deformation [172]. The surface and thus the shape of a quadrupole-deformed nucleus is commonly parameterized by [170, 172, 173]

$$R(\theta, \varphi) = R_0 \left(1 + \frac{1}{4} \sqrt{\frac{5}{\pi}} \beta \left(\cos \gamma \left(3 \cos^2 \theta - 1 \right) + \sqrt{3} \sin \gamma \sin^2 \theta \cos(2\varphi) \right) \right) \quad (6.7)$$

in its principal axes system using spherical coordinates (θ, φ). Here R_0 is the solid-angle mean radius, since

$$\frac{\iint_\Omega R(\theta, \varphi) \sin \theta \, d\theta \, d\varphi}{4\pi} = R_0 \quad (6.8)$$

holds for this average over the whole solid angle Ω, while β and γ are the quadrupole deformation parameter and the triaxiality angle, respectively. It should be noted that the volume of a nucleus

$$
\begin{aligned}
V &= \iint_\Omega \int_0^{R(\theta,\varphi)} r^2 \sin\theta \, dr \, d\theta \, d\varphi \\
&= \frac{4\pi}{3} R_0^3 \left(1 + \frac{3}{4\pi} \beta^2 + \frac{1}{28} \sqrt{\frac{5}{\pi^3}} \beta^3 \cos(3\gamma) \right)
\end{aligned}
\tag{6.9}
$$

depends on the deformation parameters in this parametrization.

The shape parametrization of Eq. (6.7) is directly obtained from the general expansion

$$
f(\theta,\varphi) = \sum_{\lambda=0}^{\infty} \sum_{\mu=-\lambda}^{\lambda} \alpha_{\lambda\mu} Y_{\lambda\mu}(\theta,\varphi)
\tag{6.10}
$$

of a complex-valued function $f(\theta,\varphi)$ defined in spherical coordinates, i.e., on the surface of a sphere, in terms of spherical harmonics $Y_{\lambda\mu}(\theta,\varphi)$ with complex-valued expansion coefficients $\alpha_{\lambda\mu}$ by the coefficient set [170, 172]

$$
\alpha_{\lambda\mu} = R_0 \cdot \begin{cases}
\sqrt{4\pi} & \text{for } \lambda = 0 \text{ and } \mu = 0 \\
\beta \cos\gamma & \text{for } \lambda = 2 \text{ and } \mu = 0 \\
\frac{1}{\sqrt{2}} \beta \sin\gamma & \text{for } \lambda = 2 \text{ and } \mu \in \{-2, 2\} \\
0 & \text{otherwise}
\end{cases}
\tag{6.11}
$$

explaining the name quadrupole deformation of otherwise spherical nuclei.

By limiting the deformation parameters to $\beta \geq 0$ and $0 \leq \gamma \leq 60°$ any set of the two parameters[5] corresponds to a unique nuclear shape [172] since

$$
\underbrace{R(0°,\varphi)}_{R_1} \geq \underbrace{R(90°,0°)}_{R_2} \geq \underbrace{R(90°,90°)}_{R_3}
\tag{6.12}
$$

holds in this case for the half-lengths of the principal axes and thus no two distinct parameter sets can yield shapes equivalent under rotation. For $\beta > 0$ and $\gamma = 0°$ the

---

[5]Expect for the obvious case of $\beta = 0$ where γ is irrelevant and the nucleus is spherical.

nucleus is prolate, meaning it is axially symmetric with one principal axis elongated. Here, its symmetry axis is the z-axis and the half-length R_1 along this axis is the longest. An oblate nucleus, characterized by axial symmetry with one shorter axis, is obtained with $\beta > 0$ and $\gamma = 60°$, where the third axis along the y-axis is this short symmetry axis here with half-length R_3. Finally, for $\beta > 0$ and $0 < \gamma < 60°$ the nucleus is triaxial, lacking axial symmetry with all three principal axes having different lengths. The relation

$$R_k = R_0 \left(1 + \sqrt{\frac{5}{4\pi}} \beta \cos\left(\gamma - \frac{2\pi}{3}(k-1) \right) \right) \tag{6.13}$$

for $k \in \{1, 2, 3\}$ allows to compactly express the three principal axes' half-lengths [31, 172], sorted by their lengths $R_1 \geq R_2 \geq R_3$ for $\beta \geq 0$ and $0 \leq \gamma \leq 60°$. These three half-lengths fully determine the shape of a quadrupole-deformed nucleus according to Eq. (6.7) since the relations

$$R_0 = \frac{1}{3}(R_1 + R_2 + R_3), \tag{6.14}$$

$$\beta = 4\sqrt{\frac{\pi}{5}} \frac{\sqrt{(R_1 - R_2)(R_1 - R_3) + (R_2 - R_3)^2}}{R_1 + R_2 + R_3}, \tag{6.15}$$

and

$$\gamma = \tan^{-1}\left(\frac{\sqrt{3}}{2} \left(\frac{R_1 - R_3}{R_2 - R_3} - \frac{1}{2} \right)^{-1} \right) \tag{6.16}$$

hold. Thus, measuring these three lengths of a quadrupole-deformed nucleus allows to directly determine its deformation parameters β and γ and thus its shape. This, however, is not trivial, as the lengths of the principal axes of a nucleus are not directly observable.

6.5.2. Relationship between the giant dipole resonance and nuclear shape

Yet, the GDR is known to be sensitive to the nuclear deformation as it splits into two or three sub-resonances in deformed nuclei. Indeed, the geometrical model of the GDR, which assumes the nucleus to be a macroscopical drop of proton and

neutron fluids and identifies the GDR as a collective isovector dipole oscillation of these two fluids against each other, allows to directly relate the resonance energies of these sub-resonances to the lengths of the principal axes of the nucleus, and thus to its deformation parameters. When assuming that this hydrodynamic oscillation of proton and neutron densities $\rho_p(\vec{r}, t)$ and $\rho_n(\vec{r}, t)$ neither changes the shape of the nucleus $R(\theta, \varphi)$ nor the constant overall nucleon density $\rho_p(\vec{r}, t) + \rho_n(\vec{r}, t)$, which is a reasonable assumption since nuclear matter is virtually incompressible, the resonance frequency

$$\widehat{f} = \frac{2.08\,u}{2\pi\,R} \tag{6.17}$$

of the GDR is found to be directly related to the nuclear radius R in a spherical nucleus via the constant propagation velocity of the nucleon density oscillation u [26–28]. By furthermore assuming that the restoring force of the dipole oscillation is the same causing the asymmetry term $a_A \frac{(N-Z)^2}{N+Z}$ in the Bethe-Weizsäcker semi-empirical mass formula, the propagation velocity u of the density oscillation can be estimated as [26–28]

$$u = \sqrt{\frac{8a_A}{m_N} \frac{NZ}{(N+Z)^2}} \overset{\text{for } ^{154}\text{Sm}}{\approx} 0.217c, \tag{6.18}$$

where $a_A \approx 22.97(19)\,\text{MeV}$ [174] is the asymmetry coefficient of the semi-empirical mass formula, m_N is the average nucleon mass and N and Z are the number of neutrons and protons of the nucleus, respectively. Hence, the resonance energy $\widehat{E}$ of the GDR is given by

$$\widehat{E} = \frac{2.08\,\hbar u}{R} \tag{6.19}$$

in this model, according to the energies of photons which are able to excite this dipole oscillation resonantly through their electromagnetic field oscillating with the frequency $\widehat{f}$. Assuming that the relation holds for all nuclear shapes, each sub-resonance energy $\widehat{E}_k$ of the GDR oscillating along the k-th principal nuclear axis can be directly related via

$$\widehat{E}_k = \frac{2.08\,\hbar u}{R_k} = \frac{2.08\,\hbar u}{R_0 \left(1 + \sqrt{\frac{5}{4\pi}}\,\beta \cos\left(\gamma - \frac{2\pi}{3}(k-1)\right) \right)} \tag{6.20}$$

to the respective axis' half-length R_k and thus to the deformation parameters β and γ using Eq. (6.13). This does not only allow to easily explain the splitting of the GDR in

deformed nuclei quantitatively, but also to directly determine the shape parameters of a nucleus from its GDR's sub-resonance energies according to the relations

$$R_0 = \frac{2.08\hbar u}{3}\left(\frac{1}{\widehat{E}_1} + \frac{1}{\widehat{E}_2} + \frac{1}{\widehat{E}_3}\right),$$ (6.21)

$$\beta = 4\sqrt{\frac{\pi}{5}}\frac{\sqrt{(\frac{1}{\widehat{E}_1} - \frac{1}{\widehat{E}_2})(\frac{1}{\widehat{E}_1} - \frac{1}{\widehat{E}_3}) + (\frac{1}{\widehat{E}_2} - \frac{1}{\widehat{E}_3})^2}}{\frac{1}{\widehat{E}_1} + \frac{1}{\widehat{E}_2} + \frac{1}{\widehat{E}_3}},$$ (6.22)

and

$$\gamma = \tan^{-1}\left(\frac{\sqrt{3}}{2}\left(\frac{\frac{1}{\widehat{E}_1} - \frac{1}{\widehat{E}_3}}{\frac{1}{\widehat{E}_2} - \frac{1}{\widehat{E}_3}} - \frac{1}{2}\right)^{-1}\right),$$ (6.23)

which are easily obtained by combining Eq. (6.20) with Eqs. (6.14) to (6.16). While for a determination of the solid-angle mean radius R_0 the propagation velocity of the density oscillation u has to be estimated according to Eq. (6.18), it is irrelevant for an extraction of the deformation parameters β and γ as it cancels out in their relations to the sub-resonance energies $\widehat{E}_k$.

6.5.3. Extraction of shape parameters from the Bayesian inference fits for ^{140}Ce and ^{154}Sm

Consequently, the fits of the geometrical model via its SLO parameters to the GDRs of ^{140}Ce and ^{154}Sm, discussed in Section 6.2, also yield information on the nuclear shapes of these nuclei. By calculating the shape parameters through Eqs. (6.21) to (6.23) for each of the 32 000 sets of the sub-resonance energies $\widehat{E}_k$ sampled in the MCMC Bayesian inference fits, samples and thus posterior distributions for these parameters are obtained for every fit. The posterior distributions are shown in Fig. 6.5.

For ^{154}Sm, both the fit considering simultaneously the photoneutron and γ-decay data on its GDR and the fit considering solely the former data set, agree overall well on the values of the mean nuclear radius R_0 and the quadrupole deformation parameter β within their uncertainties. The simultaneous fit using both data sets, however, yields more constrained distributions for both parameters with slightly shifted medians. For the triaxiality angle γ, this difference in sensitivity is much more pronounced.
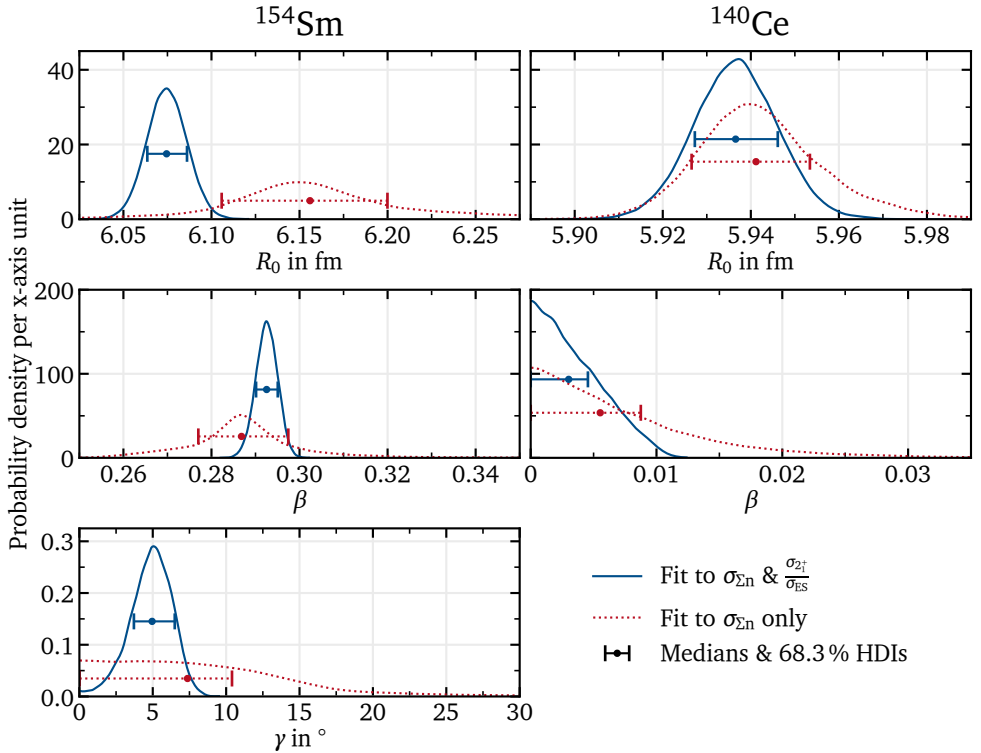
Figure 6.5.: Posterior distributions of the shape parameters of ^{154}Sm (left) and ^{140}Ce (right) obtained from the Bayesian inference fits of the geometrical model to their GDRs shown in Figs. 6.1 and 6.2, respectively. Fitting simultaneously both the respective GDR's photoneutron data and its branching ratio of 2_1^+ Raman to ES yields significantly more constrained posterior distributions of the shape parameters (solid blue) than fitting only the photoneutron data (dotted red). In particular, the triaxiality angle γ of ^{154}Sm (bottom left) is constrained by its simultaneous fit, while the fit considering solely its GDR's photoneutron data yields only a weak upper limit from a rather flat posterior distribution. Since for ^{140}Ce an axially symmetric nuclear shape was assumed for its fits, the triaxiality angle was fixed to $\gamma = 0°$ and thus not fitted. The uncertainty bars illustrate the medians and 68.3 % HDIs of the posterior distributions.

The fit considering solely the photoneutron data results in a rather flat, featureless posterior distribution for γ yielding only a 99.7 % credible upper limit of 28.6°. Fitting in addition the new γ-decay data, however, yields an almost Gaussian distribution for γ centered around 5° with a significantly lower 99.7 % credible upper limit of 8.3°.

For ^{140}Ce, the situation is similar. Both performed fits agree in their results on the mean nuclear radius R_0 and the quadrupole deformation parameter β, but the simultaneous fit provides more constrained posterior distributions for both parameters. This is especially the case for the quadrupole deformation parameter, for which both fits yield almost exponential posterior distributions favoring $\beta = 0$, i.e. a spherical nuclear shape, but considerably different 99.7 % credible upper limits for the quadrupole deformation parameter of 0.0365 and 0.0109 for the fit considering solely the photoneutron data and the simultaneous fit, respectively. Since ^{140}Ce was fitted assuming prolate axial symmetry, the triaxiality angle was fixed to $\gamma = 0°$ and was thus not determined in the fits. For the simultaneous fit to ^{140}Ce, however, it has to be once again stressed that it is up for debate whether the geometrical model's prediction for the GDR's 2_1^+ Raman scattering cross section used by this fit is applicable to spherical nuclei in the first place as discussed in Section 6.2.3.

6.5.4. Comparison to results from other approaches

Furthermore, one may question the reliability of these results in general, since multiple assumptions on the nature of the GDR's oscillation had to be made to relate its sub-resonance energies quantitatively to the shape parameters. Hence, a comparison to results obtained from other observables is appropriate to validate the here taken approach. Such a comparison is made in Table 6.2. It must be stressed that the given uncertainties for all values in Table 6.2 are purely based on experimental uncertainties and do not take into account systematic uncertainties from assumptions made in the models used for their determination, which are expected to be much larger. Hence, comparisons of the results between different approaches made in the following do not consider the given, certainly underestimated uncertainties.

First of all, the results of the geometrical model GDR fits on the mean nuclear radius R_0 can be compared to experimental values on root-mean-square charge radii $\sqrt{\langle r^2 \rangle}$. Ref. [175] provides a compilation on $\sqrt{\langle r^2 \rangle}$ values taking into account measurements from elastic electron scattering, muonic atom X-rays, K_α isotope shifts, and optical

Table 6.2.: Comparison of shape parameters of ^{140}Ce and ^{154}Sm obtained from different approaches.

Nucleus	Approach	R_0 in fm	β	γ in °
^{154}Sm	GDR $\sigma_{\Sigma n}$ and $\dfrac{\sigma_{2_1^+}}{\sigma_{ES}}$	6.075(12)	0.2925(25)	5.0(15)
	GDR $\sigma_{\Sigma n}$ only	6.156(50)	0.287(11)	$7.4^{+3.0}_{-7.4}$
	$\sqrt{\langle r^2 \rangle}$ measurements [175]	6.599(7)		
	$R_0 = 1.2\,\text{fm} \cdot A^{\frac{1}{3}}$	6.432		
	$Q(2_1^+)$ measurements [100]		0.306(6)	
	$B(E2; 0_1^+ \rightarrow 2_1^+)$ measurements [171]		0.3084(16)	
	Recommended β of Ref. [171]		0.3404(17)	
	Monte Carlo Shell Model [176, 177]		≈0.28	≈3.7
^{140}Ce	GDR $\sigma_{\Sigma n}$ and $\dfrac{\sigma_{2_1^+}}{\sigma_{ES}}$	5.9365(96)	≤0.0030(15)	
	GDR $\sigma_{\Sigma n}$	5.941(15)	≤0.0055(32)	
	$\sqrt{\langle r^2 \rangle}$ measurements [175]	6.2962(22)		
	$R_0 = 1.2\,\text{fm} \cdot A^{\frac{1}{3}}$	6.231		
	$B(E2; 0_1^+ \rightarrow 2_1^+)$ measurements [171]		0.0983(24)	
	Recommended β of Ref. [171]		0.1018(25)	

isotope shifts. The $\sqrt{\langle r^2 \rangle}$ values it lists for ^{140}Ce and ^{154}Sm were converted according to [178, p. 49]

$$R_0 = \sqrt{\frac{5}{3}} \sqrt{\langle r^2 \rangle} \tag{6.24}$$

for a direct comparison in Table 6.2 to the mean nuclear radius R_0 obtained from the GDR fits. It is found that the values based on the geometrical model of the GDR are in good agreement with the experimental values from Ref. [175]. For ^{154}Sm the two approaches deviate in their results by 8.6 % or less, while for ^{140}Ce the differences are 6.1 % or less. Considering the simplicity of the model used to obtain the R_0 values from the GDR data, this agreement is remarkable, in particular since to determine R_0, unlike for the deformation parameters β and γ, the propagation velocity of the density oscillation u had to be estimated as well.

Secondly, the here determined quadrupole deformation parameters β can be compared to values obtained from experimental $B(E2; 0_1^+ \rightarrow 2_1^+)$ transition strengths and spectroscopic quadrupole moments of the 2_1^+ state $Q_{\text{Spec}}(2_1^+)$. Both can be related to the intrinsic quadrupole moment Q_0 of the nucleus via [173, Eqs. (6.16) and (6.18)]

$$Q_{\text{Spec}}(2_1^+) = -\frac{2}{7} Q_0 \tag{6.25}$$

and

$$B(E2; 0_1^+ \rightarrow 2_1^+) = \frac{5}{16\pi} e^2 Q_0^2, \tag{6.26}$$

which itself is related to the quadrupole deformation parameter β through the relation [179, Table I]

$$Q_0 = \frac{3}{\sqrt{5\pi}} Z R_0^2 \Big(\beta + \underbrace{\frac{1}{8} \sqrt{\frac{5}{\pi}}}_{\approx 0.16} \beta^2 \Big) \tag{6.27}$$

yielding

$$\beta = 4 \sqrt{\frac{\pi}{5}} \left(\sqrt{1 + \frac{5}{6} \frac{Q_0}{Z R_0^2}} - 1 \right), \tag{6.28}$$

where Z is the atomic number of the nucleus.

The data compilation of Ref. [171] provides recommended $B(E2; 0^+_1 \to 2^+_1)$ values of 0.300(15) and 4.345(44) $e^2\,\mathrm{b}^2$ for ^{140}Ce and ^{154}Sm, respectively, while a $Q_{\mathrm{Spec}}(2^+_1)$ value of $-1.87(4)$ b for ^{154}Sm is given in Ref. [100]. These experimental values were used to calculate the β values given for comparison in Table 6.2, using the already discussed root-mean-square charge radii of Ref. [175] for the additionally required mean nuclear radius R_0. Furthermore, Ref. [171] also directly provides recommended β values based on the $B(E2; 0^+_1 \to 2^+_1)$ values in tabulated form, which are also listed in Table 6.2 for comparison. For their calculation, however, only the leading order of the Q_0-to-β relation of Eq. (6.27) as well as the approximation $R_0 = 1.2\,\mathrm{fm} \cdot A^{\frac{1}{3}}$ for the mean nuclear radius were used, which causes significant overestimation of the β values for ^{154}Sm. Using the full relation and experimental mean nuclear radii instead, the β values for ^{154}Sm obtained from both the $B(E2; 0^+_1 \to 2^+_1)$ value and the $Q_{\mathrm{Spec}}(2^+_1)$ value are in good agreement with the values obtained from the GDR fits for ^{154}Sm. Both approaches, yield deviations of less than 6 % to the β value of 0.2925(25) obtained from the simultaneous fit to the photoabsorption and γ-decay data of the GDR of ^{154}Sm.

For ^{140}Ce, the β values obtained from the $B(E2; 0^+_1 \to 2^+_1)$ value and the GDR fits deviate significantly. The latter claim ^{140}Ce to be virtually spherical, while the former suggests a slightly prolate shape. In this case, however, it is likely that the $B(E2; 0^+_1 \to 2^+_1)$ value is not a good indicator for the nuclear shape of ^{140}Ce. ^{140}Ce is a semi-magical nucleus for which one would expect a spherical shape. The relation between β and the $B(E2; 0^+_1 \to 2^+_1)$ transition strength, however, assumes a rigidly deformed nucleus and the 2^+_1 state to be a purely rotational state, which is certainly not the case for ^{140}Ce. Thus, in this case, the β value obtained from the GDR data is likely the more reliable value.

6.5.5. Conclusion on the sensitivity of the giant dipole resonance on nuclear shape

In summary, considering the overall good agreement of the results obtained on the nuclear shapes of ^{140}Ce and ^{154}Sm from the geometrical model of the GDR with those from other approaches and observables, the sensitivity and reliability of the GDR as a probe for nuclear shapes is validated. Thus, the high sensitivity of the γ decay of the GDR on its structure, already established in Section 6.2.3, carries over

to a high sensitivity of this observable on the nuclear shape as well. In particular, the data on ^{154}Sm establishes γ decay of the GDR as a novel probe to otherwise hard-to-constrain triaxiality of deformed nuclei. Without considering this work's γ-decay data it was impossible to place any sizeable constraints on the triaxiality angle γ of ^{154}Sm from its GDR's photoneutron data alone. The simultaneous fit to both data sets, however, is able to constrain the triaxiality of ^{154}Sm to a small, finite value of $\gamma = 5.0(15)°$. This result along with the obtained value of 0.2925(25) for the quadrupole deformation parameter β of ^{154}Sm are furthermore found to match well with most-recent state-of-the-art configuration interaction calculations in the Monte Carlo Shell Model, which predict $\beta \approx 0.28$ and $\gamma \approx 3.7°$ for the ground-state deformation of ^{154}Sm [176, 177]. Thus, this finding contributes to the contemporary debate on nuclear triaxial shapes [31, 176, 177, 180–185].

7. Summary and outlook

The present work has focused on the experimental investigation of γ decay of the isovector giant dipole resonance (GDR) [12], a key property of a fundamental collective nuclear excitation, which had remained poorly characterized despite decades of research on the GDR. To address this long-standing issue and overcome the limitations of the few previous experiments [37–42], a novel experimental method to systematically study γ decay of the GDR has been developed, which combines the well-established nuclear resonance fluorescence (NRF) technique with state-of-the-art laser-Compton back-scattering (LCB) photon sources. The devised approach was then successfully applied in a pilot experiment on the GDRs of the semi-magical, spherical nucleus ^{140}Ce and the well-deformed ^{154}Sm at the High Intensity γ-ray Source (HIγS).

The key technological innovation of this work lies in the selective and efficient photoexcitation of the GDR using intense, energy-tunable, fully polarized, and quasi-monochromatic photon beams available through LCB photon sources such as HIγS. This enabled the measurement of γ decay of the GDR in the induced NRF reactions with high resolution and statistics in narrow, freely selectable energy regions. Usage of linearly polarized beams, in particular, allowed for the disentanglement of γ decays of the GDR from 2_1^+ Raman and elastic scattering (ES) for the deformed ^{154}Sm, based on the in this case distinct angular distributions of these scattering processes.

Data was taken at six excitation energies, covering the full evolution of the GDRs of these nuclei. Thus, for the first time the evolution of the γ-decay branching ratio of 2_1^+ Raman to ES was studied for a deformed nucleus. Furthermore, photoactivation measurements performed simultaneously to the NRF measurements allowed for the determination of absolute cross sections of the GDR's γ-scattering processes.

For both ^{140}Ce and ^{154}Sm a smooth evolution of the γ-decay behavior of their GDRs with energy was observed. The determined γ-decay branching ratios of the order of

1 % are in agreement with previous measurements on the GDRs of heavy nuclei [35–42]. In the case of ^{140}Ce, no 2^+_1 Raman scattering on its GDR was detected, placing stringent upper limits on the cross section of this process. Conversely, for the deformed ^{154}Sm, significant γ decay of its double-humped GDR to its 2^+_1 state was found, with the 2^+_1 Raman-scattering cross section showing a notable energy dependence. For both nuclei, significant γ-decay channels of their GDRs to states other than their 2^+_1 or 0^+_1 states were not observed in the present data.

This novel experimental data set provides new unique insights into the structure of the GDR and the shapes of the studied nuclei.

The found superb agreement between the experimental results and the predictions by the geometrical model of the GDR confirm the applicability of the latter even for the γ-decay behavior of the GDR. Its high descriptive power simultaneously on the GDR's photoabsorption, ES, and 2^+_1 Raman-scattering cross sections, constitutes a compelling argument for the model's validity including its picture of the GDR as one coherent excitation whose lifetime may indeed be directly reciprocal to its width.

At the same time, γ decay is established as a highly sensitive experimental probe of the GDR's structure, capable of resolving details not accessible from photoabsorption data alone. Using the just confirmed geometrical model of the GDR, this sensitivity of the new γ-decay data was exploited to place strong constraints on the nuclear shape of ^{154}Sm, including the otherwise hard-to-constrain degree of triaxiality of contemporary interest [31, 176, 180–185]. The approach is validated by its results being in good agreement with shape parameters derived from other experimental observables as well as recent Monte Carlo Shell-Model calculations [176, 177]. Thus γ decay of the GDR is also demonstrated as a powerful tool for the study of nuclear deformation. By providing stringent constraints on nuclear shape, this method can complement other experimental approaches, enable tests of theoretical models and ultimately contribute to a more comprehensive understanding of nuclear structure, particularly in axially deformed and triaxial nuclei.

While for ^{154}Sm a non-zero, but still only small triaxiality of $\gamma = 5.0(15)°$ was found, it is now of interest to investigate nuclei with larger predicted triaxialities through this new approach, such as ^{166}Er [176], ^{164}Dy [177] and ^{188}Os [186]. Likewise, nuclei in the vicinity of the spherical-to-deformed shape phase transition [187, 188], such as ^{152}Sm and ^{150}Nd [189, 190], merit experimental attention. For these non-rigid nuclei [191, 192], it will be interesting to study how their GDRs' γ decay will behave

under the expected softening of the nuclear deformation in the vicinity of the phase transition.

Additionally, the γ-decay behavior of the GDRs of ^{152}Sm and ^{150}Nd merit experiments for a completely different reason. Recent remeasurements [166] of their photoabsorption data have questioned not only the prior existing data [21, 193], but also the presumed splitting of the GDRs of these nuclei altogether. Investigating the γ-decay behavior of their GDRs as a yet untapped, independent observable highly sensitive to the structure of the resonance could provide new insights to these cases of disputed GDR structure.

For these reasons, a corresponding experiment on ^{152}Sm has recently been proposed and accepted for beam time at the HIγS facility. Additionally, experiments on ^{232}Th, ^{208}Pb, and ^{164}Dy have already been conducted at HIγS, with the data currently awaiting analysis. The results for ^{164}Dy are expected to offer valuable insights into the triaxiality of this nucleus of current interest [177], while the data on ^{232}Th and ^{208}Pb extends the research on the γ decay of the GDR into an entirely new region of the nuclear chart, namely the actinide region. Thus, it can already be stated that this work has initiated a new campaign on GDR research, aimed at enhancing our knowledge and understanding of the GDR, nuclear deformation, and nuclear structure in general.

To this end, however, also further development of the microscopic theory of the GDR is now necessary. While the macroscopic, geometrical model has proven remarkably successful in describing this work's experimental data, the same cannot be said for the microscopic model of the GDR. At present no microscopical calculation is capable of describing the observed γ-decay behavior of the GDR. Addressing this gap will undoubtedly require significant theoretical efforts for which the findings of this work provide valuable benchmark data. Until then, the geometrical model remains the best available tool for describing the GDR's γ decay, and open questions about the true microscopic structure of the GDR, its lifetime, and the relation of its microscopical and macroscopical picture remain to be addressed by future research.

A. Spectra

The following pages present the spectra from all measurements performed on ^{140}Ce, ^{154}Sm, ^{28}Si and ^{12}C in this work's experiment, along with the fits made to them as described in Section 4.6.3. Each figure displays the spectra of one measurement stated in its caption, with each of their panels showing the spectrum of one detector. For quick reference, the List of Figures in the front matter of this document can be consulted to locate a specific measurement's spectra. The azimuthal angle of each detector is indicated by a black symbol in the top-right corner of its panel, relative to the positions of the other detectors placed at approximately equal polar angles (marked by light gray symbols), and the beam polarization plane (indicated by a green double arrow). The measured spectra are shown in black, the fit performed simultaneously to all spectra of the measurement is shown in orange, and the individual components of the fit are depicted in various colors. Vertical dashed green lines indicate the beam energy at which the FEPs of ES on the GDRs of ^{140}Ce and ^{154}Sm are located. Vertical dotted green lines mark the expected positions of the FEPs of 2_1^+ Raman scattering on the GDRs of ^{140}Ce and ^{154}Sm.

The fit function $\vec{o}_M^{(d)}$ fitted to the experimental spectra $\vec{o}_{\exp}^{(d)}$ of all detectors d is given in the most general form by the sum

$$\vec{o}_M^{(d)} = \mathcal{R}_{\mathrm{ES}}^{(d)} \cdot \vec{y}_{\mathrm{ES}} + \mathcal{R}_{2_1^+}^{(d)} \cdot \vec{y}_{2_1^+} + \mathcal{R}_{\mathrm{ENRF}}^{(d)} \cdot \vec{y}_{\mathrm{ENRF}} + \mathcal{R}_{\mathrm{M1}}^{(d)} \cdot \vec{y}_{\mathrm{M1}} + \mathcal{R}_{\mathrm{Iso}}^{(d)} \cdot \vec{y}_{\mathrm{BG}}^{(d)} + o_{\mathrm{Noise}}^{(d)}, \quad \text{(A.1)}$$

where the $\mathcal{R}_f$ are the detector-response matrices, the $\vec{y}_f$ are the fitted binned spectra of photons emitted by the reaction/source f, and $o_{\mathrm{Noise}}^{(d)}$ is the quasi-constant background noise level in the spectrum of detector d. Almost all fits utilized only an appropriate subset of this generic model. For details, refer to Section 4.6.3. The specific model components used in the fit to a measurement's spectra can be identified in the respective figure's legend at its bottom. Their fitted spectra of emitted photons

$\vec{y}_f$ are also shown in the spectra panels of the figures, scaled by the FEP efficiency $\vec{\epsilon}_f^{\text{FEP}} = \text{diag}(\mathscr{R}_f)$ of the corresponding detector to detect photons emitted by the reaction/source f, including its angular distribution effects, and offset by its noise level $o_{\text{Noise}}^{(d)}$. Thus, they are displayed isolated on top of the noise as they would appear if only the detector's full-energy response were present, with all other detector response effects absent. This allows for a direct comparison with the experimental FEPs of the spectra and, as a by-product, also visualizes the fitted constant background noise level in the detectors' spectra through the shared baseline of these illustrations of the fitted emission spectra.

The peaks around 9.3 MeV visible in the spectra measured at photon beam energies of 11.37 and 11.45 MeV are attributed to (n,γ) reactions, as discussed in Section 4.3. An exception is the peak at 9.66 MeV, observed in the spectra taken on ^{28}Si, shown in Figs. A.23 and A.24. This peak is most clearly visible in the spectra of the LaBr$_3$ detectors L3 and L7 in Fig. A.23. It is due to the photoexcited 1^+ state of ^{28}Si at 11.4460(2) MeV [102] decaying, in addition to its prominent ground-state transition, via a previously unknown, weak branching transition to the 2_1^+ state of ^{28}Si at 1.779 03(1) MeV [102] in an inelastic NRF reaction. During data analysis, this branching transition's peak was mistakenly identified as a (n,γ) background peak. Its true origin was only discovered during the writing of this work, after the analysis had already been finalized. As a result, the peak was fitted as part of the background spectrum in the fits to the ^{28}Si spectra, instead of using a specific fit component and no branching ratio was determined from it in this work.
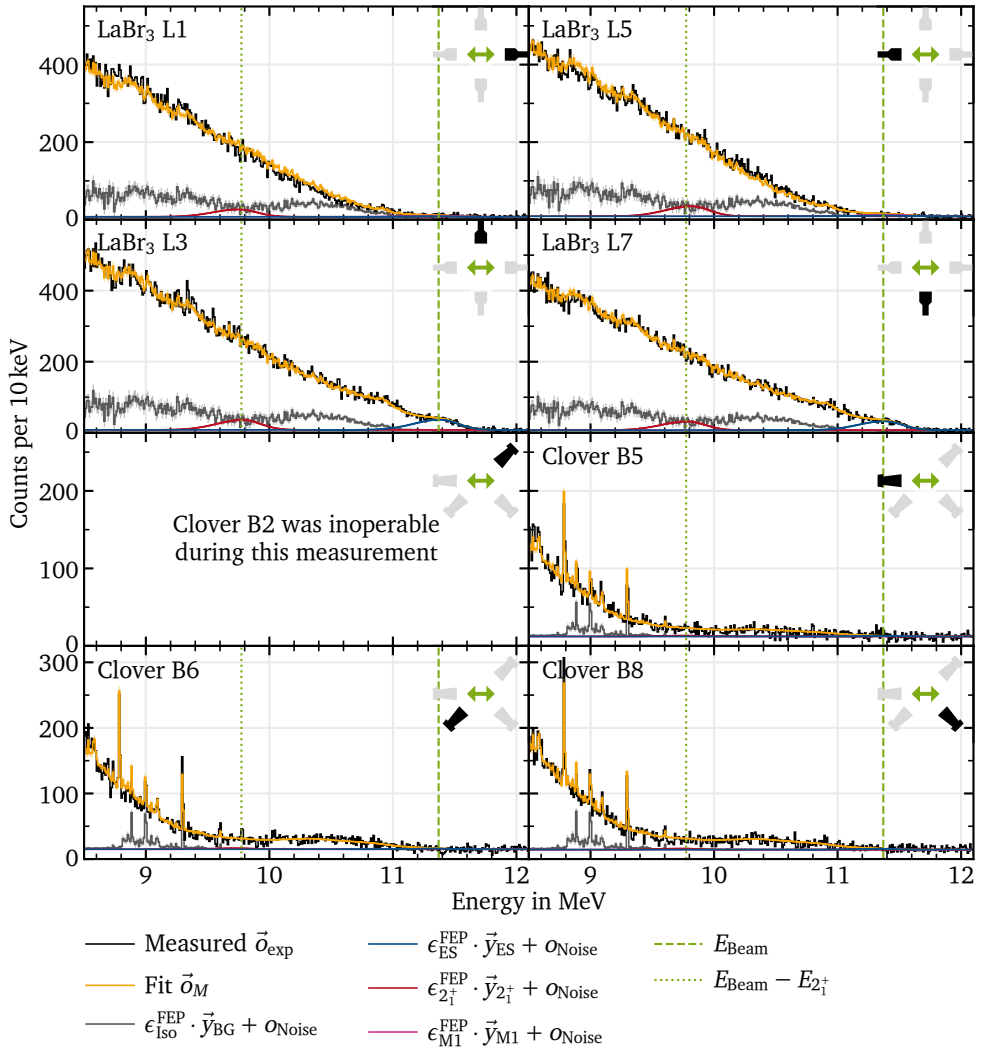
Figure A.1.: Spectra (black) taken during irradiation of ^{140}Ce by an 11.37 MeV linearly polarized photon beam along with simultaneous fit to all spectra (orange) and its components. See the remarks at the beginning of this chapter for details.
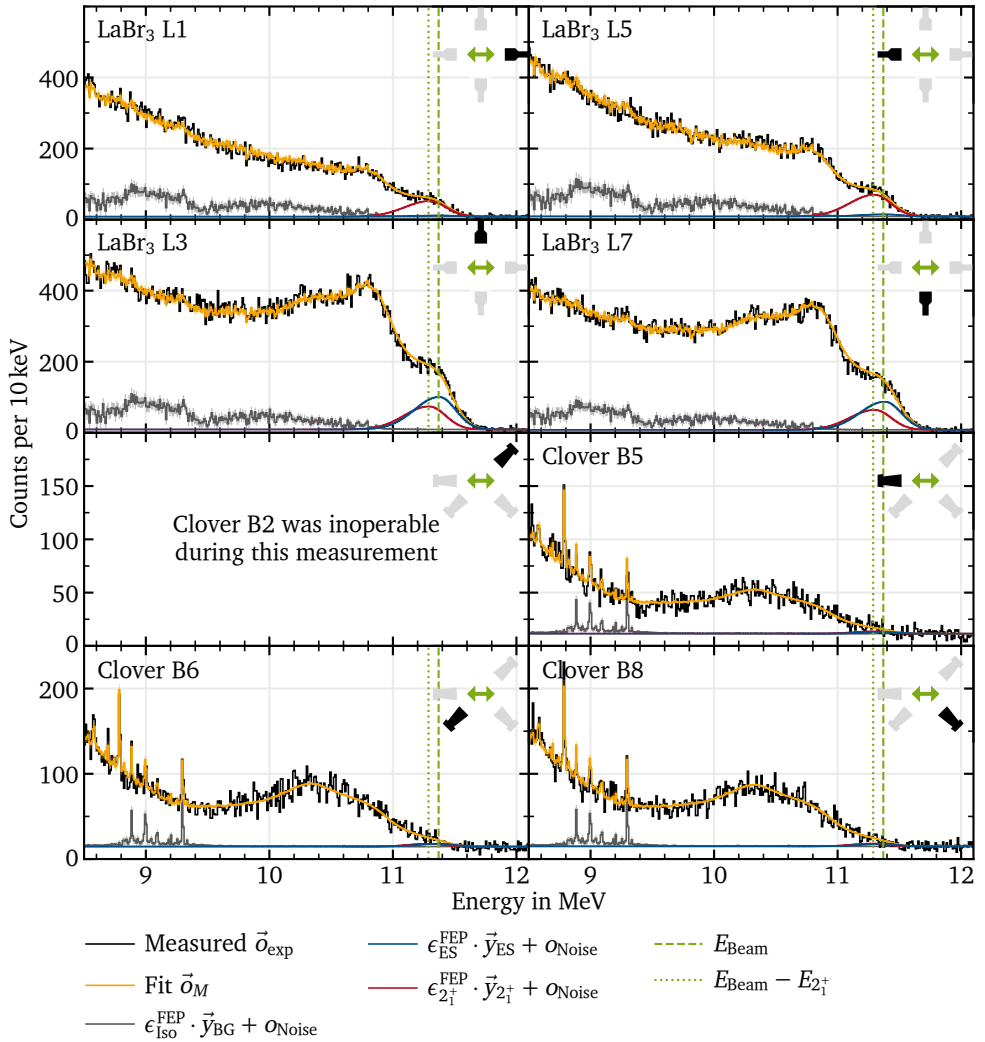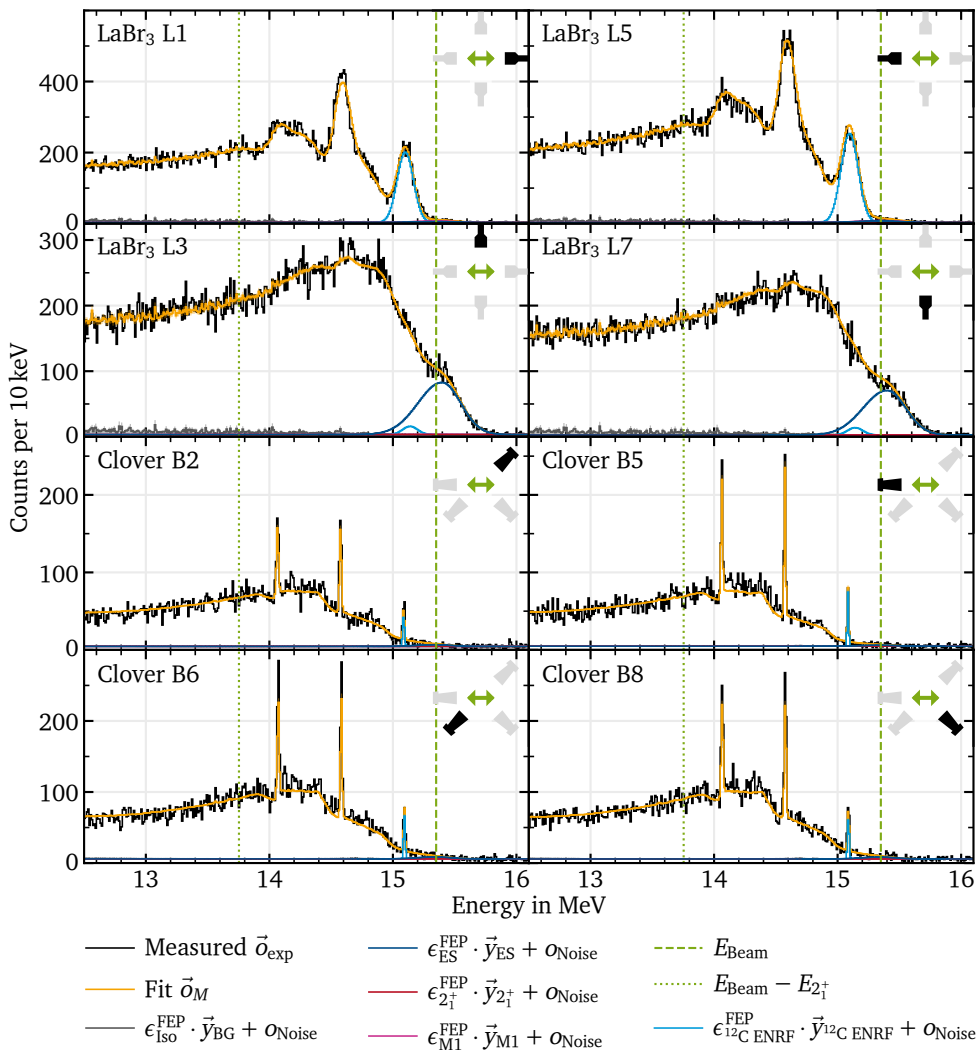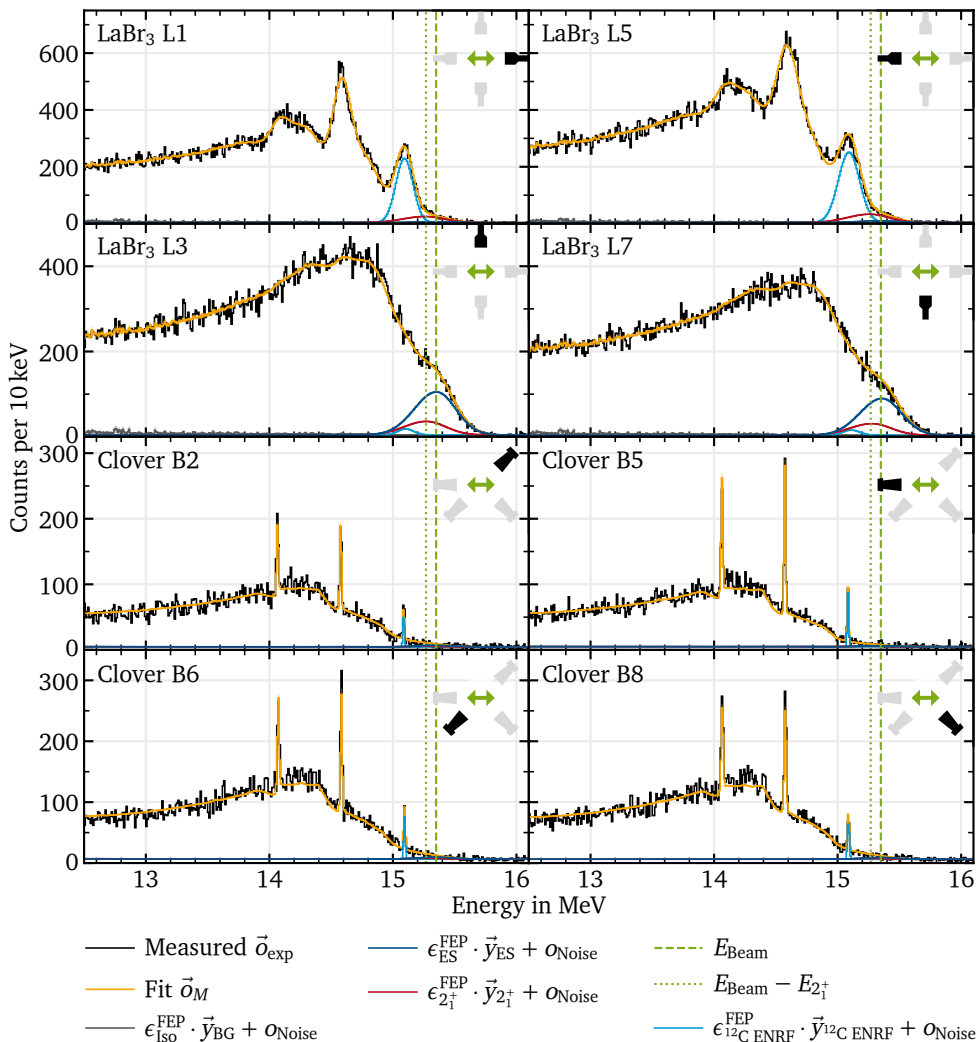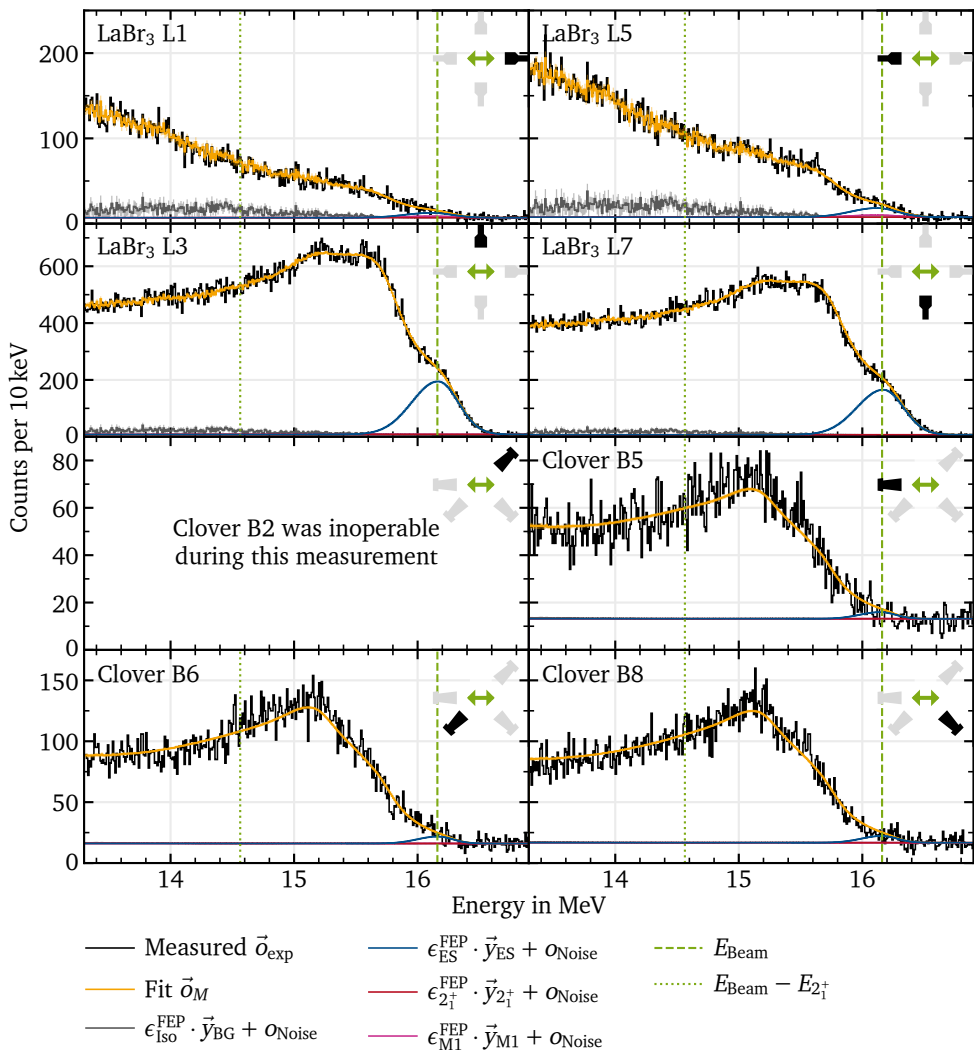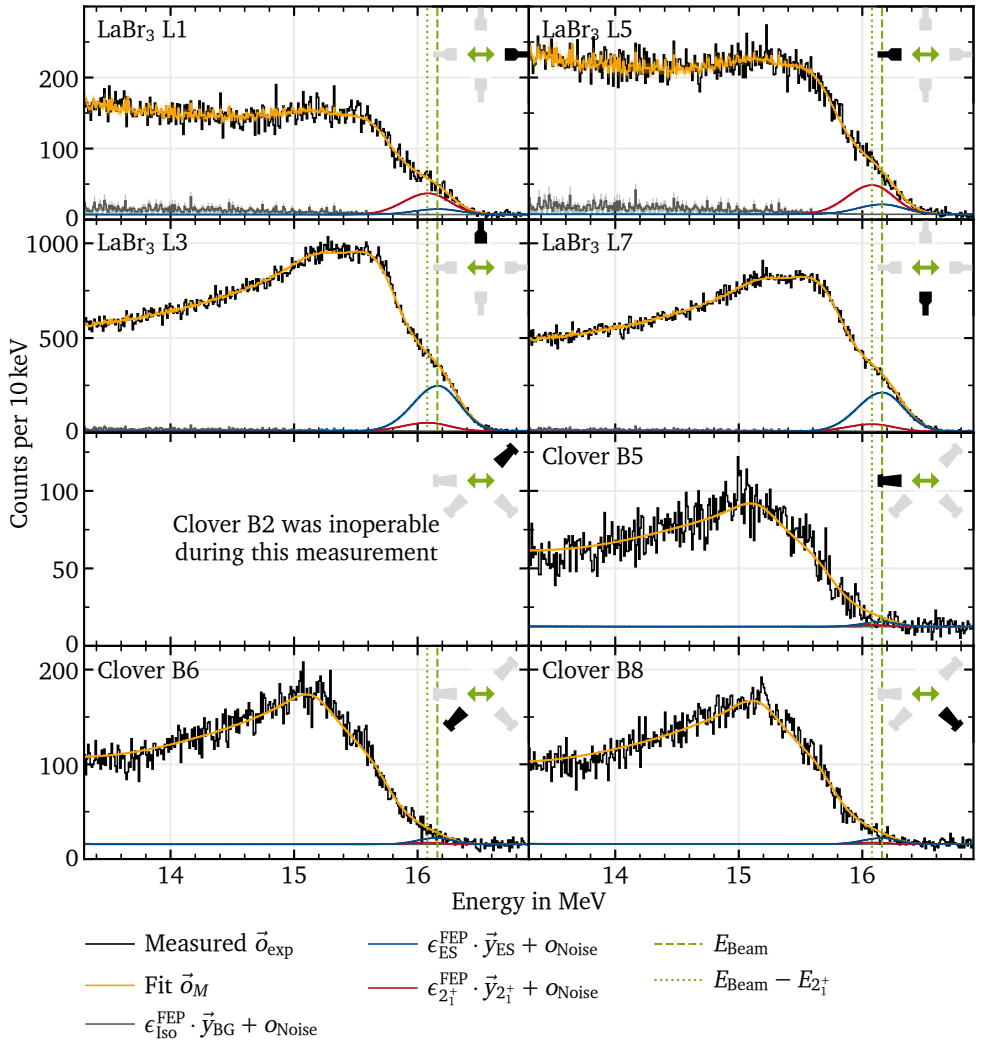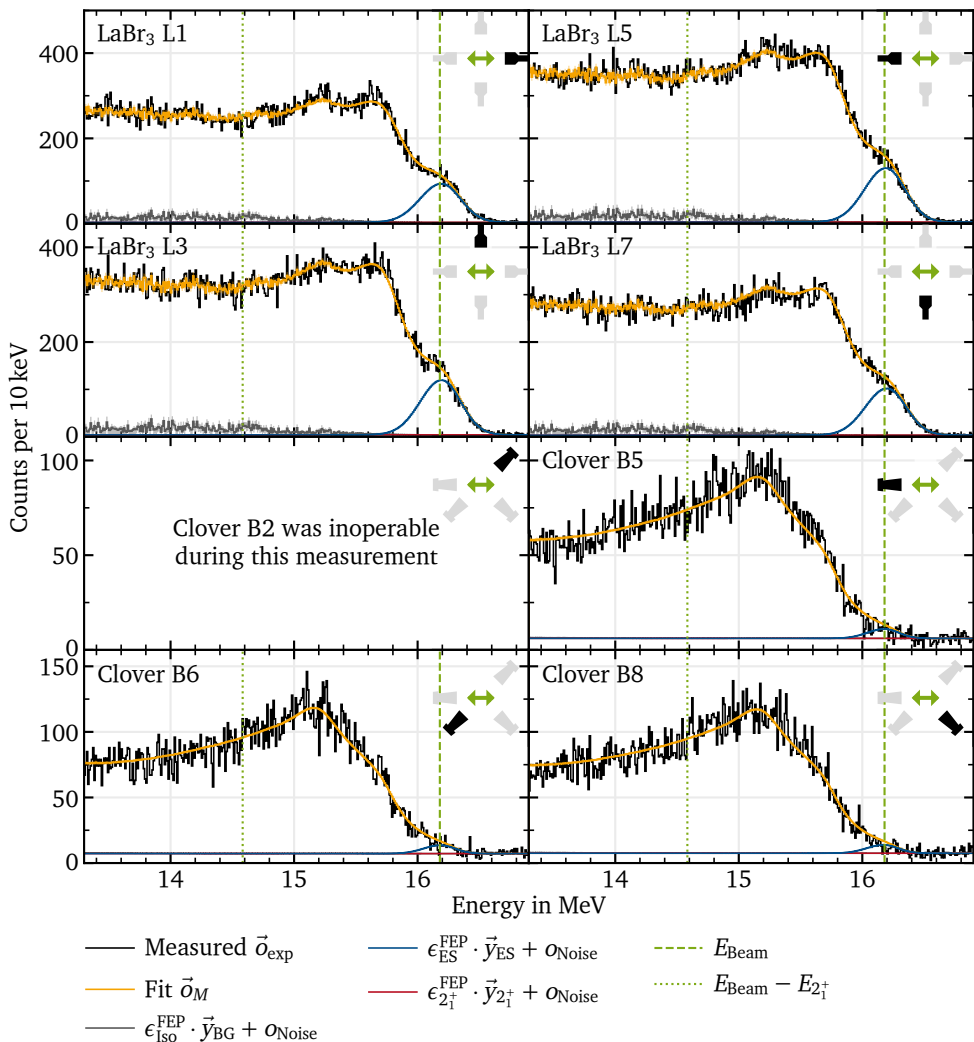
Figure A.2.: Spectra (black) taken during irradiation of ^{154}Sm by an 11.37 MeV linearly polarized photon beam along with simultaneous fit to all spectra (orange) and its components. See the remarks at the beginning of this chapter for details.
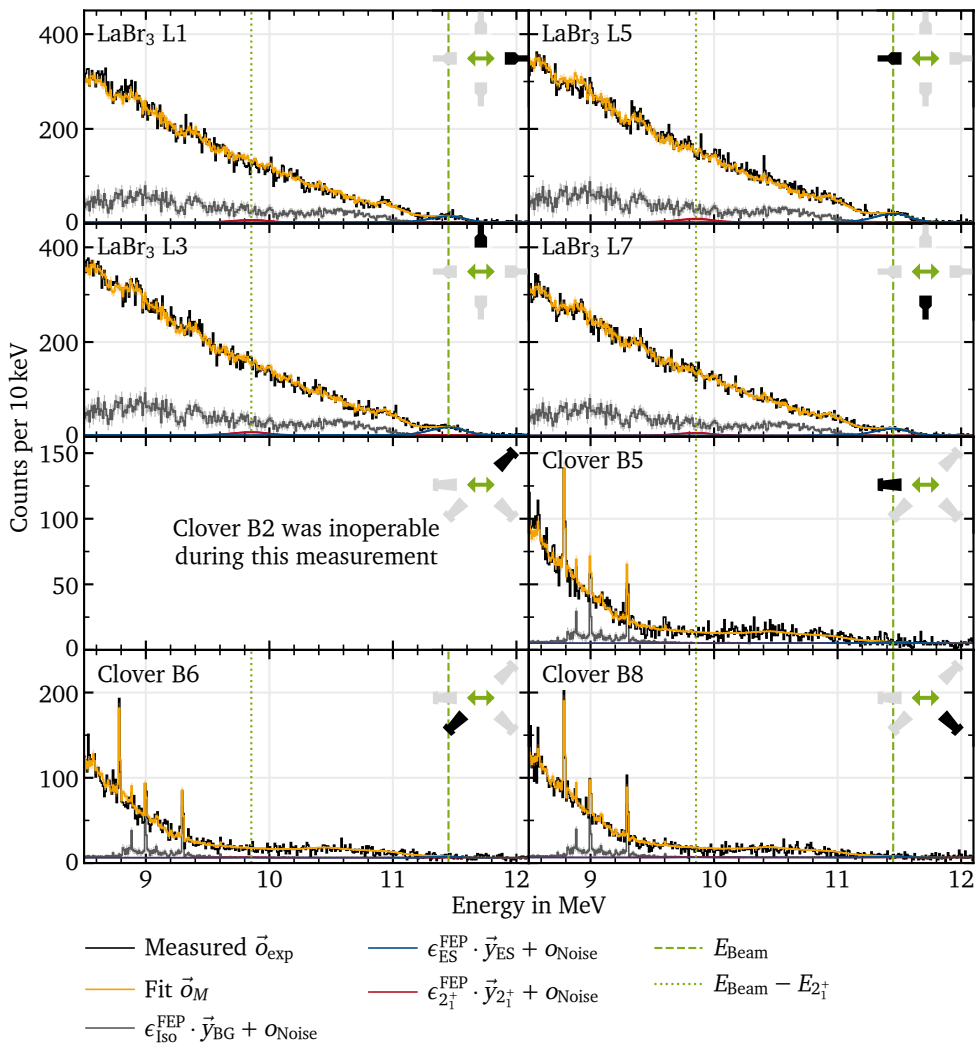
Figure A.3.: Spectra (black) taken during irradiation of ^{140}Ce by an 11.45 MeV circularly polarized photon beam along with simultaneous fit to all spectra (orange) and its components. See the remarks at the beginning of this chapter for details.
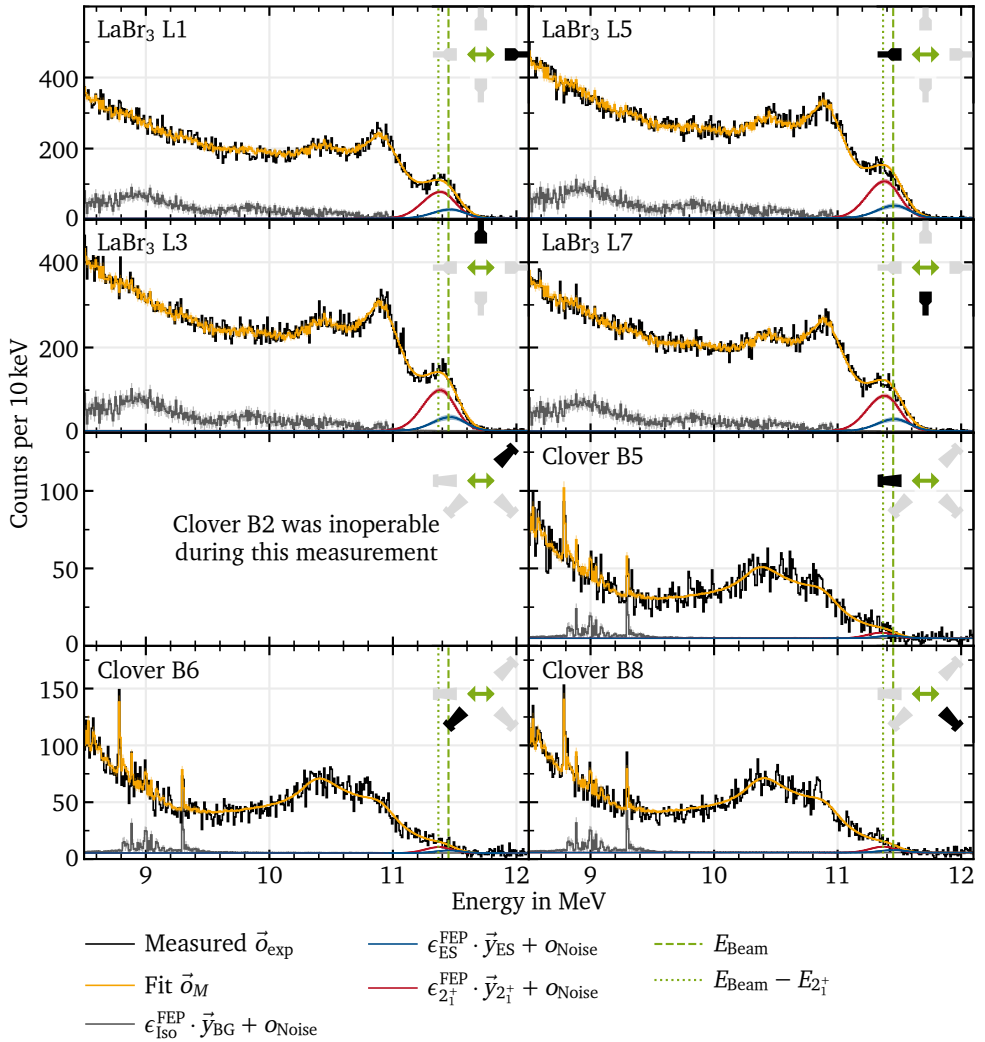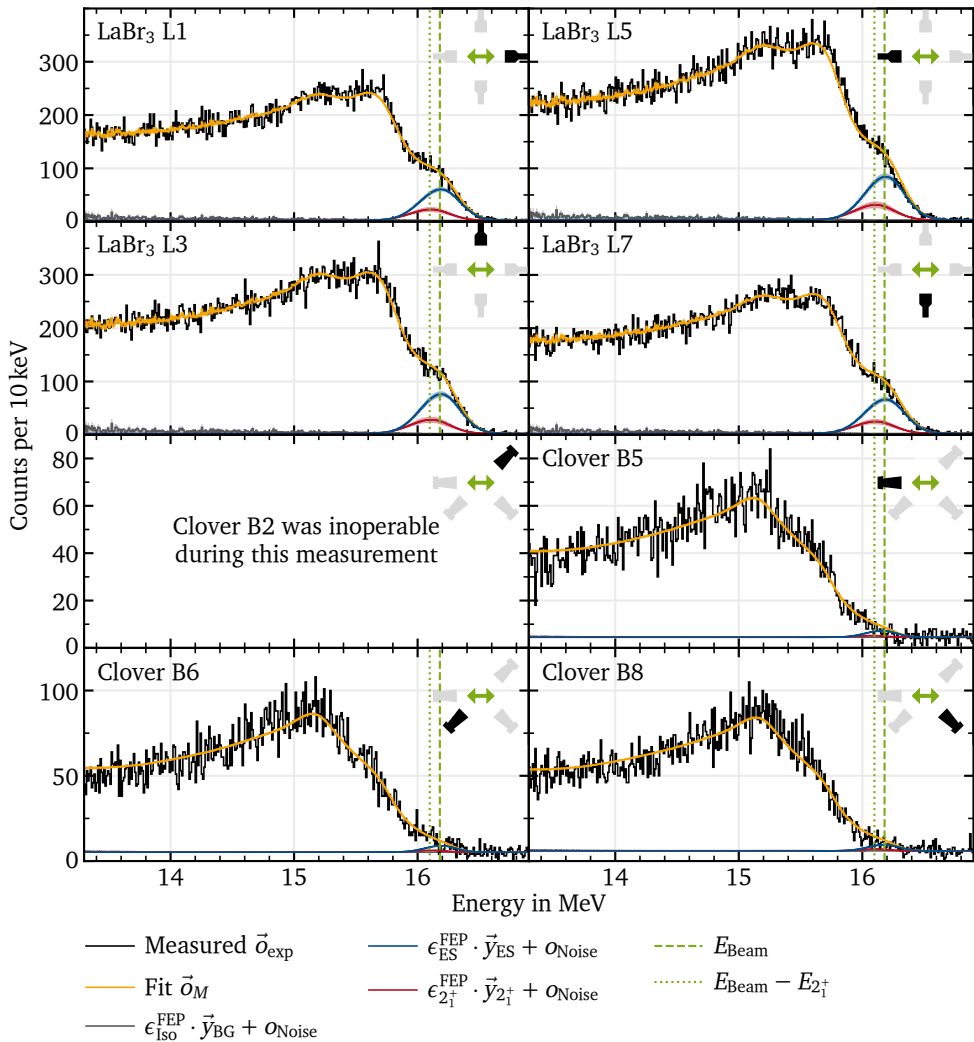
Figure A.4.: Spectra (black) taken during irradiation of ^{154}Sm by an 11.45 MeV circularly polarized photon beam along with simultaneous fit to all spectra (orange) and its components. See the remarks at the beginning of this chapter for details.
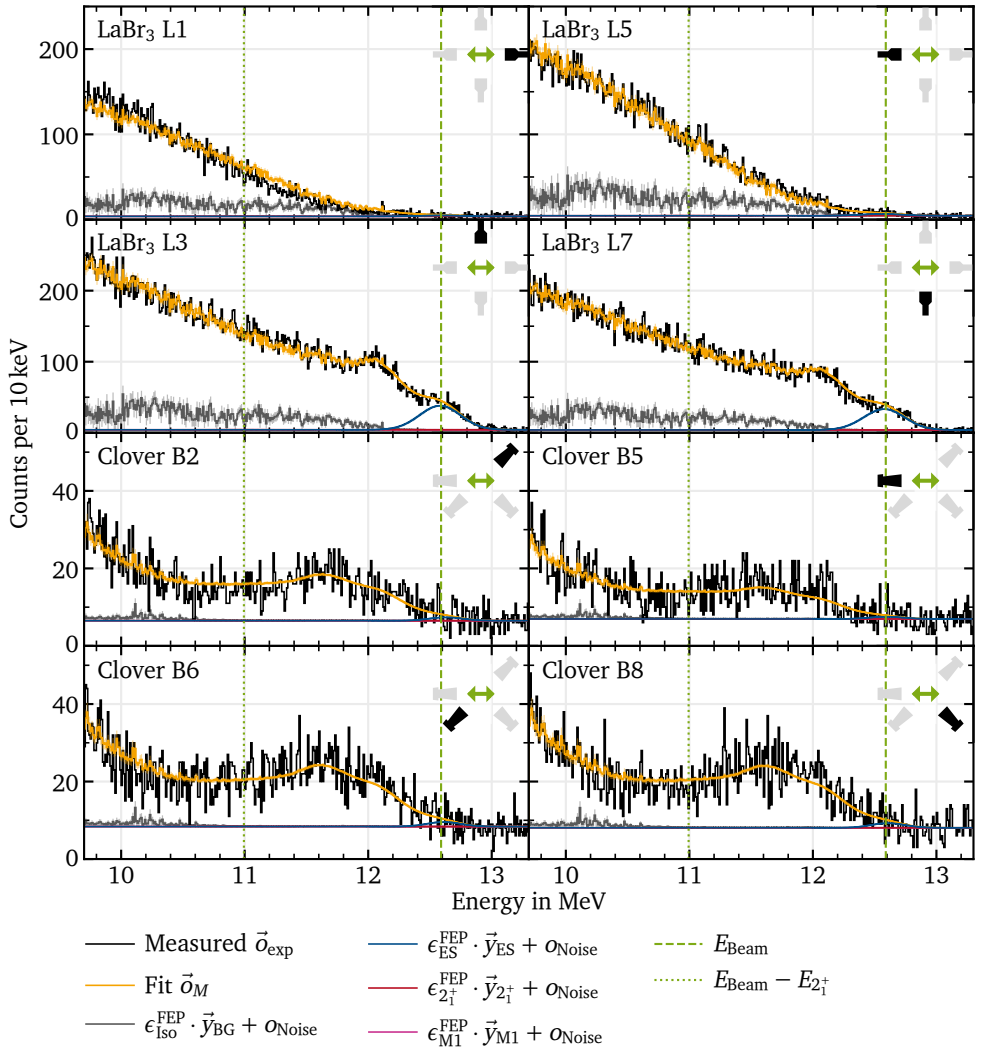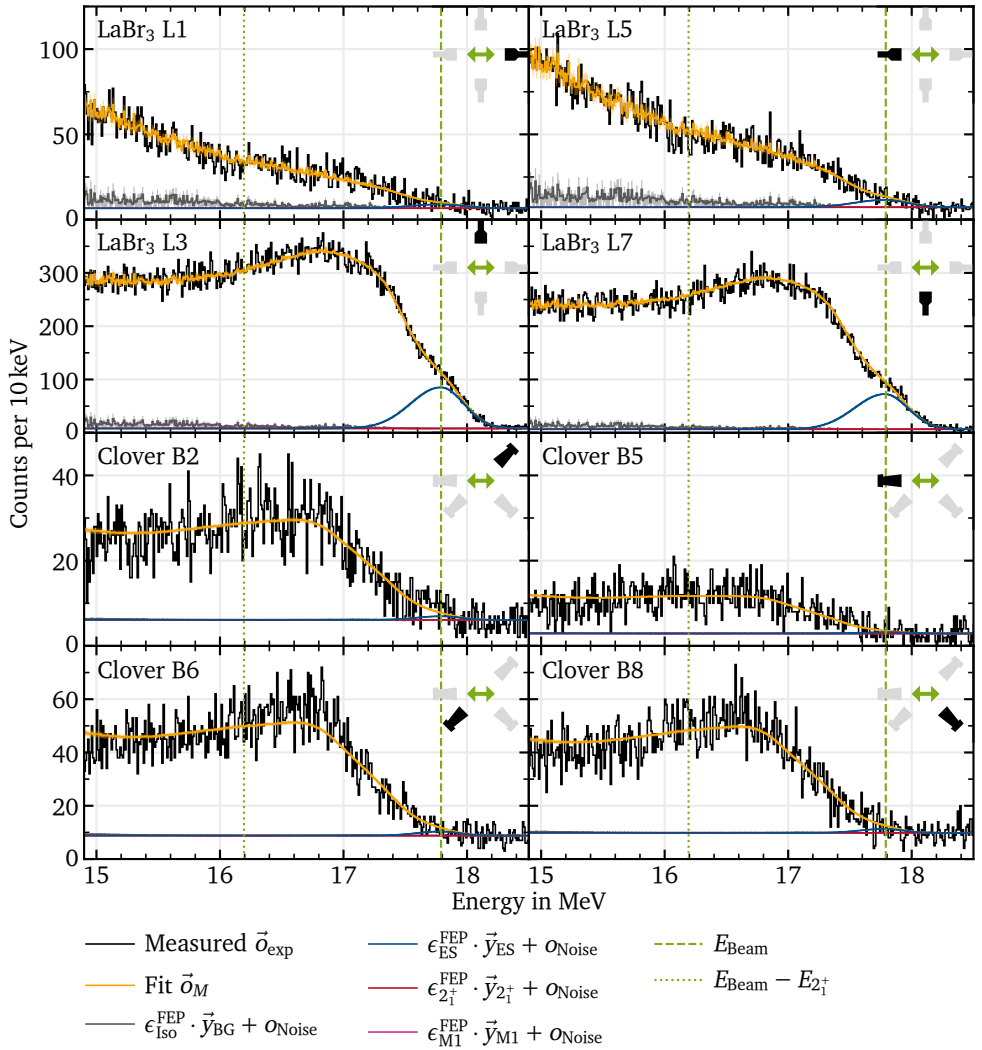
Figure A.5.: Spectra (black) taken during irradiation of ^{140}Ce by a 12.59 MeV linearly polarized photon beam along with simultaneous fit to all spectra (orange) and its components. See the remarks at the beginning of this chapter for details.
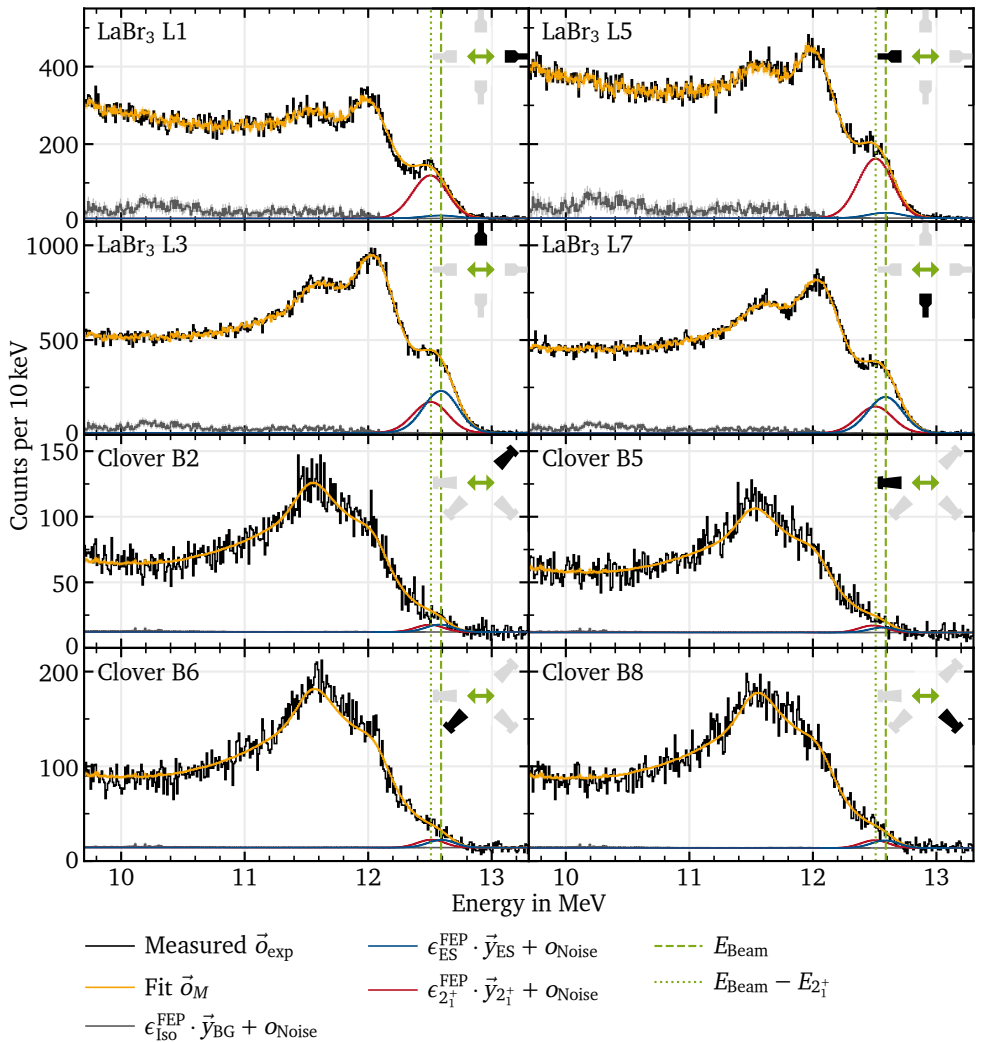
Figure A.6.: Spectra (black) taken during irradiation of ^{154}Sm by a 12.59 MeV linearly polarized photon beam along with simultaneous fit to all spectra (orange) and its components. See the remarks at the beginning of this chapter for details.
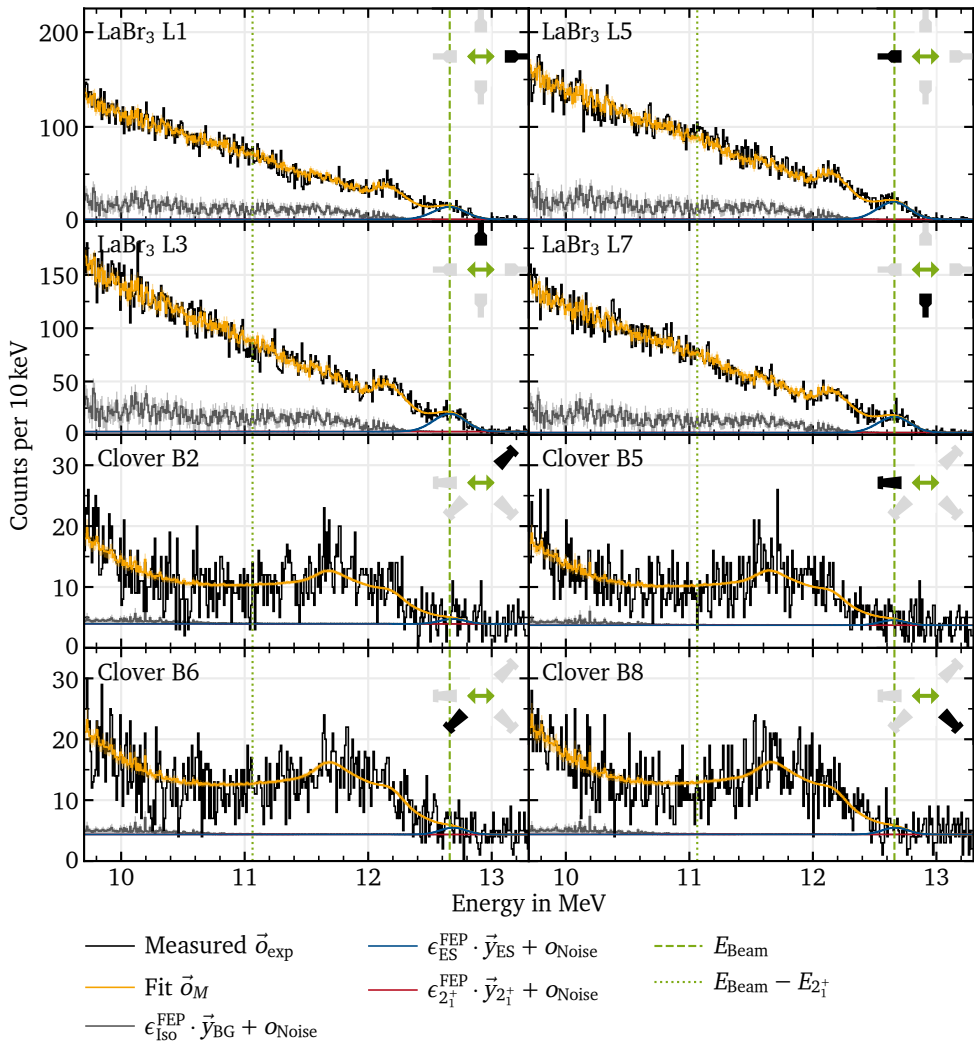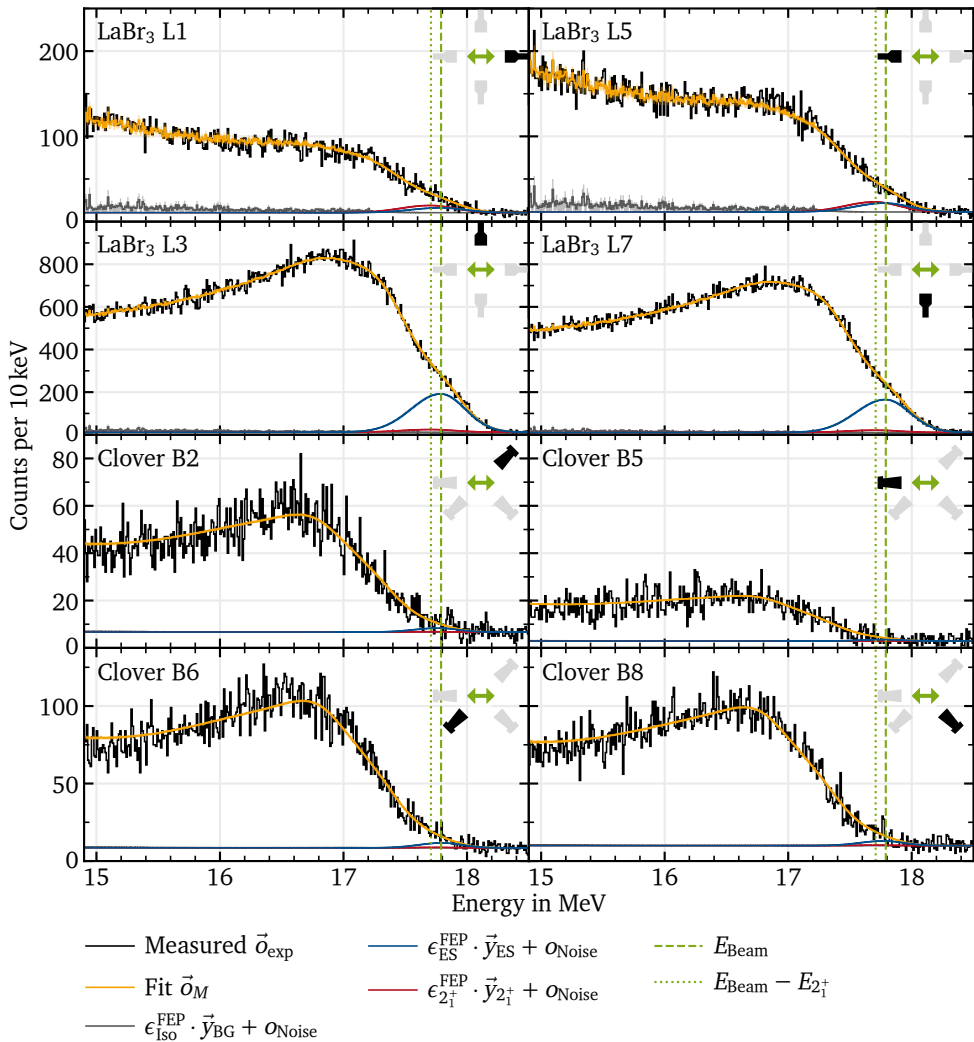
Figure A.7.: Spectra (black) taken during irradiation of ^{140}Ce by a 12.66 MeV circularly polarized photon beam along with simultaneous fit to all spectra (orange) and its components. See the remarks at the beginning of this chapter for details.
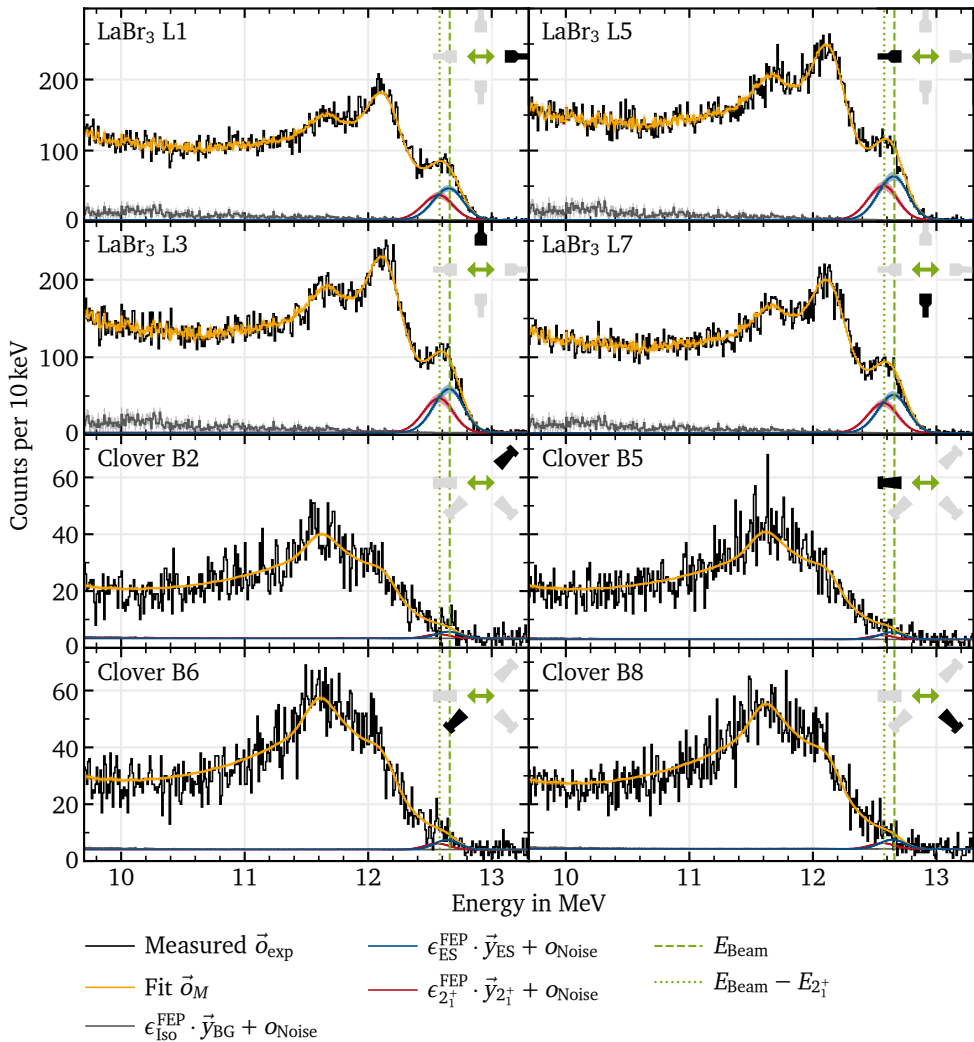
Figure A.8.: Spectra (black) taken during irradiation of ^{154}Sm by a 12.66 MeV circularly polarized photon beam along with simultaneous fit to all spectra (orange) and its components. See the remarks at the beginning of this chapter for details.
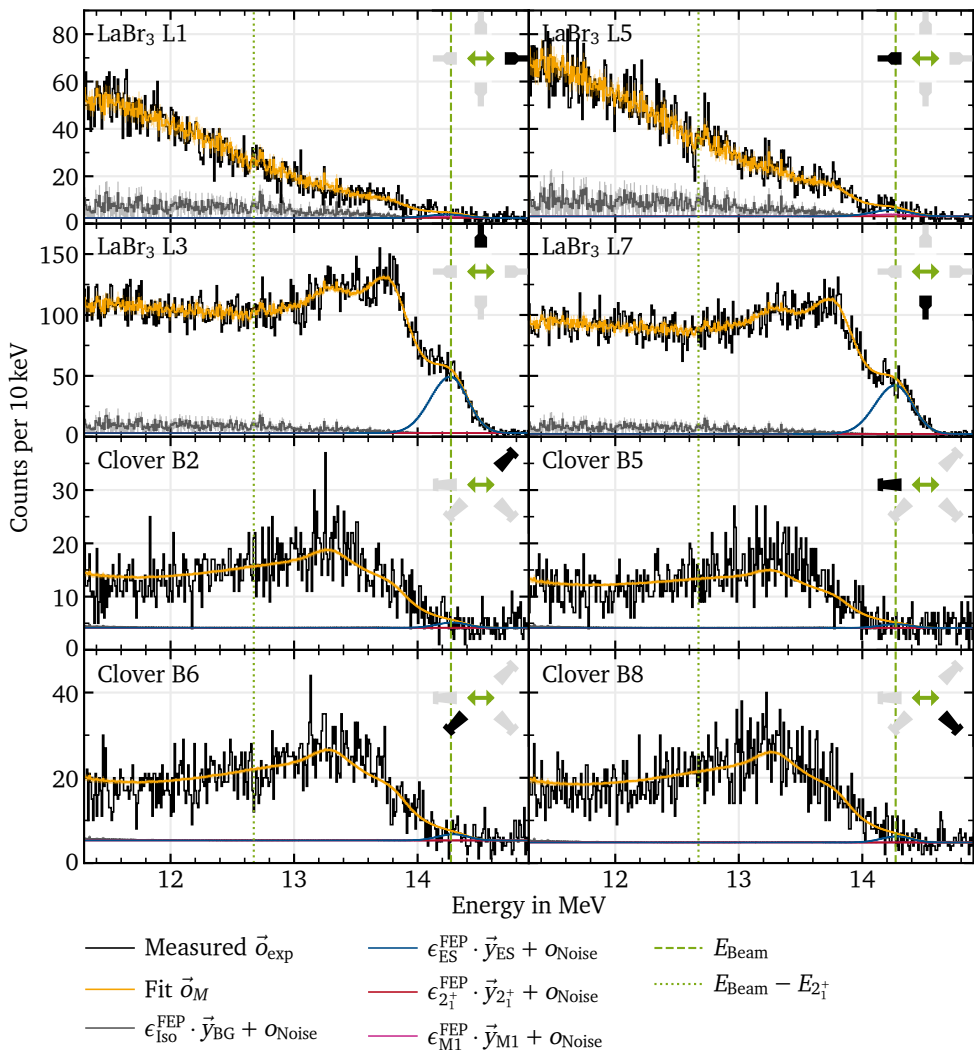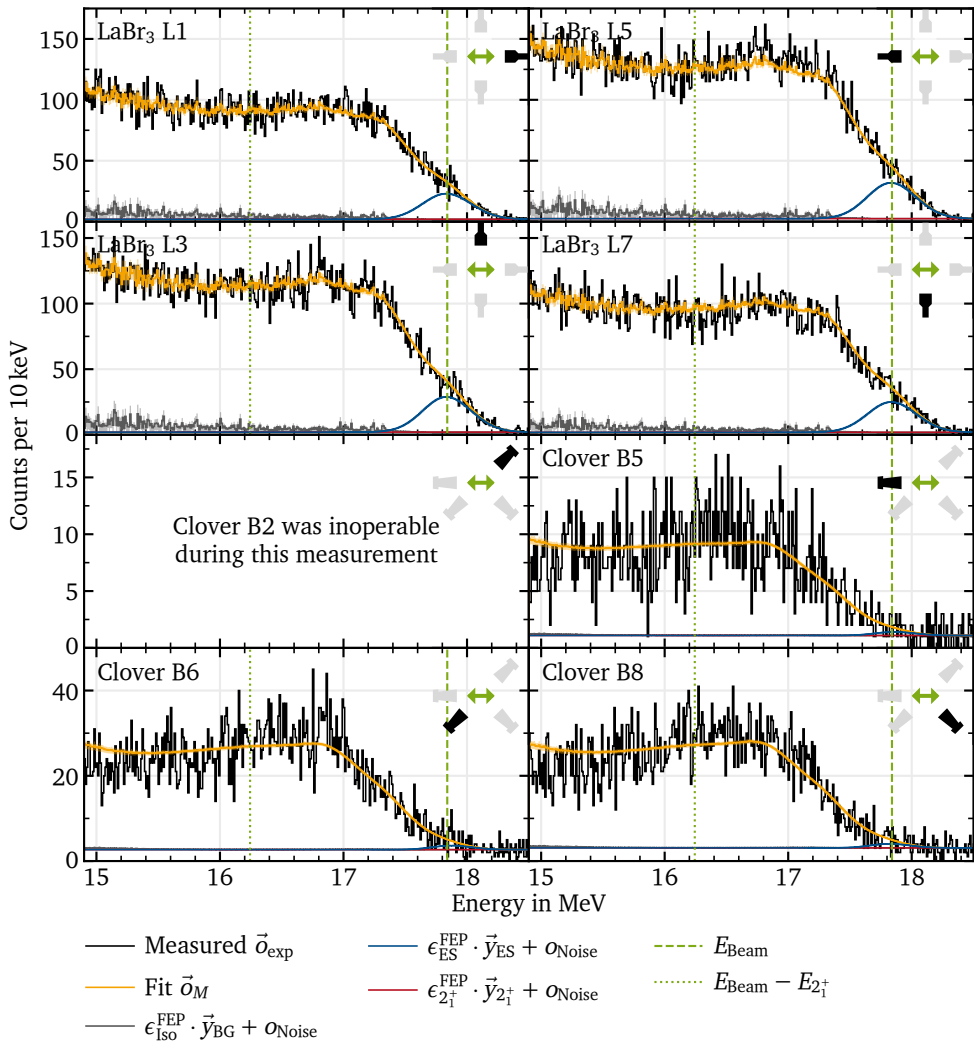
Figure A.9.: Spectra (black) taken during irradiation of ^{140}Ce by a 14.27 MeV linearly polarized photon beam along with simultaneous fit to all spectra (orange) and its components. See the remarks at the beginning of this chapter for details.
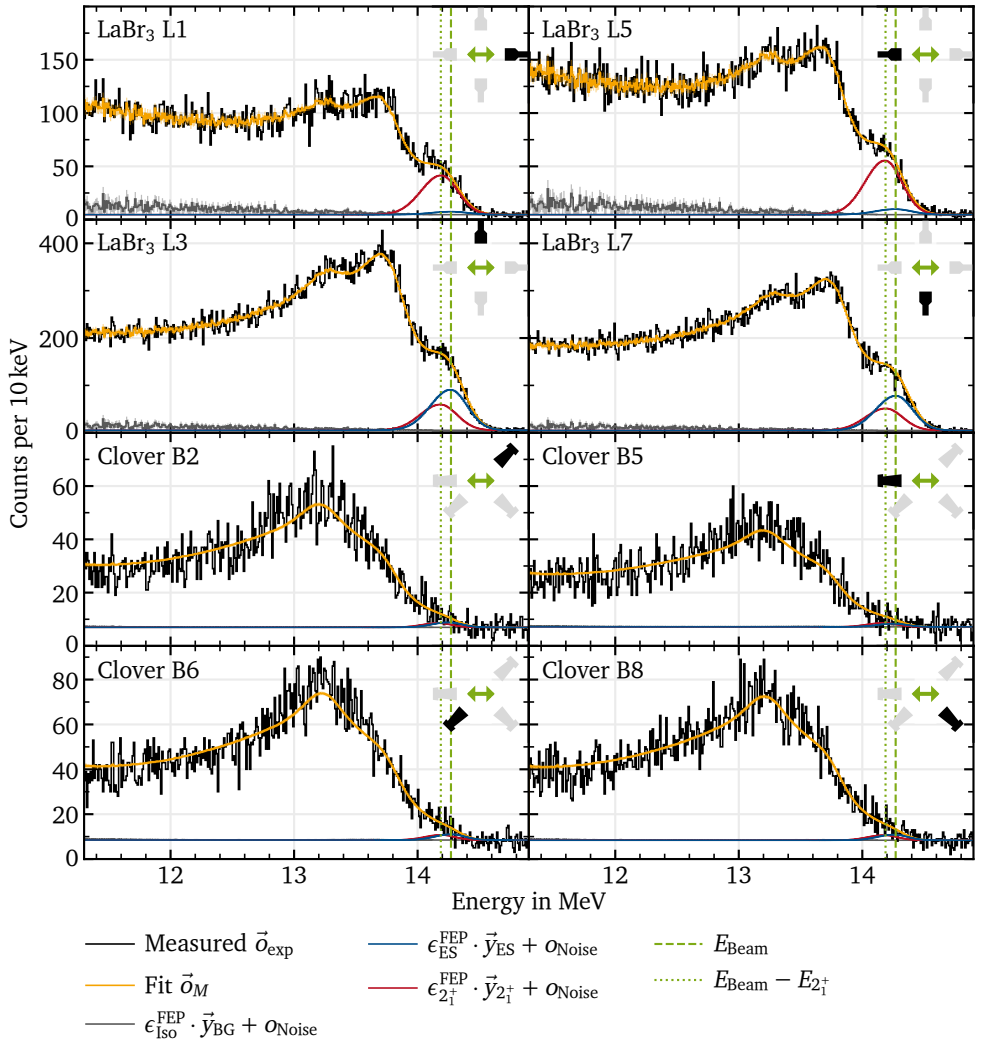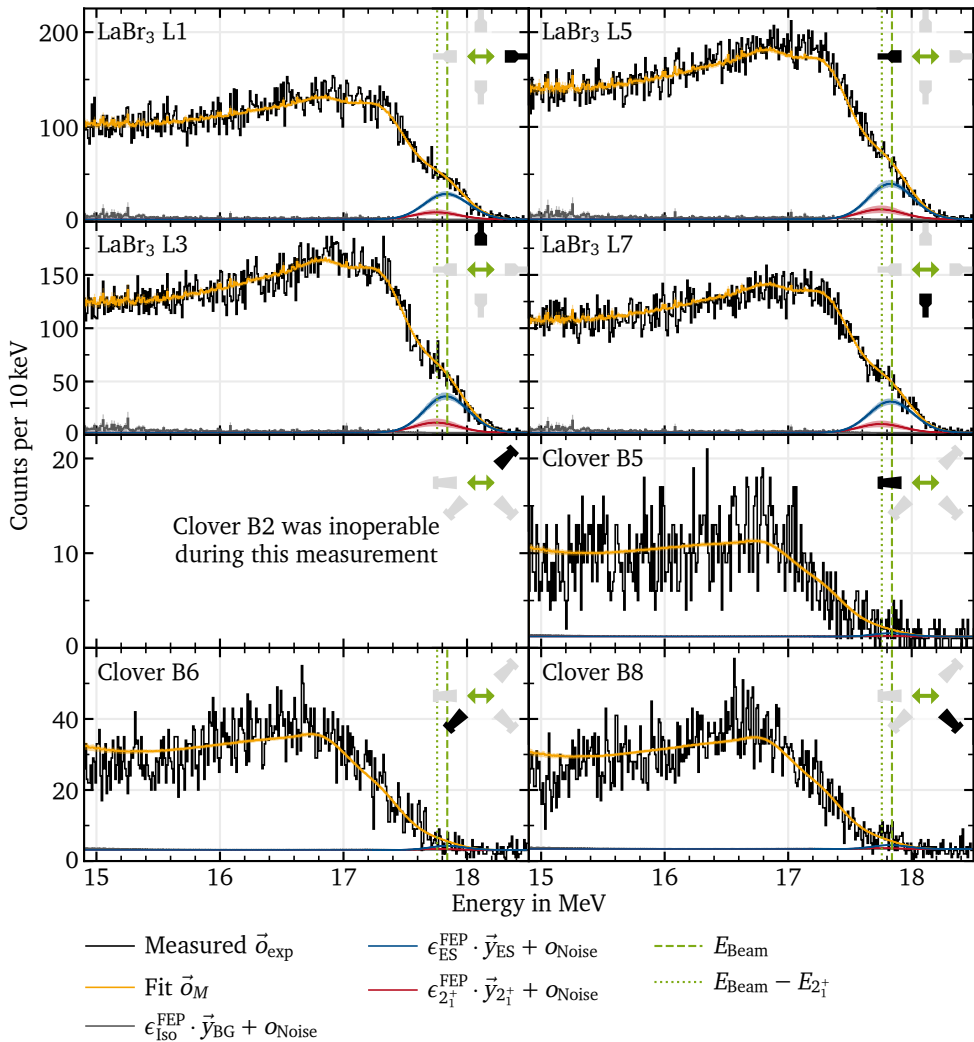
Figure A.10.: Spectra (black) taken during irradiation of ^{154}Sm by a 14.27 MeV linearly polarized photon beam along with simultaneous fit to all spectra (orange) and its components. See the remarks at the beginning of this chapter for details.
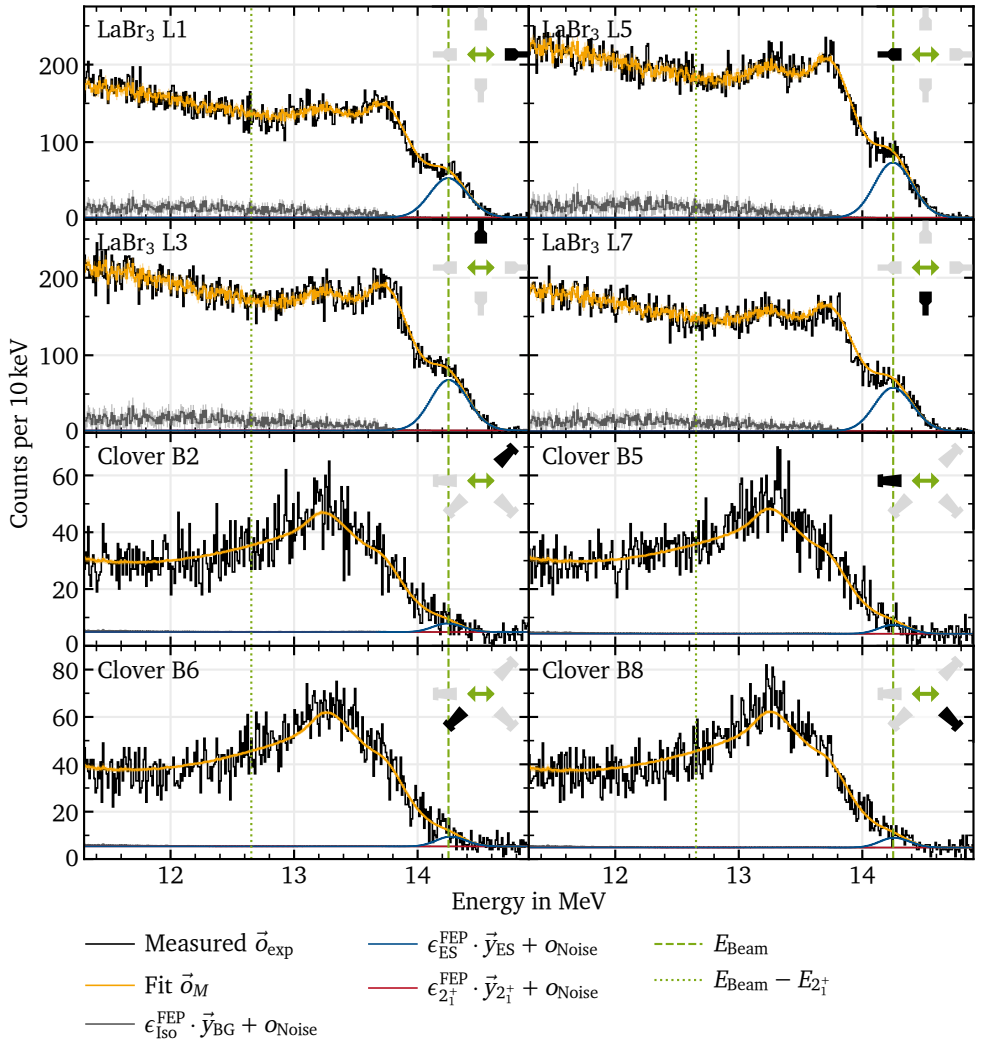
Figure A.11.: Spectra (black) taken during irradiation of ^{140}Ce by a 14.25 MeV circularly polarized photon beam along with simultaneous fit to all spectra (orange) and its components. See the remarks at the beginning of this chapter for details.
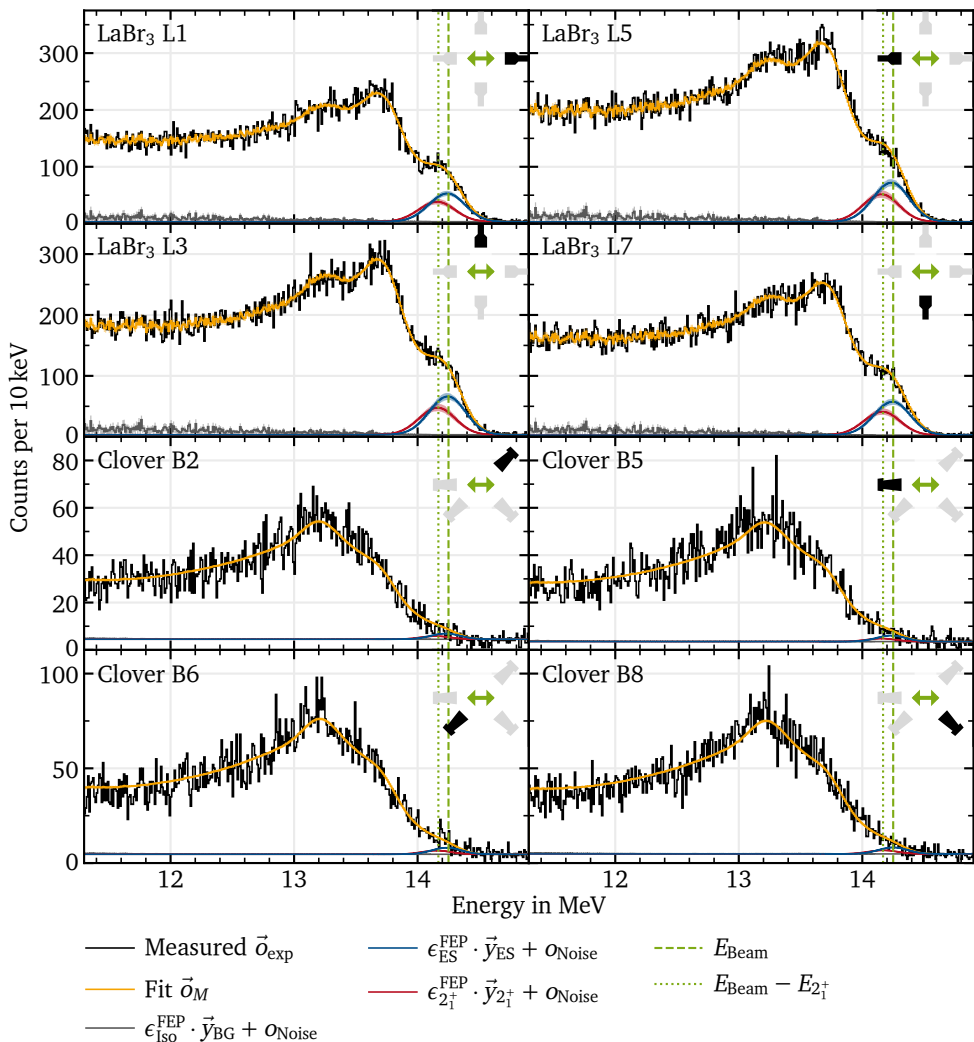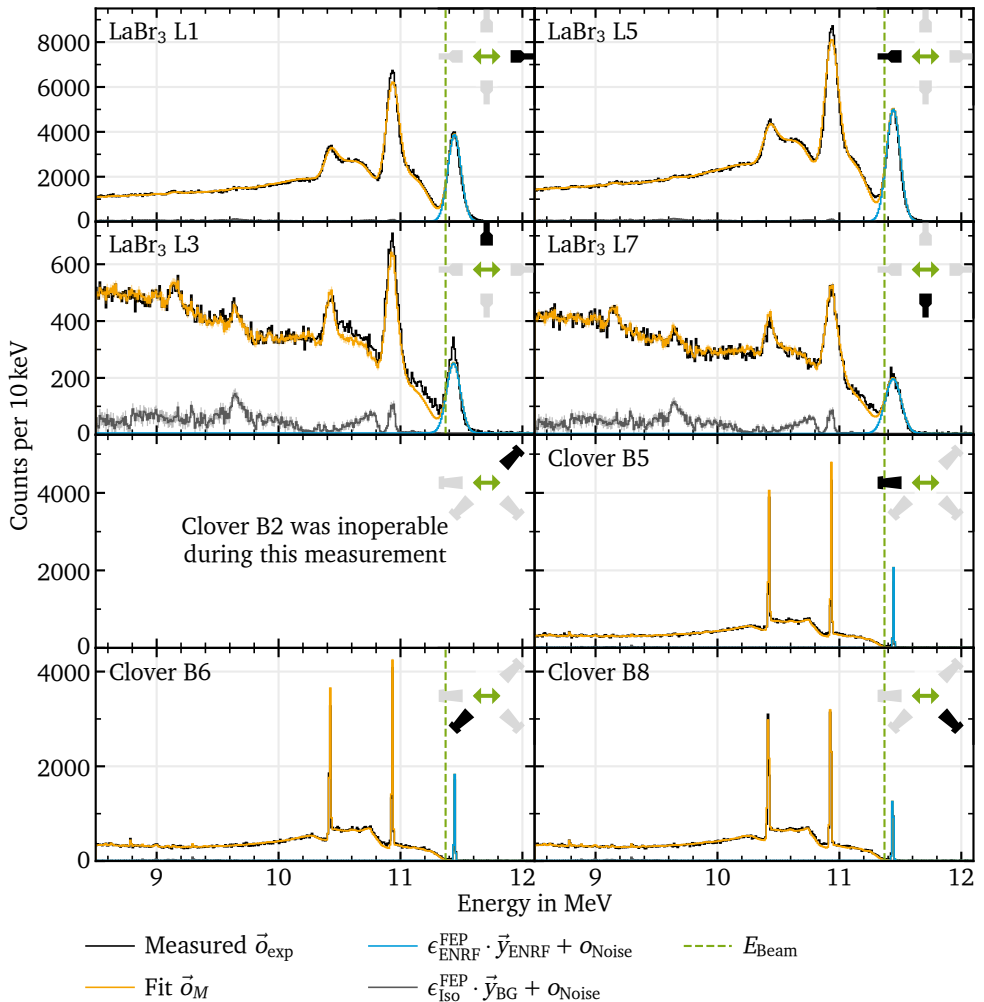
Figure A.12.: Spectra (black) taken during irradiation of ^{154}Sm by a 14.25 MeV circularly polarized photon beam along with simultaneous fit to all spectra (orange) and its components. See the remarks at the beginning of this chapter for details.

Figure A.13.: Spectra (black) taken during irradiation of ^{140}Ce by a 15.35 MeV linearly polarized photon beam along with simultaneous fit to all spectra (orange) and its components. See the remarks at the beginning of this chapter for details.
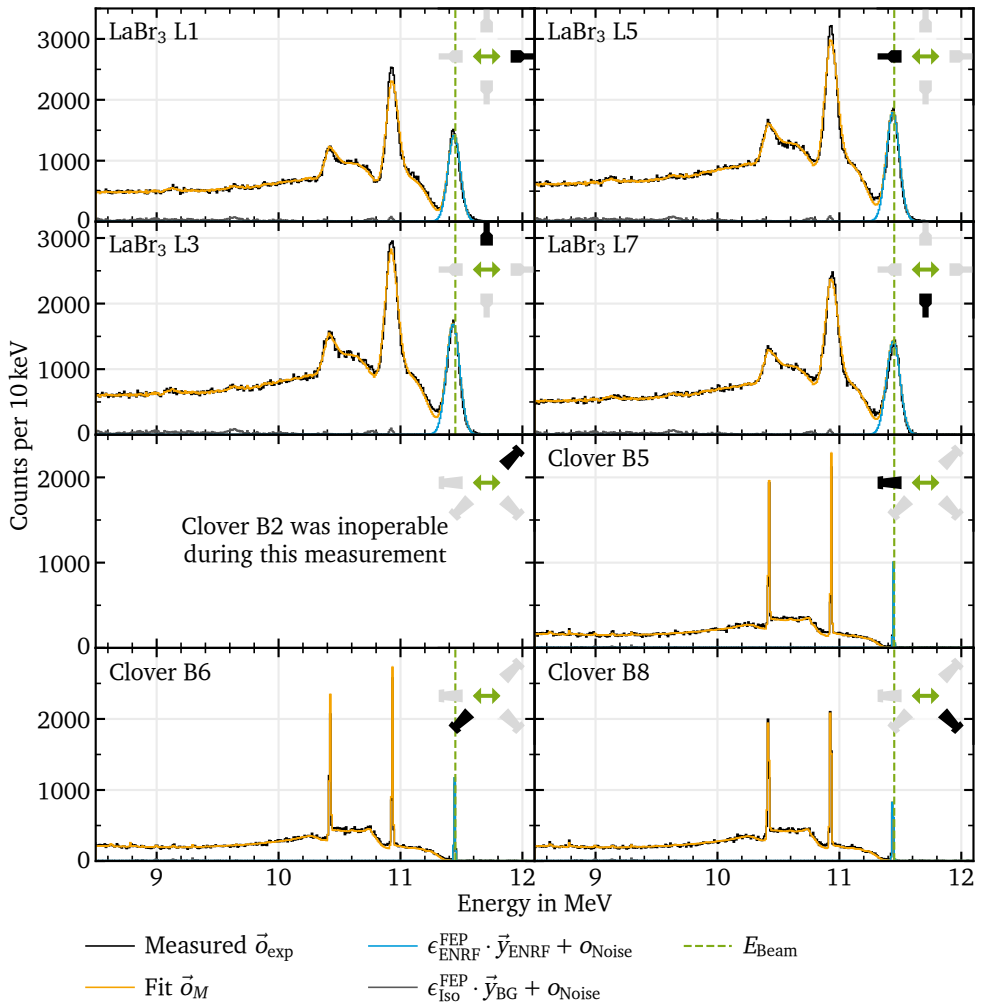
Figure A.14.: Spectra (black) taken during irradiation of ^{154}Sm by a 15.35 MeV linearly polarized photon beam along with simultaneous fit to all spectra (orange) and its components. See the remarks at the beginning of this chapter for details.
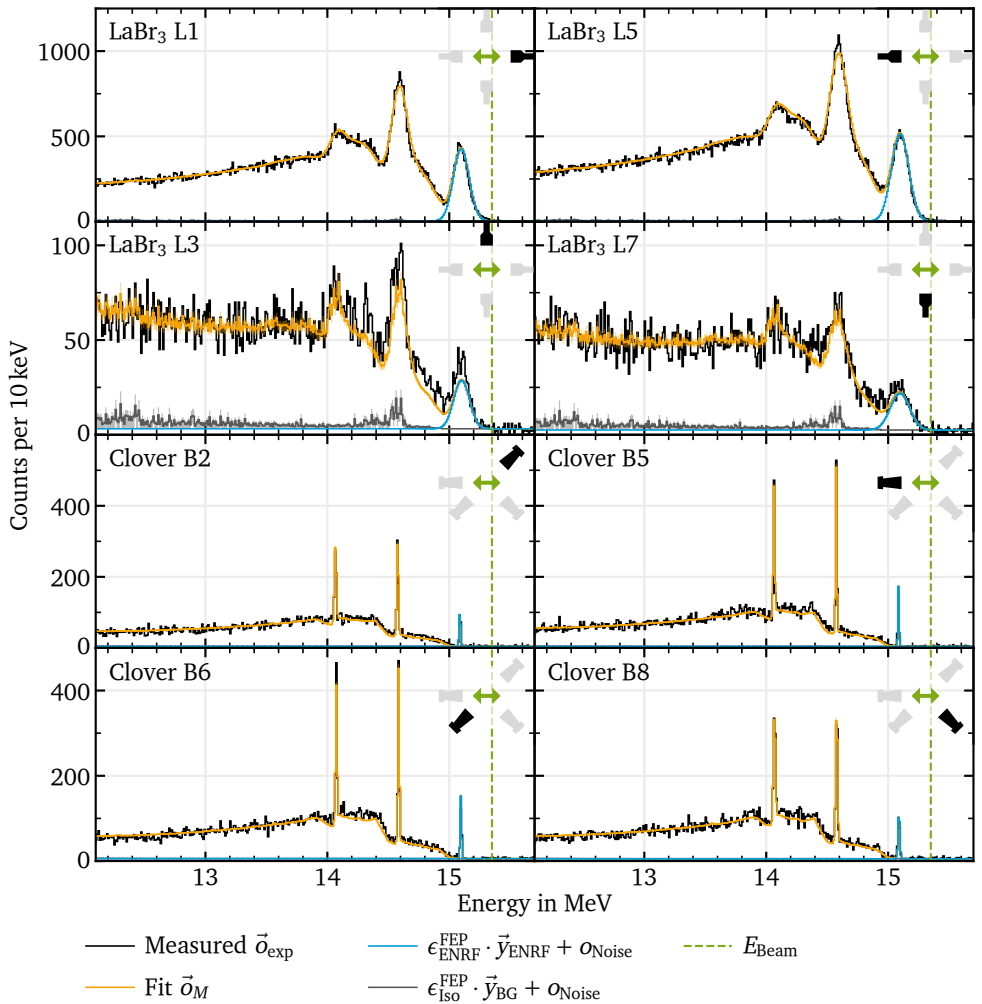
Figure A.15.: Spectra (black) taken during irradiation of ^{140}Ce by a 16.16 MeV linearly polarized photon beam along with simultaneous fit to all spectra (orange) and its components. See the remarks at the beginning of this chapter for details.

Figure A.16.: Spectra (black) taken during irradiation of ^{154}Sm by a 16.16 MeV linearly polarized photon beam along with simultaneous fit to all spectra (orange) and its components. See the remarks at the beginning of this chapter for details.
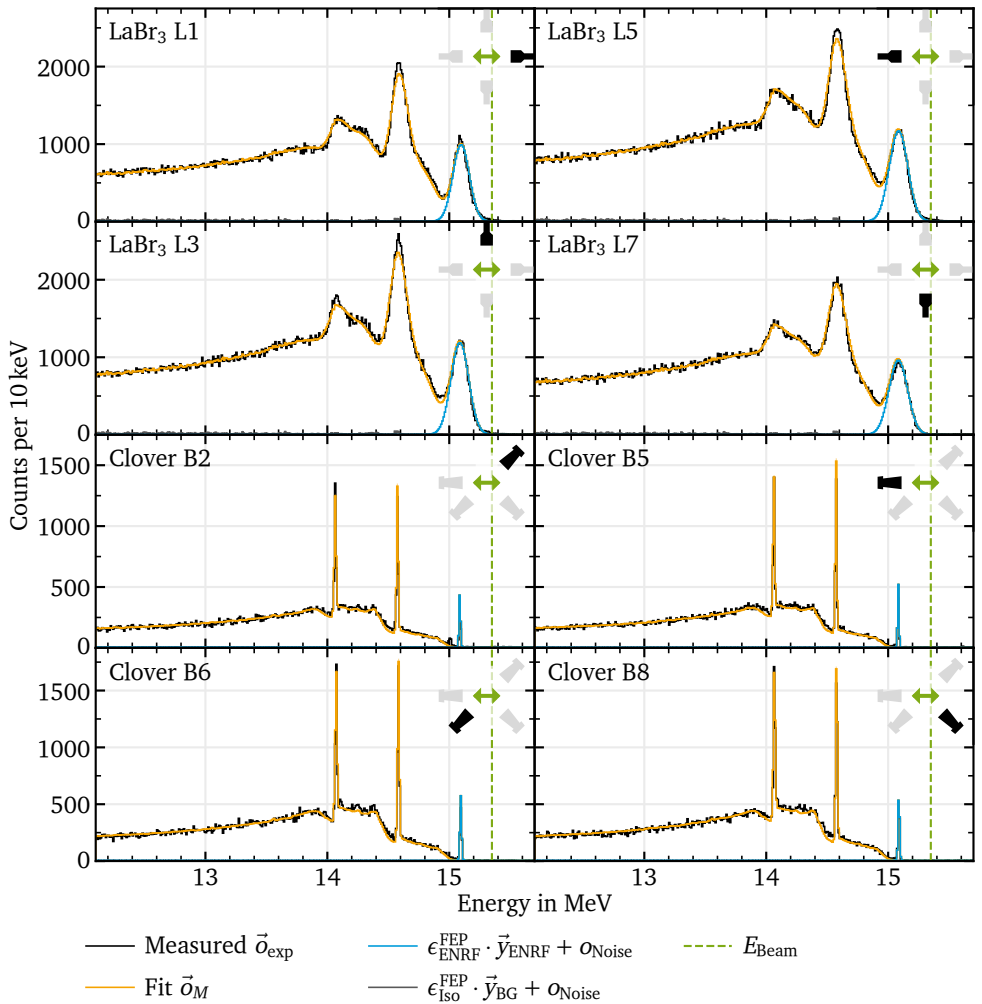
Figure A.17.: Spectra (black) taken during irradiation of ^{140}Ce by a 16.18 MeV circularly polarized photon beam along with simultaneous fit to all spectra (orange) and its components. See the remarks at the beginning of this chapter for details.

Figure A.18.: Spectra (black) taken during irradiation of ^{154}Sm by a 16.18 MeV circularly polarized photon beam along with simultaneous fit to all spectra (orange) and its components. See the remarks at the beginning of this chapter for details.

Figure A.19.: Spectra (black) taken during irradiation of ^{140}Ce by a 17.79 MeV linearly polarized photon beam along with simultaneous fit to all spectra (orange) and its components. See the remarks at the beginning of this chapter for details.

Figure A.20.: Spectra (black) taken during irradiation of ^{154}Sm by a 17.79 MeV linearly polarized photon beam along with simultaneous fit to all spectra (orange) and its components. See the remarks at the beginning of this chapter for details.

Figure A.21.: Spectra (black) taken during irradiation of ^{140}Ce by a 17.84 MeV circularly polarized photon beam along with simultaneous fit to all spectra (orange) and its components. See the remarks at the beginning of this chapter for details.

Figure A.22.: Spectra (black) taken during irradiation of ^{154}Sm by a 17.84 MeV circularly polarized photon beam along with simultaneous fit to all spectra (orange) and its components. See the remarks at the beginning of this chapter for details.

Figure A.23.: Spectra (black) taken during irradiation of ^{28}Si by an 11.37 MeV linearly polarized photon beam along with simultaneous fit to all spectra (orange) and its components. See the remarks at the beginning of this chapter for details.

Figure A.24.: Spectra (black) taken during irradiation of ^{28}Si by an 11.45 MeV circularly polarized photon beam along with simultaneous fit to all spectra (orange) and its components. See the remarks at the beginning of this chapter for details.

Figure A.25.: Spectra (black) taken during irradiation of ^{12}C by a 15.35 MeV linearly polarized photon beam along with simultaneous fit to all spectra (orange) and its components. See the remarks at the beginning of this chapter for details.

Figure A.26.: Spectra (black) taken during irradiation of ^{12}C by a 15.35 MeV circularly polarized photon beam along with simultaneous fit to all spectra (orange) and its components. See the remarks at the beginning of this chapter for details.

Bibliography

[1] A. Zilges *et al.*, Prog. Part. Nucl. Phys. **122**, 103903 (2022),
DOI: 10.1016/j.ppnp.2021.103903.

[2] U. Kneissl, H. H. Pitz, and A. Zilges, Prog. Part. Nucl. Phys. **37**, 349 (1996),
DOI: 10.1016/0146-6410(96)00055-5.

[3] S. Goriely *et al.*, Eur. Phys. J. A **55**, 172 (2019),
DOI: 10.1140/epja/i2019-12840-1.

[4] A. Tamii *et al.*, Eur. Phys. J. A **59**, 208 (2023),
DOI: 10.1140/epja/s10050-023-01081-w.

[5] M. Wiedeking and S. Goriely, Philosophical Transactions of the Royal Society A: Mathematical, Physical and Engineering Sciences **382**, 20230125 (2024),
DOI: 10.1098/rsta.2023.0125.

[6] M. Baldo and G. F. Burgio, Progress in Particle and Nuclear Physics **91**, 203 (2016),
DOI: 10.1016/j.ppnp.2016.06.006.

[7] W. Bertozzi and R. J. Ledoux, Nucl. Instrum. Methods Phys. Res. B **241**, 820 (2005),
DOI: 10.1016/j.nimb.2005.07.202.

[8] J. Pruet *et al.*, Journal of Applied Physics **99**, 123102 (2006),
DOI: 10.1063/1.2202005.

[9] T. Hayakawa *et al.*, Nucl. Instrum. Methods Phys. Res. A **621**, 695 (2010),
DOI: 10.1016/j.nima.2010.06.096.

[10] D. Habs and U. Köster, Appl. Phys. B **103**, 501 (2011),
DOI: 10.1007/s00340-010-4278-1.

[11] W. Luo *et al.*, Appl. Phys. B **122**, 8 (2016),
DOI: 10.1007/s00340-015-6292-9.

[12] M. N. Harakeh and A. Van der Woude, *Giant Resonances: Fundamental High-Frequency Modes of Nuclear Excitation*, Vol. 24, Oxford Studies in Nuclear Physics (Oxford University Press, 2001), ISBN: 978-0-19-851733-7.

[13] J. Speth and J. Wambach, *Theory Of Giant Resonances*, in *Electric and Magnetic Giant Resonances in Nuclei*, Vol. 7, edited by J. Speth, International Review of Nuclear Physics (World Scientific Publishing Company, 1991), pp. 1–97, ISBN: 978-981-450349-5, DOI: 10.1142/9789814503495_0001.

[14] J. Speth and A. van der Woude, Rep. Prog. Phys. **44**, 719 (1981), DOI: 10.1088/0034-4885/44/7/002.

[15] N. Pietralla, Eur. Phys. J. A **60**, 108 (2024), DOI: 10.1140/epja/s10050-024-01285-8.

[16] D. Savran, T. Aumann, and A. Zilges, Progress in Particle and Nuclear Physics **70**, 210 (2013), DOI: 10.1016/j.ppnp.2013.02.003.

[17] A. Bracco, E. G. Lanza, and A. Tamii, Progress in Particle and Nuclear Physics **106**, 360 (2019), DOI: 10.1016/j.ppnp.2019.02.001.

[18] U. Kneissl, N. Pietralla, and A. Zilges, J. Phys. G: Nucl. Part. Phys. **32**, R217 (2006), DOI: 10.1088/0954-3899/32/8/R01.

[19] B. L. Berman and S. C. Fultz, Rev. Mod. Phys. **47**, 713 (1975), DOI: 10.1103/RevModPhys.47.713.

[20] S. S. Dietrich and B. L. Berman, At. Data Nucl. Data Tables **38**, 199 (1988), DOI: 10.1016/0092-640X(88)90033-2.

[21] P. Carlos *et al.*, Nucl. Phys. A **225**, 171 (1974), DOI: 10.1016/0375-9474(74)90373-X.

[22] N. Otuka *et al.*, Nucl. Data Sheets **120**, 272 (2014), DOI: 10.1016/j.nds.2014.07.065.

[23] V. V. Zerkin and B. Pritychenko, Nucl. Instrum. Methods Phys. Res. A **888**, 31 (2018), DOI: 10.1016/j.nima.2018.01.045.

[24] J. P. Davidson, Rev. Mod. Phys. **37**, 105 (1965), DOI: 10.1103/RevModPhys.37.105.

[25] M. Goldhaber and E. Teller, Phys. Rev. **74**, 1046 (1948), DOI: 10.1103/PhysRev.74.1046.

[26] H. Steinwedel and J. H. D. Jensen, Z. Naturforsch. A **5**, 413 (1950), DOI: 10.1515/zna-1950-0801.

[27] J. H. D. Jensen and P. Jensen, Z. Naturforsch. A **5**, 343 (1950), DOI: 10.1515/zna-1950-0610.

[28] H. Steinwedel, J. H. D. Jensen, and P. Jensen, Phys. Rev. **79**, 1019 (1950),
DOI: 10.1103/PhysRev.79.1019.

[29] M. Danos, Nucl. Phys. **5**, 23 (1958),
DOI: 10.1016/0029-5582(58)90005-1.

[30] K. Okamoto, Phys. Rev. **110**, 143 (1958),
DOI: 10.1103/PhysRev.110.143.

[31] A. S. Davydov and G. F. Filippov, Nucl. Phys. **8**, 237 (1958),
DOI: 10.1016/0029-5582(58)90153-6.

[32] W. Thomas, Naturwiss. **13**, 627 (1925),
DOI: 10.1007/BF01558908.

[33] W. Kuhn, Z. Phys. **33**, 408 (1925),
DOI: 10.1007/BF01328322.

[34] F. Reiche and W. Thomas, Z. Phys. **34**, 510 (1925),
DOI: 10.1007/BF01328494.

[35] J. R. Beene *et al.*, Phys. Rev. C **41**, 920 (1990),
DOI: 10.1103/PhysRevC.41.920.

[36] K. Boretzky *et al.*, Phys. Lett. B **384**, 30 (1996),
DOI: 10.1016/0370-2693(96)00797-6.

[37] M. Hass, R. Moreh, and D. Salzmann, Phys. Lett. B **36**, 68 (1971),
DOI: 10.1016/0370-2693(71)90109-2.

[38] T. Bar-Noy and R. Moreh, Nucl. Phys. A **229**, 417 (1974),
DOI: 10.1016/0375-9474(74)90661-7.

[39] H. E. Jackson, G. E. Thomas, and K. J. Wetzel, Phys. Rev. C **11**, 1664 (1975),
DOI: 10.1103/PhysRevC.11.1664.

[40] E. G. Fuller and E. Hayward, Nucl. Phys. **30**, 613 (1962),
DOI: 10.1016/0029-5582(62)90081-0.

[41] A. M. Nathan and R. Moreh, Phys. Lett. B **91**, 38 (1980),
DOI: 10.1016/0370-2693(80)90657-7.

[42] S. D. Hoblit and A. M. Nathan, Phys. Rev. C **44**, 2372 (1991),
DOI: 10.1103/PhysRevC.44.2372.

[43] A. M. Baldin, Sov. Phys. J. Exp. Theor. Phys. **10**, 142 (1960),
URL: http://jetp.ras.ru/cgi-bin/e/index/e/10/1/p142?a=list (visited on 2024-08-21).

[44] E. Hayward, *Photonuclear Reactions*, NBS monograph (U.S. National Bureau of Standards, Gaithersburg, MD, USA, 1970),
DOI: 10.6028/NBS.MONO.118.

[45] Z. Marić and P. Möbius, Nucl. Phys. **10**, 135 (1959),
DOI: 10.1016/0029-5582(59)90198-1.

[46] H. R. Weller *et al.*, Prog. Part. Nucl. Phys. **62**, 257 (2009),
DOI: 10.1016/j.ppnp.2008.07.001.

[47] C. R. Howell *et al.*, J. Phys. G: Nucl. Part. Phys. **49**, 010502 (2021),
DOI: 10.1088/1361-6471/ac2827.

[48] H. R. Weller, M. W. Ahmed, and Y. K. Wu, Nucl. Phys. News **25**, 19 (2015),
DOI: 10.1080/10619127.2015.1035932.

[49] R. Hajima, Phys. Procedia **84**, Proceedings of the International Conference "Synchrotron and Free electron laser Radiation: generation and application" (SFR-2016), July 4 - 7, 2016, Novosibirsk, Russia, 35 (2016),
DOI: 10.1016/j.phpro.2016.11.007.

[50] W. Bothe and W. Gentner, Z. Phys. **106**, 236 (1937),
DOI: 10.1007/BF01340320.

[51] G. C. Baldwin and G. S. Klaiber, Phys. Rev. **71**, 3 (1947),
DOI: 10.1103/PhysRev.71.3.

[52] G. C. Baldwin and G. S. Klaiber, Phys. Rev. **73**, 1156 (1948),
DOI: 10.1103/PhysRev.73.1156.

[53] P. F. Bortignon, A. Bracco, and R. A. Broglia, *Giant Resonances: Nuclear Structure at Finite Temperature* (Harwood Academic Publishers, 1998), ISBN: 978-905702570-9,
DOI: 10.1201/9780203753224.

[54] N. Bohr, Nature **141**, 326 (1938),
DOI: 10.1038/141326a0.

[55] A. Migdal, J. Phys. USSR **8**, 331 (1944).

[56] B. S. Ishkhanov and I. M. Kapitonov, Phys. Usp. **64**, 141 (2021),
DOI: 10.3367/UFNe.2020.02.038725.

[57] J. P. Connerade, J. M. Esteva, and R. C. Karnatak, eds., *Giant Resonances in Atoms, Molecules, and Solids*, 1st ed., NATO ASI Series B: Physics (Springer Science+Business Media, LLC, 1987), ISBN: 978-0-306-42564-6,
DOI: 10.1007/978-1-4899-2004-1.

[58] D. L. Ederer, Phys. Rev. Lett. **13**, 760 (1964),
DOI: 10.1103/PhysRevLett.13.760.

[59] A. P. Lukirskii, I. A. Brytov, and T. M. Zimkina, Opt. Spektrosk. **17**, 234 (1964).

[60] J. A. R. Samson, Adv. Atom Mol. Phys. **2**, 177 (1966),
DOI: 10.1016/S0065-2199(08)60219-5.

[61] G. Wendin, Phys. Lett. A **46**, 119 (1973),
DOI: 10.1016/0375-9601(73)90054-6.

[62] A. D. Shiner *et al.*, Nat. Phys. **7**, 464 (2011),
DOI: 10.1038/nphys1940.

[63] S. Pabst and R. Santra, Phys. Rev. Lett. **111**, 233005 (2013),
DOI: 10.1103/PhysRevLett.111.233005.

[64] W. A. de Heer *et al.*, Phys. Rev. Lett. **59**, 1805 (1987),
DOI: 10.1103/PhysRevLett.59.1805.

[65] W. Hoheisel *et al.*, Phys. Rev. Lett. **60**, 1649 (1988),
DOI: 10.1103/PhysRevLett.60.1649.

[66] J. Tiggesbäumker *et al.*, Chem. Phys. Lett. **190**, 42 (1992),
DOI: 10.1016/0009-2614(92)86099-4.

[67] G. Gensterblum *et al.*, Phys. Rev. Lett. **67**, 2171 (1991),
DOI: 10.1103/PhysRevLett.67.2171.

[68] I. V. Hertel *et al.*, Phys. Rev. Lett. **68**, 784 (1992),
DOI: 10.1103/PhysRevLett.68.784.

[69] J. Kleemann *et al.*, *Dataset and Analysis Codes for "Gamma decay of the ^{154}Sm Isovector Giant Dipole Resonance: Smekal-Raman Scattering as a Novel Probe of Nuclear Ground-State Deformation"*, TUdatalib, Technische Universität Darmstadt, 2024,
DOI: 10.48328/tudatalib-1472.

[70] J. Kleemann *et al.*, Phys. Rev. Lett., to be published (2025), arXiv:2406.19695.

[71] F. R. Metzger, Prog. Nucl. Phys. **7**, 54 (1959).

[72] U. E. P. Berg and U. Kneissl, Annu. Rev. Nucl. Part. Sci. **37**, 33 (1987),
DOI: 10.1146/annurev.ns.37.120187.000341.

[73] J. Isaak and N. Pietralla, *Probing Nuclear Structure with Photon Beams*, in *Handbook of Nuclear Physics*, edited by I. Tanihata, H. Toki, and T. Kajino (Springer Nature Singapore, Singapore, 2022), pp. 1–45, ISBN: 978-981-158818-1,
DOI: 10.1007/978-981-15-8818-1_2-1.

[74] R. L. Mössbauer, Z. Phys. **151**, 124 (1958),
DOI: 10.1007/BF01344210.

[75] K. S. Krane, R. M. Steffen, and R. M. Wheeler, At. Data Nucl. Data Tables **11**, 351 (1973),
DOI: 10.1016/S0092-640X(73)80016-6.

[76] K. S. Krane and R. M. Steffen, Phys. Rev. C **2**, 724 (1970),
DOI: 10.1103/PhysRevC.2.724.

[77] A. Bohr and B. R. Mottelson, *Nuclear Structure Volume I* (W.A. Benjamin, Inc., 1969).

[78] C. Eckart, Rev. Mod. Phys. **2**, 305 (1930),
      DOI: 10.1103/RevModPhys.2.305.

[79] E. Wigner, *Gruppentheorie und ihre Anwendung auf die Quantenmechanik der Atomspektren*, de (Vieweg+Teubner Verlag, 1931), ISBN: 978-3-66300642-8,
      DOI: 10.1007/978-3-663-02555-9.

[80] U. Friman-Gayer *et al.*, Phys. Rev. Lett. **126**, 102501 (2021),
      DOI: 10.1103/PhysRevLett.126.102501.

[81] J. D. Jackson, *Classical Electrodynamics*, 3rd ed. (John Wiley & Sons, Inc., New York, NY, USA, 1999), ISBN: 978-0-471-30932-1.

[82] R. M. Steffen and K. Alder, *Angular Distribution and Correlation of Gamma Rays*, in *The Electromagnetic Interaction in Nuclear Spectroscopy*, edited by W. D. Hamilton (North-Holland, Amsterdam, Netherlands, 1975) Chap. 12, pp. 505–582, ISBN: 978-0-444-10519-6.

[83] L. W. Fagg and S. S. Hanna, Rev. Mod. Phys. **31**, 711 (1959),
      DOI: 10.1103/RevModPhys.31.711.

[84] C. Iliadis and U. Friman-Gayer, Eur. Phys. J. A **57**, 190 (2021),
      DOI: 10.1140/epja/s10050-021-00472-1.

[85] N. Pietralla *et al.*, Phys. Rev. Lett. **88**, 012502 (2001),
      DOI: 10.1103/PhysRevLett.88.012502.

[86] N. Pietralla *et al.*, Nucl. Instrum. Methods Phys. Res. A **483**, Proceedings of the 23rd International Free Electron Laser Conference and 8th FEL Users Workshop, 556 (2002),
      DOI: 10.1016/S0168-9002(02)00381-9.

[87] C. M. Davisson, *Interaction of γ-Radiation with Matter*, in *Alpha-, Beta- and Gamma-Ray Spectroscopy*, Vol. 1, edited by K. Siegbahn (North-Holland Publishing Company, Amsterdam, Netherlands, 1965), pp. 37–78, ISBN: 978-0-444-10695-7.

[88] J. D. Bjorken and S. D. Drell, *Relativistic Quantum Mechanics*, Pure & Applied Physics S. (McGraw-Hill, 1965), ISBN: 978-0-07-005493-6.

[89] J. Als-Nielsen and D. McMorrow, *Elements of modern X-ray physics*, 2nd ed. (John Wiley & Sons, Ltd, 2011), ISBN: 978-0-470-97395-0,
      DOI: 10.1002/9781119998365.

[90] D. Drechsel, B. Pasquini, and M. Vanderhaeghen, Phys. Rep. **378**, 99 (2003),
      DOI: 10.1016/S0370-1573(02)00636-1.

[91] G. F. Bertsch, P. F. Bortignon, and R. A. Broglia, Rev. Mod. Phys. **55**, 287 (1983),
      DOI: 10.1103/RevModPhys.55.287.

[92] S. Bhagavantam, *Scattering of light and the Raman effect* (Chemical Publishing Company, Inc., 1942).

[93] G. Alaga *et al.*, Dan. Mat. Fys. Medd. **29**, 1 (1955).

[94] F. R. Arutyunian and V. A. Tumanian, Physics Letters **4**, 176 (1963), DOI: 10.1016/0031-9163(63)90351-2.

[95] R. H. Milburn, Phys. Rev. Lett. **10**, 75 (1963), DOI: 10.1103/PhysRevLett.10.75.

[96] Y. K. Wu, Private communication, 2024.

[97] A. D. Ayangeakaa, U. Friman-Gayer, and R. V. F. Janssens, *The Clover Array for Nuclear Structure Studies at HIγS*, Innovation News Network, 2021, URL: https://innovationnewsnetwork.com/nuclear-structure/10491 (visited on 2024-07-19).

[98] A. Leprêtre *et al.*, Nucl. Phys. A **258**, 350 (1976), DOI: 10.1016/0375-9474(76)90011-7.

[99] N. Nica, Nucl. Data Sheets **154**, 1 (2018), DOI: 10.1016/j.nds.2018.11.002.

[100] C. W. Reich, Nucl. Data Sheets **110**, 2257 (2009), DOI: 10.1016/j.nds.2009.09.001.

[101] J. H. Kelley, J. E. Purcell, and C. G. Sheu, Nucl. Phys. A **968**, 71 (2017), DOI: 10.1016/j.nuclphysa.2017.07.015.

[102] M. Shamsuzzoha Basunia, Nucl. Data Sheets **114**, 1189 (2013), DOI: 10.1016/j.nds.2013.10.001.

[103] M. Berglund and M. E. Wieser, Pure Appl. Chem. **83**, 397 (2011), DOI: 10.1351/PAC-REP-10-06-02.

[104] N. Nica, Nucl. Data Sheets **170**, 1 (2020), DOI: 10.1016/j.nds.2020.11.001.

[105] H. Xiaolong, Nucl. Data Sheets **108**, 1093 (2007), DOI: 10.1016/j.nds.2007.05.001.

[106] P. K. Joshi *et al.*, Nucl. Data Sheets **138**, 1 (2016), DOI: 10.1016/j.nds.2016.11.001.

[107] K. Prifti, *Absolute photon flux determination for nuclear resonance fluorescence experiments above the neutron separation threshold*, Master's thesis (Technische Universität Darmstadt, 2023).

[108] K. Prifti, *Revised analysis of this work's activation data*, Private communication, 2024.

[109]   *Electronic logbook used for documentation of this work's experiment*, 2022,
        URL: https://elog.ikp.physik.tu-darmstadt.de/clovershare (visited on 2024-07-19).

[110]   C. Sun, *Characterizations and Diagnostics of Compton Light Source*, PhD thesis (Duke
        University, 2009),
        URL: https://hdl.handle.net/10161/1579.

[111]   H. Junde, H. Su, and Y. Dong, Nucl. Data Sheets **112**, 1513 (2011),
        DOI: 10.1016/j.nds.2011.04.004.

[112]   M. J. Martin, Nucl. Data Sheets **114**, 1497 (2013),
        DOI: 10.1016/j.nds.2013.11.001.

[113]   F. Lüke, *mvme – mesytec VME data acquisition*, version 1.4.5, mesytec GmbH & Co. KG,
        2022,
        URL: https://github.com/flueke/mvme (visited on 2024-07-19).

[114]   F. Lüke, *mvme – mesytec VME data acquisition*, Manual, version 1.14.1.1, mesytec
        GmbH & Co. KG (2024-19),
        URL: https://mesytec.com/downloads/mvme/mvme.pdf (visited on 2024-07-19).

[115]   Python Software Foundation, *The Python Language Reference*, version 3.11, 2022,
        URL: https://docs.python.org/3.11/reference (visited on 2024-07-19).

[116]   Python Software Foundation, *CPython*, version 3.11.3, 2023,
        URL: https://python.org (visited on 2024-07-19).

[117]   R. Kumar *et al.*, J. Open Source Softw. **4**, 1143 (2019),
        DOI: 10.21105/joss.01143.

[118]   O. A. Martin *et al.*, *ArviZ: Exploratory analysis of Bayesian models with Python*, ver-
        sion 0.17.0, 2023,
        DOI: 10.5281/zenodo.10436212,
        URL: https://github.com/arviz-devs/arviz.

[119]   H. Schreiner, S. Liu, and A. Goel, *Hist: Histogramming for analysis powered by boost-
        histogram*, version 2.7.2, 2023,
        DOI: 10.5281/zenodo.8338901,
        URL: https://github.com/scikit-hep/hist.

[120]   Jupyter Widgets Team, *ipywidgets: Interactive Widgets for the Jupyter Notebook*, ver-
        sion 8.1.1, 2023,
        URL: https://github.com/jupyter-widgets/ipywidgets.

[121]   T. Kluyver *et al.*, in Positioning and Power in Academic Publishing: Players, Agents and
        Agendas, edited by F. Loizides and B. Scmidt (2016), pp. 87–90,
        DOI: 10.3233/978-1-61499-649-1-87.

[122] Project Jupyter, *JupyterLab: JupyterLab computational environment*, version 4.0.10, 2023,
URL: https://github.com/jupyterlab/jupyterlab.

[123] J. D. Hunter, Comput. Sci. Eng. **9**, 90 (2007),
DOI: 10.1109/MCSE.2007.55.

[124] Matplotlib Development Team, *Matplotlib: Visualization with Python*, version 3.8.2, 2023,
DOI: 10.5281/zenodo.10150955,
URL: https://github.com/matplotlib/matplotlib.

[125] C. R. Harris *et al.*, Nature **585**, 357 (2020),
DOI: 10.1038/s41586-020-2649-2.

[126] NumPy Project, *NumPy: The fundamental package for scientific computing with Python*, version 1.26.3, 2024,
URL: https://github.com/numpy/numpy.

[127] D. Phan, N. Pradhan, and M. Jankowiak, arXiv **1912.11554**, 1 (2019),
DOI: 10.48550/arXiv.1912.11554.

[128] E. Bingham *et al.*, J. Mach. Learn. Res. **20**, 1 (2019),
URL: http://jmlr.org/papers/v20/18-403.html.

[129] D. Phan, N. Pradhan, M. Jankowiak, *et al.*, *NumPyro: Probabilistic programming with NumPy powered by JAX for autograd and JIT compilation to GPU/TPU/CPU*, version 0.13.2, 2023,
URL: https://github.com/pyro-ppl/numpyro.

[130] J. Salvatier, T. V. Wiecki, and C. Fonnesbeck, PeerJ Comput. Sci. **2**, e55 (2016),
DOI: 10.7717/peerj-cs.55.

[131] O. Abril-Pla *et al.*, PeerJ Comput. Sci. **9**, e1516 (2023),
DOI: 10.7717/peerj-cs.1516.

[132] T. Wiecki *et al.*, *PyMC: Bayesian Modeling and Probabilistic Programming in Python*, version 5.10.3, 2023,
DOI: 10.5281/zenodo.10418134,
URL: https://github.com/pymc-devs/pymc.

[133] P. Virtanen *et al.*, Nat. Methods **17**, 261 (2020),
DOI: 10.1038/s41592-019-0686-2.

[134] R. Gommers *et al.*, *SciPy*, version v1.11.4, 2023,
DOI: 10.5281/zenodo.10155614,
URL: https://github.com/scipy/scipy.

[135] E. O. Lebigot, *Uncertainties: a Python package for calculations with uncertainties*, version 3.1.7, 2022,
URL: https://github.com/lmfit/uncertainties.

[136] J. Pivarski *et al.*, *Uproot: ROOT I/O in pure Python and NumPy*, version 5.2.2, 2024,
DOI: 10.5281/zenodo.10573980,
URL: https://github.com/scikit-hep/uproot5.

[137] R. Brun and F. Rademakers, Nucl. Instrum. Meth. A **389**, 81 (1997),
DOI: 10.1016/S0168-9002(97)00048-X.

[138] I. Antcheva *et al.*, Comput. Phys. Commun. **180**, 2499 (2009),
DOI: 10.1016/j.cpc.2009.08.005.

[139] J. Mayer *et al.*, *HDTV: Nuclear spectrum analysis tool*, version 24.01, 2024,
URL: https://github.com/janmayer/hdtv (visited on 2024-07-19).

[140] U. Friman-Gayer, J. Kleemann, and O. Papst, *utr: Geant4 simulation of the Upper Target Room (UTR) at the HIGS facility*, version 2024.01, 2024,
DOI: 10.5281/zenodo.10837233,
URL: https://github.com/u-eff-gee/utr.

[141] S. Agostinelli *et al.* (Geant4 collaboration), Nucl. Instrum. Methods Phys. Res. A **506**, 250 (2003),
DOI: 10.1016/S0168-9002(03)01368-8.

[142] J. Allison *et al.* (Geant4 collaboration), IEEE Trans. Nucl. Sci. **53**, 270 (2006),
DOI: 10.1109/TNS.2006.869826.

[143] J. Allison *et al.* (Geant4 collaboration), Nucl. Instrum. Methods Phys. Res. A **835**, 186 (2016),
DOI: 10.1016/j.nima.2016.06.125.

[144] G. Knoll, *Radiation Detection and Measurement*, 4th ed. (John Wiley & Sons, New York, NY, USA, 2010), ISBN: 978-0-470-13148-0.

[145] G. R. Gilmore, *Practical Gamma-ray Spectroscopy*, 2nd ed. (John Wiley & Sons, New York, NY, USA, 2008), ISBN: 978-0-470-86196-7,
DOI: 10.1002/9780470861981.

[146] E. Browne and J. K. Tuli, Nucl. Data Sheets **114**, 1849 (2013),
DOI: 10.1016/j.nds.2013.11.002.

[147] International Atomic Energy Agency, *Database of Prompt Gamma Rays from Slow Neutron Capture for Elemental Analysis* (International Atomic Energy Agency, Vienna, Austria, 2007), ISBN: 978-920101306-4,
URL: https://iaea.org/publications/7030.

[148] National Nuclear Data Center, *Thermal Neutron Capture γ's (CapGam)*, Brookhaven National Laboratory, Upton, NY, USA,
URL: https://nndc.bnl.gov/capgam (visited on 2024-07-23).

[149] J. Chen, Nucl. Data Sheets **140**, 1 (2017),
DOI: 10.1016/j.nds.2017.02.001.

[150] M. J. Martin, Nucl. Data Sheets **108**, 1583 (2007),
DOI: 10.1016/j.nds.2007.07.001.

[151] J. Mayer *et al.*, Nucl. Instrum. Methods Phys. Res. A **972**, 164102 (2020),
DOI: 10.1016/j.nima.2020.164102.

[152] B. Blank *et al.*, Nucl. Instrum. Methods Phys. Res. A **776**, 34 (2015),
DOI: 10.1016/j.nima.2014.12.071.

[153] S. Hurtado, M. García-León, and R. García-Tenorio, Nucl. Instrum. Methods Phys. Res. A **518**, 764 (2004),
DOI: 10.1016/j.nima.2003.09.057.

[154] G. Gosta *et al.*, Nucl. Instrum. Methods Phys. Res. A **879**, 92 (2018),
DOI: 10.1016/j.nima.2017.10.018.

[155] M. Hult *et al.*, Appl. Radiat. Isot. **147**, 182 (2019),
DOI: 10.1016/j.apradiso.2019.02.019.

[156] R. Berndt and P. Mortreau, Nucl. Instrum. Methods Phys. Res. A **694**, 341 (2012),
DOI: 10.1016/j.nima.2012.07.006.

[157] D. Savran *et al.*, Phys. Rev. C **106**, 044324 (2022),
DOI: 10.1103/PhysRevC.106.044324.

[158] B. Löher, *Probing the Decay Characteristics of the Pygmy Dipole Resonance in the Semi-Magic Nucleus* ^{140}Ce *with γ-γ Coincidence Measurements*, doctoral thesis (Johannes Gutenberg-Universität Mainz, 2014),
DOI: 10.25358/openscience-2861.

[159] J. Isaak, *Investigation of decay properties of the Pygmy Dipole Resonance and photon strength functions on excited states in (γ̅, γ′γ″) reactions*, doctoral thesis (Johannes Gutenberg-Universität Mainz, 2016),
DOI: 10.25358/openscience-4613.

[160] A. Gelman *et al.*, *Bayesian data analysis*, 3rd ed. (Chapman & Hall/CRC, 2014), ISBN: 978-1-4398-4095-5.

[161] S. Brooks *et al.*, *Handbook of Markov Chain Monte Carlo* (Chapman and Hall/CRC, 2011), ISBN: 978-0-429-13850-8,
DOI: 10.1201/b10905.

[162] S. C. Fultz *et al.*, Phys. Rev. **127**, 1273 (1962),
DOI: 10.1103/PhysRev.127.1273.

[163] W. J. Huang *et al.*, Chin. Phys. C **45**, 030002 (2021),
DOI: 10.1088/1674-1137/abddb0.

[164] M. Wang *et al.*, Chin. Phys. C **45**, 030003 (2021),
DOI: 10.1088/1674-1137/abddaf.

[165] V. Yu. Ponomarev and A. Krasznahorkay, Nucl. Phys. A **550**, 150 (1992),
DOI: 10.1016/0375-9474(92)91136-D.

[166] L. M. Donaldson *et al.*, Phys. Lett. B **776**, 133 (2018),
DOI: 10.1016/j.physletb.2017.11.025.

[167] K. Goeke and J. Speth, Annu. Rev. Nucl. Part. Sci. **32**, 65 (1982),
DOI: 10.1146/annurev.ns.32.120182.000433.

[168] P. von Neumann-Cosel *et al.*, Eur. Phys. J. A **55**, 224 (2019),
DOI: 10.1140/epja/i2019-12795-1.

[169] W. L. Lv, Y. F. Niu, and G. Colò, Phys. Rev. C **103**, 064321 (2021),
DOI: 10.1103/PhysRevC.103.064321.

[170] A. Bohr and B. R. Mottelson, *Nuclear Structure Volume II* (W.A. Benjamin, Inc., 1975),
ISBN: 978-0-8053-1016-0.

[171] B. Pritychenko *et al.*, At. Data Nucl. Data Tables **107**, 1 (2016),
DOI: 10.1016/j.adt.2015.10.001.

[172] W. Greiner and J. A. Maruhn, *Nuclear Models* (Springer Berlin, Heidelberg, Berlin, Germany, 1996), ISBN: 978-3-540-59180-1,
DOI: 10.1007/978-3-642-60970-1.

[173] R. F. Casten, *Nuclear Structure from a Simple Perspective* (Oxford University Press, 1990),
ISBN: 978-0-19-504599-4.

[174] S. Gjorgievska *et al.*, Nucl. Eng. Des. **426**, 113403 (2024),
DOI: 10.1016/j.nucengdes.2024.113403.

[175] I. Angeli, At. Data Nucl. Data Tables **87**, 185 (2004),
DOI: 10.1016/j.adt.2004.04.002.

[176] T. Otsuka *et al.*, Phys. Rev. Lett. **123**, 222502 (2019),
DOI: 10.1103/PhysRevLett.123.222502.

[177] T. Otsuka *et al.*, arXiv **2303.11299**, 1 (2024),
DOI: 10.48550/arXiv.2303.11299.

[178]   K. S. Krane, *Introductory Nuclear Physics*, en, 3rd ed. (John Wiley & Sons, 1987), ISBN: 978-0-471-80553-3.

[179]   K. E. G. Löbner, M. Vetter, and V. Hönig, At. Data Nucl. Data Tables **7**, 495 (1970), DOI: 10.1016/S0092-640X(18)30059-7.

[180]   E. Grosse, A. R. Junghans, and R. Massarczyk, Eur. Phys. J. A **53**, 225 (2017), DOI: 10.1140/epja/i2017-12415-2.

[181]   E. Grosse, A. R. Junghans, and J. N. Wilson, Phys. Scr. **92**, 114003 (2017), DOI: 10.1088/1402-4896/aa8607.

[182]   M. Lettmann *et al.*, Phys. Rev. C **96**, 011301(R) (2017), DOI: 10.1103/PhysRevC.96.011301.

[183]   Y. Toh *et al.*, Phys. Rev. C **87**, 041304(R) (2013), DOI: 10.1103/PhysRevC.87.041304.

[184]   L. Guo, J. A. Maruhn, and P.-G. Reinhard, Phys. Rev. C **76**, 034317 (2007), DOI: 10.1103/PhysRevC.76.034317.

[185]   A. D. Ayangeakaa *et al.*, Phys. Rev. C **107**, 044314 (2023), DOI: 10.1103/PhysRevC.107.044314.

[186]   A. Hayashi, K. Hara, and P. Ring, Phys. Rev. Lett. **53**, 337 (1984), DOI: 10.1103/PhysRevLett.53.337.

[187]   F. Iachello, Phys. Rev. Lett. **87**, 052502 (2001), DOI: 10.1103/PhysRevLett.87.052502.

[188]   N. Pietralla and O. M. Gorbachenko, Phys. Rev. C **70**, 011304(R) (2004), DOI: 10.1103/PhysRevC.70.011304.

[189]   R. F. Casten and N. V. Zamfir, Phys. Rev. Lett. **87**, 052503 (2001), DOI: 10.1103/PhysRevLett.87.052503.

[190]   R. Krücken *et al.*, Phys. Rev. Lett. **88**, 232501 (2002), DOI: 10.1103/PhysRevLett.88.232501.

[191]   T. Möller *et al.*, Phys. Rev. C **86**, 031305(R) (2012), DOI: 10.1103/PhysRevC.86.031305.

[192]   A. Krugmann *et al.*, J. Phys. G: Nucl. and Part. Phys. **38**, 065102 (2011), DOI: 10.1088/0954-3899/38/6/065102.

[193]   P. Carlos *et al.*, Nucl. Phys. A **172**, 437 (1971), DOI: 10.1016/0375-9474(71)90725-1.

Acknowledgements

Finally, I would like to express my gratitude to all those who have supported me throughout these past years, whether directly or indirectly. Their unwavering encouragement and assistance have been invaluable, and without them, this work would not have been possible.

First and foremost, I am deeply indebted to my supervisor, **Prof. Dr. Dr. h. c. mult. Norbert Pietralla**, who granted me the opportunity to pursue a doctoral degree and has been a constant source of guidance, support, and great ideas throughout this journey. Years ago, he sparked my interest in nuclear physics and welcomed me into his research group during my undergraduate studies. Since then, he has continuously provided me with fascinating and challenging research topics, first for my Bachelor's and Master's theses and finally for my doctoral research project culminating in this dissertation. Throughout this time, he has always encouraged me to pursue my interests, challenged me to strive further, and ultimately helped me grow as a scientist. I am also thankful for the opportunities he provided me with to attend several international conferences, where I was able to present my work and learn from the broader scientific community. Furthermore, he also enabled me to participate in various experiments at unique facilities around the world, opportunities from which I gained invaluable experience. His guidance, expertise, and encouragement have not only shaped this dissertation but also significantly influenced my personal and professional development. I am very grateful for the many opportunities to discuss, learn, and grow under his mentorship.

Next, I would like to thank **Dr. Volker Werner** for his continuous assistance, guidance, and encouragement throughout my time in Prof. Pietralla's research group. As my initial point of contact, he led me to join the group and has been an invaluable mentor ever since. Not only did he consistently offer helpful advice and feedback, but also an open ear to my questions and concerns, regardless of how trivial they might have

seemed. In particular, he allowed me to both vent my frustrations and share my excitement, whenever necessary. Thus, he has been a pillar to rely on throughout my time in the group for which I am very grateful.

Likewise, I would like to express my gratitude to **Dr. Johann Isaak** for many of the same reasons. Alongside Volker, he has been my go-to person for questions, advice, and feedback, always willing to assist and provide valuable input to my work. In particular, I am thankful for his efforts in organizing and his support in conducting this work's experiment at the HIγS facility in times of the COVID-19 pandemic. Without his dedication, this project would not have been possible

Another person to whom I owe a great deal of gratitude for making this work possible is my former office mate **Dr. Udo Friman-Gayer**. After receiving his doctorate in Prof. Pietralla's group, he moved to the U.S. to work at HIγS just before the onset of the pandemic. Despite the challenging circumstances, he then willingly served as my local substitute, conducting this work's experiment on my physical behalf at HIγS. His commitment was instrumental to the success of this project.

Speaking of long-time office mates, I would also like to thank **Dr. Tobias Beck** and **Dr. Oliver Papst**, alongside Udo, for their friendship, support, and our many fruitful and sometimes not-so-fruitful, but always entertaining discussions. I have learned a lot from all three of them, not only concerning science but also life in general. For instance, Udo laid much of the groundwork regarding Monte Carlo analysis techniques and software tools, which I and many others in the group were able to build upon. Tobias taught me a great deal about theoretical models and concepts, which are essential for understanding the physics behind the data. Oliver and I first met over a decade ago when we began our studies, and we have supported each other throughout our academic journeys, even before becoming office mates. To Oliver, I am especially grateful for sharing his extensive expertise in computational tools and technology with me, which made a significant contribution to this work. The time spent with Udo, Tobias, and Oliver in the office was always a pleasure and left lasting memories.

Returning to the experimental aspects, I am deeply thankful to everyone at HIγS for their efforts in conducting this work's experiment and providing invaluable support during the challenging times of the COVID-19 pandemic. This includes the accelerator group, who provided perfect beam conditions for the experiment, and the local experimental group, who set up the experiment and collected excellent data. In particular, I would like to express my gratitude to **Prof. Dr. Robert Janssens**, **Prof.**

und **Sammy** für ihre enge Freundschaft und Unterstützung bedanken, die für mich von unschätzbarem Wert sind. Ein besonderer Dank gilt meinem Bruder **Christian**, auf den ich mich stets verlassen kann und der mir wann immer nötig mit Rat und Tat zur Seite stand. Für diesen Rückhalt bin ich ihm außerordentlich dankbar. Der abschließende und größte Dank gebührt meinen Eltern, **Claudia** und **Jürgen**, für ihre unermüdliche Unterstützung, ihren steten Zuspruch und ihre bedingungslose Liebe, die sie mir schon mein ganzes Leben lang entgegenbringen. Ohne sie wäre ich niemals so weit gekommen, und es lässt sich kaum in Worte fassen, wie dankbar ich ihnen für alles bin.

Academic Curriculum Vitae

Name: Jörn Nils Kleemann
Date of birth: *Removed in this digital version*
Place of birth: Frankfurt am Main, Germany
Nationality: German
ORCID iD: ⓘ https://orcid.org/0000-0003-2596-3762

Higher Education

2019–2024   **Doctoral studies at the Institute for Nuclear Physics, Department of Physics, Technische Universität Darmstadt, Darmstadt, Germany**
Degree: Dr. rer. nat.
Specialization: Experimental nuclear structure physics
Thesis supervisor: Prof. Dr. Dr. h. c. mult. Norbert Pietralla
Thesis title: *Probing the Giant Dipole Resonance Using Nuclear Resonance Fluorescence*
Overall grade: *Excellent*

2016–2018   **Master studies in Physics at the Technische Universität Darmstadt, Darmstadt, Germany**
Degree: Master of Science
Specialization: Nuclear physics
Thesis supervisor: Prof. Dr. Dr. h. c. mult. Norbert Pietralla
Thesis title: *Decay Characteristics of the Scissors Mode of the $0\nu\beta\beta$-Decay Mother ^{150}Nd*
Thesis grade: 1.0 (*very good*)
Overall grade: 1.21 (*very good*)

2013–2016	**Bachelor studies in Physics at the Technische Universität Darmstadt, Darmstadt, Germany**
	Degree: Bachelor of Science
	Thesis supervisor: Prof. Dr. Dr. h. c. mult. Norbert Pietralla
	Thesis title: *Zerfallsverhalten der Scherenmode in der $0\nu\beta\beta$-Tochter ^{150}Sm*
	Thesis grade: 1.0 (*very good*)
	Overall grade: 1.27 (*very good*)
2004–2013	**Secondary school education at the Goethe-Gymnasium, Frankfurt am Main, Germany**
	Degree: Abitur
	Advanced courses: Physics, mathematics and English
	Bilingual English classes: History and biology classes in English, Obtained the international Baccalaureate Diploma in English
	Overall grade: 1.0 (*very good*)

Awards

2015–2017	**Deutschlandstipendium scholarship of the Technische Universität Darmstadt**
	Supported by the Bosch Rexroth AG
2013–2014	**Deutschlandstipendium scholarship of the Technische Universität Darmstadt**
	Supported by the Dr. Ing. Wilhelm und Maria Kirmser foundation

Peer-Reviewed Publications

[A1] T. Beck, V. Werner, N. Pietralla, M. Bhike, N. Cooper, U. Friman-Gayer, J. Isaak, R. V. Jolos, **J. Kleemann**, Krishichayan, O. Papst, W. Tornow, C. Bernards, B. P. Crider, R. S. Ilieva, B. Löher, C. Mihai, F. Naqvi, S. Pascu, E. E. Peters, F. M. Prados-Estevez, T. J. Ross, D. Savran, J. R. Vanhoy and A. Zilges, Phys. Rev. Lett. **125**, 092501 (2020), DOI: 10.1103/PhysRevLett.125.092501.

[A2]   O. Papst, V. Werner, J. Isaak, N. Pietralla, T. Beck, C. Bernards, M. Bhike, N. Cooper, B. P. Crider, U. Friman-Gayer, **J. Kleemann**, Krishichayan, B. Löher, F. Naqvi, E. E. Peters, F. M. Prados-Estévez, R. S. Ilieva, T. J. Ross, D. Savran, W. Tornow and J. R. Vanhoy, Phys. Rev. C **102**, 034323 (2020), DOI: 10.1103/PhysRevC.102.034323.

[A3]   J. Sinclair, M. Scheck, S. W. Finch, Krishichayan, U. Friman-Gayer, W. Tornow, G. Battaglia, T. Beck, R. Chapman, M. M. R. Chishti, C. Fransen, R. Gonzales, E. Hoemann, J. Isaak, R. V. F. Janssens, D. A. Jaroszynski, S. Johnson, M. D. Jones, J. M. Keatings, N. Kelly, **J. Kleemann**, D. Little, B. Löher, K. R. Mashtakov, M. Müscher, D. O'Donnell, O. Papst, E. E. Peters, D. Savran, M. Schilling, R. Schwengner, P. Spagnoletti, M. Spieker, V. Werner, J. Wilhelmy, O. Wieland, S. W. Yates and A. Zilges, Eur. Phys. J. A **56**, 105 (2020), DOI: 10.1140/epja/s10050-020-00118-8.

[A4]   A. Yaneva, D. Kocheva, G. Rainovski, J. Jolie, N. Pietralla, A. Blazhev, A. Dewald, M. Djongolov, C. Fransen, K. A. Gladnishki, C. Henrich, I. Homm, K. E. Ide, P. R. John, D. Kalaydjieva, V. Karayonchev, R. Kern, **J. Kleemann**, T. Kröll, C. Müller-Gatermann, M. Scheck, P. Spagnoletti, M. Stoyanova and V. Werner, Eur. Phys. J. A **56**, 246 (2020), DOI: 10.1140/epja/s10050-020-00259-w.

[A5]   K. E. Ide, T. Beck, V. Werner, M. Berger, S. W. Finch, U. Friman-Gayer, **J. Kleemann**, Krishichayan, B. Löher, O. Papst, N. Pietralla, D. Savran, W. Tornow, M. Weinert, J. Wiederhold and A. Zilges, Phys. Rev. C **103**, 054302 (2021), DOI: 10.1103/PhysRevC.103.054302.

[A6]   D. Kalaydjieva, D. Kocheva, G. Rainovski, V. Karayonchev, J. Jolie, N. Pietralla, M. Beckers, A. Blazhev, A. Dewald, M. Djongolov, A. Esmaylzadeh, C. Fransen, K. A. Gladnishki, A. Goldkuhle, C. Henrich, I. Homm, K. E. Ide, P. R. John, R. Kern, **J. Kleemann**, T. Kröll, C. Müller-Gatermann, M. Scheck, P. Spagnoletti, M. Stoyanova, K. Stoychev, V. Werner, A. Yaneva, S. S. Dimitrova, G. De Gregorio, H. Näidja and A. Gargano, Phys. Rev. C **104**, 024311 (2021), DOI: 10.1103/PhysRevC.104.024311.

[A7]   **J. Kleemann**, T. Beck, U. Friman-Gayer, N. Pietralla, V. Werner, S. W. Finch, J. Kotila, Krishichayan, B. Löher, H. Pai, O. Papst, W. Tornow, M. Weinert and A. Zilges, Phys. Rev. C **104**, L061302 (2021), DOI: 10.1103/PhysRevC.104.L061302.

[A8]   R. Schwengner, R. Massarczyk, M. Scheck, W. Tornow, G. Battaglia, T. Beck, D. Bemmerer, N. Benouaret, R. Beyer, M. Butterling, F. Fiedler, S. W. Finch, C. Fransen, U. Friman-Gayer, A. Frotscher, R. Gonzalez, M. Grieger, A. Hartmann, T. Hensel, E. Hoemann, H. Hoffmann, R. V. F. Janssens, S. Johnson, M. D. Jones, A. R. Junghans, N.

Kelly, **J. Kleemann**, Krishichayan, D. R. Little, F. Ludwig, S. E. Müller, D. O'Donnell, O. Papst, E. Pirovano, J. Sinclair, M. P. Takács, S. Turkat, S. Urlaß, A. Wagner, V. Werner, O. Wieland and J. Wilhelmy, Phys. Rev. C **103**, 024312 (2021),
DOI: 10.1103/PhysRevC.103.024312.

[A9]   D. Savran, J. Isaak, R. Schwengner, R. Massarczyk, M. Scheck, W. Tornow, G. Battaglia, T. Beck, S. W. Finch, C. Fransen, U. Friman-Gayer, R. Gonzalez, E. Hoemann, R. V. F. Janssens, S. R. Johnson, M. D. Jones, **J. Kleemann**, Krishichayan, D. R. Little, D. O'Donnell, O. Papst, N. Pietralla, J. Sinclair, V. Werner, O. Wieland and J. Wilhelmy, Phys. Rev. C **106**, 044324 (2022),
DOI: 10.1103/PhysRevC.106.044324.

[A10] A. Tamii, L. Pellegri, P.-A. Söderström, D. Allard, S. Goriely, T. Inakura, E. Khan, E. Kido, M. Kimura, E. Litvinova, S. Nagataki, P. v. Neumann-Cosel, N. Pietralla, N. Shimizu, N. Tsoneva, Y. Utsuno, S. Adachi, P. Adsley, A. Bahini, D. Balabanski, B. Baret, J. A. C. Bekker, S. D. Binda, E. Boicu, A. Bracco, I. Brandherm, M. Brezeanu, J. W. Brummer, F. Camera, F. C. L. Crespi, R. Dalal, L. M. Donaldson, Y. Fujikawa, T. Furuno, H. Haoning, R. Higuchi, Y. Honda, A. Gavrilescu, A. Inoue, J. Isaak, H. Jivan, P. Jones, S. Jongile, O. Just, T. Kawabata, T. Khumalo, J. Kiener, **J. Kleemann**, N. Kobayashi, Y. Koshio, A. Kuşoğlu, K. C. W. Li, K. L. Malatji, R. E. Molaeng, H. Motoki, M. Murata, A. A. Netshiya, R. Neveling, R. Niina, S. Okamoto, S. Ota, O. Papst, E. Parizot, T. Petruse, M. S. Reen, P. Ring, K. Sakanashi, E. Sideras-Haddad, S. Siem, M. Spall, T. Suda, T. Sudo, Y. Taniguchi, V. Tatischeff, H. Utsunomiya, H. Wang, V. Werner, H. Wibowo, M. Wiedeking, O. Wieland, Y. Xu, Z. H. Yang and P. Collaboration, Eur. Phys. J. A **59**, 208 (2023),
DOI: 10.1140/epja/s10050-023-01081-w.

[A11] M. Beuschlein, V. Werner, U. Friman-Gayer, **J. Kleemann**, O. Papst, N. Pietralla, E. Açiksöz, U. Ahmed, S. Aslanidou, L. Atar, T. Beck, M. Berger, I. Brandherm, D. Choudhury, A. Coban, M. L. Cortés, A. D'Alessio, J. Hauf, M. Hilcker, K. E. Ide, J. Isaak, I. Jurosevic, P. Koseoglou, R. Kern, C. Kremer, C. M. Nickel, F. Niederschuh, H. Pai, K. Prifti, P. C. Ries, G. Steinhilber, T. Stetz, M. Tamkas, M. Thürauf, J. Vogel, J. Wiederhold, R. Zidarova and M. Zweidinger, Phys. Rev. C **110**, 054304 (2024),
DOI: 10.1103/PhysRevC.110.054304.

[A12] **J. Kleemann**, N. Pietralla, U. Friman-Gayer, J. Isaak, O. Papst, K. Prifti, V. Werner, A. D. Ayangeakaa, T. Beck, G. Colò, M. L. Cortés, S. Finch, M. Fulghieri, D. Gribble, K. E. Ide, X. K.-H. James, R. V. F. Janssens, S. Johnson, P. Koseoglou, Krishichayan, D. Savran and W. Tornow, Phys. Rev. Lett., to be published (2025), arXiv:2406.19695.

Conference Proceedings

[C1]   U. Gayer, V. Werner, T. Beck, S. Finch, **J. Kleemann**, Krishichayan, B. Löher, O. Papst, N. Pietralla, P. C. Ries, D. Savran, M. Weinert and W. Tornow, EPJ Web Conf. **194**, 02004 (2018),
DOI: 10.1051/epjconf/201819402004.

[C2]   V. Werner, U. Gayer, **J. Kleemann**, T. Beck, M. Bhike, V. Derya, J. Isaak, Krishichayan, B. Löher, L. Mertes, H. Pai, O. Papst, N. Pietralla, P. C. Ries, C. Romig, D. Savran, M. Schilling, W. Tornow, J. Wilhelmy and M. Zweidinger, J. Phys. Conf. Ser. **1056**, 012061 (2018),
DOI: 10.1088/1742-6596/1056/1/012061.

[C3]   M. Stoyanova, V. Karayonchev, G. Rainovski, J. Jolie, N. Pietralla, A. Blazhev, A. Dewald, M. Djongolov, A. Esmaylzadeh, C. Fransen, J. Garbe, L. Gerhard, K. A. Gladnishki, K. Ide, P. R. John, R. Kern, **J. Kleemann**, D. Kocheva, T. Kröll, C. Müller-Gatermann, J.-M. Régis, P. Spagnoletti, V. Werner and A. Yaneva, J. Phys. Conf. Ser. **1555**, 012019 (2020),
DOI: 10.1088/1742-6596/1555/1/012019.

[C4]   P. Koseoglou, M. L. Cortés, J. Isaak, V. Werner, O. Papst, **J. Kleemann**, M. Beuschlein, N. Pietralla, U. Ahmed, K. E. Ide, I. Jurosevic, C. Nickel, M. Spall, T. Stetz and R. Zidarova, HNPS Adv. Nucl. Phys. **28**, 154 (2022),
DOI: 10.12681/hnps.3717.

Datasets

[D1]   **J. Kleemann**, N. Pietralla, U. Friman-Gayer, J. Isaak, O. Papst, K. Prifti, V. Werner, A. D. Ayangeakaa, T. Beck, G. Colò, M. L. Cortés, S. Finch, M. Fulghieri, D. Gribble, K. E. Ide, X. K.-H. James, R. V. F. Janssens, S. Johnson, P. Koseoglou, Krishichayan, D. Savran and W. Tornow, *Dataset and Analysis Codes for "Gamma decay of the* ^{154}*Sm Isovector Giant Dipole Resonance: Smekal-Raman Scattering as a Novel Probe of Nuclear Ground-State Deformation"*, TUdatalib, Technische Universität Darmstadt, 2024,
DOI: 10.48328/tudatalib-1472.